Data Integrity and Electronic Calibrations for the Neutral Current Detector Phase Measurement of the 8B Solar Neutrino Flux at the Sudbury Neutrino Observatory

Gary A. Cox-Mobrand

A dissertation submitted in partial fulfillment
of the requirements for the degree of

Doctor of Philosophy

University of Washington

2008

Program Authorized to Offer Degree: Physics

University of Washington
Graduate School

This is to certify that I have examined this copy of a doctoral dissertation by

Gary A. Cox-Mobrand

and have found that it is complete and satisfactory in all respects,
and that any and all revisions required by the final
examining committee have been made.

Chair of the Supervisory Committee:

John F. Wilkerson

Reading Committee:

John F. Wilkerson

R. G. Hamish Robertson

Jens H. Gundlach

Date:

Signature____________________________

Date_______________________________

University of Washington

Abstract

Data Integrity and Electronic Calibrations for the Neutral Current Detector Phase Measurement of the 8B Solar Neutrino Flux at the Sudbury Neutrino Observatory

Gary A. Cox-Mobrand

Chair of the Supervisory Committee:
Professor John F. Wilkerson
Physics

The Sudbury Neutrino Observatory (SNO) is a heavy water Cherenkov detector that observed solar neutrinos via elastic-scattering, charge-current and neutral-current interactions. SNO was designed to measure the flux the total ^{8}B solar neutrino flux in three separate phases, making each measurement under a different set of detector conditions and detection mechanisms. In the third phase, an array of ^{3}He proportional counters was installed, called Neutral Current Detectors (NCDs), which detected neutrons liberated in the neutral-current interactions with deuterium.

The neutrino flux can be measured in the NCD phase by identification of neutron capture events via pulse-shape analysis techniques. To accomplish this, the transformation of the neutron capture signals caused by the NCD electronics and data acquisition system (NCD DAQ) must be well known. The NCD DAQ electronics model was developed and quantified, resulting in a small contribution to the systematic uncertainties of neutron identification. Of the four currently proposed neutron identification methods, the parameters which characterize the logarithmic amplification of pulse shapes contribute 1.65%, 0.65%, 0.05% and 0.0% to the systematic uncertainty in the number of identified neutrons.

A mechanical problem in two NCDs was discovered that caused the detectors to disconnect from the signal cable with little evidence of being disconnected. The work presented here identified two NCDs that suffered from this mechanical problem and estimated the amount of time that each NCD was disconnected. The remaining NCDs are shown to be unaffected by this problem and an upper limit on the amount of time disconnected was estimated. This was accomplished by an analysis of the rate of thermal noise triggers, an instrumental background noise event. The detected rates of background alphas were also measured to test for anomalously low rates. It was determined that these two NCDs should be removed from the final neutrino flux analysis, with an estimate that their exclusion improved the accuracy of the NCD phase neutrino flux measurement by 1.5%.

TABLE OF CONTENTS

Page

List of Figures iv

List of Tables viii

Glossary ix

Chapter 1: Introduction 1
  1.1 Solar Neutrinos 2
  1.2 Previous Solar Neutrino Flux Measurements 4
  1.3 Neutrino Oscillations 8

Chapter 2: The Sudbury Neutrino Observatory 14
  2.1 Detector Overview 14
  2.2 Combined Neutrino Oscillation Measurements 22
  2.3 An Independent Solar Neutrino Flux Measurement: Phase III 23

Chapter 3: The Neutral Current Detectors 27
  3.1 Overview 27
  3.2 NCD Array Description 28
  3.3 Signal and Backgrounds 35

Chapter 4: NCD Data Acquisition 48
  4.1 Data Acquisition Goals and Overview 48
  4.2 Signal Readout Hardware 50
  4.3 Supporting Hardware and Software 57
  4.4 Electronics Calibration Hardware 63

Chapter 5: The NCD Empirical Electronics Model and Electronics Calibrations 65
- 5.1 The Electronics Model 66
- 5.2 Electronics Calibration Introduction 77
- 5.3 Weekly Calibration Routines 80
- 5.4 Analysis Procedures and Results 85
- 5.5 Conclusion 100

Chapter 6: Resistive Coupler Disconnect 104
- 6.1 Overview 104
- 6.2 The Resistive Coupler and NCD Cable Bell 104
- 6.3 An Observation of Event Rate Change 109
- 6.4 The NCD Resistive Coupler Disconnect Electronics Calibration . . . 113
- 6.5 Conclusions 114

Chapter 7: Background Event Analysis 117
- 7.1 Electronic Noise Events 117
- 7.2 Baseline Noise Event Rates 118
- 7.3 Data Set for Noise Analysis 120
- 7.4 Selecting Baseline Noise Type Events 122
- 7.5 Data Selection 135
- 7.6 Analysis Procedure 137
- 7.7 Noise Event Distributions 140
- 7.8 Estimates and Limits on RCD Dead-time 151
- 7.9 Noise Rate Analysis Conclusions 155

Chapter 8: Examination of Alpha Rates 157
- 8.1 Expected Rate of Alphas Through NCD Phase 160
- 8.2 Binned Average Rates 164
- 8.3 Alpha Rate Model 169
- 8.4 Alpha Rate Monte Carlo 172
- 8.5 Constant Rate Fits to NCD Data 177
- 8.6 Conclusions of the Constant Rate Measurements 185

Chapter 9: Conclusions: Impact On The Neutral Current Flux Measurement 188
9.1 Improvements to the Methods 188
9.2 Logamp Calibration Parameter Impact on Systematic Uncertainties in the Neutrino Flux 190
9.3 Comparison of RCD Observational Methods 193
9.4 RCD Impact 194
9.5 Runs Removed From The Final Data Set 196
9.6 Final Remarks 197

Bibliography 198

Appendix A: Removed NCDs 204

Appendix B: Pulse Reflections 206
B.1 Pulse Reflections Between Two Mediums with Different Impedance . 206
B.2 NCD Reflections 207
B.3 The Third Reflection 210
B.4 The Final Reflection Equation 211

Appendix C: NCD String Number to String Name Conversion 212

Appendix D: Detector Performance 213
D.1 Oscilloscope Trigger Checks 213
D.2 Shaper/ADC Acquisition Checks 216

Appendix E: Noise Analysis Fits 220

LIST OF FIGURES

Figure Number Page

1.1 The Solar Proton-Proton fusion reaction chain. 3
1.2 Solar Neutrino Flux Spectrum. 5

2.1 SNO Detector Schematic. 16
2.2 SNO Phase I Event Observable Distributions 21
2.3 Global best-fit two-neutrino solar neutrino oscillation parameters . . . 25
2.4 Global best-fit neutrino oscillation parameters with iso-CC/NC flux contours. 26

3.1 SNO + NCD Schematic. 29
3.2 Schematic of a Neutral Current Detector 31
3.3 NCD Array. 34
3.4 Decay chain for ^{238}U and ^{232}Th. 38
3.5 NCD energy spectrum. 40
3.6 Specific energy loss for two alphas, a triton and proton in the NCD gas. 42
3.7 Two alpha events at different track orientations. 44
3.8 Two events with energies of 770 keV. 45
3.9 Z-position peaks in an alpha event. 47

4.1 The NCD Data Acquisition System 49
4.2 NCD cable bell diagram. 51
4.3 The resistive coupler diagram. 52

5.1 NCD Electronics Model 67
5.2 Preamplifier Model. 69
5.3 Shaper/ADC data model. 70
5.4 MUX/Logamp/Scope Electronics Model. 72
5.5 Electronics Calibration Pulse Generator Model. 76
5.6 Electronic calibration square wave reflections example. 77

5.7 The logamp calibration pulse. 81
5.8 Logamp calibration sine wave simulation. 88
5.9 Logamp calibration fitting. 90
5.10 Logamp calibration results for NCD string 22; parameters a, b, and c. 91
5.11 Logamp calibration results for NCD string 22; parameters Δt and $V^{ADC}_{PreTrig}$. 92
5.12 Logamp calibration results for run 54278; parameters a, b, and c. . . . 94
5.13 Logamp calibration results for run 54278; parameters Δt and $V^{ADC}_{PreTrig}$. 95
5.14 Gaussian fit to measured logamp parameters a on NCD string 2. . . . 96
5.15 Measured logamp parameter a on NCDs 1 and 31. 97
5.16 The average NCD string 31 logamp calibration trigger pulses in runs 55665 and 55610. 98
5.17 Threshold calibration example; NCD string 16, run 54532. 101
5.18 Linearity calibration example; NCD string 15. 102
5.19 Extended linearity example. 102
5.20 Non-log behavior in the log amplifier. 103

6.1 The resistive coupler diagram. 105
6.2 NCD cable bell diagram. 106
6.3 Trigger-Pulse Reflections. 108
6.4 NCD 22 MuxScope event rate during RCD on NCD 31 and 1. 110
6.5 NCD 1 MUX+Scope event rate during RCD on NCD 31 and 1. . . . 111
6.6 NCD 31 MuxScope event rate during RCD on NCD 31 and 1. 112
6.7 RCD during logamp calibration run 62288. 114
6.8 NRE pulse. 115
6.9 NRE Trigger pulse peak difference example. 115
6.10 NRE results. 116

7.1 Examples of common background events. 119
7.2 Noise Analysis Pulse Regions. 124
7.3 Distribution of the amplitude asymmetry for baseline noise events. . . 125
7.4 Distribution of the standard deviation of noise region baseline noise. . 126
7.5 Distribution of the small signal region integration. 127
7.6 Distribution of the Maximum Pulse Amplitude. 128

7.7 Distribution of the standard deviation of noise region baseline noise. . 131
7.8 Distribution of Flatness Parameter for baseline noise. 134
7.9 Examples of Noise Rate Distributions 139
7.10 Noise Rate Distributions 144
7.11 Noise Rate Distributions in Pre-NRE period (NCDs 1, 31 and 36) . . 147
7.12 Noise Rate Distributions in Post-NRE period (NCDs 1, 7, 21, 23, 37 and 31) 149
7.13 Noise Rate Distributions 150

8.1 Estimated rate of alphas in an average 10-m NCD. 165
8.2 Distribution of run lengths in the NCD phase. 168
8.3 Rate of Events with $E > 1.0$ MeV on NCD 10. 171
8.4 Monte Carlo distribution of alphas per day. 174
8.5 Monte Carlo distribution of alphas per day. 175
8.6 Ratio between the Monte Carlo Standard Deviation and $\sqrt{\bar{N}}$. 175
8.7 Distribution of the measured pull in 5000 Monte Carlo ensembles. . . 177
8.8 Residuals to the average number of alphas on NCDs 0, 1, 3 and 8. . . 180
8.9 Residual to the average number of alphas on NCDs 7, 12, 19 and 34. 181
8.10 Residual to the average number of alphas on NCDs 24, 28 and 38. . . 183
8.11 P-value distribution of goodness-of-fit tests for constant alpha rate measurement. 184
8.12 Pull versus NCD for constant alpha rate measurement. 184
8.13 Pull Distribution for constant rate fits. 185

B.1 Two coupled transmission lines. 206
B.2 NCD transmission via resistive coupler. 208
B.3 NCD transmission via resistive coupler. 209
B.4 NCD cable to preamp. 210

D.1 Instances of zero oscilloscope triggers. 215
D.2 Distribution of Δt 217
D.3 Distribution of Δt_{max} 217

E.1 Noise Rate Distributions Fits: Open Data Set NCDs 0 to 8 220
E.2 Noise Rate Distributions Fits: Open Data Set NCDs 9 to 17 221
E.3 Noise Rate Distributions Fits: Open Data Set NCDs 18 to 26 222

E.4 Noise Rate Distributions Fits: Open Data Set NCDs 27 to 35 223
E.5 Noise Rate Distributions Fits: Open Data Set NCDs 36 to 39 224
E.6 Noise Rate Distributions Fits: Pre-NRE Data Set NCDs 0 to 8 225
E.7 Noise Rate Distributions Fits: Pre-NRE Data Set NCDs 9 to 17 . . . 226
E.8 Noise Rate Distributions Fits: Pre-NRE Data Set NCDs 18 to 26 . . 227
E.9 Noise Rate Distributions Fits: Pre-NRE Data Set NCDs 27 to 35 . . 228
E.10 Noise Rate Distributions Fits: Pre-NRE Data Set NCDs 36 to 39 . . 229
E.11 Noise Rate Distributions Fits: Post-NRE Data Set NCDs 0 to 8 . . . 230
E.12 Noise Rate Distributions Fits: Post-NRE Data Set NCDs 9 to 17 . . 231
E.13 Noise Rate Distributions Fits: Post-NRE Data Set NCDs 18 to 26 . . 232
E.14 Noise Rate Distributions Fits: Post-NRE Data Set NCDs 27 to 35 . . 233
E.15 Noise Rate Distributions Fits: Post-NRE Data Set NCDs 36 to 39 . . 234
E.16 Noise Rate Distributions Fits for NCD 36, $T = 240$ min. 235

LIST OF TABLES

Table Number Page

3.1 Some physical characteristics of the NCDs. 32

5.1 Measurement of some NCD electronics model parameters. 79
5.2 Logamp Parameters for NCD 22 in run 54278. 89
5.3 NCDs connected to MUX box number. 93

7.1 Noise Analysis Data Sets 136
7.2 Poisson-fits to noise events in the open data set. 141
7.3 Poisson-fits to noise events in the pre-NRE data set. 142
7.4 Poisson-fits to noise events in the post-NRE data set. 143
7.5 Pre-NRE Expected Number of Zero Event Bins for NCDs 1, 31 and 36. 146
7.6 Estimates of RCD Dead-time on NCDs 1 and 31. 152
7.7 Estimates of RCD Dead-time using $N_{obs} = \sum \hat{A}$. 153
7.8 Estimates of RCD Dead-time using $N_{obs} = \sum N_{120}$. 154

8.1 Alpha Rates and U/Th Contamination in a 10-m NCD. 163
8.2 Estimated rate of $\alpha/\mathrm{m}^2{\cdot}\mathrm{day}$. 167
8.3 Estimated number of alpha events on NCD string 36 for different size time bins. 168
8.4 Calculated values of k for different scenarios of alpha rates. 176
8.5 Constant alpha rate fit results. 179
8.6 Alpha rates more than three standard deviations from the mean. . . . 182

C.1 NCD string number to name conversion. 212

D.1 Instances of locked-out oscilloscopes. 216
D.2 Runs removed by the $\Delta t_{max} > 70$ seconds cut. 218
D.3 Runs removed by the $\Delta t_{max}^{\text{scope } 0/1} > 100$ seconds cut. 218

E.1 Poisson-fits to noise events on NCD 36 for $T = 240$ min. 235

GLOSSARY

CNO CYCLE: The series of hydrogen-burning reactions in the Sun that produces 2% of the Sun's energy.

DAQ: Data Acquisition System

GTID: Global Trigger Identification is a number assigned to each event.

NCD: Neutral Current Detector is a ^{3}He-filled proportional counter that detects thermalized neutrons.

NRE: **N**eutral Current Detector **R**esistive Coupler Disconnect **E**lectronics Calibration was a calibration pulse injected into the NCD preamp to observe RCD.

MSW: The MSW effect (Mikheyev, Smirnov and Wolfentstein) describes the enhancement of neutrino oscillations when neutrinos propagate in matter.

MTC: Master Trigger Card synchronizes the GTIDs in the PMT and NCD DAQs.

MUX: Multiplexer.

ORCA: The Object-orineted Real-time Control and Acquisition software problem which ran the NCD DAQ.

PMT: Photo-multiplier tube

PP CHAIN: The proton-proton fusion chain which provides 98% of the Sun's energy.

QSNO: The C++ based analysis package for SNO that is maintained at Queen's University in Kingston, Ontario.

RCD: Resistive Coupler Disconnect is the situation when the resistive coupler at the junction between the NCD and the NCD cable becomes disconnected.

SNO: Sudbury Neutrino Observatory

SNOMAN: The SNO Monte Carlo and Analysis package used in this work to generate a set of baseline noise events.

SNP: The Solar Neutrino Problem was the discrepancy between the measured and predicted flux of solar neutrinos.

ACKNOWLEDGMENTS

Without the support of many people, this dissertation would have not been completed. I have colleagues, friends and family to thank.

I thank my advisor, John Wilkerson, for supporting me through seven and a half years at the UW. The other faculty members that I worked with closely were Hamish Robertson, Peter Doe, and Aksel Hallin. They have helped me significantly in various ways and were excellent people to be around.

The technical and administrative staff were of enormous help in all phases of the NCD experiment and navigating life at CENPA. Mark Howe, John Amsbaugh, Tom Burritt, Allan Myers, and Tim Van Wechel were great to work with and always helpful. I also thank Barb Fulton, Kate Higgins, Debra Nastaj, and Victoria Clarkson, possibly the most crucial people to the functioning of CENPA, for their help with everything from payroll to travel documentation to planning parties in the CENPA lunch room.

I made many friends at CENPA and within the SNO collaboration. There are way too many to completely list, but I wouldn't have had such a fun time in Seattle and Sudbury without all of them. However, I must specifically thank Sean McGee and Charles Duba, whom I met while working on SNO, and would later become the Minister and Best Man at my wedding.

I thank my wonderful family for their support: my mother, Karen, my father, Gary, sisters Jennifer and Joan, and my grandfather, Forrest. Without their care and understanding, I wouldn't have persevered through the precarious moments or had so many good ones. I surely would not have completed this dissertation without all of them. My wife's family has been really great to me. I thank Lars, Katie, Linnéa, and

Erik "the Ninja" Mobrand for letting me feel comfortable in their home. Thanks to Lars and Katie for letting Amanda and I live on Vashon during the last few months while finishing this dissertation. It was quite nice to be able to take a break and look outside at the Puget Sound and the Cascades. Special thanks to Katie for some very useful editing and for always offering to help in any way that she could. I also thank her and Kate Higgins for assisting me with printing and submitting the final draft.

Finally, I thank my amazing wife, Amanda. She has endured through the most stressful moments of the past year. You are my best friend, I love you, and I will never forget all of the sacrifices that you've made for me.

Chapter 1

INTRODUCTION

The Sudbury Neutrino Observatory (SNO) was constructed for the primary purpose of solving the Solar Neutrino Problem. Simply put, the Solar Neutrino Problem may be defined as the discrepancy between the measured flux of electron neutrinos emitted by the Sun and the theoretically predicted flux. The problem was originally discovered by Davis and Bahcall [1, 2], and verified by numerous solar neutrino flux measurements thereafter. The favored proposed solution to the Solar Neutrino Problem is that neutrinos were changing to different neutrinos flavor before arriving at the detector. Recent results from the first two measurements at SNO unambiguously showed that neutrinos from the Sun were changing from electron neutrinos to either muon or tau neutrinos. The final measurement at SNO utilizes an array of ^{3}He proportional-counters to measure the neutrino flux, which is the subject of this dissertation.

This dissertation begins by presenting solar neutrino flux predictions, previous solar neutrino flux measurements, which provide motivation for the construction of the SNO, and a brief description of neutrino oscillations. In Chapter 2, a description of the SNO detector is given, along with a summary of the results already obtained. Next, the Neutral Current Detectors (NCDs) are described (Chapter 3), followed by descriptions of the data acquisition system (Chapter 4), the calibration of the NCD electronics (Chapter 5), and analysis of NCD data for the purpose of ensuring detector integrity tests as they pertain to detector live-time and efficiencies (Chapter 6 - 8). The ultimate goal of this work is to help produce the most accurate and precise measurement of ^{8}B solar neutrinos. The final chapter describes the impact of this work on the neutrino flux measurement made by the NCDs.

1.1 Solar Neutrinos

The original, and still current, motivation to measure the flux of solar neutrinos, was to test the validity of solar models. Neutrinos are the ideal messenger for delivering information about fusion reactions at the solar core. Optical measurements of the Sun are not useful due to the radiative opacity of the Sun – photons at the solar core may take 10,000 years to emerge, losing all information about their initial conditions. Neutrinos, however, have extremely small interaction rates with matter, and easily pass from their origin through the Sun without interacting. Thus, it was realized, that neutrino flux and energy spectrum measurements could provide valuable tests of solar models.

The Sun's energy is generated in the fusion of four protons into an alpha particle, while emitting two positrons and two electron neutrinos, along with an energy release of 26.7 MeV.

$$4p \rightarrow \alpha + 2e^{+} + 2\nu_e \tag{1.1}$$

Approximately 98% of the energy generated by fusion comes from the chain of reactions called the solar pp-chain, which requires the presence of different light elements in the solar core (Fig. 1.1). The remaining 2% of the energy is produced by the carbon-nitrogen-oxygen (CNO) cycle. Bethe initially developed both of these possible reaction cycles for energy generation in the Sun, for which he won the Nobel Prize [3]. However, initially it was not clear which of these two chains were the dominant source of solar energy.

Bethe first argued that the CNO cycle should be the dominant energy source in the Sun. As it turned out, the Sun must be slightly more massive for the CNO cycle to dominate. Bahcall noted that one conclusion from the solar neutrino flux measurements by Davis [2] was that the pp-chain dominates the fusion processes in our

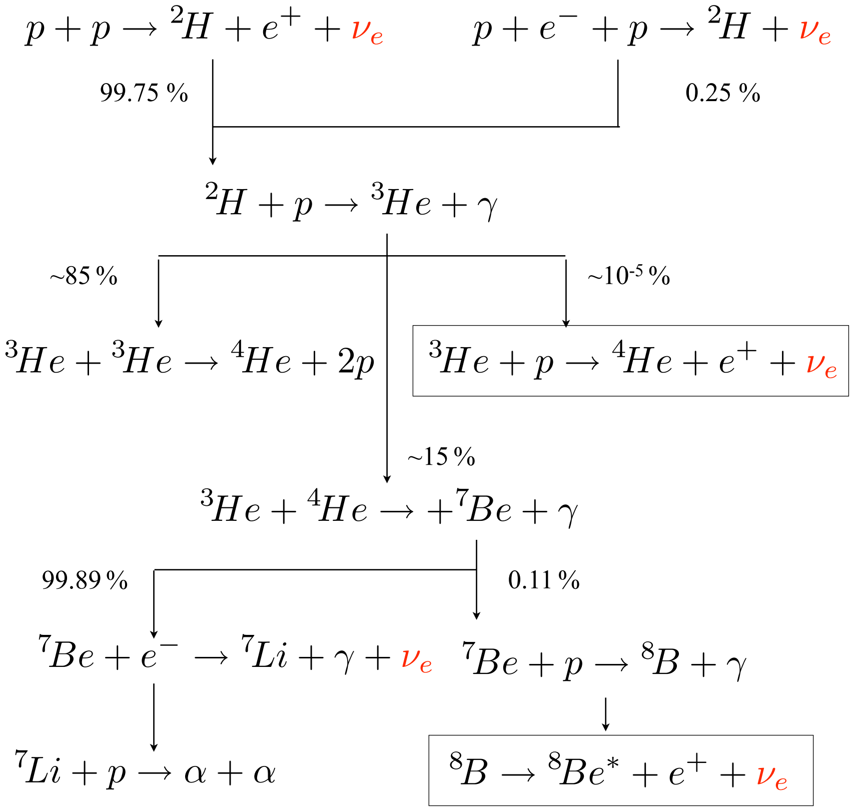

Figure 1.1: The pp-chain of nuclear reactions in the solar core. The Sudbury Neutrino Observatory is sensitive to the neutrinos produced in the reactions that are outlined by a box. Listed are the relative frequency (in percent) at each branching point in the chain [4].

Sun. For if the CNO cycle were dominant, the measured neutrino flux would have been greater by about an order of magnitude [5]. Today, the questions about solar models have progressed to a more detailed level. The precision has significantly increased for both theoretical calculations and experimental measurements of properties of the Sun, including the neutrino flux. Furthermore, including the phenomenon of matter-enhanced neutrino oscillations has resulted in good agreements between the measurements and predictions of the neutrino flux, ending the 30-year Solar Neutrino Problem. One recent development in standard solar model calculations is a new measurement for the metal abundances in the Sun. The new measurements find the abundances to be significantly smaller than previously estimated [6, 7]. This has subsequently resulted in significantly new theoretical outputs from standard solar models and are now in disagreement with helioseismological measurements. Furthermore, the predicted ^{8}B solar neutrino fluxes using the newer and older measurements of abundances flank the most recent measurements by SNO. The Bahcall-Serenelli 2005 model (BS05 OP) using the older heavy-element abundances predicts a flux of $5.491^{+0.948}_{-0.809} \times 10^{6}$ cm^{-2} s^{-1}, while the same model using the lower abundances (BS05 AGS, OP) predicts a flux of $4.459^{+0.564}_{-0.500} \times 10^{6}$ cm^{-2} s^{-1} [8]. The previous SNO measurement was $5.21 \pm 0.47 \times 10^{6}$ cm^{-2} s^{-1} [9]. Thus, it is imperative that the final phase at SNO, the Neutral Current Detector phase, produces an accurate and precise flux measurement, that when combined with all other previous measurements, results in a significant constraint on the flux so as to possibly rule out or constrain these different solar models [10].

Combining the Bahcall-Serenelli (BS05) model with the neutrino fluxes from electron capture onto ^{13}N, ^{15}O, and ^{17}F, as recently calculated by Stonehill et. al. [11], the entire flux spectrum is shown in Fig. 1.2. For the SNO experiment, the threshold of neutrino interactions is 2.2 MeV, thus making SNO primarily sensitive to the neutrino emitted by the decay of ^{8}B, but will also detect some neutrinos from *hep* reactions and the aforementioned electron-captures.

1.2 Previous Solar Neutrino Flux Measurements

While it has already been mentioned that SNO has measured a ^{8}B solar neutrino flux that is consistent with solar models and that the Solar Neutrino Problem (SNP) has been put to rest, an historical perspective of solar neutrino flux measurements provides motivation for the development of the neutrino oscillation models and the

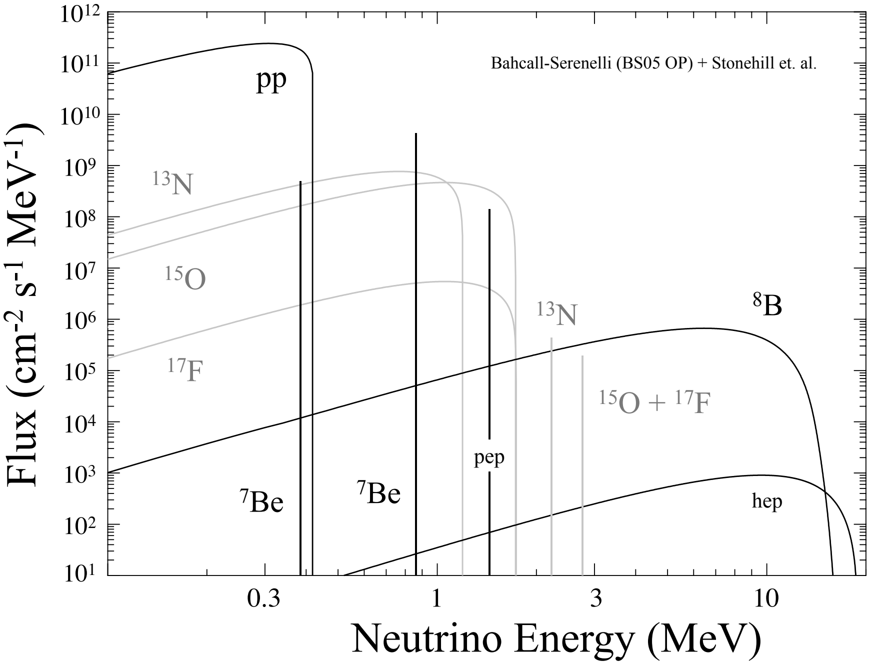

Figure 1.2: The neutrino energy spectrum from the Bahcall-Serenelli standard solar model, using the lower (older) heavy-element abundances [12], combined with the neutrinos generated in electron-captures. The black lines indicate the neutrino spectrum from the pp-chain, while the grey lines indicate neutrinos from the CNO cycle. Figure is modified from [11].

subsequent construction of the SNO.

The original motivation for Ray Davis' solar neutrino flux measurement in 1968 at the Homestake mine in Lead, South Dakota, was to verify models of the Sun and to make the first ever observations of solar neutrinos. A chronological review of the events which led Bahcall, Davis and others to investigate the solar neutrino flux can be found in the Appendix of [5]. The Homestake experiment ran for 30 years, producing a consistent measurement, that culminated in the final average value of 2.56 ± 0.23 SNU – one SNU (Solar Neutrino Unit) is equal to 10^{-36} neutrino captures [target atom$]^{-1}$ s^{-1}. The 2004 SSM (BP04) predicts that Davis' chlorine experiment should observe 8.5 ± 1.8 SNU, assuming that neutrinos do not oscillate [13].

The Homestake experiment detected neutrinos by absorption onto ^{37}Cl atoms within a large tank filled with 615 metric tons of C_2Cl_4, tetrachloroethylene. The detection mechanism was

$$\nu_e +^{37}\mathrm{Cl} \rightarrow \ ^{37}\mathrm{Ar} + e^- \tag{1.2}$$

which has a neutrino-energy threshold of 0.814 MeV, making this experiment sensitive to neutrinos from different solar fusion reactions, but particularly sensitive above 5.8 MeV to the neutrinos emitted by the ^{8}B decay [14]. Every two to three months, the ^{37}Ar atoms were extracted from the tank and were observed to decay in a small proportional counter. Measuring the number of decays of ^{37}Ar over time allowed for the extraction of the number of neutrino absorptions (Eq. 1.2) that occurred during the data set.

The predicted flux of neutrinos from the decay of ^{8}B is highly sensitive to the temperature at the solar interior: $\phi(^8\mathrm{B}) \propto T^{\beta}$, where β is around 24 or 25 [15]. This fact, coupled with the extremely small number of ^{37}Ar atoms produced and measured in each data set at Homestake, led many to wonder about the accuracy of the measurement and prediction, and the meaning of their comparison. Combined with evidence consistent with *massless* neutrinos, which would prevent neutrino oscillations, this became known as the Solar Neutrino Problem (SNP) – the discrepancy between the measured and predicted solar neutrino flux.

After the Homestake collaboration published their initial results, new solar neutrino experiments were designed and built. Two new experiments began taking data in 1990 utilizing a different neutrino detection technique. In the SAGE and the GALLEX/GNO experiments, the neutrino flux was measured by extracting the ^{71}Ge atoms produced in the inverse beta decay reaction $^{71}\mathrm{Ga}(\nu_e, e^-)^{71}\mathrm{Ge}$. The threshold for this reaction is 0.233 MeV, lower than the threshold of the Homestake experiment, which made these experiments sensitive to a large portion of the entire solar neutrino flux (Fig. 1.1). More importantly, the lower threshold allowed for the measurement of the neutrino flux from the p-p reaction, which has the highest rate and lowest theoretical uncertainty of all the neutrino-producing solar reactions. The rate of neutrino interactions were measured by observing the decay of ^{71}Ge and determining the number of ^{71}Ge atoms produced by inverse beta decay. Both experiments measured a reduced electron neutrino capture rate compared to the predicted rate of 131^{+12}_{-10} SNU [13]. Respectively, the SAGE and GALLEX/GNO experiments measured a flux of $70.8^{+6.5}_{-6.1}$ SNU [16] and 69.3 ± 5.5 SNU [17]. Again, the flux of electron neutrinos from the Sun was measured to be significantly less than the predicted flux.

A third type of solar neutrino experiments were water-Cherenkov detectors. Solar neutrinos were detected in these experiments via elastic scattering on electrons within large volumes of ultra-pure water. The electrons produced Cherenkov-radiation that was then detected by an array of photomultiplier tubes. This different neutrino detection mechanism provided some advantages. First, the elastic scattering interaction is primarily sensitive to electron neutrinos, but may also scatter with the other neutrino flavors via the neutral-current, albeit at a much lower rate. Second, these detectors were able to observe neutrino interactions in "real-time." Third, the directional information of the scattered electrons then provided conclusive evidence that the measured interactions were indeed coming from the Sun. The analysis thresholds for these experiments were in the 5-10 MeV range, which made them primarily sensitive to the ^{8}B neutrinos.

The first of these water-Cherenkov detectors was the Kamiokande experiment, which used the inner-most 680 tons of the total detector mass of three kilotons of pure water as the neutrino target. Combining data from January 1987 to February 1995, the flux of ^{8}B electron neutrinos was measured to be $2.8 \pm 0.4 \times 10^{6}$ cm^{-2} s^{-1} [18]. Following the Kamiokande experiment, the Super-Kamiokande (SuperK) experiment began taking data in 1996. With the same detection mechanism, but now using 50 kilotons of water, the SuperK experiment measured the ^{8}B solar electron neutrino flux to be $2.35 \pm 0.08 \times 10^6$ cm^{-2} s^{-1} [19]. Both of these measurements were slightly less than half of the neutrino flux predicted by the standard solar model (BP05 OP), $5.491^{+0.948}_{-0.809} \times 10^6$ cm^{-2} s^{-1} [8]. One explanation for the discrepancy between prediction and measurement was that electron neutrinos were changing to neutrinos of different flavors before they arrived at Earth and were thus undetected in these experiments.

In 1985, Herb Chen proposed a new water-Cherenkov detector that would definitively test the neutrino flavor changing hypothesis in a way that was independent of solar model predictions [20]. His proposal was to use heavy water as the neutrino target. Solar neutrinos can interact with deuterium in three distinct ways. Like before in Kamiokande and SuperK, neutrinos may elastically scatter electrons in the heavy water, producing measurable Cherenkov light. With deuterium, neutrinos may also interact via the charge-current and neutral-current interaction channels. The charge-current interaction is allowed only for electron neutrinos with energy greater than 1.44 MeV. As such, the rate of charge-current interactions is proportional to the flux of electron neutrinos from the Sun. All active flavors of neutrinos that have an energy greater than 2.23 MeV may interact with deuterium via the neutral-current interaction. The rate of neutral-current interactions is thus proportional to the total flux of active neutrinos. Thus, by using deuterium, the total flux of all neutrino flavors and the flux of electron neutrinos could be measured simultaneously and test the idea of neutrino flavor change. This proposal lead to the construction of the SNO and ultimately the solution to the SNP. The SNO detector is described in Chapter 2 along with the most recent results combined with other neutrino oscillation measurements.

1.3 Neutrino Oscillations

Neutrino oscillations, originally proposed as the solution to the solar neutrino problem [21], is now widely accepted due to the overwhelming amount of evidence. Not only do neutrino oscillation models fit the solar neutrino data well, it has also been observed to be consistent with measurements of atmospheric, nuclear reactor-produced, and accelerator-produced neutrino flux measurements, providing a robust model over different ranges of energy and propagation lengths. The following gives a brief overview of neutrino properties and neutrino oscillations.

In the Standard Model of particle physics, neutrinos are fermions that interact with matter through the weak interaction by exchange of either a $W^{\pm}$ or Z^0 boson, respectively called the charge-current and neutral-current interactions. The flavor of a neutrino is defined by the lepton that accompanies it in a charged-current interaction and so may be an electron, muon, or tau neutrino (or anti-neutrino). In the Standard Model, neutrinos are also purely left-handed, without right-handed fields and subsequently massless. However, in order for neutrino oscillations to occur, neutrinos must have a mass[1]. Thus the Standard Model must be extended to accommodate these observations.

Neutrino oscillations occur if the flavor eigenstates, ν_e, ν_μ, or ν_τ are not the same as the particle eigenstates that propagate in space, called the mass eigenstates, ν_1, ν_2, and ν_3[2]. Since these are the basis states, a neutrino, in general, may exist as a linear combination of them. For example, an electron neutrino is written as a linear combination of the mass eigenstates

$$|\nu_e\rangle = \sum_{i=1}^{N=3} a_i |\nu_i\rangle \tag{1.3}$$

In general, the flavor and mass basis states are related to each other by the unitary mixing matrix $\mathbf{U}$, called the Pontecorvo Maki Nakagawa Sakata (PMNS) matrix after those who originally developed it [23, 24, 25]. The mixing matrix is parameterized, ignoring CP-violation and Majorana phase factors, by three mixing angles, θ_{12}, θ_{23}

---

[1] Technically, at least one neutrino must have a non-zero mass.

[2] Only three active neutrino species are considered here, which is consistent with measurements of the decay-width of the Z^0 boson [22].

and θ_{13}. The relationship between the flavor and mass basis states is

$$\begin{pmatrix} \nu_e \\ \nu_\mu \\ \nu_\tau \end{pmatrix} = \mathbf{U} \begin{pmatrix} \nu_1 \\ \nu_2 \\ \nu_3 \end{pmatrix} \tag{1.4}$$

where

$$\mathbf{U} = \begin{pmatrix} c_{12}c_{13} & s_{12}c_{13} & s_{13} \\ -s_{12}c_{23} - s_{13}s_{23}c_{12} & c_{12}c_{23} - s_{12}s_{13}s_{23} & s_{23}c_{13} \\ s_{12}s_{23} - s_{13}c_{12}c_{23} & -s_{23}c_{12} - s_{12}s_{13}c_{23} & c_{13}c_{23} \end{pmatrix} \tag{1.5}$$

and $c_{12} = \cos\theta_{12}$, $s_{12} = \sin\theta_{12}$, etc.

To show how this mixing results in neutrino oscillations, consider an electron neutrino produced at time $t = 0$. Initially it is a linear combination of the mass states $|\nu_e(0)\rangle = \Sigma_j U_{1j}|\nu_j\rangle$. When the neutrino propagates in time, the mass states acquire different relative phases that are related to their mass eigenvalues $|\nu_e(t)\rangle = \Sigma_j U_{1j}e^{-iE_jt}|\nu_j\rangle$, where E_j is the total energy of the jth mass eigenstate. Then, the probability for the neutrino, which was initially an electron neutrino, to be observed in the flavor state $|\nu_\alpha\rangle$ at some later time t can be expressed as

$$P(\nu_e \to \nu_\alpha) = |\langle\nu_\alpha|\nu_e(t)\rangle|^2 = \left|\sum_j U_{1j}U^\star_{\alpha j}e^{-iE_jt}\right|^2 \tag{1.6}$$

Using the approximations that neutrinos are very relativistic, the mass eigenstates all have the same momentum, $E_i = \sqrt{p^2 + m_i^2} \simeq p + m_i^2/2p$, and that $E \approx p$ and $t \approx L$, where L is the distance traveled at the speed of light, the probability becomes

$$P(\nu_e \to \nu_\alpha) = \left|\sum_j U_{1j}U^\star_{\alpha j}e^{-im_j^2L/2E}\right|^2 \tag{1.7}$$

where the common phase e^{-iEt} was dropped since it cancels when squaring the term in brackets. Thus, the probability for an electron neutrino to oscillate into a different flavor depends upon the mixing angles, θ_{ij}, and, as can be seen with some algebra, the differences in the squares of the masses, $\Delta m_{ij}^2 = m_i^2 - m_j^2$.

1.3.1 Solar Neutrinos: Two-Neutrino Approximation

To further illustrate the oscillation phenomenon dependence on the mixing angles and mass square difference, consider the survival probability for the case of just two neutrino flavors, for simplicity. In this situation we can write the equivalent of Eq. 1.4-1.5

$$\begin{pmatrix} \nu_a \\ \nu_b \end{pmatrix} = \begin{pmatrix} \cos\theta & \sin\theta \\ -\sin\theta & \cos\theta \end{pmatrix} \begin{pmatrix} \nu_1 \\ \nu_2 \end{pmatrix} \tag{1.8}$$

A neutrino that begins at $t = 0$ as ν_a and propagates in time, is written as a

$$|\nu_a(t)\rangle = e^{-iE_1 t}\cos\theta|\nu_1\rangle + e^{-iE_2 t}\sin\theta|\nu_2\rangle \tag{1.9}$$

where $E_i^2 = p_i^2 + m_i^2$. Under the approximation that the neutrino states have the same momentum, p, and that $E_i \approx p + m_i^2/2E$, Eq. 1.9 may be written

$$|\nu_a(t)\rangle = e^{-im_1^2 t/2E}\cos\theta|\nu_1\rangle + e^{-im_2^2 t/2E}\sin\theta|\nu_2\rangle \tag{1.10}$$

where the common phase was dropped here since it will be of no consequence when the term is squared to calculate the probability. The amplitude of observing $|\nu_a(t)\rangle$ in state $|\nu_b\rangle$ is then given by

$$\langle\nu_b|\nu_a(t)\rangle = e^{-im_1^2 t/2E}\sin\theta\cos\theta + e^{-im_2^2 t/2E}\sin\theta\cos\theta \tag{1.11}$$

Squaring this term and setting $t = L$ gives the probability of observing the neutrino as a different flavor

$$P(\nu_a \to \nu_b) = \sin^2 2\theta \sin^2\left(1.27\Delta m_{21}^2 \frac{L}{E}\right) \tag{1.12}$$

where L is the propagation length in meters, E is in GeV and Δm_{21}^2 is in eV^2. The survival probability for ν_a is just 1 - $P(\nu_a \to \nu_b)$.

For solar neutrinos, the oscillation model may be approximated to this special two-neutrino case because of the small size of the Δm_{21}^2 relative to Δm_{13}^2 and Δm_{23}^2 and the smallness of the mixing angle θ_{13}. Although θ_{13} has not yet been measured, upper limits on this parameter are small enough to consider the two-neutrino case for solar neutrinos [26]. The relationship between the survival probability of an electron neutrino in the three-neutrino model to the survival probability in the simplified two-neutrino case is approximately

$$P(\nu_e \to \nu_e)_{3\nu} \approx \cos^4\theta_{13} P(\nu_e \to \nu_e)_{2\nu} + \sin^4\theta_{13} \tag{1.13}$$

As such, the survival and oscillation probabilities of a solar electron neutrino is sufficiently described by

$$P(\nu_e \to \nu_e) = 1 - P(\nu_e \to \nu_\mu) = 1 - \sin^2 2\theta_{12} \sin^2\left(1.27\Delta m^2_{21}\frac{L}{E}\right) \tag{1.14}$$

The MSW Effect

The above discussion considered neutrinos propagating through a vacuum, whereas electron neutrinos produced in the fusion reactions at the solar core must first propagate out of the solar interior before reaching the vacuum of space. During this journey, all flavors of neutrinos may interact with the solar matter via the neutral-current, but since there are no muons or taus present, only electron neutrinos interact via charge-current [27]. The additional charge-current interaction between electron neutrinos and the solar matter is parameterized effectively as an additional potential that is proportional to electron-density of the Sun, which varies as a function of the radius. Conceptually, this extra forward-scattering channel slows down the propagation of the electron neutrino component of the neutrino, which can be thought of as an effective increase in mass. Since the oscillation phenomenon occurs because the phases of the mass states are not equal, it is easy to imagine that this interaction would have an effect on the survival probability of the electron neutrino as it propagates the solar interior, depending on the vacuum mixing angle, mass-squared difference and the solar electron-density [28, 29]. The result is that, if the solar electron-density is sufficiently smooth, electron neutrinos may oscillate to muon neutrinos before exiting from the solar interior. This effect, developed by Mikheyev, Smirnov and Wolfentstein, called the MSW effect, was initially an attractive explanation of the solar neutrino problem because it was believed that the parameters of the PMNS matrix would be small, similar to the parameters of the CKM matrix in the quark sector. However, in the end, a combination of large mixing angles and the MSW-enhancement of neutrino oscillations is required to explain all of the measured neutrino data. A good discussion of this phenomenon can be found in [5].

Chapter 2

THE SUDBURY NEUTRINO OBSERVATORY

Following Herb Chen's proposal, a collaboration was formed to build the Sudbury Neutrino Observatory (SNO) in order to address the Solar Neutrino Problem. Construction began in 1990 and the first results were published in 2001 [30]. There were three phases of the SNO experiment, and the work presented in this dissertation was done entirely on the third phase. This chapter will give an overview of the SNO detector and present the SNO results from the first and second phases, and in combination with other neutrino oscillation experimental results. The chapter will conclude with a discussion of the expected sensitivity of the final phase of the experiment.

2.1 Detector Overview

SNO (Fig. 2.1), was a heavy water Cherenkov neutrino detector located 2092 meters underground in INCO's Creighton nickel mine near Sudbury, Ontario, Canada, in a cavity created for the experiment [31]. One thousand metric tonnes of heavy water (D_2O) served as the target for solar neutrinos. The heavy water was contained within a spherical acrylic vessel (AV) 12 m in diameter and surrounded by approximately 9500 inward-looking photomultiplier tubes (PMTs) that were fixed to a spherical PMT support structure (PSUP) 17.8 m in diameter. Between the AV and the walls of the cavity were approximately 7400 tonnes of ultra-pure H_2O, which provided physical support to the apparatus and shielded it from radioactivity in the rock wall. There were two regions of pure water – one region between the AV and the PSUP, and the other between the PSUP and rock wall.

SNO detected solar neutrinos emitted by the decay of ^{8}B and produced in the *hep* reaction (Fig. 1.1 and 1.2) through one of three interactions: the charged-current (CC), neutral-current (NC), and elastic scattering (ES) interactions. The presence of the heavy water, unique to SNO, allowed for the CC and NC reactions between neutrinos and deuterium.

$$\nu_{\mathrm{e}} + \mathrm{d} \rightarrow \mathrm{p} + \mathrm{p} + \mathrm{e}^- \qquad \mathrm{Q} = -1.44\ \mathrm{MeV} \tag{CC}$$

$$\nu_{\mathrm{x}} + \mathrm{e}^- \rightarrow \nu_{\mathrm{x}} + \mathrm{e}^- \tag{ES}$$

$$\nu_{\mathrm{x}} + \mathrm{d} \rightarrow \nu_{\mathrm{x}} + \mathrm{p} + \mathrm{n} \qquad \mathrm{Q} = -2.23\ \mathrm{MeV} \tag{NC}$$

The CC and ES reactions produced an energetic electron, which emitted Cherenkov radiation that was detected by the PMT array. In the first two phases of SNO, the neutron produced in the NC reaction underwent a secondary reaction that subsequently produced Cherenkov radiation. Characteristic properties of the Cherenkov radiation allowed these events (on the order of 10 per day) to be distinguished from background events. In general, for each event detected by the PMT array, the kinetic energy of the electron, position of interaction within the AV, direction of the Cherenkov radiation cone relative to the direction of the incident neutrinos (the angle to the solar core), and calculated parameter that measured the isotropy of the Cherenkov light were measured by reconstructing the event based upon the timing of the PMT triggers and total charge collected. The use of these observable parameters to extract the neutrino flux will be shown in § 2.1.1 and 2.1.2. In the third phase at SNO, the neutron released in the NC reaction, however, was detected using a method that was nearly independent of the PMT array.

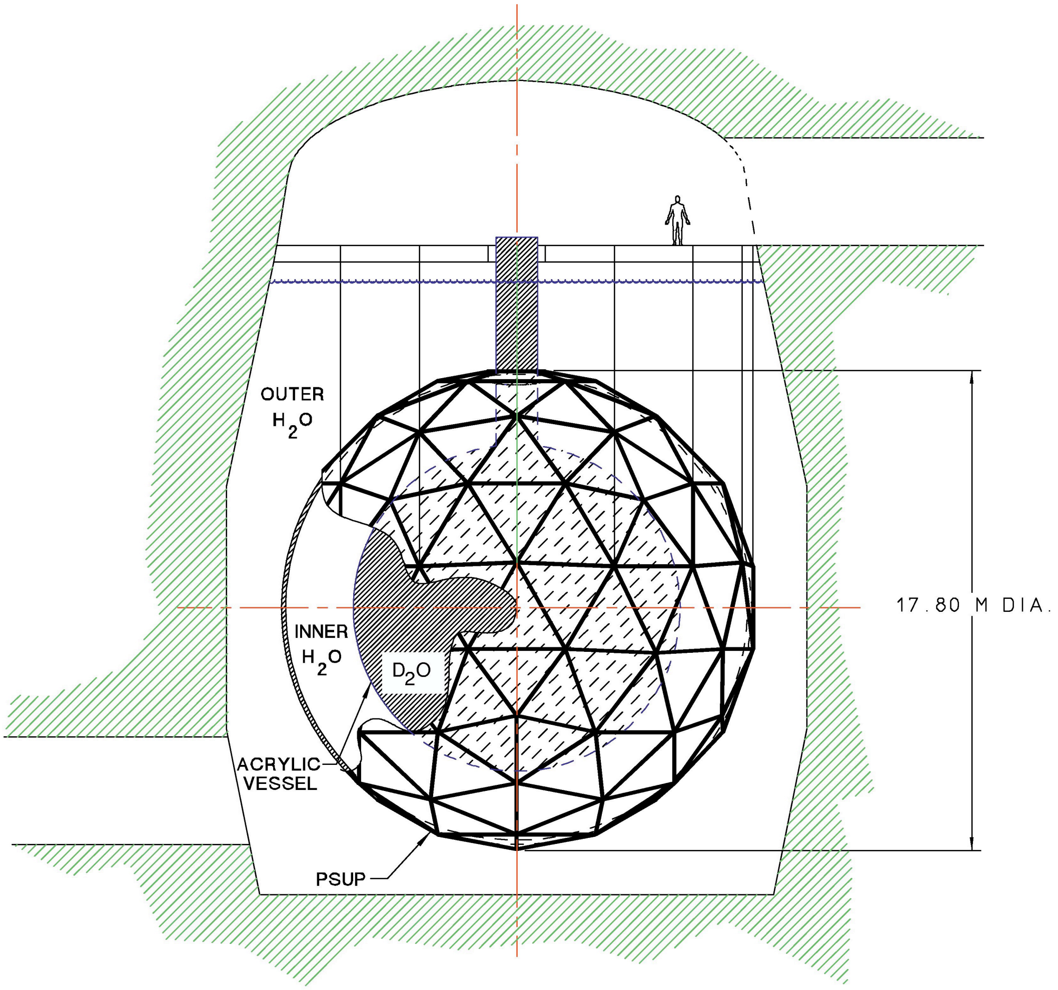

Figure 2.1: The SNO detector located in the underground cavity. Shown here are the acrylic vessel (AV), which holds the heavy water neutrino target, the PSUP, which supports the PMT array, and the inner and outer pure water regions. The vertical lines connecting the PSUP to the "deck" indicate support ropes . The electronics for the experiment are located on the deck, and the underground control room is in an adjacent room at deck-level, but is not shown here [31].

The Charged Current Interaction

In CC interactions at SNO, an electron neutrino was absorbed, and the deuteron was converted into two protons and a Cherenkov-radiating electron, through exchange of a W^- boson [32].

$$\nu_{\mathrm{e}} + \mathrm{d} \rightarrow \mathrm{p} + \mathrm{p} + \mathrm{e}^-$$

The threshold for this reaction is 1.44 MeV. Neutrinos from the Sun, of course, may be as energetic as 18.6 MeV (*hep*). The CC reactions involving the other neutrino flavors, $\nu_\mu(\nu_\tau) \rightarrow \mathrm{p}+\mathrm{p}+\mu^-(\tau^-)$, are energetically forbidden because the masses of the μ^- and τ^- leptons are significantly greater than the most energetic solar neutrinos.

The total energy of Cherenkov radiation produced in this reaction is proportional to the energy of the incident ν_e, and allowed for the measurement of the ν_e energy spectrum. This was especially useful since the MSW oscillation survival probability of ν_e is energy dependent (Eq. 1.14), and any observed spectral distortions would be evidence of neutrino oscillations. The energy spectrum of the CC events were also different from the energy spectrum of the ES and NC reactions, a property that was useful in the first two neutrino flux measurements. In addition, the outgoing electron tends to be emitted in the direction away from the incoming neutrino. The angular distribution of CC reactions is approximately $\propto 1 - 1/3\cos\theta_\odot$, where $\theta_\odot$ is the angle between the outgoing electron and incident solar neutrino [33].

The Elastic Scattering Interaction

Neutrinos of all flavors may elastically scatter electrons in heavy water by neutral current exchange of a Z-boson. Thus, the rate of ES reaction was related to the total flux of solar neutrinos of all flavors. This reaction was previously utilized by the Kamiokande and SuperK experiments for their solar neutrino flux measurements.

$$\nu_{\mathrm{x}} + \mathrm{e}^- \rightarrow \nu_{\mathrm{x}} + \mathrm{e}^-$$

In addition, ν_es may also scatter electrons through the exchange of a W-boson. Because of this extra interaction channel, and despite the destructive interference term in the ES Lagrangian [34, 35], the ES reaction occurs about six times more frequently for ν_e than for ν_μ or ν_τ. However, neither the neutrino flavor nor the type of exchange boson is distinguishable in SNO.

The Cherenkov radiation from the recoil electron was detected by the PMT array, and was highly correlated to the direction of the incident neutrino. The forward-peaked distribution of this reaction confirmed the Sun as the source of neutrinos and was useful in the statistical separation of ES events from the CC and NC events detected by the PMT array.

The Neutral Current Interaction

The NC interaction, an exchange of a Z boson, occurs with equal probability for all neutrino flavors, and is thus sensitive to the total neutrino flux without preference for a particular neutrino flavor (contrast this with the ES reaction). For a neutrino of any flavor with an energy greater than 2.2 MeV, a NC interaction disintegrates a deuteron into its constituent neutron and proton.

$$\nu_{\mathrm{x}} + \mathrm{d} \rightarrow \nu_{\mathrm{x}} + \mathrm{p} + \mathrm{n}$$

The thermalized neutron was then detected in three distinct ways, defining the three phases of the SNO experiment. These distinct phases at SNO provided robust reproducibility of the total neutrino flux measurement. A short description of each neutron detection mechanism is given in the subsequent sections of this chapter.

Thermalized neutrons, however, may be produced in various other background reactions. These neutrons are completely indistinguishable from neutrons produced in the NC interaction. Of primary concern is photodisintegration of deuterium by γs with $E > 2.2$ MeV. Photons of these energies are produced in the decays of ^{214}Bi and ^{208}Tl, which are found in the decay chains of ^{238}U and ^{232}Th, respectively. Neutrons are also produced in several (α,n) reactions. To limit these backgrounds, the levels of radioactive contamination within detector materials was strictly limited and measured. To limit the number of background photodisintegration neutrons to less than 10% of the expected signal rate from solar neutrino, the SNO design goal for amount of U and Th was less than 45×10^{-15} g/g and 3×10^{-15} g/g, respectively, in the D_2O. For the H_2O, the goals were a factor of 10 higher than for the D_2O. All material within SNO had strict limits on the allowed amount of U and Th contamination (see [31, 36]for details). In addition, cosmic-ray muon produced spallation neutrons. However, by locating the detector deep underground, the total number of incident cosmic-ray muons was limited to a few per hour and the spallation neutrons were easily removed by a data veto when the cosmic-ray muon interaction was detected [37, 38].

The neutrino flavor-dependence of these reactions allowed SNO to simultaneously measure the total flux of all neutrinos and the flux of just electron neutrinos. These flux measurements have confirmed standard solar models and verified neutrino flavor change. When the results from other experiments are combined with SNO results, tight restrictions have been placed on the allowed values of the neutrino oscillation parameters θ_{12} and Δm^2_{21} (Eq. 1.14).

In the next sections of this chapter, the NC reaction detection mechanism for each phase will be described. The results form the first two SNO measurements and the goals of the final flux measurement will be given.

2.1.1 Results from SNO Phase I: D_2O

In the SNO Phase I, the thermalized neutrons from the NC reaction captured on deuterium, releasing a 6.25 MeV γ. The γ then Compton-scattered an electron or produced an e^+e^- pair, which then produced a Cherenkov radiation cone [30, 39, 36]. After cutting out instrumental noise events, the neutrino candidate events were reconstructed. For each event, the effective kinetic energy of the recoil electron in the CC or ES reactions or the energy of the γ from neutron capture (T_{eff}), the volume-weighted radial location within the AV (R^3)[1], and the angle between the direction of the Cherenkov light cone and the direction of the Sun ($\cos\theta_{\odot}$) were measured. The probability distribution functions of these three variables (T_{eff}, R^3, $\cos\theta_{\odot}$) for the CC, ES and NC reactions and background sources were generated from a detailed Monte Carlo simulation of the SNO detector, in conjunction with a full suite of detector calibrations. An extended maximum-likelihood fit was then used to extract the number of CC, ES, and NC events and subsequently determine the total ^{8}B solar neutrino flux, ϕ_{total}, the electron neutrino flux ϕ_e, and the combined neutrino flux from the other flavors $\phi_{\mu\tau}$ (Fig. 2.2).

The measured fluxes from the Phase I data set were, in units of 10^6 cm^{-2} s^{-1} [36]

$$\phi_{total} = 5.09^{+0.44}_{-0.43}(\text{stat.})^{+0.46}_{-0.43}(\text{syst.}) \tag{2.1}$$

$$\phi_e = 1.76^{+0.05}_{-0.05}(\text{stat.})^{+0.09}_{-0.09}(\text{syst.}) \tag{2.2}$$

$$\phi_{\mu\tau} = 3.41^{+0.45}_{-0.45}(\text{stat.})^{+0.48}_{-0.45}(\text{syst.}) \tag{2.3}$$

2.1.2 Results from SNO Phase II: Salt

In Phase II, two metric tons of NaCl were added to the heavy water. The ^{35}Cl provided a more efficient mechanism for thermal neutron capture - the cross-section of neutron capture onto ^{35}Cl is 44 b compared to 0.5 mb for capture on deuterium. After neutron capture, an excited ^{35}Cl relaxes into its ground-state, releasing multiple γs with total energy of 8.6 MeV. The increased cross-section and increased total event energy further distinguished NC events from CC and ES events in Phase II [9, 40].

The analysis for Phase II proceeded similarly to the Phase I analysis except that a new observable parameter was introduced, β_{14}. Neutron capture onto ^{35}Cl could

---

[1] $R^3 = 1.0$ is the position of the AV, $R_{AV} = 600.5$ cm.

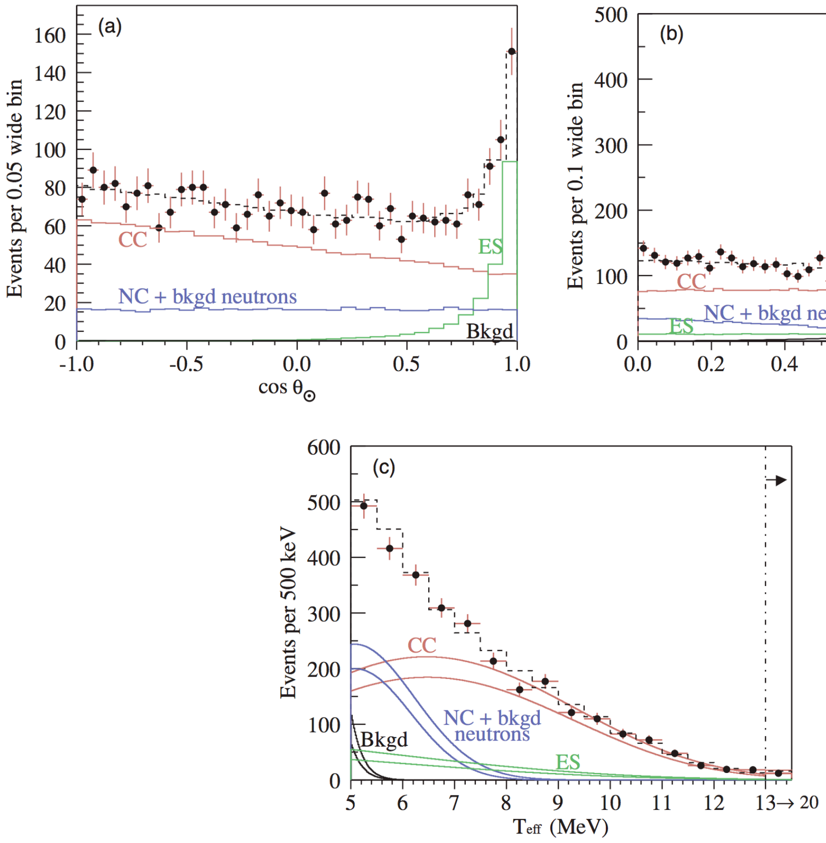

Figure 2.2: The candidate neutrino events and background neutron captures in SNO Phase I after removal of instrumental backgrounds are plotted as a function of (a) the reconstructed angle relative to the Sun, $\cos\theta_{\odot}$, (b) the volume-weighted radial position, R^3, and (c) the effective energy of the recoil electron or energy of the γ produced by neutron capture , T_{eff}. Also shown are the Monte Carlo PDFs for the CC, NC, ES events and backgrounds, which were fit to the data [36].

generate up to 3 γs, as opposed to just one γ for capture on deuterium in Phase I. Because of the multiple γs, the Cherenkov radiation was dispersed more isotropically than the Cherenkov radiation from the single electron in the CC and ES reaction. The parameter β_{14} was a measure of the isotropy of the distribution of PMT triggers in each event and was added to the set of observable parameters for the signal separation in the extended maximum-likelihood fit. Also in the Phase II maximum-likelihood fit, the kinetic energy parameter T_{eff} was not included in the fits to extract "energy-unconstrained" rates of CC, ES and NC events [41, 40, 4].

The energy-unconstrained neutrino fluxes measured in Phase II, assuming an undistorted ^{8}B solar neutrino energy spectrum to reproduce the measured CC, ES and NC event rates, were, in units of 10^6 cm^{-2} s^{-1} [40]

$$\phi_{total} = 4.94^{+0.21}_{-0.21}(\text{stat.})^{+0.38}_{-0.34}(\text{syst.}) \tag{2.4}$$

$$\phi_{e} = 1.68^{+0.06}_{-0.06}(\text{stat.})^{+0.08}_{-0.09}(\text{syst.}) \tag{2.5}$$

$$\phi_{\mu\tau} = 3.26^{+0.25}_{-0.25}(\text{stat.})^{+0.40}_{-0.35}(\text{syst.}) \tag{2.6}$$

The results from the first two phases of SNO are in agreement with the standard solar model predictions of the total ^{8}B solar neutrino flux and with previous solar neutrino flux measurements. The measurement of the non-electron neutrino component of the solar neutrino flux ($\phi_{\mu\tau}$) in Phase II is greater than 6.5 standard deviations from the null hypothesis of no neutrino flavor change.

2.2 Combined Neutrino Oscillation Measurements

The results from Phase I and II may be combined, along with results from the KamLAND experiment, to place restrictions on the allowed region in the $\sin^2\theta_{12}$-Δm^2_{21} space. The KamLAND experiment detected anti-neutrinos that were emitted by nuclear reactors in Japan. Assuming CPT invariance, the KamLAND experiment was sensitive to the same oscillation parameters as solar neutrino experiments and provided an excellent confirmation of past experimental results. A measurement of the energy spectrum of the $\bar{\nu_e}$ observed, for the first time, distortions that are consistent with neutrino oscillations [42]. A two-neutrino oscillation analysis that included data from the previous solar neutrino experiments, KamLAND, and the SNO flux measurements of Phase I and II, resulted in the best-fit measurements of $\Delta m^2_{21} =$

$8.0^{+0.6}_{-0.4} \times 10^{-5}$ eV^2 and $\tan^2\theta_{12} = 0.45^{+0.09}_{-0.07}$, and is known as the Large Mixing Angle (LMA) solution to the Solar Neutrino Problem [40] (Fig. 2.3).

2.3 An Independent Solar Neutrino Flux Measurement: Phase III

The goal of Phase III at SNO is to make a total neutrino flux measurement in a unique way that would separate the NC reaction events from the CC and ES reactions. By detecting the neutrons with a nearly separate apparatus, the rate of NC interactions are measured independent of the CC and ES interaction rates. Thus, the correlations between the total flux, ϕ_{total}, and the electron neutrino flux, ϕ_e, found in the maximum-likelihood fits of Phase I and II would nearly vanish. In the analysis of Phase III data, the number of NC events, measured by the separate apparatus, will be constrained in the maximum-likelihood fits to the energy, radial, and $\cos\theta$ PDFs.

Using proportional counters is a well-known technique for thermal neutron detection and can provide an event-by-event separation of the NC events. Large cross-sections for neutron capture in ^{3}He-, ^{6}Li-, and ^{10}B-gas counters provide for reliable neutron detection [43]. Neutron capture onto ^{3}He was chosen since it produces an energetic proton-triton pair

$$\mathrm{n} +^3 \mathrm{He} \rightarrow \mathrm{p} + \mathrm{t} \qquad \mathrm{Q} = 764\ \mathrm{keV} \tag{2.7}$$

that is distinguishable from background events caused by ionizing alphas [44] and because of its superior neutron capture cross-section of 5330 barns [43]. After the NaCl from Phase II was removed from the heavy water, an array of ^{3}He proportional counters, called Neutral Current Detectors (NCDs) was installed into SNO.

The primary goal for the NCD phase is to make an independent measurement of the ^{8}B solar neutrino flux, ϕ_{total}, in a way that breaks the statistical correlations between the NC and CC reaction rates with a precision that is comparable to or better than the previous two measurements – the expected total uncertainty in the flux measurement before the NCD phase began was about 2% less than the measured uncertainty in Phase II. Reproducibility of the solar neutrino flux measurement with an effectively different experiment with different systematic uncertainties will also be a valuable addition to the set of solar neutrino flux measurements. In addition, an effort is being made to reduce the level of low energy background events in order to reduce the analysis threshold for the CC and ES reactions. The goal is to observe the low energy spectral distortions (below the Phase II threshold of 5.5 MeV) associated with neutrino oscillations. Finally, a combined analysis of the Phase I, II, and III data should result in further restrictions on the oscillation parameters and could possibly rule out certain standard solar model scenarios. Fig. 2.4 shows the currently allowed region of the solar neutrino oscillation parameters for a combined analysis of solar neutrino and KamLAND data in a three-neutrino oscillation model along with the expected contours for constant ratios of the CC/NC flux rates at SNO [45]. As can be seen in Fig. 2.4, a reduced uncertainty in the CC/NC flux rate ratio in Phase III will contribute primarily to an enhanced measurement of the mixing angle, θ_{12}.

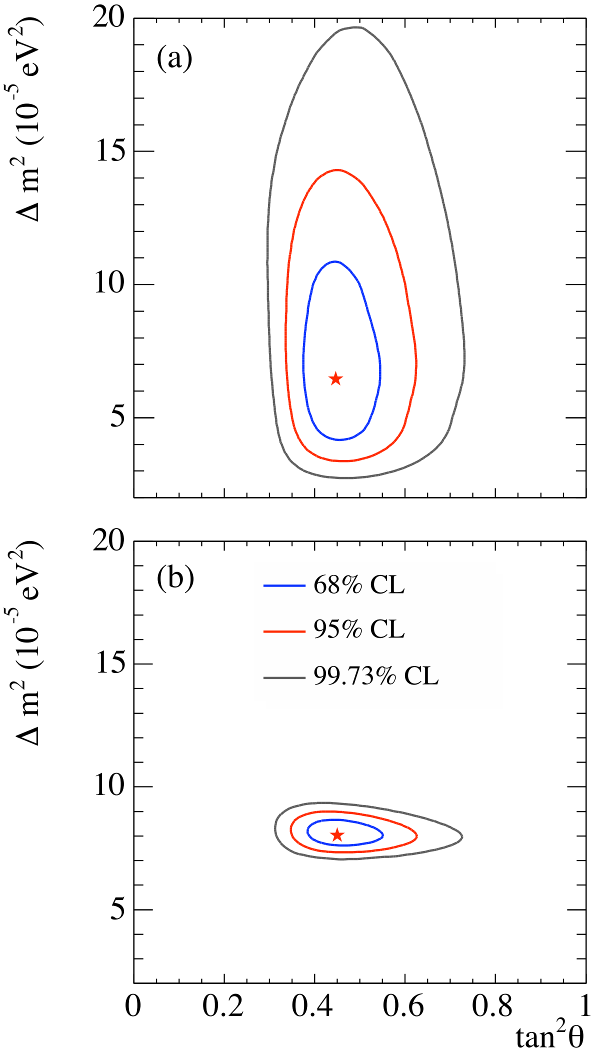

Figure 2.3: The confidence-level (CL) contours for the best-fit MSW-enhanced two-neutrino oscillation parameters (a) from the combined analysis of all solar neutrino flux measurements, and (b) including the results of the KamLAND experiment. The best-fit parameters in (a) are $\Delta m^2_{21} = 6.5^{+4.4}_{-2.3} \times 10^{-5}$ eV^2 and $\tan^2\theta_{12} = 0.45^{+0.09}_{-0.08}$, and in (b) are $\Delta m^2_{21} = 8.0^{+0.6}_{-0.4} \times 10^{-5}$ eV^2 and $\tan^2\theta_{12} = 0.45^{+0.09}_{-0.07}$ [40].

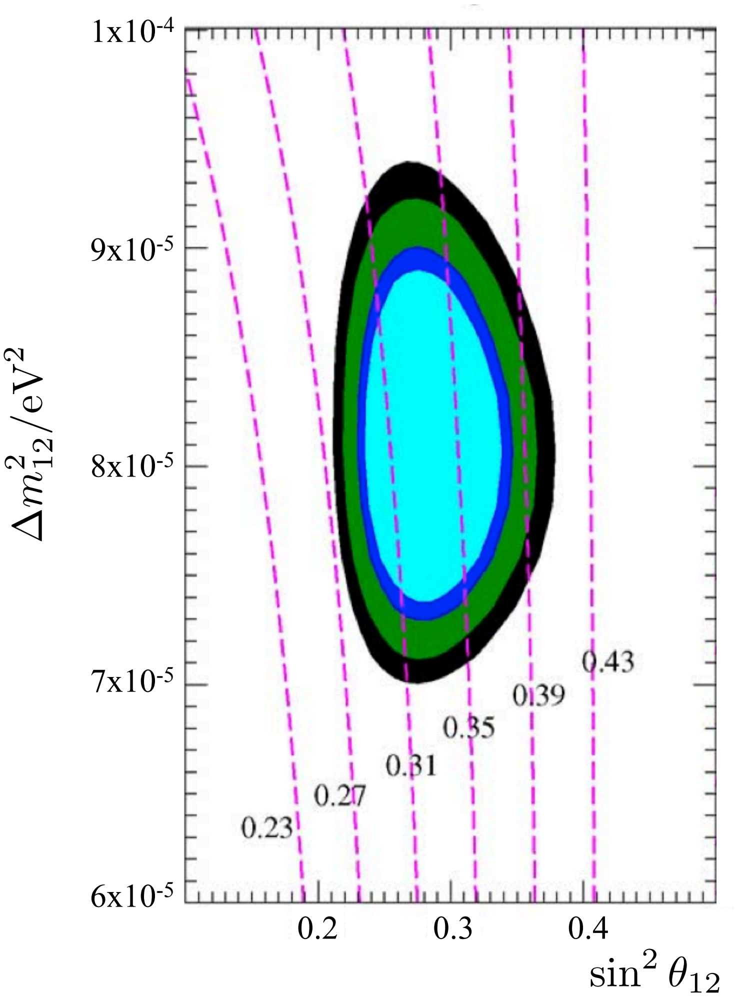

Figure 2.4: The 90%, 95%, 99% and 99.73% CL contours for the best-fit MSW-enhanced solar neutrino oscillation parameters in a three-neutrino oscillation model from an analysis of all solar neutrino and KamLAND data combined. The dashed lines are contours for constant CC/NC flux ratios at SNO [45].

Chapter 3

THE NEUTRAL CURRENT DETECTORS

3.1 Overview

In the final phase of SNO, an array of ^{3}He proportional counters was installed vertically inside the AV (Fig. 3.1). The NCDs were designed to detect thermalized neutrons produced in the NC interaction (Eq. NC) by neutron capture and production of a proton-triton pair

$$\mathrm{n} + {}^3\mathrm{He} \rightarrow \mathrm{p} + \mathrm{t} \quad Q = 764 \text{ keV} \tag{3.1}$$

In this reaction, the proton and triton are emitted in opposite directions with respective energies of 573 and 191 keV. These charged particles ionized the NCD gas producing a series of electrons and ions which generated a current signal along the proportional counter's anode. The current profile of this event and measured energy provided the necessary information to identify thermal neutron capture from other ionizing alpha particles within the NCD gas volume. The rate of neutrons detected minus the rate of neutrons produced by non-neutrino reactions was proportional to the flux of solar neutrinos. Thus, a major effort required for this experiment was to develop methods to identify neutrons from backgrounds and accurately estimate the number of neutrons produced by other sources. Generally, the number of neutrons produced by neutrino interactions and measured by the NCDs, N_ν, within a fiducial volume $V_{fid} = 4/3\pi R^3$ can be expressed as

$$N_\nu = T_{live} \int_0^R \int_\Omega \int_{2.2 \text{ MeV}}^\infty \frac{d\phi_\nu(E)}{dE}\, \sigma_{NC}(E)\, \epsilon(r,\theta,\phi)\rho\, r^2\, d\Omega\, dE \tag{3.2}$$

where $\phi_\nu(E)$ is the solar neutrino flux, $\sigma_{NC}(E)$ is the neutral-current interaction cross-section with deuterium, ρ is the deuterium number density, $\epsilon(r,\theta,\phi)$ is the overall

NCD detection efficiency, which includes the neutron capture and event identification efficiency, and T_{live} is the live-time of the NCD phase. This dissertation focuses primarily on decreasing the uncertainties and inaccuracies in the event identification efficiency factor of $\epsilon(r, \theta, \phi)$ and the T_{live} parameters, as will be discussed in later chapters.

This chapter will provide a brief description of the NCD detectors and their installation – many detailed descriptions exist elsewhere [47, 48, 49, 50, 51, 52, 53]. Understanding the events that were to be measured by the NCDs was critical for measuring the solar neutrino flux and subsequently the data acquisition design and electronic calibrations.

3.2 NCD Array Description

The NCDs were specially constructed for the purpose of this experiment since an important requirement of these detectors was that they had very low levels of activity from U and Th – levels that were unavailable in standard commercial products. All components of these detectors were chosen and constructed with tight constraints on their radiopurity. As well, the NCDs were designed to fully contain the He gas without leaks under water at pressures up to 3.18 atm at the bottom of the AV, and without significant leaching into the heavy water.

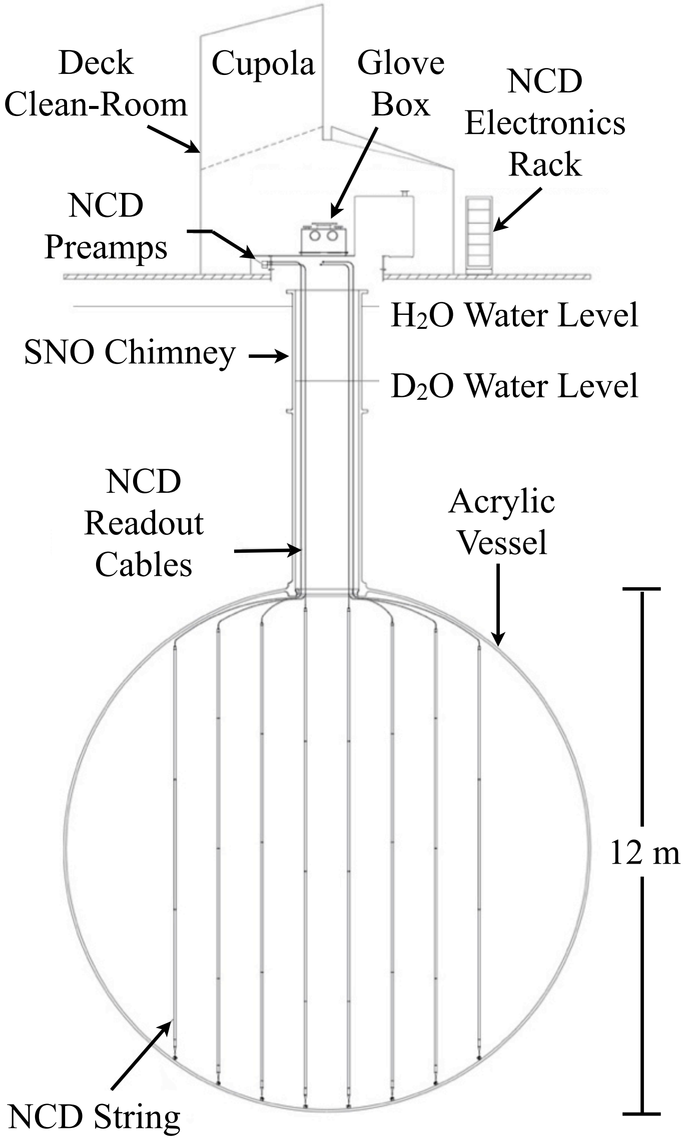

Figure 3.1: The NCD strings are three or four NCD segments that are welded together, end-on-end, to form a 9- to 11-m proportional counter "string". The NCD array is 40 NCD strings which were installed vertically inside SNO's Acrylic Vessel. Figure is modified from [46].

3.2.1 NCD String Characteristics

The NCDs were constructed in 2.0-, 2.5-, and 3.0-meter counter *segments* that were identical (except for their lengths). The outer walls of each segment, which account for the majority of the NCD material, were constructed by Mirotech, Ltd. from nickel tubes that were fabricated through a chemical-vapor-deposition (CVD) process onto an aluminum mandrel. This process produces a very pure nickel body. Each segment was fitted with end-caps at both ends, which connected an external copper endplug to the 50-micron copper anode wire strung down the center of the segments. Fused silica insulating feed-throughs were used to shield the anode wire in the end-cap regions. Events in this region were undesirable because energy spectra and pulse shape of events in the end-cap region would have been distorted due to the non-uniform electric field. The shielding reduced the number of events detected near the end-caps, effectively producing an in-active section of the NCD. The individual NCD counter segments were electrically connected by nickel couplers (Fig. 3.2(b)) and eventually welded together into an array of 40 *strings* with total lengths ranging from 9 to 11 meters. The segments of 36 of the NCD strings were filled with a mixture of ^{3}He and CF$_4$ gas. The segments of 4 strings were filled with ^{4}He and CF$_4$ gas for the purpose of background measurements[1]. Initially, the NCD array consisted of 96 strings, but after the results from Phase I of SNO, the array was reduced to just 40 strings.. For more information on the reduction of the NCD array see § 4.2 of [52]. Some physical characteristics of the NCDs are listed in Table 3.1 and a schematic of the NCD string and a junction between two segments is shown in Fig. 3.2.

Typically, proportional counters are read out from both ends for the purpose of determining the position of the event along the anode wire of the counter, also called the event's z-position. Due to material and mechanical constraints, and to lessen the reduction of Cherenkov light from CC and ES reactions caused by the presence of the

---

[1] Neutrons do not capture on ^{4}He.

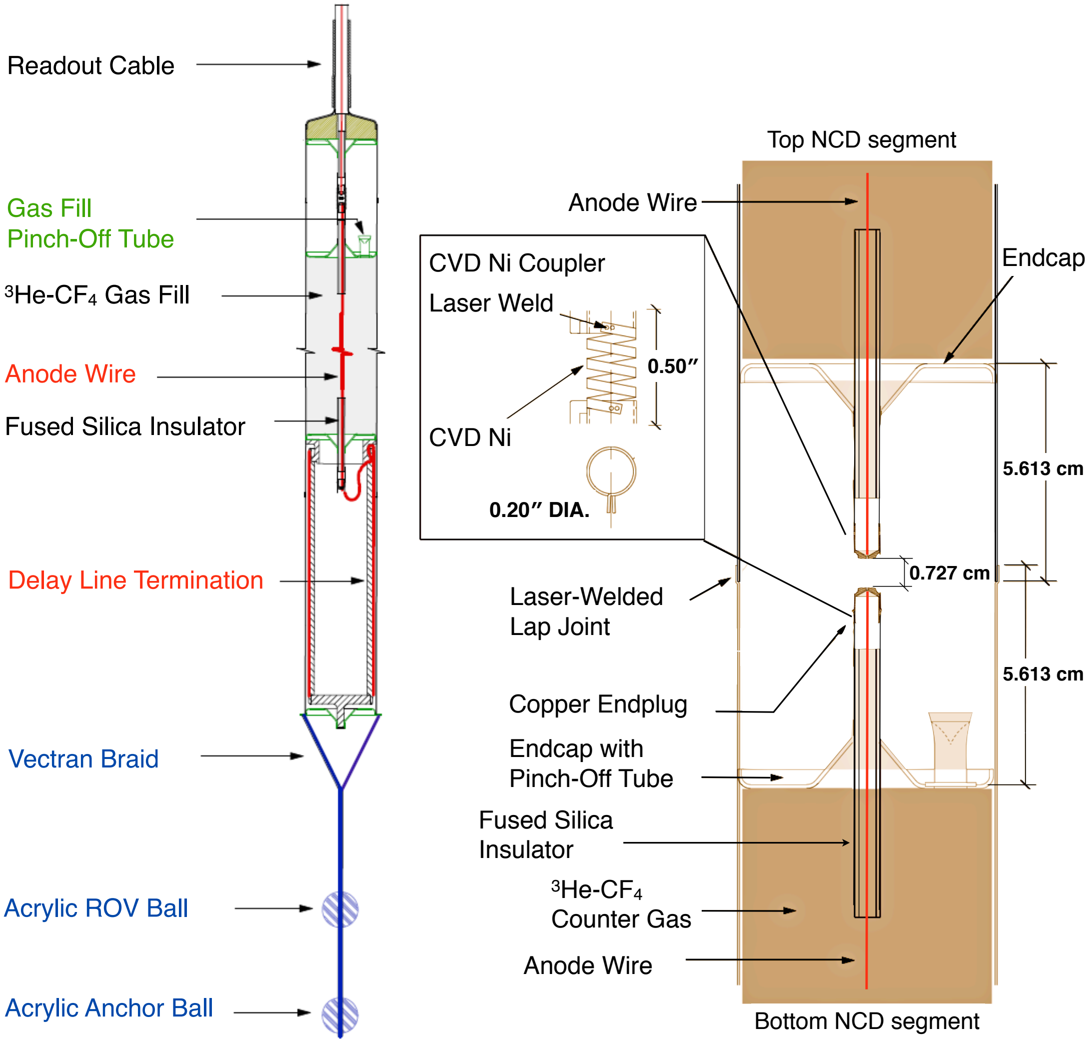

(a) Full NCD String

(b) NCD Segment Junction

Figure 3.2: Schematic of (a) an NCD string and (b) the junction between two NCD segments [47].

Table 3.1: Some physical characteristics of the NCDs.

Segment Length	200, 250, 300 cm
Inner Diameter	5.08 cm
Wall Thickness	$0.036^{+0.012}_{-0.000}$ cm
Cu Anode Diameter	50 μm
Gas Mixture	
^{3}He:CF$_4$	85:15 by volume
^{4}He:CF$_4$	85:15 by volume
Installed String Lengths	9 - 11 m
Total Installed Array Length	398 m
Total Installed Array Inner Area	63.52 m^2

NCD array, the NCDs were single-ended-readout proportional counters. To facilitate the measurement of an event's z-position, an open-ended delay line was welded to the bottom of each NCD string. The delay line was a copper circuit etched on flexible circuit sheet and wrapped around an acrylic core 19-cm in length, which was housed inside a CVD nickel tube. The delay lines coupled directly to the external copper endplug of the bottom segment of each NCD string. Each delay line had a round-trip signal propagation time of approximately 90 ns [47]. As will be shown in § 3.3.3, an event's z-position was determined from the time-delayed pulse-reflection, which was enhanced by the delay line.

3.2.2 Summary of Installation

The NCD strings were installed vertically on a 1-m square lattice at anchor points along the bottom of the AV. (Fig. 3.3). The anchor points were put in place during the construction of the AV before the beginning of SNO Phase I. The installation of the NCDs occurred in two phases due to space restrictions in the underground laboratory. During the "pre-deployment" phase some of the NCD segments were welded together into sections such that no section exceeded 5.5 m – the maximum length that would fit vertically within the Deck Clean Room (Fig. 3.1). Also during the pre-deployment phase, an anchor assembly, made from acrylic spheres and vectran rope, was connected to the delay line nickel housing on each NCD string. During deployment, the lower sections of the NCD strings were lowered into the SNO chimney and the final welds were done above the chimney before the entire string was lowered into the AV. After a neutron calibration source was used to verify the integrity of the string, the string was then maneuvered by an underwater remotely-operated vehicle into their AV anchor points. The acrylic spheres were mounted into the anchor points using the buoyant force of the NCDs to secure them in place. Although the author significantly contributed to this operation, commissioning of the NCD array and its installation of the data acquisition system, the reader is referred to a thorough description written by Stonehill [52] (Chapters 3 and 4).

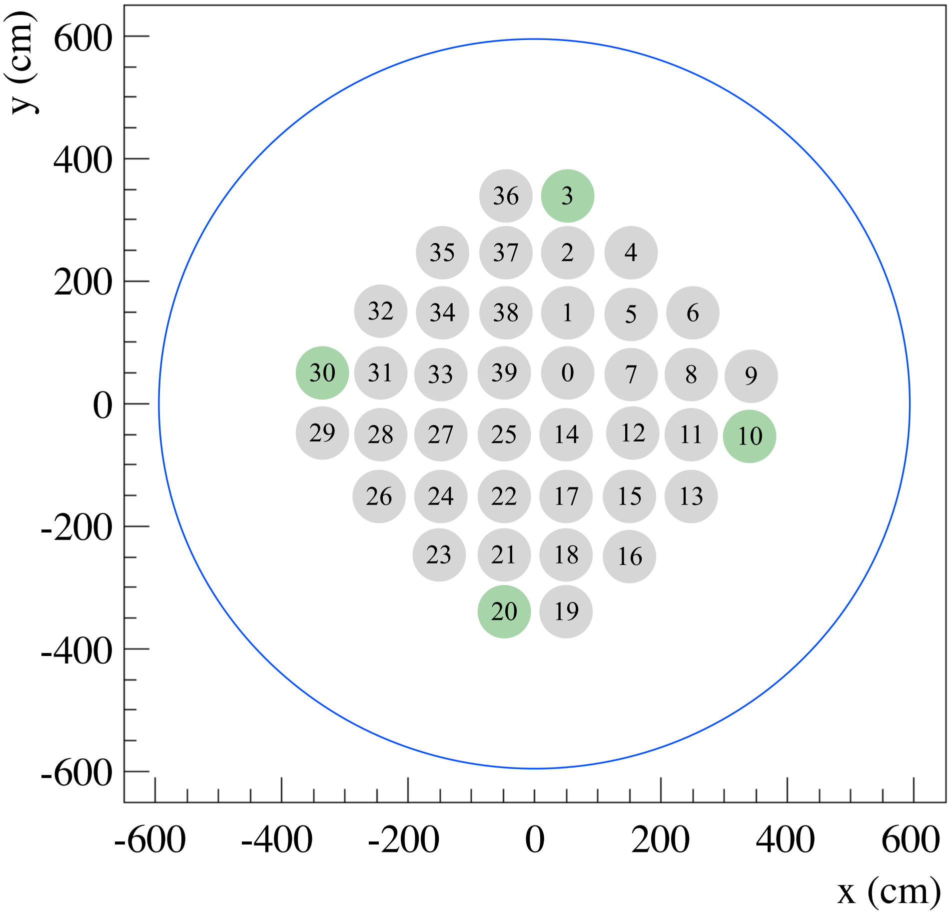

Figure 3.3: A schematic of the NCD array as they were installed in the AV indicating the locations of the strings in the SNO coordinate system. Strings 3, 10, 20 and 30 were filled with ^{4}He. The blue circle with a radius of 600 cm indicates the equator of the AV. Note that the size of the NCDs are not drawn to scale. Some SNO documents use an alphanumeric naming convention and the conversion from NCD string number to name is found in Table C.1. Figure is modified from [47].

3.3 Signal and Backgrounds

Generally, there were three types of events in the NCDs: neutrons from solar neutrino interactions and background sources, alphas from decaying nuclei, and instrumental noise events. The energy and pulse-shape characteristics of neutron capture and alpha events, along with the rate at which they occur, motivated the design of the NCD data acquisition system and calibrations, which is discussed in the next two chapters. Measuring the rate of alpha events in the NCDs was necessary for two primary reasons. First, in the energy range of interest for neutron captures, 150 keV to 900 keV, alphas and neutrons produced events with similar energy (§ 3.3.1). Thus, alphas were a background to the neutron signal. Second, total alpha rates provided a way to measure of the amounts of ^{238}U and ^{232}Th impurities in the NCDs. Since nuclei with ^{238}U and ^{232}Th decay chains produce background neutrons through photodisintegration and (α,n) reactions with ^{2}H and ^{17,18}O, measuring the amount of ^{238}U and ^{232}Th in the NCDs is important for estimating the rate of this background.

Contributions to the number of neutrons measured by the NCDs has either been estimated or previously measured. Based on the measured flux from the previous SNO measurements, solar neutrinos were expected to produce about 12.6 neutrons per day, isotropically dispersed throughout the AV. Besides neutrons from solar neutrino interactions, neutrons could have been produced by interactions with neutrinos and anti-neutrinos emitted from supernovae[2], gammas with $E > 2.223$ MeV that could disintegrate deuterium, cosmic-ray muon spallation, (α,n) reactions involving various detector components, terrestrial and atmospheric anti-neutrino interactions, and fission of ^{238}U. The expected number of neutrons produced by U, Th and Rn contamination of the D$_2$O, based upon the measured U and Th levels in SNO's Phase I, and produced by terrestrial and atmospheric anti-neutrinos was estimated to be about 1.4 neutrons per day in the NCD phase (Table B.2 of [50]). The number of neutrons

---

[2] A supernova was not detected during any phase at SNO.

produced by photodisintegration and (α,n) reactions from contamination in the NCDs and external sources was previously estimated for the original 96-string NCD array[3]. Because of the proximity of the 96-string NCD array to the AV, the different overall amount of NCD material, and the difference in detection efficiency between the 96-string and 40-string array, it is difficult to translate the previously made estimates of neutron backgrounds made by Heeger, Dunmore and Robertson [38, 50] to estimates of the number of background neutrons to expect in the NCD phase. These studies estimated a total rate of about 0.5 background neutrons per day caused by the NCD array and cables (∼4% of the BP00 SSM). The rate of neutron production within the AV by cosmic-ray muons was measured by Ahmad, using data from the first few months of SNO's Phase I, to be 11.5 ± 0.7 neutrons per day [37]. In the Phase I data set, muon-induced neutrons were completely removed by tagging the muon and cutting the subsequent 20 seconds of data. This same removal efficiency is expected for the NCD phase. Overall, the total rate of neutrons produced in the AV per day should be around 24 neutrons per day. The measurement and estimate of background neutrons for the NCD phase is currently underway.

Alpha particles are emitted by various naturally occurring nuclei within the U and Th decay chains (Fig. 3.4). The CVD process left behind trace amounts of ^{238}U, ^{232}Th and their progeny that were dispersed throughout the volume of the NCD nickel bodies (and also in other components of the NCD array apparatus). Furthermore, before being filled with He gas during construction, about half of the NCD nickel bodies were stored in an underground location near Index, Washington, for the purpose of shielding them from cosmic rays[4]. In that location, high levels of radon were found to have plated ^{210}Pb and ^{210}Po along the inner and outer surfaces. Subsequently, electropolishing and acid etching procedures removed the majority of that contamination,

---

[3] Recall that before SNO Phase I, the NCD array was designed to consist of 96 NCD strings, but was reduced to 40 strings.

[4] Of the 96 original NCD strings, only half were constructed out of nickel bodies that had been stored underground.

but not completely. The half-life for ^{210}Po is 138 days, small enough that the plated ^{210}Po would have decayed away before the NCDs were installed into SNO. However, the rate of 5.3-MeV alphas was measured to be apparently stable during the last month of NCD commissioning data and the first month of NCD production data[5], implying that the presence of ^{210}Po was supported by ^{210}Pb, which has a half-life of 22.3 years and beta-decays to ^{210}Po [52]. For this reason, the 5.3-MeV alpha from the decay of ^{210}Po is the most significant source of non-instrumental background events in the NCDs [50].

The neutron capture efficiency of the NCD array is preliminarily determined to be approximately 26.01%. Thus, the number of neutrons captured by the NCD array is expected to be about 3.4 neutrons per day (excluding muon-induced neutrons). In the first month of data from the installed array of NCDs, the total rate of all non-instrumental events above 150 keV, excluding neutrons produced by muons, was measured to be 227.4 ± 3.8 per day [52], or about 0.003 Hz. An analysis presented in Chapter 8 shows that the rate of non-instrumental events above 1.0 MeV remained constant on all fully functioning NCDs during the entire NCD phase. It should be pointed out that the original estimate of the rate of NCD events, which was used for determining the NCD data acquisition system design, was different than this measurement, partly because of the unexpected ^{210}Po-decays and the change in the size of the NCD array from 96 strings to 40. However, the rate of events was still expected to be about this order of magnitude.

In addition to events from neutrons and alphas, the majority of events in the NCDs were instrumental backgrounds. Instrumental events are produced by the NCD electronics and data acquisition hardware, microdischarges in the NCDs, NCD delay lines or preamps, or, due to very low thresholds, thermal baseline noise events. The total event rate in the NCD phase, including all instrumental noise events, was nominally

---

[5] Although the statistics were low in Stonehill's measurement, there was no observed decrease in the rate of alphas in the NCD phase.

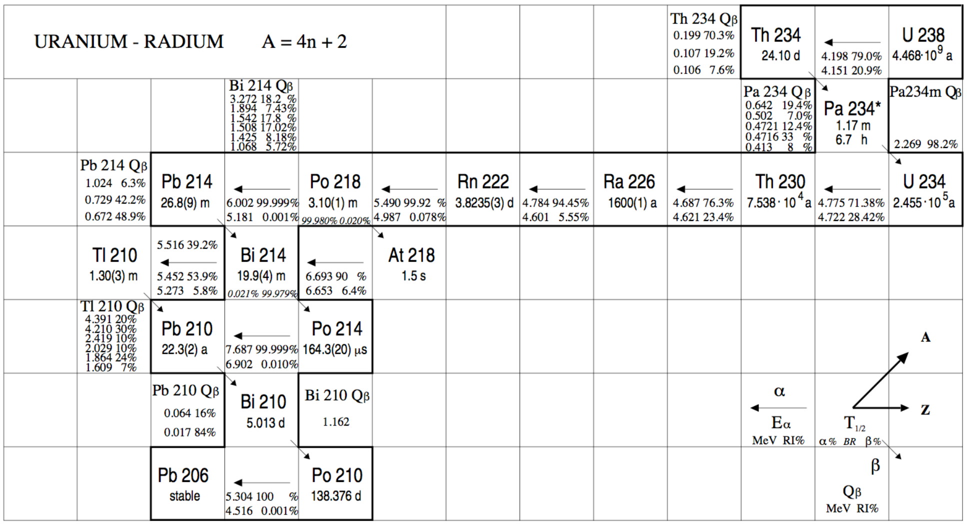

(a) ^{238}U decay chain (Radium series)

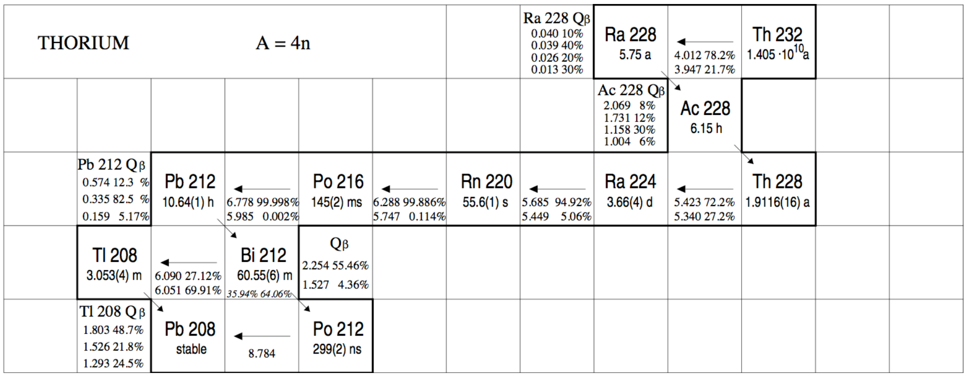

(b) ^{232}Th decay chain (Thorium series)

Figure 3.4: Shown here are half-lives, branching ratios and decay modes for nuclei within the ^{238}U and ^{232}Th decay chains. Figure is from [54].

around 0.15 Hz. More discussion of instrumental events is given in Chapter 7, where an analysis of the stability of the rate of thermal baseline noise events is presented.

3.3.1 NCD Energy Spectrum

Neutrons and alphas produced events in the NCDs with energies ranging from 191 keV up to 8.78 MeV. The total kinetic energy of a proton-triton pair produced in neutron capture (Eq. 3.1) events is 764 keV, where the energy of the proton and triton are 573 keV and 191 keV, respectively. However, the size of the proportional counter relative to the length of the ionizing particle tracks in the NCDs affected the resulting energy spectrum of events. In neutron captures, the proton and triton would sometimes strike the NCD wall before depositing all of the 764 keV of energy into the gas: the "wall-effect" [43]. The wall-effect is clearly seen in the energy spectrum of events during an AmBe calibration source run (Fig. 3.5(a)). The energies of the alphas emitted in the U and Th decay chains range from 3.94 MeV (^{232}Th) up to 8.78 MeV (^{212}Po) – Fig. 3.4. Alpha particles emitted from the interior surface of the NCDs from the ^{210}Po decays (*surface* alphas) could deposit only a fraction of their total energy due to the wall-effect. As well, alpha particles that were emitted by nuclei embedded in the NCD body (*bulk* alphas from the ^{238}U and ^{232}Th decay chains) lost energy in collisions within the nickel bodies before entering the NCD gas volume. Bulk alphas were also subject to the wall-effect. Both of these effects contributed to the low-energy tail of alpha events that extended down below the neutron energy region, shown in Fig. 3.5(b). In addition, space-charge effects resulted in reduced charge collection for alphas with certain track orientations relative to the NCD anode and is the reason for the 5.3-MeV ^{210}Po alpha-peak to be found at 4.9 MeV instead of 5.3 MeV [52].

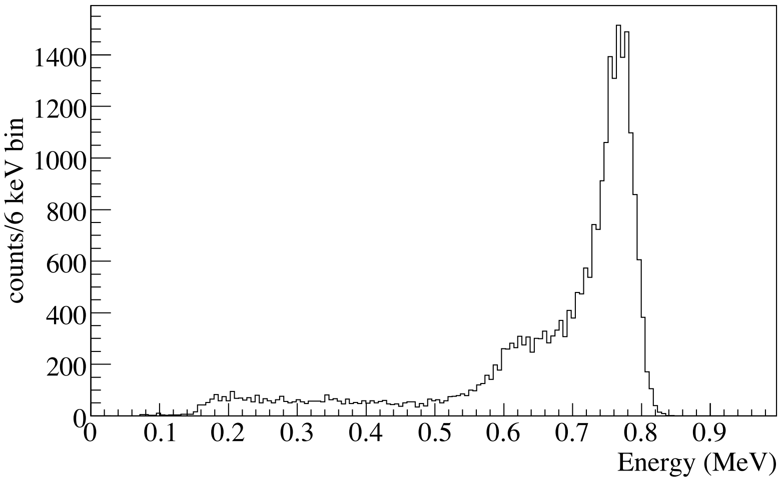

(a) AmBe neutron source - NCD string 39.

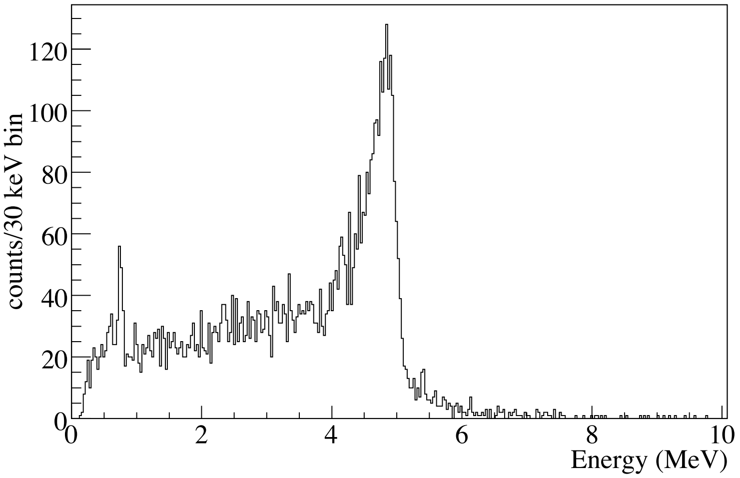

(b) Open data set.

Figure 3.5: The energy spectrum for NCD events (a) measured on NCD string 39 in the presence of a neutron source at the center of the AV, and (b) for the 36 ^{3}He-filled NCDs during the "open" data set - which is approximately the first month's worth of NCD data. Instrumental backgrounds have been removed.

3.3.2 Alpha and Proton-Triton Pulse Shapes

Increasing the signal-to-background ratio can be done through analysis of the current signal profile, or pulse shape, to further separate the neutron events from the alpha backgrounds. The pulse shape of neutron captures and alphas depended upon the rate of energy loss inside the NCD gas and the orientation of the ionizing particles relative to the NCD anode. An understanding of the pulse shapes was necessary to design the NCD data acquisition system.

The specific energy loss of an ionizing particle as it traversed the NCD gas, the orientation of the particle's track relative to the anode, and the mobility of the secondary positive ions toward the NCD body wall contributed to the shape of the current signals. For the proton, triton and alpha particles in the NCDs, the chosen method for determining the specific energy loss was to use the Stopping and Range of Ions in Matter (SRIM) numerical method [55]. The specific energy loss, $-dE/dx$, for a proton-triton pair, a 5.5-MeV alpha and a 764-keV alpha are shown in Fig. 3.6. These calculations are called Bragg curves.

The classical Bethe-Bloch treatment of energy loss for ionizing particles in a medium provides some qualitative insight to the SRIM calculations. According to the Bethe-Bloch formula, for an ionizing particle of velocity $\beta = v/c$, the specific energy loss as it travels through a medium is

$$-\frac{dE}{dx} = \frac{4\pi r_e^2 m_e c^2 N_A}{A\beta^2} z^2 Z \left[\frac{1}{2}\ln\frac{2m_e v^2 T_{max}}{I^2} - \ln\left(1-\beta^2\right) - \beta^2\right] \tag{3.3}$$

where r_e is the classical electron radius, m_e is the electron rest mass , N_A is Avogadro's Number, ze is the charge of the ionizing particle (e being the charge of the electron), A and Z are the atomic mass and atomic number of the medium, T_{max} is the maximum kinetic energy that may be imparted to a free electron in a collision in the medium, and I is the average excitation and ionization potential of the medium [57]. According to Eq. 3.3, particles with the same charge have similar specific energy losses. Initially, when the particle is at its maximum velocity, the rate of energy loss begins to increase

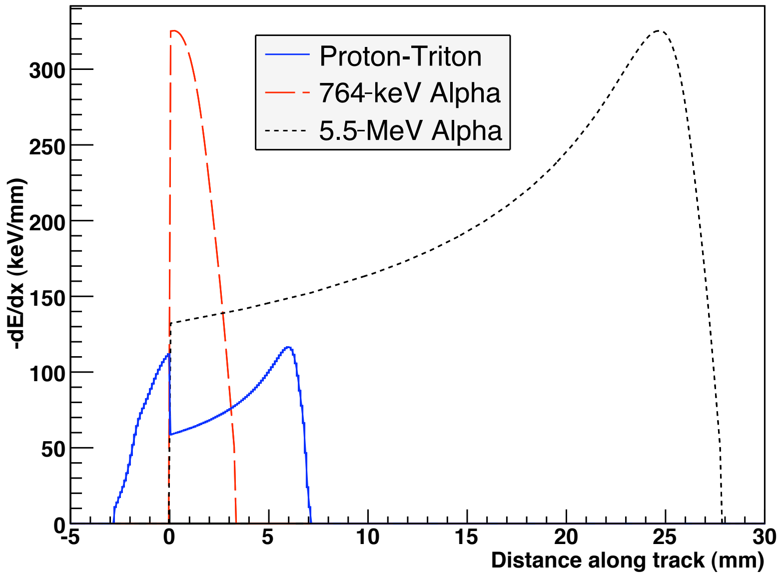

Figure 3.6: The specific energy loss for a proton, triton and two alphas of different energy in the NCD gas. These curves were calculated numerically by the SRIM program. In the proton-triton pair, the proton moves in the positive direction and the triton moves in the negative direction. The data used to produce this plot was obtained from SRIM tables generated by B. Monreal [56].

as the particle traverses the gas and its velocity decreases. Eventually, in the context of the Bethe-Bloche equation, the energy of the particle decreases below the ionization potential of the gas and the rate of energy loss falls to zero. However, this equation fails at low energies, requiring more sophisticated calculations for accurate estimates of the specific energy loss (the SRIM calculations) [43].

The orientation of the particle track relative to a proportional counter's anode wire also affects the pulse shape. Primary electrons produced along the particle track could take a few microseconds to drift toward the anode. When they reach the avalanche region, the secondary electrons are produced. The current at the anode due to the primary and secondary electrons can be expressed as

$$i = \frac{dE}{dx}\frac{dx}{dr}q\frac{\gamma}{I}\left(\frac{dt_d(r)}{dr}\right)^{-1} \tag{3.4}$$

where dx/dr represents the orientation of the track relative to the anode, γ is the gas gain, q is the charge of the electron, and $dt_d(r)/dr$ is the reciprocal of the electron drift velocity [58]. However, the electrons only contribute about 2% of the total charge of the signal, while the remainder of the charge in the event signal is due to the secondary positive-ion drift [43]. The orientation of the track determines the time evolution of the secondary electron production in the avalanche region and subsequently the time evolution of the drift of the secondary positive-ions from the avalanche region to the NCD body wall. The secondary ion drift is responsible for the "ion tail" of the signal which provides the distinguishing characteristics of the pulse shape. The drift time of the secondary ions can be as long as a millisecond, though the time for half of the charge of the signal to evolve is only around two microseconds [59].

Particle tracks in the NCDs had two extremes orientations: perpendicular to the anode and parallel to the anode. Of course, the particle tracks were always somewhere between, but visualizing these two extremes gives a qualitative understanding to the pulse shapes. The primary electrons from the parallel tracks arrived at the avalanche region at nearly the same time. Subsequently, the secondary ions all drifted away from the anode at the same rate. The resulting pulse shape was a sharp negative spike followed by a slowly decreasing current, the ion tail. It was more difficult to determine the type of particle when the track was more parallel to the anode than when it was more perpendicular. This was because the distinguishing characteristics in the ion tail, associated with a particle's Bragg curve, were lost when the track was oriented parallel to the anode. At the other extreme, when a track was oriented perpendicular to the anode, the primary electrons that were closest to the anode arrived first, followed by the electrons from further away. The primary and secondary positive ions then also drifted away at different rates. This orientation preserved the shape of the Bragg curve and resulted in a wider pulse. For example, in Fig. 3.7, two events of similar energy that were clearly in the alpha energy region ($E > 1$ MeV) had different shapes. Because the Bragg curve for alphas at this energy was wider, one can conclude that the wider event was caused by an alpha particle with a track that was more perpendicularly oriented relative to the anode while the narrower event was more parallel.

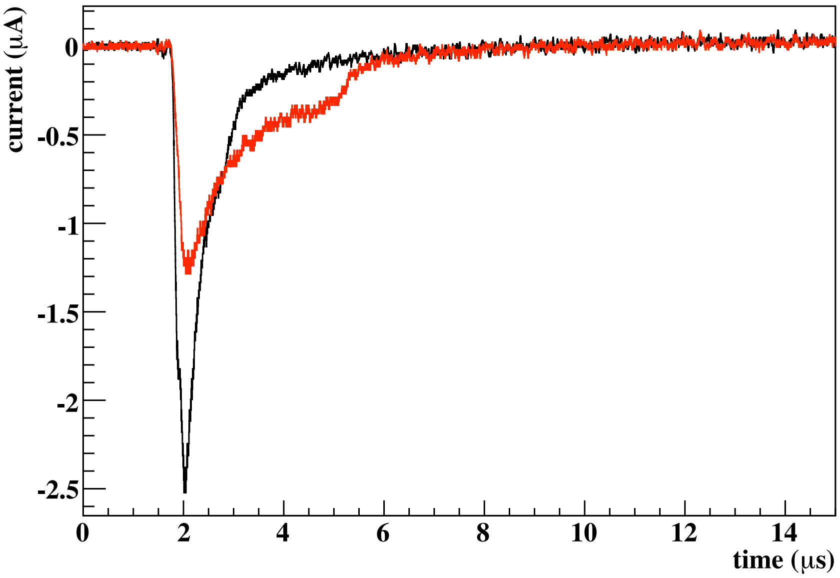

Figure 3.7: Two alpha events with different track orientations relative to the NCD anode. The wider pulse (in red, $E = 4.60$ MeV) was more perpendicular to the anode than the narrower pulse (in black, $E = 4.66$ MeV).

In the neutron energy region (150 keV $< E <$ 900 keV), event characterization was slightly more complicated since both neutrons and alphas produced events in this energy range. Alpha and proton-triton tracks that were parallel to the anode were less distinguishable because, for the reasons given above, they produced a similar pulse shape. Proton-triton tracks *perpendicular* to the anode created a more distinguishable signal that exhibited the features found in their Bragg curves. Alphas that deposited low amounts of energy ($E < 900$ keV) and parallel proton-triton tracks generally had smaller pulse widths. Fig. 3.8 shows two pulses with the same energy, but noticeably different pulse shapes. The double-peak structure in the Bragg curves for proton-tritons (Fig. 3.6) can be seen in the wider pulse.

Work is currently being done by members of the collaboration on a sophisticated Monte Carlo simulation of NCD pulse shapes. The Monte Carlo includes effects not discussed here, such as space charge, alpha and proton-triton track straggling, and alphas from the NCD anode, which will improve neutron capture identification [60, 61].

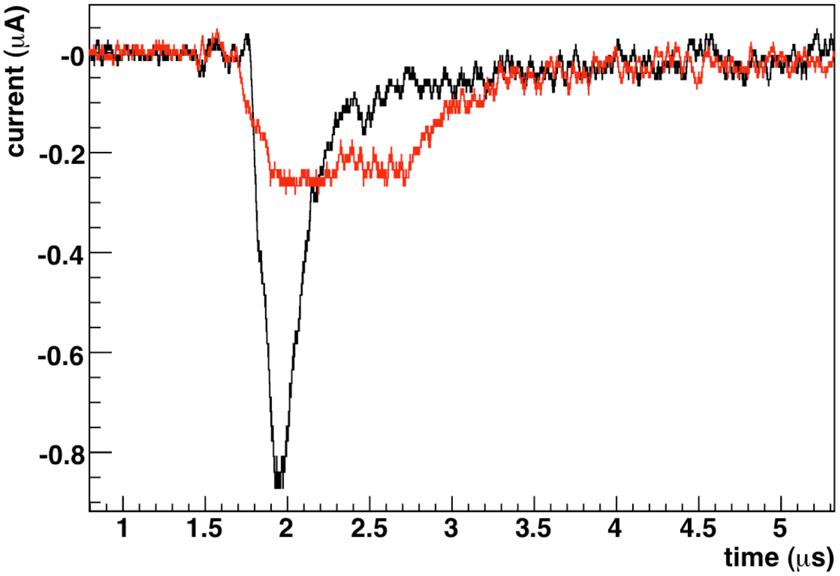

Figure 3.8: Two events with different track orientations relative to the NCD anode, both measured to have 0.77 MeV of energy. The wider pulse (red) can only be produced by a proton-triton event that is oriented perpendicular to the NCD anode.

3.3.3 Vertical Resolution

In order to accurately measure the solar neutrino flux, a fiducial volume defines the size of the neutrino target and is chosen for its low levels of background. Because the NCDs were on a fixed x-y grid, determining if an event occurred within a fiducial volume was reduced to measuring the vertical position, or z-position, of the event. When current collected on the anode of the NCD, the signal did not propagate in a preferred direction. Rather, the signal split with one portion of the current propagating toward the read-out cable and the other portion toward the bottom of the NCD. (The exact ratio of the current amplitude of the signal propagating toward the read-out cable to the signal propagating toward the bottom of the NCD is determined by the z-position of the event due to charge division along the anode [43]. Charge division has been exploited by other groups to measure the z-position of events in ^{3}He proportional counters with single-ended readout, but was determined to be unsuitable for the NCDs [62, 63, 64, 59].) The result was an output signal that appeared as a sum of two signals similar in amplitude and shape[6] but delayed in time. The delay line increased the time between the split signals by about 80-90 ns. The measured delay time, Δt, was related to the z-position by $\Delta t = t_d + 2z/v_c$, where t_d is the added time from the delay line and $v_c = 0.86c$ is the velocity of propagation of the signal [65]. Time-domain or Fourier spectrum analysis can potentially be used to determine the z-position of events [50]. Furthermore, the delay lines enhanced the ability to determine problems with the integrity of the NCDs and were helpful in quality assurance analysis. An example of a pulse shape that clearly shows the delay is found in Fig. 3.9

The NCD Data Acquisition system was designed under consideration of the expected characteristics of events in the NCDs just described here. In particular, the total rate of events, range of event energies and current amplitudes, the need for pulse-shape discrimination of neutron captures from alpha events, and the desire for

---

[6] This is not exactly correct since the two portions of the signal underwent different transformations because one traversed a greater distance in the NCD than the other.

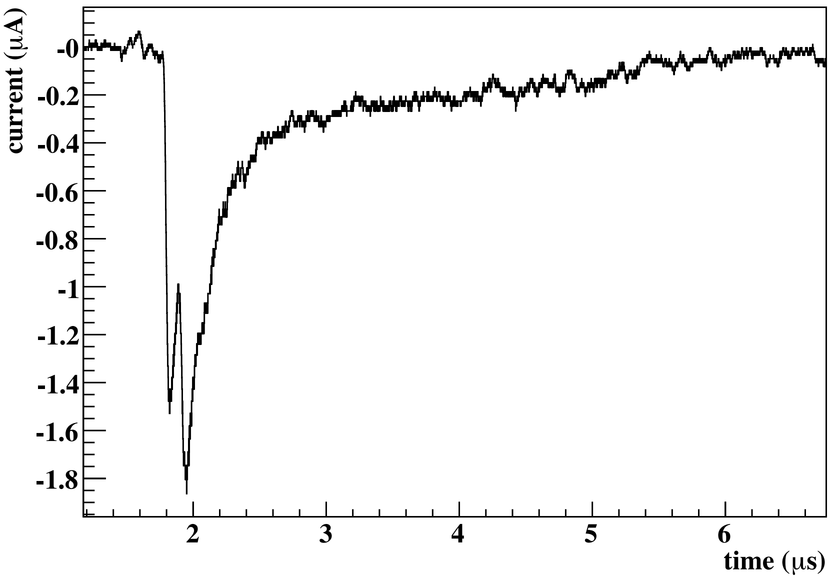

Figure 3.9: The double-peak of the signal (E = 2.97 MeV) around t = 1.8 and 2.0 μs was used to determine the z-position of NCD events. The distance between the peaks is 126 ns, placing it about 5.3 m above the delay line.

z-position determination were motiving factors in the design of the data acquisition.

Chapter 4

NCD DATA ACQUISITION

4.1 Data Acquisition Goals and Overview

The NCD Data Acquisition (NCD DAQ) was designed to facilitate identification of neutron capture events, be capable of measuring the expected event rate from a nearby galactic supernova, provide for an accurate calculation of detector live-time, integrate into SNO's PMT system, remain capable of running independently from the PMTs so that the NCD system can be "supernova-live", and be controlled remotely from the surface control room [58]. The DAQ was designed around the use of two digitizing oscilloscopes that recorded the pulse shape information for particle identification and VME-based shaper/ADC cards that measured the total energy of the signal, which could be read out at up to 20 kHz with minimal dead-time losses. A local galactic supernova event (< 10 kpc), though not detected during the NCD phase, was expected to produce hundreds of events over a duration of ten seconds [66]. The maximum data throughput of the dual-oscilloscopes was limited to 2 Hz (entirely sufficient for solar neutrino data), thus necessitating the shaper/ADC cards. The purpose of this chapter is to provide an overview of the data acquisition system in order to discuss the calibrations and data integrity analysis. This chapter is broken into two sections. First, the front-end cables, preamplifier and detector components through which NCD signals propagated and were recorded are described. Then, the remaining hardware and software which supported these devices, controled the hardware and wrote the events to disk will be described. Finally, a description of the hardware built to calibrate the DAQ is given.

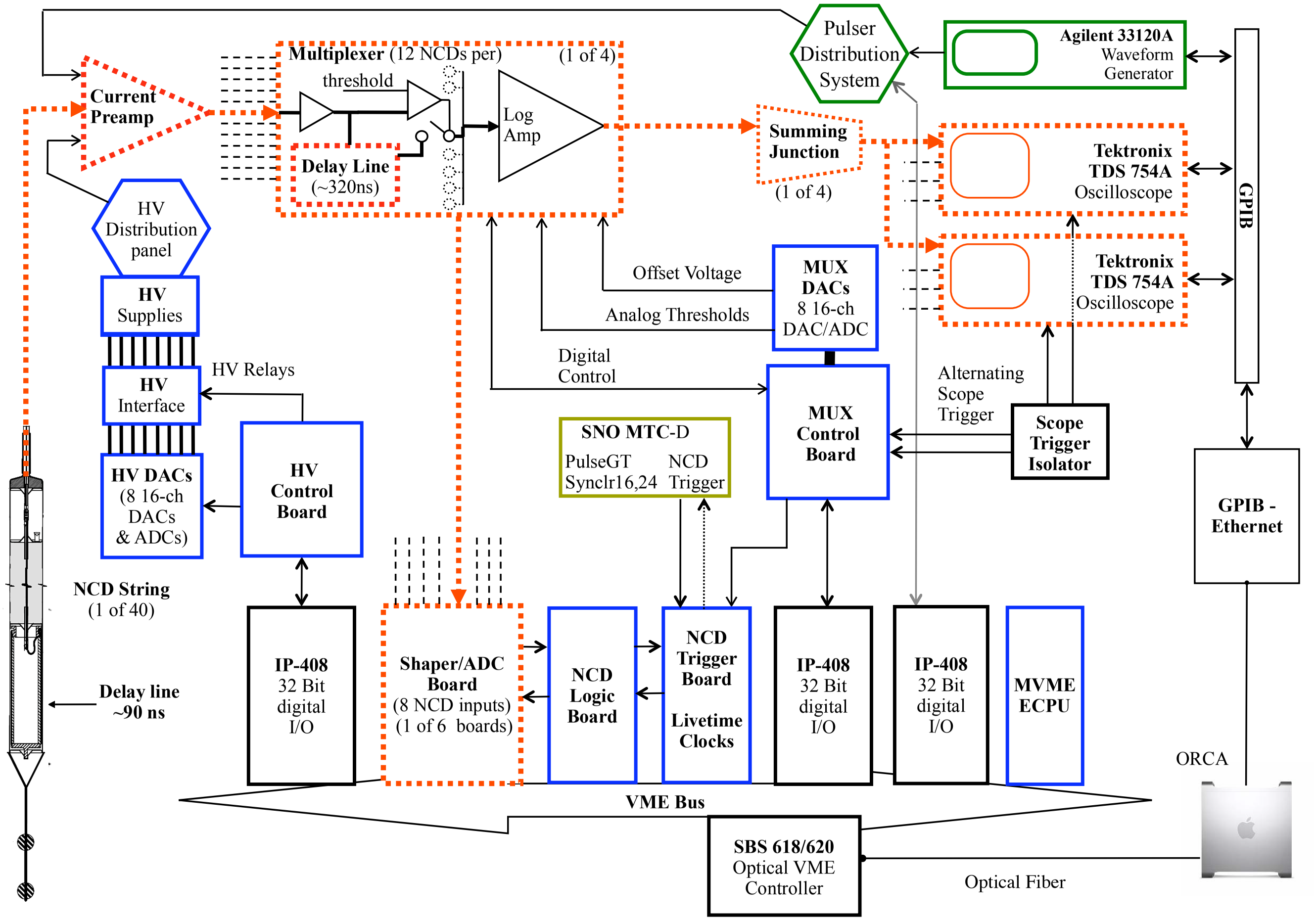

NCD Flow Chart Rev. H, 3/28/07

Figure 4.1: The NCD Data Acquisition System [47]. The hardware outlined in dashed-red are the primary acquisition hardware through which NCD signals propagate and are recorded.

4.2 Signal Readout Hardware

The signal readout hardware included the NCD cables, resistive coupler, current-preamplifiers, multiplexers (MUX), digital oscilloscopes, and shaper/ADC cards as indicated in Fig. 4.1.

4.2.1 Front-End Electronics

The front-end electronics included, but were not limited to[1], the resistive coupler, the NCD cable and the preamplifier. Each NCD string was coupled to its NCD cable via a resistive coupler inside a NCD cable bell (Fig. 4.2). Each NCD cable was then connected to a current-preamplifier. The purpose of the front-end components were to amplify NCD signals and prepare them for digitization while minimizing noise over the entire dynamic range and maintaining the pulse fidelity necessary for particle identification [59].

Resistive Coupler and the NCD cable

The purpose of the resistive coupler was to match the impedance of the NCD string to the NCD cable so that NCD current signals were transmitted to the DAQ without reflections at junctions between components. The characteristic impedance for signals propagating along the NCD strings was calculated to be 415 Ω [59], whereas, due to design constraints, the characteristic impedance of the NCD cables was 93 Ω. Thus, the resistive coupler's total resistance was set to 325 Ω, increasing the total electrical load on the NCD string output to 418 Ω, nearly equal to the characteristic impedance of the NCD.

The resistive coupler was a teflon ring 1.06 inches in diameter and 1.23 cm in width (Fig. 4.3) that connected the NCD copper endplug to the NCD cable bell (Fig. 4.2).

---

[1] The NCD components such as the anode wire and feedthroughs were also considered front-end components and are discussed elsewhere [59].

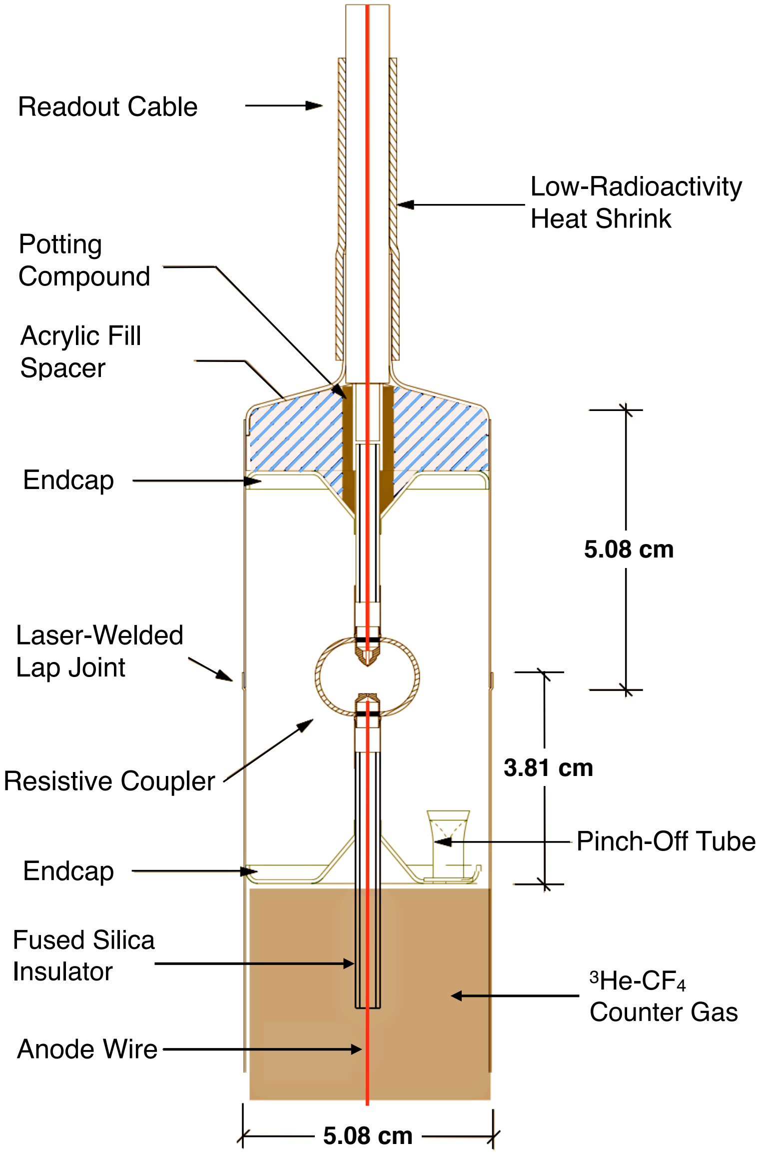

Figure 4.2: Each NCD string's uppermost segment connects to the NCD cable via the resistive coupler and the NCD cable bell [47].

On opposite sides of the the ring were circular holes surrounded by a nickel collar that were connected by "Stablohm" resistance wire that looped back and forth along grooves on the outer side of the Teflon ring. The length of the resistance wire was 11 inches, resulting in a total resistance of 325 Ω. The nickel collars connected to the copper endplugs of the NCD string and the cable bell (Fig. 4.2).

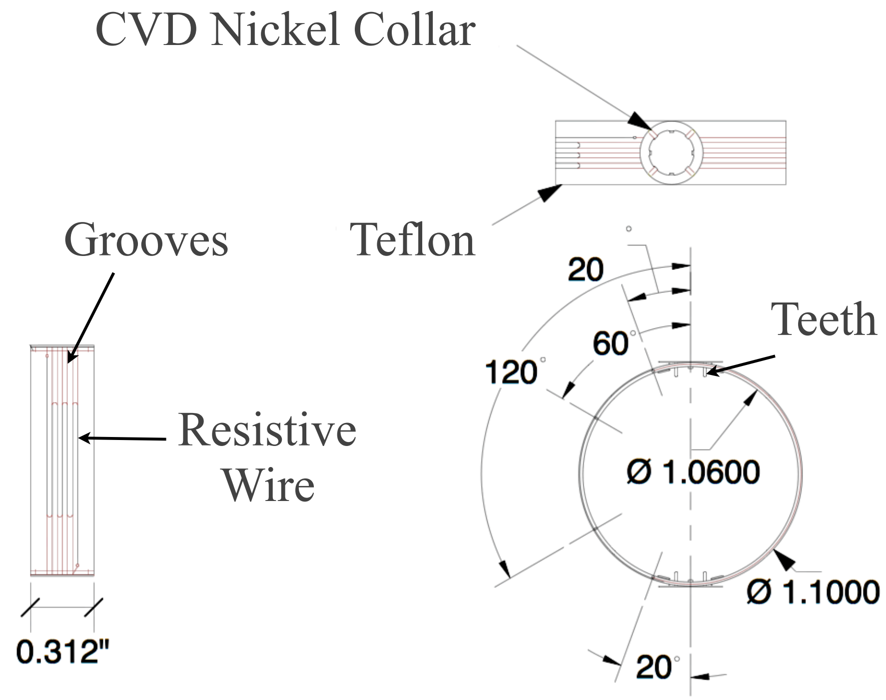

Figure 4.3: A schematic diagram of the resistive coupler. Modified from [50].

The NCD cables were specially constructed 93-Ω cables with a 0.5-mm copper central conductor, surrounded by a woven-ribbon copper ground shield. They were cut to an appropriate length for each NCD. To reduce stress at the connection to the uppermost NCD segment of each string, they were constructed with a low-density polyethylene dielectric and high-density polyethylene jacket such that the cables were slightly buoyant. These materials were also chosen to minimize radioactive backgrounds. [49, 59]. High voltage was supplied to the cables via the preamplifier box, described in the next section.

Current Preamplifier

The preamplifier linearly transformed the current signal into a voltage signal at a gain of 27.5 mV/μA. The input impedance of each preamp that was connected to the NCD cable was tuned to the impedance of the NCD cable, 93 Ω, to prevent reflections, as mentioned above. The impedance at each preamplifier output was 50 Ω. The preamplifier outputs were connected to a multiplexer input channel by Belden 88240 RG-58 cables.

Each preamplifier was housed in an individual metal box that provided additional inputs for the NCD high voltage and electronic-calibration pulse. The high voltage supplies that held the NCD anode at 1950 volts were coupled to the NCD cables within the preamplifier box. The calibration pulse injection input was coupled to the preamplifier and NCD signal input via a 100-kΩ resistor. The high impedance coupling of the pulse injection input and the high voltage supply input to the NCD input and preamplifier restricted NCD signals from propagating into the calibration and high voltage lines. The preamplifier boxes were housed inside the Deck Clean-Room within a circular metal raceway surrounding the SNO chimney port that provided shielding to reduce electromagnetic interference from nearby electronics (Fig. 3.1). The NCD cables were fed up the chimney and through the inner wall of the raceway to their preamplifier inputs.

4.2.2 Signal Digitization

In § 3.3 it was noted that the average neutron-plus-alpha event rate per day for the NCD array was about 230 events per day. This low rate allowed for an event digitizing system that used two, four-channel digital oscilloscopes and four multiplexers (MUX) to record signals from the 40 NCDs[2]. With two oscilloscopes, one oscilloscope could be

---

[2] The NCD DAQ was originally designed to record the data from up to 96 NCD strings using two oscilloscopes and 8 MUX.

busy reading out data, while the other oscilloscope was available for event digitization, minimizing the number of missed simultaneous events [49].

Multiplexers

The purpose of the four MUX was to efficiently direct the output of the 40 NCD strings into one of four channels on each digital oscilloscope. Each MUX box had 12 input channels that received signals from NCD preamplifiers. Input signals on each of the 12 channels were split into two parallel 1x buffer amplifiers. The output of one of these amplifiers was connected to an input channel on a shaper/ADC card. Signals propagated to the shaper/ADC cards without discrimination since each shaper/ADC channel had a separate threshold. The other amplifier output was connected to a 320-ns delay line, a noninductively-wound RG-58 cable housed within the MUX box, and a discriminator. An external device (§ 4.3.2) provided an analog threshold voltage level for each MUX input channel that was used by the MUX box discriminator circuitry. Input signals of sufficient current-amplitude were multiplexed together with any signals above threshold from the other 12 channels.[3] The multiplexed signals were then logarithmically amplified and fed to a single output that was connected to the summing junction and digital oscilloscopes.

Logarithmic Amplifier

The smallest current signal expected in the NCDs was 200 nA from a perpendicularly oriented neutron capture event, while the largest expected current from the higher energy alphas was about 29 μA [59]. In order to accommodate this dynamic range of amplitudes, maximizing the use of the 8-bit oscilloscope digitization, the signals were logarithmically amplified after they were multiplexed and before they were digitized. The end result of logarithmic amplification was that small amplitude signals and

---

[3] However, due to the low event rate, 99.7% of all MUX events in the NCD phase were associated with a signal from only one MUX channel.

large amplitude signals had roughly the same uncertainty in each time-bin of the digitized waveform. Without the use of a logamp, the vertical scaling of the digital oscilloscope would have been set at such a level as to accommodate the large current signals within the 8-bit ADC of the digital oscilloscope. This would have resulted in a large fractional error on small amplitude signals [67]. The logamp chosen for the NCD DAQ was the Analog Devices AD8307 [68].

A negative DC-offset was added to the signal just at the input of the logamp. The output of the logamp was always of negative polarity regardless of the input signal polarity, and thus would rectify noise without the offset. Although all physics signals had negative polarity, the electronic noise along the baseline was bipolar. Without the negative DC-offset, the positive polarity components of the thermal noise would have been inverted, effectively shifting the baseline of the output signal in the negative direction, and could have possibly caused issues in identifying thermal noise and electromagnetic interference events. The DC-offset level was approximately set to -15 mV, and varied by a few mV on each MUX channel [67, 69].

Oscilloscopes

The oscilloscopes were Tektronix TDS754A digital oscilloscopes with 8-bit ADCs [70]. They were capable of sampling at 1 GS/sec when all four channels were used – satisfying the requirement of at least 500 MS/s sampling for the purpose of event z-position measurements [49]. The recorded waveform length could range from 1,000 points to 50,000 points. At 1GS/sec, this corresponds to a range of 1- to 50-μs waveform lengths. Transfer of the waveform across the GPIB to disk depended on the size of the waveform. To balance the needs of pulse shape analysis and DAQ dead-time, the chosen waveform length was 15,000 points (15 μs).

The nominal setting on each channel for the vertical resolution during data acquisition was 50 mV/div, which is 500 mV to span the 256 ADC values (there are 10 vertical divisions). The vertical offset was set to ∼130 mV above zero (2.6 divisions) in order to maximize the use of the 8-bit ADC for the negative polarity pulses while still retaining the ability to measure the few positive polarity electrical discharge events sometimes seen[4]. The time-offset position was adjusted to 10% of the waveform length, which for the NCD experiment was 1.5 μs from the beginning of the digitized waveform. This created a 1.5 μs region of the waveform called the pre-trigger – a period when the MUX channel switch was not closed and the voltage signal at the input of the logamp was just the applied negative DC-offset.

There were two oscilloscopes, each with four input channels. To utilize both oscilloscopes, the log output of the MUX was propagated at the summing junction to two outputs, one for each oscilloscope. The oscilloscopes were externally triggered by a TTL signal from the MUX Controller Board (§ 4.3.2) to the scope's auxiliary trigger, which allowed the DAQ to control the digitization of both oscilloscopes so that only one scope digitized an event while the other remained available. Events on MUX X were recorded on channel X of both scopes, where $X = 0, 1, 2$ or 3. The oscilloscopes were labeled as scope 0 and scope 1 within the data acquisition and analysis software programs, which is how they will be referred to later in this document.

4.2.3 Event Energy Measurements - Shaper/ADC Cards

Due to the long readout-time of a digitized waveform, about one second for a 15,000-point waveform, a nearly separate system composed of the VME-based shaper/ADC cards was constructed to measure the energy of NCD signals. The shaper/ADC cards were capable of acquiring events at a maximum rate of about 20 kHz, sufficient for recording the rate of neutrons produced from a supernova burst. There were eight input channels per shaper/ADC board and six boards in the VME crate. Each channel was independent and had its own shaping, 6-μs signal integration and ADC,

---

[4] During the pre-deployment welding phase there were unexpected discharge events which had positive polarity and large amplitudes. These problems were solved, but the vertical offset remained at this level in order to diagnose possible future problems during data acquisition.

and individually programmable thresholds and gains [48, 49]. The ADCs were 12-bit MAX120 chips and were calibrated to energy using the characteristic shape of the neutron energy spectrum by determining the linear conversion of ADC values to the 764 keV peak and the 191 keV cut-off. The gains on each shaper/ADC channel were set such that the energy range spanned by the 12 bits was from zero to 11.9 MeV. The higher readout rate also facilitated the neutron capture efficiency calibrations of the NCD array. The rate from the AmBe neutron-source was about 25 Hz and using just the digitizing scopes would have required significantly more time to measure the capture efficiencies of the NCDs to the same level of precision.

To simplify the live-time measurements, at the occurrence of an event on a particular shaper/ADC channel, all other channels on that board and the remaining boards were prohibited from acquiring data until the event was read out and cleared. Each shaper/ADC board was equipped with input and output TTL signal logic connectors. The TTL logic signal instructed the shaper/ADC cards to stop data acquisition, and was relayed to all shaper/ADC cards via the NCD Logic Board and the NCD Trigger Card (§ 4.3.3).

4.3 Supporting Hardware and Software

In this section, the remaining "support" hardware in the system, the data acquisition software program, and the readout algorithms are described. An overview diagram of the data acquisition components is found in Fig. 4.1. More information is available elsewhere [49, 71, 72].

The end result of the NCD DAQ was the transmission of event data packets over the local ethernet to programs which built events from both systems into a single analyzable data file. Each data file corresponds to one period of acquisition called a "run", which was limited in duration to seven hours. Each event in the run file contained all of the available information about the event and was stored to disk in ZEBRA and ROOT file formats. Also, the state of the detector was recorded for each run and stored in a set of databanks for access during analysis.

4.3.1 Software Control and User Interface

The SNO Hardware Acquisition Real-time Control (SHaRC) was built primarily to control the PMT system. The NCD DAQ utilized the Object-oriented Real-time Control and Acquisition (ORCA) program, the next-generation version of SHaRC. ORCA was designed to also *be controlled by* an external program through an internet communication protocol. SHaRC was modified to use this feature so that under normal operations, SHaRC controled both systems and the detector operator interfaced with just SHaRC.

The ORCA was an object-oriented, multi-threaded program on an Apple G5 Macintosh personal computer running the Mac OS X operating system. The Macintosh computer was located underground next to the two racks that housed the NCD DAQ hardware. The NCD DAQ computer connected to the VME crate via a PCI-card that was connected by a fiber-optic cable to the SBS 620 VME Controller Card. A GPIB to Ethernet controller box interfaced all GPIB-based devices (the digital oscilloscopes and the HP/Agilent Waveform Generator) to the NCD DAQ computer on an isolated local network.

Each hardware component of the NCD DAQ was represented as an object in the ORCA graphical user interface. In addition, run control, data readout, data manipulation and observation tasks were represented. These objects were grouped together to define data flow and hardware communications. Interfaces within ORCA were also used to set the MUX channel thresholds, the DC-level offset at the input of the logamp, and the shaper/ADC channel thresholds and gains, as well as many other low-level hardware parameters [71].

4.3.2 MUX Support Hardware

The complete MUX system was composed of two separate devices that worked in conjunction with the four MUX boxes. The threshold levels for each MUX channel were set on the MUX DAC/ADC board. The MUX Controller Board interfaced with each MUX box and with the MUX DAC/ADC board, controlling the reading/writing of thresholds and communication of event information through a 40-pin ribbon cable connection to each MUX box.

MUX Channel Thresholds

The MUX channel thresholds were set on the MUX DAC/ADC board that connected to each MUX through a 26-pin ribbon cable. There was one MUX DAC/ADC board that housed eight sets of 8-bit DAC/ADC chip-sets to support eight MUX boxes. Each DAC held a MUX channel's analog threshold down on differential pair lines on the 26-pin ribbon cable. The ADCs provided a way to read back the thresholds values set on the DAC. Each chip-set stored 13 values – a threshold for each of the 12 MUX channels and the DC-offset supplied at the input of the logamp. The ORCA interface for the MUX thresholds displayed the ADC value and allowed the detector operator to set each DAC.

MUX Controller Board

The MUX Controller Board (MUXCB) interfaced the MUX and MUX DAC/ADC boards to the system. The MUXCB monitored and collected MUX event information, triggered the oscilloscopes, and read and wrote MUX channel thresholds to the MUX DAC/ADC board. The DAQ computer connected to the MUXCB via a 32-channel input/output I/O card, the IP-408, which resided in an AVME9660 VMEbus carrier board in the VME crate. A 50-pin ribbon cable connected the carrier board to the MUXCB.

An event on a MUX channel was registered by the MUXCB when a MUX discriminator latched. The MUXCB then sent a logic signal to the NCD Trigger Card to inform the DAQ of the event and triggered an oscilloscope to begin digitization. During normal operations, the MUXCB alternated the scope triggers between the two scopes. However, each scope had an output busy status line that could be polled by the MUXCB. Upon request from ORCA, the MUXCB provided two 32-bit MUX event registers that contained information on which MUX channel fired, the busy-line status of the oscilloscopes, and which oscilloscope digitized the event. The MUX registers and the digitized waveform were packaged by ORCA into a single event. If the selected scope was busy at the time of the event, then the scope trigger was not initiated and the MUX registers were packaged into an event without a digitized waveform[5].

4.3.3 Data Readout Algorithm Overview

To complete the chapter, this section will briefly describe the functions of a programmable embedded Central Processing Unit (eCPU) and the NCD Trigger Card and how they are used in conjunction with ORCA to record MUX events, digitized waveforms and shaper/ADC events to disk. First the functions performed by NCD Trigger Card and eCPU are described. Then, as examples, the steps taken by the various components to process a shaper/ADC event and a MUX event are described. The descriptions in this subsection are mostly paraphrased from Duba's Ph.D. dissertation [49].

NCD Trigger Card

The NCD Trigger Card (NTC) resided in the VME crate and was the hardware interface between the NCD system and the PMT system, as well as the hardware

---

[5] The original design called for the MUX to trigger the other scope in this circumstance if it were not busy, but this operation was prevented due to a hardware bug in the MUXCB.

interface between the eCPU and the MUX and shaper/ADC systems. The NTC performed four tasks; it registered events on the MUX and shaper/ADC systems; it controlled four scalers that counted NCD system live-time, shaper/ADC live-time, MUX live-time, and oscilloscope live-time; it notified the PMT system of NCD events; and it relayed MUX and shaper/ADC event triggers to the eCPU.

Trigger pulses from the MUX and shaper/ADC systems were sent to the NTC to indicate the presence of a signal above their respective thresholds. The MUXCB sent a NIM-logic trigger signal directly to the MUX trigger input on the NTC. The TTL lock-out signal from each shaper/ADC board ran through a digital OR on the NCD Logic Board that connected to the shaper/ADC trigger input on the NTC. When a shaper/ADC trigger occurred, the NTC relayed the TTL lock-out signal back to the NCD Logic Board, which fanned-out the inhibit signal to all of the shaper/ADC boards, preventing further ADC conversions. When either a MUX or shaper/ADC trigger pulse was received, the NTC set an internal MUX trigger-bit or shaper/ADC trigger-bit to on. The bit status was readable by the eCPU, which continuously polled these bits during data acquisition. When a bit was on, the eCPU performed a series of tasks to read out the appropriate hardware.

A 10 MHz clock resided on the NTC to provide live-time information for the various NCD hardware. The 10 MHz clock was divided down to 1-MHz precision and then split into four separate 40-bit scalers. The scalers were read at the beginning and end of each run, and at fifteen minute intervals during the run. The four scalers separately counted the total time of the run, the shaper/ADC live-time, the MUX live-time, and the oscilloscope availability live-time. Each scaler only incremented when the respective system was available for event acquisition.

Within SNO, events were assigned a unique global trigger identification number (GTID) in order to ensure proper correlation of PMT triggers and NCD triggers to a single event. Located on the NTC is a 24-bit GTID register that increments in-step with the GTID registers of the PMT system whenever a NCD or PMT event occurs.

The NTC communicates with the SNO Master Trigger Card, which collects all event triggers and notifies the PMT system and NCD system to increment their GTID registers simultaneously. The GTID number is packaged into each event packet when written to disk.

Embedded CPU

To maximize the speed of the data acquisition by limiting short-term DAQ computer functions from interfering with event readout, a VME-based programmable eCPU, the Motorola MV167, was utilized to poll and read the VME-based hardware. Event information was placed in a dual-port memory (DPM) buffer that could be read and written to by both the eCPU and ORCA, thereby freeing ORCA to complete other tasks (such as reading out the digitized waveforms and processing events to disk). The DPM was located on the SBS 620 VME Controller Card and the eCPU resided on a separate 6-U sized VME card.

The DPM was used to store shaper/ADC event registers in a FIFO circular buffer that could be asynchronously read out by ORCA. The information passed to ORCA via the DPM was the event's channel, time of occurrence, GTID and ADC value.

The MUX event registers did not utilize a FIFO buffer in the DPM memory-space. To indicate new MUX events, memory space for two registers were defined in the DPM and used to pass an event indicator between the eCPU and ORCA. One register could be written to by the eCPU and read by ORCA, and vice-versa for the other register. When the eCPU read the MUX trigger-bit set to on, the eCPU incremented its writable register. ORCA would read this increment, which initiated separate processing threads within ORCA to read the MUX event registers from the MUXCB and to read out the digitize waveform, if one was triggered. Before reading out the oscilloscopes, ORCA acknowledged the event by incrementing its register to equal the eCPU's register.

Shaper/ADC Readout

An event on a shaper/ADC that had an energy above threshold was converted to an ADC value. The shaper/ADC system was inhibited from further data acquisition, as previously described, and the eCPU read the shaper/ADC board information and ADC value into the DPM circular buffer. ORCA then read out the DPM and packed the shaper/ADC event information into an event packet that was copied to disk and sent via local ethernet to an external computer that combined NCD and PMT events. Once the shaper/ADC board information was read, the eCPU cleared the event registers and the inhibit signal was released. The system was then ready for the next event.

MUX and Digitized Waveform Readout

An event that occured on the MUX system with a current above threshold initiated the following actions. The MUXCB sent a MUX trigger signal to the NCD Trigger Card. The NTC then sent an event pulse to the MTC-D, incrementing the system-wide GTID value. When the event occurred, the MUXCB independently triggered the oscilloscopes to digitize the waveform. ORCA was then notified of the event through the DPM MUX registers, described in the previous section. The MUX event information, obtained by ORCA from the MUXCB, was combined with the digitized waveform, downloaded from the appropriate oscilloscope over GPIB, into an event packet, written to disk and shipped to an external event-building computer that combined NCD and PMT events. Once the MUX registers had been read, ORCA re-initialized the MUX system, and the system was ready for the next event.

4.4 Electronics Calibration Hardware

In order to calibrate the electronics, a known signal was injected into the pulser input of the preamplifier and then recorded by the NCD DAQ in the usual way. The goal was to compare the input signal with the measured signal, and then characterize the transformation caused by the NCD DAQ. The electronic calibration pulse hardware were an Agilent 33120 Arbitrary Waveform Generator [73], the Pulser Distribution System (PDS) and a 30-dB attenuator (Fig. 4.1).

The waveform generator was controlled by ORCA via a GPIB interface and was programmed to output a variety of arbitrary waveforms for the calibrations. Because the minimum peak-to-peak voltage output of the waveform generator was 25 mV, a 30dB attenuator at the output of the waveform generator was used to reduce the amplitude of the signal before it was connected to the input of the PDS so that injected signals could be of the same amplitudes as NCD signals.

The PDS was a fan-out device used specifically for the calibration pulse that connected an individual output to each of the pulser inputs on the preamplifiers. The input calibration pulse was amplified by a factor of 7.22 through an AD8055 amplifier and then distributed to each PDS output. The PDS was controlled through a 50-pin ribbon cable to the VME daughter-board holding an IP-408 card [49]. The individual outputs could be set to on/off states. Thus, any subset of the NCD preamps could be chosen to receive the calibration signal from the waveform generator. Typically, for calibrations that required the digitized waveform record, a signal was injected into one NCD preamp at a time.

Electronic calibrations were performed once a week during data acquisition and are the subject of the next chapter.

Chapter 5

THE NCD EMPIRICAL ELECTRONICS MODEL AND ELECTRONICS CALIBRATIONS

The calibration and characterization of the NCD electronics are required for the neutrino flux analysis. Signals from the NCDs were recorded in ADC values in the digitized waveforms and in the shaper/ADC cards. It is necessary to transfrom these raw data into current pulses and energies. The threshold levels for each shaper/ADC and MUX channel must be determined since they are directly related to the neutron detection efficiency of the NCDs. Finally, the electronics transfer function of the DAQ must be characterized in order to perform precision pulse-shape analysis. The goal of the electronics calibration is to measure the parameters that describe the NCD electronics model and make the results available so that they may be used to transform the NCD data into a calibrated data set that can be used for the final data analysis. A Monte Carlo simulation of the NCD experiment will also access these data to produce simulated data sets.

The raw shaper/ADC spectrum is to be converted into an energy spectrum by utilizing data from neutron source calibration data and the electronics calibration linearity measurements described in this chapter. In addition, the linearity calibrations measured the response of the shaper/ADC channels over the *entire* expected range of energies and determined the minimum threshold for analog-to-digital conversion for each channel.

In order to analyze digitized waveforms for the purpose of event identification and background rejection, the electronics transfer function and signal amplifications of the channels were determined. NCD signals were linearly amplified in the preamp and MUX, then logarithmically amplified in the MUX and finally converted from a voltage signal at the input of the oscilloscopes to a digital waveform. Each component of the system, including the NCD strings and cables, affect the pulse shape due to varying bandwidth restrictions and has been characterized.

5.1 The Electronics Model

An electronics model of the NCD DAQ is used to simulate the propagation of NCD signals and certain electronics calibration pulses through the system. Components of the DAQ are typically grouped together into a single operation or parameter in order to simplify the model and facilitate the measurement of the necessary system properties. Once the electronics model was defined and parameterized, the electronics calibrations were carried out to measure those parameters.

The electronics model (Fig. 5.1) consists of four sections:

- NCD string, NCD delay line and NCD cable
- Preamplifier Unit
- Read-out Hardware
    - Digitization Hardware (MUX/Logamp/Scope)
    - Shaper/ADC
- Electronics Calibration Waveform Generator

5.1.1 NCD string, delay line, and cable

The NCD string, NCD delay line, and NCD cable, shown in Fig. 5.1, are modeled as passive low-pass filters and a time-delay caused by a pulse propagation time. The characteristic time constants and the signal propagation time along each NCD string, cable, and delay line have been measured. The NCD string and cable are better described as transmission lines, but for the purposes of calibrating the NCD DAQ

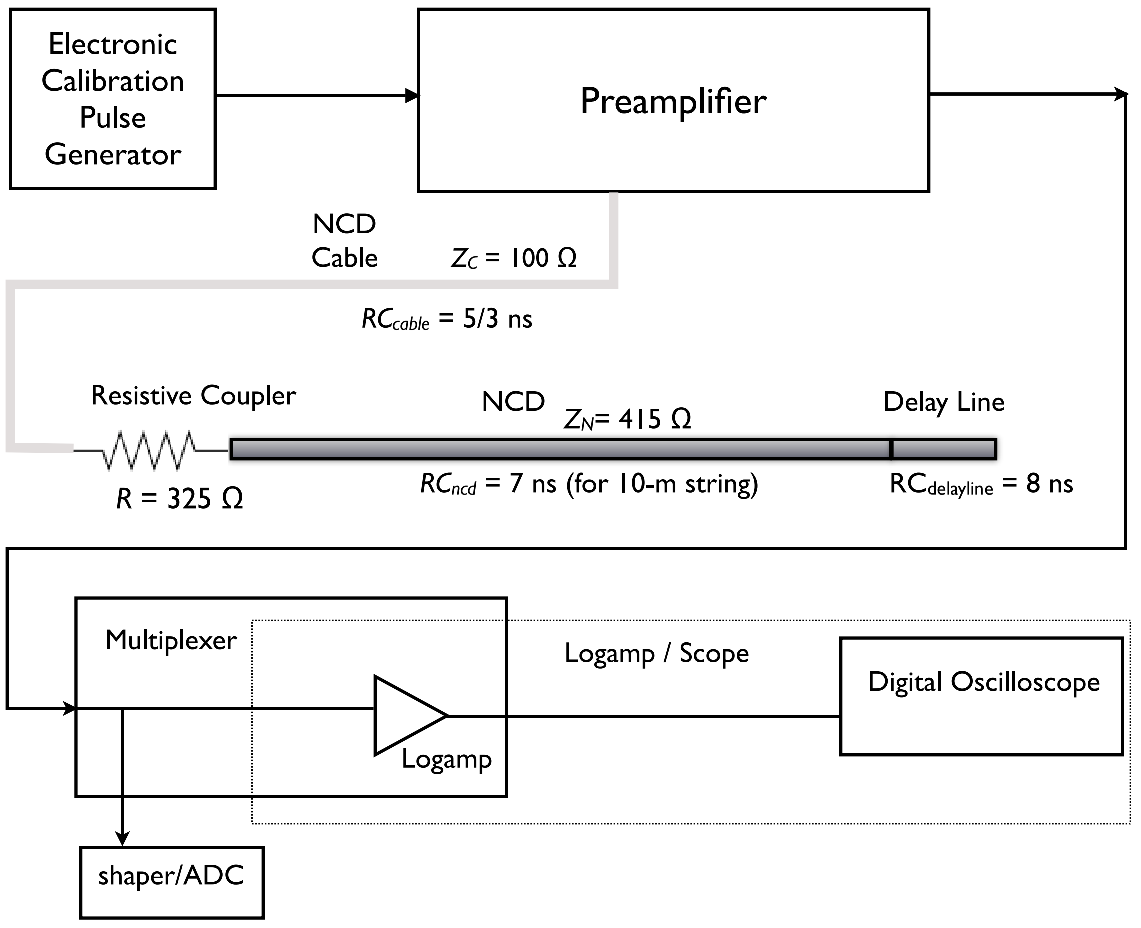

Figure 5.1: A general overview of the NCD Electronics Model.

this simplification adequately describes the transformation of electronic calibration pulses that propagated through these components. As will be explained in § 5.1.4, electronics calibration pulses partially propagated down the NCD cable, string, and delay line and the effect on the electronics calibration pulse was modeled.

5.1.2 Preamplifier Unit

The model for the preamplifier unit has three main components (Fig. 5.2). First, there is the preamp itself, with a measured amplification of 27.5 ± 0.2 mV/μA (§ 4.2.1). At the output of the preamp, there are two passive filters, a low-pass and high-pass, RC_{low} and RC_{high}, with characteristic time constants of 3.3 ns and 58 μs, respectively. These filters represent the overall bandwidth of the preamplifier unit. At the calibration pulse input, there is a 100-kΩ resistor that has a parasitic capacitance.

Input signals from the NCDs are treated differently than electronics calibration signals arriving from the pulser input. NCD signals are amplified and bandwidth limited by the aforementioned low- and high-pass filters. Only the calibration pulses propagate through the 100-kΩ resistor .

The 100-kΩ resistor with a parasitic capacitance is modeled as the sum of the input signal transformed by a passive high-pass filter and amplified, with the original input signal (Eq. 5.1). The averaged value of the amplification factor, g_{pc}, and time constant, RC_{pc}, in the parasitic capacitance model for each preamp is 8.5 ± 0.7 and 1.6 ± 0.1 ns, respectively. A calibration pulse, $V_{pulser}(t)$, is converted to a current at the point N_p and can be expressed as

$$I_{N_p}(t) = \frac{V_{pulser}(t)}{100.05\ \mathrm{k}\Omega} + \frac{g_{pc}}{100.05\ \mathrm{k}\Omega} \cdot \left[V_{pulser}(t) - \frac{1}{RC_{pc}} e^{-t/RC_{pc}} \int_0^t V_{pulser}(\tau) e^{\tau/RC_{pc}} d\tau \right] \quad (5.1)$$

The 2x amplifier shown in the figure compensates for the split in the signal between the two paths in the parasitic capacitance model, but is not explicitly included in Eq. 5.1.

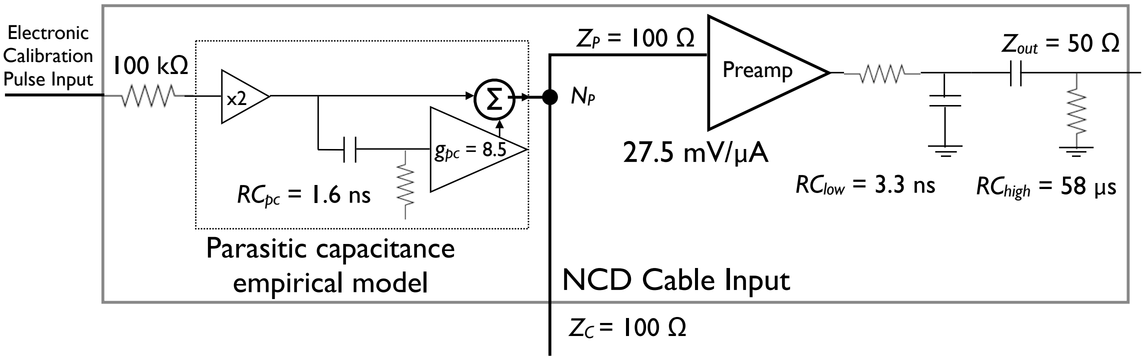

Figure 5.2: Preamplifier Unit Model. The (Σ) symbol indicates that the output of the junction equals the sum of the input signals.

5.1.3 Read-out Hardware

The read-out hardware consisted of the digitization components (MUX, logamp and oscilloscope) and the VME-based shaper/ADC cards, which measured the energy of events.

The shaper/ADC cards

The shaper/ADC cards received events from the preamplifiers (via a buffer in the MUX units) and integrated them to measure the energy of the event. Because the shaper/ADCs did not measure any pulse shape information and the pulse shape transformations did not affect the measured event energy, the effects due to the electronic transfer function are not calculated for shaper/ADC analysis and calibrations. The simplified electronics model for shaper/ADC data is shown in Fig. 5.3.

There were six shaper/ADC cards with eight input channels on each card; there was one channel for each NCD string and eight spare channels. Events with a sufficient energy (greater than a programmable threshold for each channel) were linearly converted by a 12-bit ADC. The conversion value (gain) and offset of the ADC, and the threshold level for each channel were measured separately in the electronics calibrations.

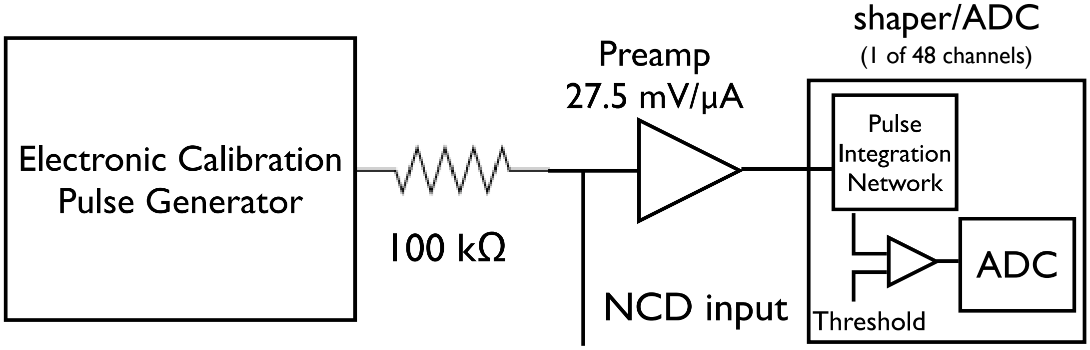

Figure 5.3: Electronics model for analysis of shaper/ADC data.

MUX/Logamp/Scope Model

There are three main sections of the MUX/Logamp/Scope model (Fig. 5.4(a)): the pre-logamp bandpass, the Logamp/Scope, and the post-logamp bandpass and digitization. The circuitry before the logamp is bandwidth limited and modeled as a single passive low-pass filter, RC_{LPF1}. This is followed by the Logamp/Scope section which includes linear gain in the MUX, the logarithmic amplification, and the oscilloscope ADC conversion. The post-Logamp section includes another passive low-pass filter, RC_{LPF2}, to represent the bandwidth limitations in the actual logamp and post-logamp components, such as the cables and summing junction. This section concludes with the digitization of the signal.

The simulation model of the oscilloscope is performed in two stages and I will attempt to explain carefully how this works. The MUX linear and logarithmic amplifiers, along with oscilloscope's ADC conversion of the output of the logamp are combined into a single transformation, as will been shown later in this section. The primary reason for this was to simplify the model into a single transformation to ease the final data analysis efforts. At point **B** in the model (Fig. 5.4(a)), the amplitude of a simulated signal was a fractional value in the *units* of the oscilloscope's ADC values, but not yet "digitized". Furthermore, because the amplitude of a simulated signal was in fractional values at point **B**, the signal could then propagate through second low-pass filter (RC_{LPF2}) without incurring significant rounding errors. Finally, the digitization occurred by rounding each point in the waveform to the nearest integer. The simplified model is shown in Fig. 5.4(b), which will be developed in the next section.

Logamp/Scope Model

The Logamp/Scope section is the most complicated portion of the electronics model. This section combines the DC-offsets (§ 4.2.2), the logamp, the linear gains in the internal MUX circuitry, a post-logamp offset, and the scope offset setting into a single transformation characterized by five parameters.

Each of the components in the model correspond to a physical aspect of the MUX, logamp or oscillscope, or correspond to a group of real hardware components. The MUX delay time, Δt, represents the length of the delay line for each channel in the MUX. For each MUX box, there is a single DC-offset intentionally added at the input of the logamp, $V_{LogOffset}$ (§ 4.2.2). The actual offset at the input to the logamp may vary by a few mV for each MUX channel and is included in the model as $V_{ChanOffset}$. The internal electronics of the MUX have various linear gains before the signal arrives at the logamp and the total amplification is parameterized as g_{MUX-1}. Each MUX has a single logarithmic amplifier. After the logamp, the MUX electronics includes other amplifiers, g_{MUX-2}, and a DC-offset $V_{PostLog}$. The oscilloscope vertical offset, V_{Scope}, is included in the model before the signal is converted into the ADC units of the oscilloscope. The scope offset could be placed anywhere in the model after the logamp, but is placed here for convenience. The 8-bit ADC conversion of input

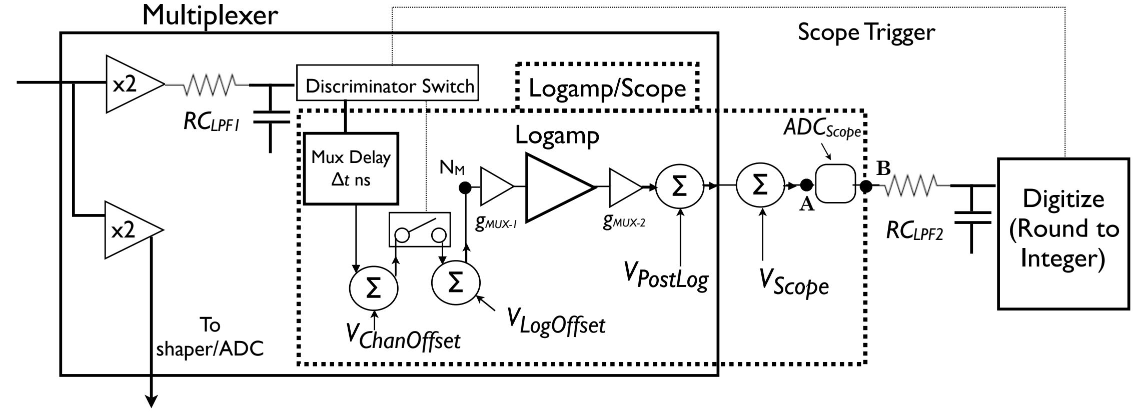

(a) Full MUX/Logamp/Scope Electronics Model.

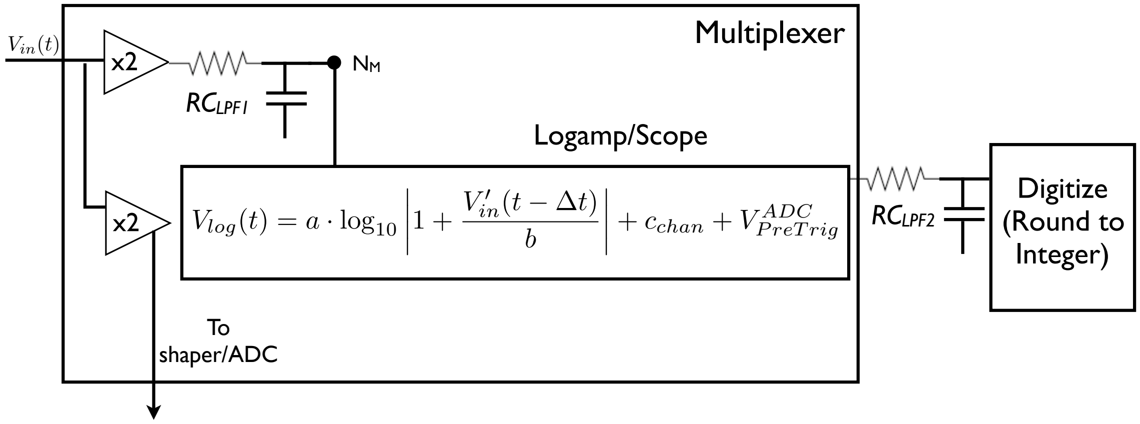

(b) Simplified MUX/Logamp/Scope Electronics model

Figure 5.4: The MUX/Logamp/Scope Electronics Model with all components (a) and in its simplified form (b). The (Σ) symbol used in (a) indicates that the output of the junction equals the sum of the input signals.

voltage to a digital value, ADC_{Scope}, is determined by the volts/division setting on the oscilloscope.

An explanation of the model used to reduce these components to five measurable parameters is now presented. The general equation for the logarithmic amplification of a signal, V_o, is

$$V_{log} = V_\gamma \cdot \log_{10} \left| \frac{V_o}{V_{intercept}} \right|$$

where $V_{intercept}$ is a characteristic of the logamp[1] and V_γ is the slope voltage in units of volts/20 dB. [68]. Consider an input signal on a particular MUX channel, $V_{in}(t)$. Including the various gains, offsets and time delay in the MUX/Logamp/Scope (Fig. 5.4(a)), but not yet including the ADC_{Scope}, the signal at point **A** is

$$V_{log}(t) = V_\gamma \cdot g_{MUX-2} \cdot \log_{10} \left| \frac{(V'_{in}(t - \Delta t) + V_{LogOffset} + V_{ChanOffset}) \cdot g_{MUX-1}}{V_{intercept}} \right| + V_{postLog} + V_{scope} \quad (5.2)$$

where $V'_{in}(t)$ indicates the input signal was bandwidth limited by the MUX (RC_{LPF1}). In the pre-trigger region of the waveform (§ 4.2.2) before the MUX switch has been closed[2], $V'_{in}(t) = 0$ and $V_{ChanOffset} = 0$, yet $V_{LogOffset}$ is nonzero. The output of the logamp in the pre-trigger region of the signal, $V_{PreTrig}$, is

$$V_{PreTrig} = V_\gamma \cdot g_{MUX-2} \cdot \log_{10} \left| \frac{V_{LogOffset} \cdot g_{MUX-1}}{V_{intercept}} \right| + V_{PostLog} + V_{Scope}$$

Now, including the oscilloscope ADC conversion and making the following substitutions

$$a \equiv ADC_{Scope} \cdot V_\gamma \cdot g_{MUX-2}$$

$$c_{log} \equiv a \cdot \log_{10} \left| \frac{V_{LogOffset} \cdot g_{MUX-1}}{V_{intercept}} \right|$$

$$V^{ADC}_{PostLog} \equiv ADC_{Scope} \cdot V_{PostLog}$$

$$V^{ADC}_{Scope} \equiv ADC_{Scope} \cdot V_{Scope}$$

the pre-trigger amplitude at point **B** becomes

$$V^{ADC}_{PreTrig} = ADC_{Scope} \cdot V_{PreTrig} = c_{log} + V^{ADC}_{postLog} + V^{ADC}_{scope} \quad (5.3)$$

---

[1] For an ideal logamp, the output voltage would be zero when $V_o = V_{intercept}$.

[2] Note there are 1500 points at the beginning of the digitized waveforms before the MUX switch closes where the voltage at the input to the logamp is just the logamp DC-offset.

Including the oscilloscope ADC conversion in Eq. 5.2, the pulse at point **B** is

$$V_{log}(t) = a \cdot \log_{10} \left| \frac{(V'_{in}(t-\Delta t) + V_{LogOffset} + V_{ChanOffset}) \cdot g_{MUX-1}}{V_{intercept}} \right| + V^{ADC}_{PostLog} + V^{ADC}_{Scope} \quad (5.4)$$

Defining a new variable, $c_{log+chan}$, similar to c_{log}

$$c_{log+chan} = a \cdot \log_{10} \left| \frac{(V_{LogOffset} + V_{ChanOffset}) \cdot g_{MUX-1}}{V_{intercept}} \right|$$

Eq. 5.4 may be written as

$$\begin{aligned} V_{log}(t) &= a \cdot \log_{10} \left| 1 + \frac{V'_{in}(t-\Delta t)}{b} \right| + c_{log+chan} + V^{ADC}_{PostLog} + V^{ADC}_{Scope} \\ &= a \cdot \log_{10} \left| 1 + \frac{V'_{in}(t-\Delta t)}{b} \right| + c_{log+chan} - c_{log} + (c_{log} + V^{ADC}_{PostLog} + V^{ADC}_{Scope}) \end{aligned}$$

where $b = V_{LogOffset} + V_{ChanOffset}$

Finally, defining one last parameter, c_{chan}

$$c_{chan} \equiv c_{log+chan} - c_{log} = a \cdot \log_{10} \left| 1 + \frac{V_{ChanOffset}}{V_{LogOffset}} \right|$$

and using Eq. 5.3, the output signal from the Logamp/Scope section of the electronics model (Fig. 5.4(b)) can be expressed as

$$V_{log}(t) = a \cdot \log_{10} \left| 1 + \frac{V'_{in}(t-\Delta t)}{b} \right| + c_{chan} + V^{ADC}_{PreTrig} \quad (5.5)$$

The parameters $a, b, c_{chan}, \Delta t$, and $V^{ADC}_{PreTrig}$ constitute the set of parameters called the "logamp parameters". This parameterization of the MUX/Logamp/Scope significantly simplifies the transformation of the signal at the input of the MUX to a logarithmically amplified digitized waveform, or vice versa.

The next step in the model is accounting for the bandwidth limitation due to the logamp, components in the MUX after the logamp, and the cables that connect the output of the MUX to the Summing Junction and oscilloscope channels. This is modeled as a single passive low-pass filter, (RC_{LPF2}). Finally, to complete the

MUX/Logamp/Scope model, digitization of the amplitude was done by rounding to the nearest integer[3].

Because there are components in the model that are MUX-channel dependent and oscilloscope dependent (there are two oscilloscopes in the DAQ), there were two sets of logamp parameters to be measured for each NCD string. The electronics calibrations measured these parameters and the current threshold level of digitization separately for each NCD string.

5.1.4 Electronics Calibration Pulse Generation

The HP/Agilent Arbitrary Waveform Generator, a 30-dB attenuator and the pulser distribution system (PDS), described in § 4.4, are grouped as one unit which produces a waveform that is bandwidth limited at high frequencies (Fig. 5.5). This system injects a defined pulse into the front-end of the electronics at the preamp, which is then propagated through the DAQ and measured by the shaper/ADC and digitization hardware. In the model, the pulser generates a voltage signal with unlimited bandwidth. That simulated signal is then attenuated and passed to the PDS, which has a gain, g_{pds}, and modeled with a passive low-pass filter with a characteristic time constant, $RC_{pds} = 19$ ns.

Pulse Reflections

Calibration signals from the PDS do not propagate directly into the preamp. At the input of the preamplifier unit, the calibration signals pass through the 100-kΩ resistor, which connects to the NCD cable input and the preamp. The effect of the 100-kΩ resistor has already been mentioned (§ 5.1.2). At the junction of the two paths, $\mathrm{N_P}$ in Fig. 5.2, half of the signal propagates directly into the preamp and the other half propagates down the NCD cable. Reflections occur due to the impedance

---

[3] Technically, this could have produced an amplitude that was out of bounds of the 0 - 255 ADC value, but no simulated signals have amplitudes large enough to exceed that limitation.

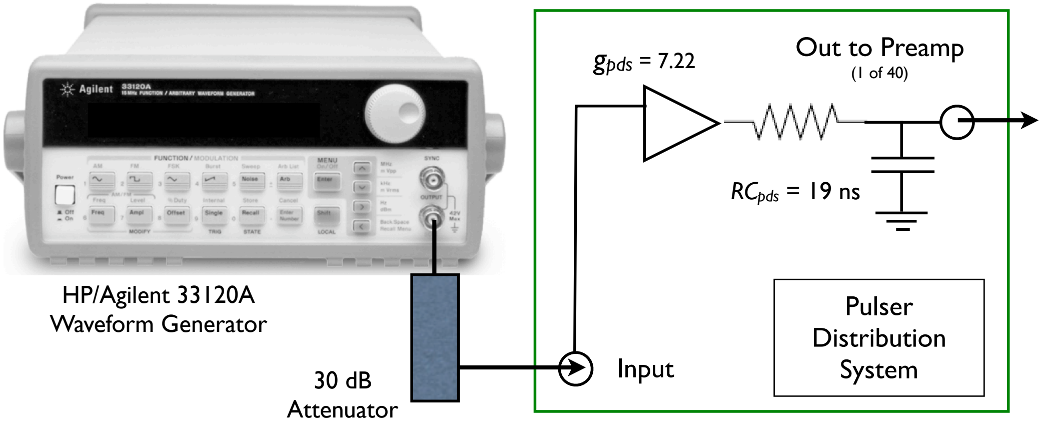

Figure 5.5: Electronics Calibration Pulse Generator Model.

mismatch between the NCD cable and the resistive coupler plus NCD string. A signal propagating along the NCD cable ($Z_C = 100\ \Omega$) toward the NCD string sees an impedance of $R + Z_N = 740\ \Omega$ (Fig. 5.1). At the resistive coupler, most of the signal is reflected back toward the preamplifier unit and the remainder propagates into the NCD string. More reflections in the system may occur, but only the significant contributions are considered. For a current signal that arrives at $\mathrm{N_P}$ from the pulser input, $I_{N_p}(t)$, the current that arrives at the input of the preamp, $I_p(t)$, is given by

$$I_p(t) = \frac{Z_C}{Z_P + Z_C} I_{N_p}(t) + \frac{Z_P}{Z_P + Z_C} \left\{ \frac{R + Z_N - Z_C}{Z_{sum}} \cdot I'_{N_p}(t - \delta t_1) + \right.$$
$$\left. \frac{4 Z_N Z_C}{Z^2_{sum}} \cdot I''_{N_p}(t - \delta t_1 - \delta t_2) + \frac{2 Z_N Z_C \cdot (R + Z_C - Z_N)}{Z^3_{sum}} \cdot I'''_{N_p}(t - \delta t_1 - 2\delta t_2) \right\} \quad (5.6)$$

where δt_1 is the time for a pulse to propagate down the NCD cable to the NCD string and return, and δt_2 is the time for a pulse to propagate from the top of the NCD string through the delay line and back to the resistive coupler. The impedances in Eq. 5.6 are for the resistive coupler (R), the NCD cable (Z_C), the NCD string (Z_N), the preamp (Z_P), and $Z_{sum} = Z_C + R + Z_N$ (Appendix B). The primed currents,

$I'_{N_p}(t)$, $I''_{N_p}(t)$, and $I'''_{N_p}(t)$, indicate that these current signals have been transformed by the electronics transfer function of the NCD cable, NCD string and NCD delay line (§ 5.1.1).

A narrow rectangular pulse (78 ns) injected into a preamplifier as part of the logamp calibration routine provides an example of the pulse reflections and transformation effects on calibration signals (Fig. 5.6).

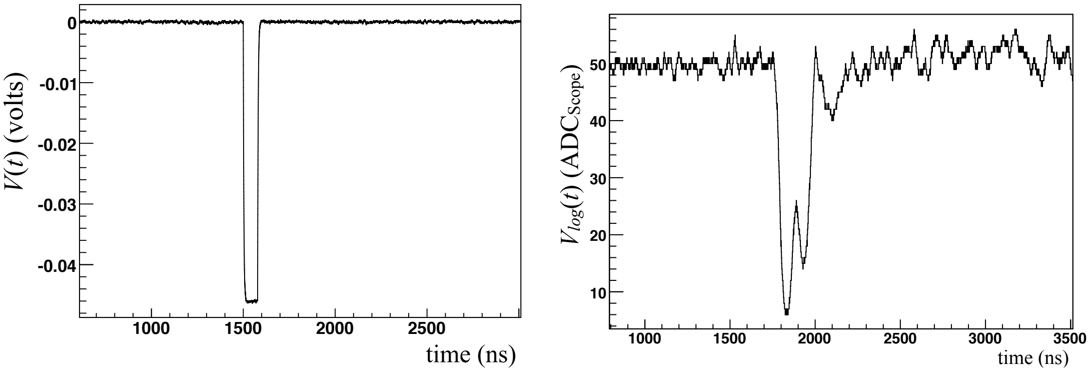

(a) Simulated from the HP Pulser.

(b) Recorded by an oscilloscope.

Figure 5.6: A 78 ns rectangular pulse injected into the pulser input of the preamp is reflected and transmitted along the NCD string and NCD cable and is transformed by bandwidth limitations of various hardware. The pulse from the HP pulser (a), is a simulated pulse, while the digitized signal (b) is a recorded pulse.

5.2 *Electronics Calibration Introduction*

The primary goal of the NCD Electronics Calibration (NCD ECA) was to measure the parameters of the electronics model, so that the transformations of the NCD signals as they propagated through the DAQ were quantified. The measurements of the NCD electronics model parameters are also directly related to the measured neutron detection efficiency of the NCD array, the energy calibration of events for each NCD string and pulse-shape analysis methods. In addition, the ECAs were designed to provide a frequent test of the DAQ and electronics, ensuring high data quality. To achieve these goals, a series of weekly tasks were designed to measure

- the Charge threshold level for each shaper/ADC channel
- the Current threshold level for each MUX channel
- the Linear response for each shaper/ADC and digitization channel[4]
- the MUX/Logamp/Scope model parameters for each MUX channel (2 sets of parameters per channel)

The linear response and thresholds for both the shaper/ADC and the MUX channels could be measured using the same calibration signals. Thus, there were three separate electronics calibration routines that were carried out each week: the Linearity Task, the Threshold Task, and the Logamp Task. However, some parameters of the electronics model could not be measured by the weekly routines and are the subject of the following sub-section.

5.2.1 Ex-situ Electronics Calibration

After the NCD DAQ had been installed and commissioned, a special set of electronic calibration data was acquired in April 2005 to determine the parameters of the model that could not be measured by the weekly electronics calibrations. Specifically, these parameters were the characteristic time constants (RCs) and gains of the HP Pulser, attenuator, pulser distribution system, preamplifiers, and the characteristic time constants of the low-pass filters of the MUX model. To perform these measurements, the various DAQ components were configured together in non-standard ways and the HP Pulser was used to inject signals through individual components to measure their response. This was an invasive procedure that required a significant reconfiguration of the DAQ hardware, and was thus performed only once during the NCD phase. Also,

---

[4] Digitized waveforms may be “de-logged” and their integral charge should scale linearly with increased input amplitudes.

using a similar technique, the characteristic time constants of the passive low-pass filters used in the model of the NCD strings, delay lines and cables, were measured from data taken at the UW laboratory.

The results are presented in Table 5.1. Details of these measurements can be found elsewhere [74]. The rest of the chapter is devoted to the weekly calibrations and their results.

Table 5.1: NCD Electronics model parameters. *Note that RC_{ncd} is not really a RC per length. For each NCD, RC_{ncd} was measured and the average value per NCD string length is reported here.

Parameter	Value
Attenuator 1	29.70 ± 0.10 dB
Attenuator 2	30.19 ± 0.10 dB
PDS gain (g_{pds})	7.22 ± 0.05
RC_{pds}	19.15 ± 0.15 ns
RC_{pc}	1.6 ± 0.1 ns
g_{pc}	8.5 ± 0.7
Preamp gain	27.5 ± 0.2 mV/μA
Preamp RC_{low}	3.3 ± 0.2 ns
Preamp RC_{high}	58 ± 3 μs
NCD cable $RC_{cable}^{round-trip}$	5.5 ± 0.5 ns
NCD cable $RC_{cable}^{one-way}$	3.3 ± 0.3 ns
NCD RC_{ncd}*	0.71 ± 0.3 ns/m
Delay Line $RC_{delayline}$	5.5 ± 0.7 ns
MUX RC_{LPF1}	13.3 ± 0.6 ns
MUX RC_{LPF2}	16.7 ± 1.8 ns

5.3 Weekly Calibration Routines

The Logamp, Threshold and Linearity Tasks were initiated each week by the detector operator. Each task selected a defined waveform that had been pre-loaded into the HP/Agilent pulser's volatile memory, which can store up to four arbitrary waveforms at a time. The rate at which these pulses were injected into the PDS was set for the particular task. Then, the PDS distributed the signal to each NCD string's preamp in succession. The transformation of the injected waveforms from the pulser were simulated and then compared with the measured digitized signals and shaper/ADC values to calibrate the DAQ.

To reduce the amount of time when the NCDs were not acquiring data for neutrino flux analysis, the NCD ECA Tasks were minimized to one and a half hours each week. Once a month, that amount of time was increased for an extended Linearity Task, as discussed below.

5.3.1 Logamp Task

The logamp calibration pulse is an offset, single-cycle sine wave (Fig. 5.7) preceded by a narrow rectangular pulse, called the trigger-pulse. The ∼1-MHz sine wave (998.4 ns in width) was selected because it has a smoothly varying, well-defined shape and frequency characteristics similar to the expected NCD signals. This facilitated simulation of the transformation of the calibration pulse as it propagated through the electronics and allowed for $V'_{in}(t)$ in Eq. 5.5 to be accurately calculated. The amplitude of the sine wave was chosen so that the range of input signal amplitudes covered the range of the expected NCD signal amplitudes. The trigger-pulse forced digitization to begin a few microseconds before the arrival of the sine wave signal. This allowed for a better measurement of the baseline offset (c_{chan}). The trigger-pulse was also used for examination of the pulse reflections (§ 5.1.4 and Fig. 5.6).

This task repeatedly injected the logamp calibration pulse into each NCD preamp

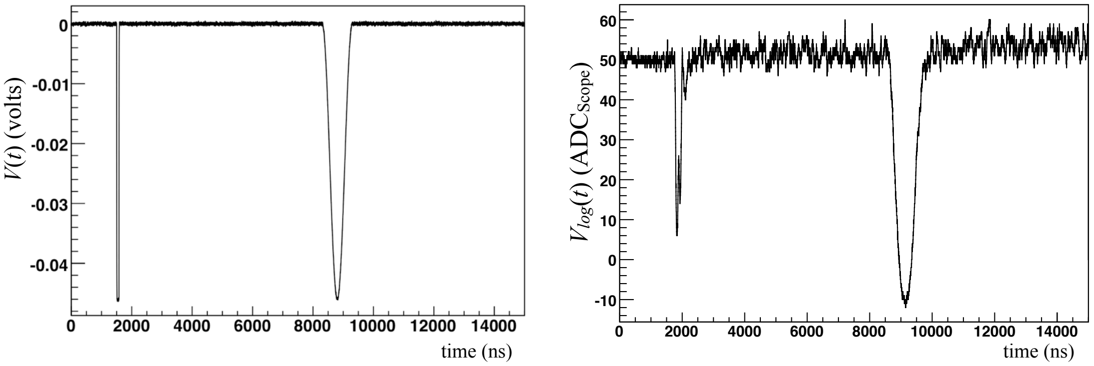

(a) Simulated from the HP Pulser.

(b) Recorded by an oscilloscope.

Figure 5.7: The logamp calibration pulse.

at a rate of 3 Hz for a duration of 15 seconds. Since the data acquisition rate of the digitized pulses was limited to 2 Hz, this produced approximately 30 pulses per NCD string that were recorded by the oscilloscopes. There were two oscilloscope channels for each NCD string, and the analysis of approximately 15 pulses determined each set of logamp parameters for the weekly calibration of each NCD string.

Two extended sets of logamp calibrations were acquired to gain more statistics in a single run. Four channels, each on different MUX, were injected with approximately 800 logamp calibration pulses. This "high-statistics" data were recorded in run number 52499. A "medium-statistics" acquisition of logamp calibration pulses occurred in run 58404. In this run, approximately 160 calibration pulses were injected into each channel. These extended logamp calibrations were done to verify the gaussian distribution of the measured logamp parameters, since each week's sample size was relatively small.

The analysis of the logamp pulse involved a χ^2-minimization routine which estimated the set of five logamp parameters that best fit a simulated signal to the measured pulse. The logamp parameters were measured for each calibration pulse. For the weekly calibrations, the average of the measured parameters were reported as that week's measurement.

5.3.2 Threshold Task

The Threshold Task injected offset, single-cycle, sine waves (the entire pulse is of negative-polarity) with varying amplitudes and a constant width of 1.1 μs. For this task, all NCD preamp's were pulsed simultaneously with varying pulse amplitudes for 5 seconds at a constant rate of 20 Hz. The pulser amplitude ranged from 26 mV to 95 mV, stepping in 1 mV increments. The range of these amplitudes extended above and below each channel's threshold level. Sine waves were chosen for this measurement because the calibration pulse amplitude and calculation of the total injected charge is more stable with sine waves than with signals that are not smooth, such as a rectangular or triangular pulses. The high-frequency components of non-smooth waveforms can produce transient currents which can be difficult to accurately calculate for each channel.

The threshold levels for the shaper/ADC and MUX channel determined by the analysis of these pulses were measured in units of the HP/Agilent pulser's amplitude of the injected signal and, for the shaper/ADC channels, in units shaper/ADC bin value (0 - 2047). From these values, the charge and current threshold levels may be calculated for the shaper/ADC and MUX channels, respectively.

5.3.3 Linearity Task

The Linearity task injected negative-polarity rectangular pulses of increasing amplitude at a rate of 50 Hz into each NCD preamp, one preamp at a time. The rectangular pulses were 1.1 μs wide with amplitudes 625, 505, 385, 265, and 145 mV. Once a month, the range of these amplitudes was increased for an "Extended" Linearity Task. The extended amplitudes ranged from 1001 mV to 51 mV in 50 mV steps. Rectangular pulses were used since the start and stop times of the pulse were easily determined, which facilitated integration of digitized waveforms in the analysis. The measured charge of the signal as a function of the calculated input charge was fit to a line, which measured the gain and offset of each channel and tested the channel's linear response. Since the digitized waveforms were logarithmically amplified and recorded by the oscilloscopes, they were first "de-logged" (inverting Eq. 5.5) for the MUX channel linearity analysis. This became a test of the linearity of the MUX as much as a test of the measured logamp parameters.

5.3.4 Hardware and Calibration Routine Changes

In April 2005, about five months after the detector was fully commissioned and taking production data, a few minor alterations to the calibration procedures and hardware were made. These changes coincided with the some of the work done to measure the parameters of the electronics model that were not easily accessible (§ 5.2.1). The original attenuator attached to the output of the HP/Agilent pulser was found to make a poor connection with the pulser and was replaced with one that was more stable and secure (§ 5.1.4). Both attenuators were measured precisely, and are listed in Table 5.1 [74].

The logamp calibration pulse was also altered at this time. The trigger-pulse width was reduced from 234 ns to 78 ns, about the smallest that could be produced and still reliably trigger the MUX channel. Further reduction in the width of the trigger-pulse would reduce the amplitude due to pulse reflections and bandwidth limitations. As well, the time between the trigger-pulse and the sine wave was increased from 2.69 μs to 6.72 μs. The 58 μs integrator (high-pass filter) in the preamp caused a slight build-up of charge along the baseline when signals propagated through it. Reducing the trigger-pulse width and moving the sine wave further away from the trigger-pulse was an attempt to reduce the charge build-up along the baseline in the sine wave region of the pulse. These changes were incorporated into the model and simulations of calibration pulses, and should have no effect on the estimated parameters.

Another change to the calibration pulses occurred as a result of fixing a bug in the software that programmed the HP pulser, in June, 2006. The calibration pulses were defined in the ORCA software as an array of 10,000 single-precision floating point values between -1 and 1. The array was downloaded to one of the four memory locations allocated for arbitrary waveforms in the HP pulser. The total width in time of the 10,000-point pulse was controlled by setting the frequency parameter of the HP pulser to the inverse of the desired width ($T = 1/f$). Similarly, the amplitude of output signal was set by the peak-to-peak voltage of the HP pulser. For example, the array that defined the logamp calibration pulse was 100 values of -1, followed by 8,620 values of 0, and then 1,280 values that ranged from zero to -1 back to zero in a sinusoidal fashion. The frequency and peak-to-peak voltage were set on the HP pulser to 128.205 kHz and 750 mV, respectively. Initially, it was noticed that when the HP pulser's frequency setting was equal to particular integer values, such as 100 kHz or 10 kHz, the output pulse exhibited unexplained DC-offset behaviors. In fact, avoidance of this behavior was the reason that the threshold- and linearity-task calibration pulses were 1.1 μs wide instead of 1 μs and that the sine wave component of the logamp calibration pulse 998.4 ns in width. The problem turned out to be that by starting the 10,000 point array with a value of -1 and ending with a value of zero, the waveform was undefined according to the rules of the HP pulser's arbitrary waveform specifications. The solution was to pad the beginning and end of each 10,000-point waveform by 50 points that were equal to zero and to then appropriately adjust the HP pulser frequency such that the width of the original pulse was unchanged. However, this software change did result in a slight difference in the logamp calibration pulse.

The unintentional change to the logamp calibration pulse was an increase in the time between the trigger-pulse and sine wave of the logamp calibration pulse of about 14 ns[5], which is clearly seen as a shift in the measured values of Δt presented in the next section. Further observations of various different programmed waveforms

---

[5] No change in the linearity and threshold calibration pulse was observed.

before and after the software change confirmed that the shape of the sine wave was unaltered; there was not a phase-shift in the sine wave and the amplitude and width were unchanged. This observation is supported by the *lack* of an observed change in the measurements of the other logamp model parameters – the parameters a, b, c_{chan} and $V^{ADC}_{PreTrig}$ remained unchanged. Only the time between the trigger-pulse and the start of the sine wave appeared to have increased, which the cause of has still not been discovered. In the end, however, this does not present a problem for the neutrino flux analysis since there is no dependence in the pulse-shape analysis techniques on Δt.

5.4 Analysis Procedures and Results

Within a day after each calibration task acquired data, various analysis routines automatically processed the data. Besides measuring the logamp parameters, thresholds and linear responses, the analysis programs searched for significant deviations from previous measurements, determined if the detector hardware settings were not in a nominal state, updated a webpage, and sent an email to a select few members of the electronics calibration group. Members of the group monitored the results and the appointed NCD ECA “czar” verified each week’s calibration[6].

The results show there were notable, but accountable, changes in the measured parameters over the course of the experiment, as will be seen in the discussion of the logamp calibration results. Most of these changes occurred immediately following the special ECA measurements in April 2005 (§ 5.2.1), which required a temporary reconfiguration of the DAQ. It appears that the DAQ system was not returned to its previous state. A discussion of the impact of these variations on the measurement of the neutrino flux is presented in § 9.2. After this incident, the hardware was not physically altered and most of the logamp parameters remained stable for the remainder of the NCD phase. The other noticeable feature of the results is the shift

---

[6] Thanks to Jürgen Wendland and Brent VanDevender for being the NCD ECA Czars.

in the logamp parameter Δt, caused by a change in the software, as mentioned above (§ 5.3.4).

The logamp parameters for two NCD strings showed significant deviations that are not accounted for by the hardware and calibration pulse changes mentioned in the previous paragraph. The logamp parameters for NCD string 1 exhibited sporadic variations while the parameters for the NCD string 31 showed an abrupt change. Investigation of this problem is introduced below (§ 5.4.1) and further discussed in Ch. 6.

Non-linearities in the system were measured on the shaper/ADC channels and digitized waveforms. The non-linearity in the integrated charge of the "de-logged" waveforms is explained by the fact that the logamps do not behave as perfect log amplifiers [68, 74, 69]. A corrective model for this effect was developed, but was not ultimately implemented due to the small systematic uncertainties introduced by the logamp parameters on the neutrino flux measurement, making these changes unnecessary. The non-linearities in the shaper/ADC channels were also of negligible size.

5.4.1 Logamp Parameters

Estimation of the logamp parameters was accomplished in several steps. First, the logamp calibration signals were identified from the within the data set[7] using a simple pulse-shape recognition algorithm. Next, a multi-step routine determined the logamp model parameters by measuring the baseline offset and using a two-step χ^2-minimization routine for each digitized waveform. Recall, each NCD string had two digitization paths due to the dual-scope DAQ and thus had two sets of logamp parameters that were measured in each calibration run. For each logamp calibration

---

[7] Since the NCDs were at voltage, the normal set of background and signal events were also contained in the calibration data and the calibration algorithm had to be capable of ignoring these signals.

run, the logamp parameters reported for each NCD digitization path were the average of the measured parameters found from each event.

For each recognized digitized logamp calibration pulse, $V_{dig}(t)$, the following procedures were done to measure the logamp parameters. First, the $V^{ADC}_{PreTrig}$ value was measured by finding the mean of the first 1000 points of the digitized waveform (Fig. 5.7(b)). Next, a multi-step fitting routine was used to find the best-fit logamp parameters which minimized the function χ^2,

$$\chi^2 = \sum_{i=k}^{k+n} \left(\frac{V_{dig}(i) - V_{log}(\vec{x}, i)}{\sigma_i} \right)^2$$

where $V_{log}(\vec{x}, i)$ is given in Eq. 5.5,

$$V_{log}(\vec{x}, t) = a \cdot \log_{10} \left| 1 + \frac{V'_{in}(t - \Delta t)}{b} \right| + c_{chan} + V^{ADC}_{PreTrig},$$

and $\vec{x}$ represents the logamp parameters a, b, c_{chan}, and Δt. The uncertainties on the i'th point of the digitized waveform, σ_i, were set to 1 oscilloscope ADC bit, for all i. The values k and n defined a range of interest within the calibration pulse that included just the sine wave. The range was determined separately for each NCD string by using the known time structure of the calibration pulse and the pulse - propagation times of the reflected signals (δt_1 and δt_2 in Eq. 5.6). In order to perform this fit, the signal that arrived at the input of the Logamp/Scope, $V'_{in}(t)$, was simulated numerically using the electronics model. A comparison of the simulated signal, $V'_{in}(t)$, and a measured logamp calibration pulse from the MUX *linear* output (Fig. 5.8) shows agreement between the simulated signal and the signal at the input of the Logamp/Scope. The residuals of each data point to the simulated pulse are within a 1-bit uncertainty. In this figure, the simulated signal has been scaled and vertically offset according to the settings on the oscilloscope and delayed in time by an amount equal to the MUX delay line time.

The remaining logamp parameters were measured by minimizing χ^2 twice, under slightly different conditions. The first minimization of χ^2 served two purposes. In

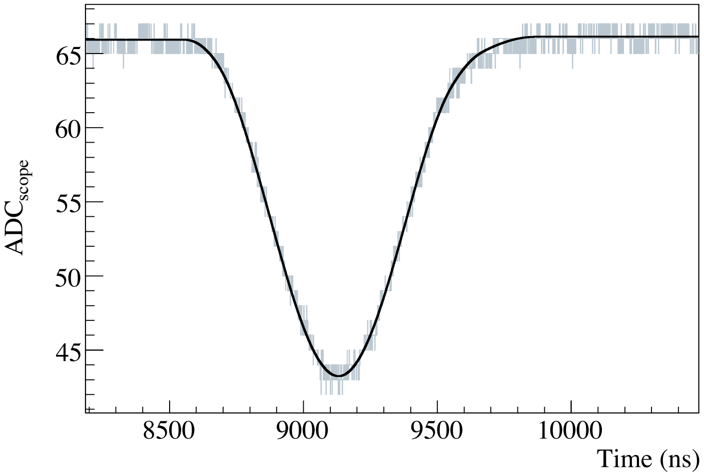

Figure 5.8: The signal at the input of the MUX box can be accurately simulated. The data, in grey, is from the linear output of the MUX and recorded by the oscilloscope (NCD 22, run 52357). The black trace is the simulated logamp calibration pulse at the input to the MUX and has been scaled according to the oscilloscope settings and delayed in time by the appropriate amount to simulate MUX delay line.

the first minimization, the range defined by k and n included the $\sim 6\ \mu s$ of baseline between the trigger-pulse and the sine wave along with the full period of the sine wave – approximately between the times 3000 ns and 11,000 ns (Fig. 5.7(b)). In this fit, the parameter c_{chan} was estimated and then fixed for the subsequent fit. The first minimization was also a test of the pulse-shape recognition routine and verified the general position of the sine wave in the calibration pulse (if the fit was poor or χ^2 would not converge, the event was discarded). After the initial fit, the region of interest was restricted to just the sine wave portion of the signal between points in time when the signal reached 10% and 90% of the maximum amplitude. The final fit estimated the remaining parameters a, b, and Δt. The logamp parameters a and b are better estimated when the input signal amplitude is large (and negative), which is one reason for the 2nd fit to the waveform in the limited region of interest (Fig. 5.9(a)). This procedure was done for each logamp calibration pulse and the reported results were the mean of the individual measurements, with an uncertainty on each parameter given by the standard deviation of mean for that calibration run.

Calibration Analysis Examples

The results from NCD string 22 were chosen to be presented as an example. Typical values for the logamp parameters on NCD 22 are found in Table 5.2 and an example of a logamp calibration pulse (Fig. 5.9(a)) and its de-logged equivalent (Fig. 5.9(b)) are shown.

Table 5.2: The mean logamp parameters for NCD 22 (scope 0) as measured in run 54278.

Logamp Parameter	Value
a	-87.9 ± 0.6 $\mathrm{ADC}_{\mathrm{Scope}}$
b	-8.4 ± 0.1 mV
c_{chan}	5.05 ± 0.05 $\mathrm{ADC}_{\mathrm{Scope}}$
Δt	263.5 ± 0.4 ns
$V_{PreTrig}^{ADC}$	51.49 ± 0.05 $\mathrm{ADC}_{\mathrm{Scope}}$

From the plots of the logamp parameters on NCD string 22 (oscilloscope 0) over the course of the NCD experiment (Figs. 5.10, 5.11), one can see a few obvious features, which are common among the logamp calibration results for the other NCDs. A shift in logamp parameters (April, 2005) and the change in Δt (June, 2006), have already been explained as due to hardware and calibration pulse changes (§ 5.3.4).

It is clear that there are variations in $V_{PreTrig}^{ADC}$ that are greater than the uncertainty measured on this parameter each week (Fig. 5.11(b)). Analysis of the high-statistics

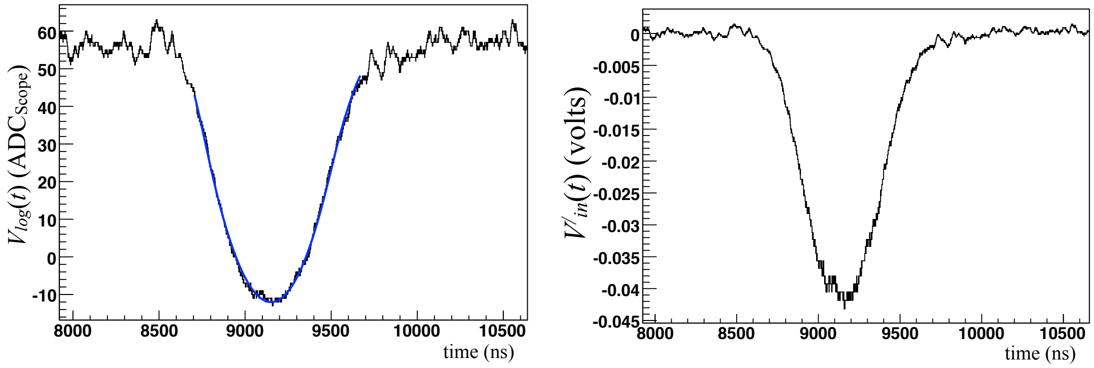

(a) Calibration with fit.

(b) De-logged.

Figure 5.9: (a) An example of a logamp calibration pulse with the best-fit curve. (b) The same signal that has been "de-logged" with the logamp parameters of the best-fit curve. This event was recorded on NCD string 22 and oscilloscope 0 during run 54278.

logamp calibration run shows that $V^{ADC}_{PreTrig}$ does not significantly change over the $\sim$ 8.5 minutes that each channel is pulsed, implying that the variation is slower than 8.5 minutes. This could pose a problem with data analysis since it would make it difficult to reconstruct NCD events. However, the difference between the maximum and minimum of the average measured value of $V^{ADC}_{PreTrig}$ over the two-years of the experiment is less than 1 ADC_{Scope} bit, the size of the error on each point in the waveform. Also, since $V^{ADC}_{PreTrig}$ is estimated by measuring the mean of the pre-trigger region of the pulse, the $V^{ADC}_{PreTrig}$ can be measured on an event-by-event basis. This should, therefore, not affect the results of neutron identification. In fact, an analysis on the impact of the logamp parameters on neutron identification analysis methods show that this parameter indeed does not affect the results.

Comparison of the parameters between NCDs is useful in finding problems and produces confidence in the electronics readout system since some of the parameters ought to be similar between NCD strings that are connected to common hardware.

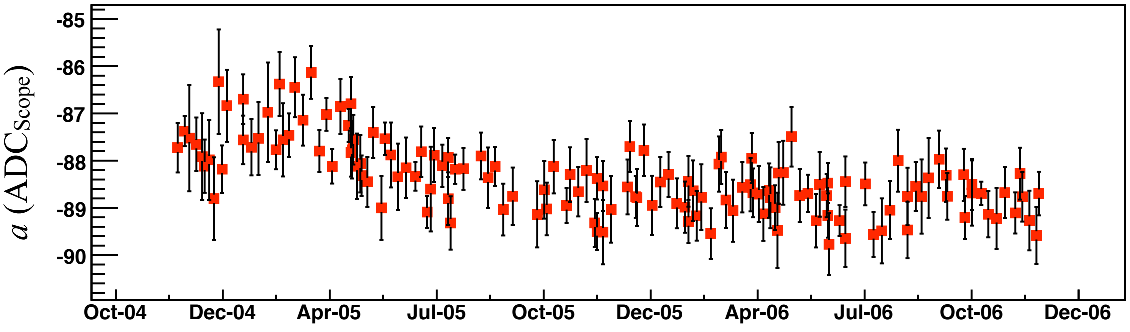

(a) Logamp parameter a.

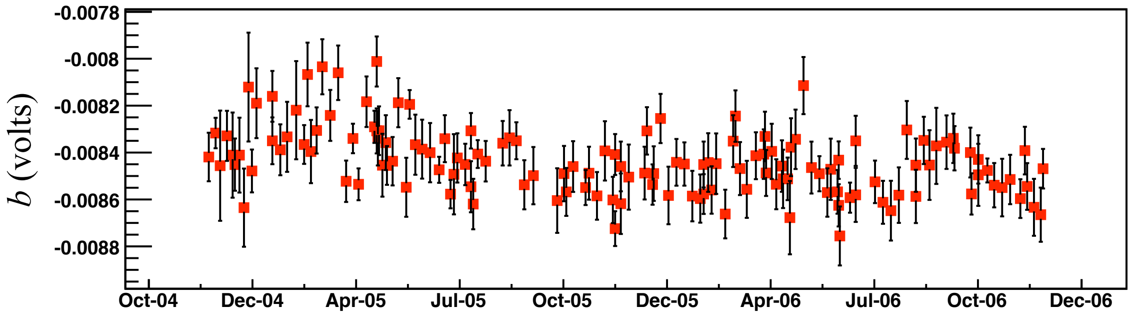

(b) Logamp parameter b.

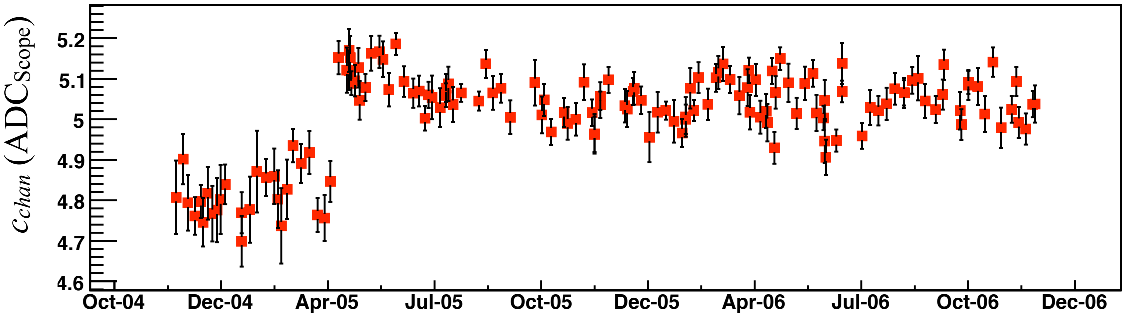

(c) Logamp parameter c_{chan}.

Figure 5.10: The estimated logamp parameters a, b, and c_{chan} for calibration events on NCD string 22 and oscilloscope 0.

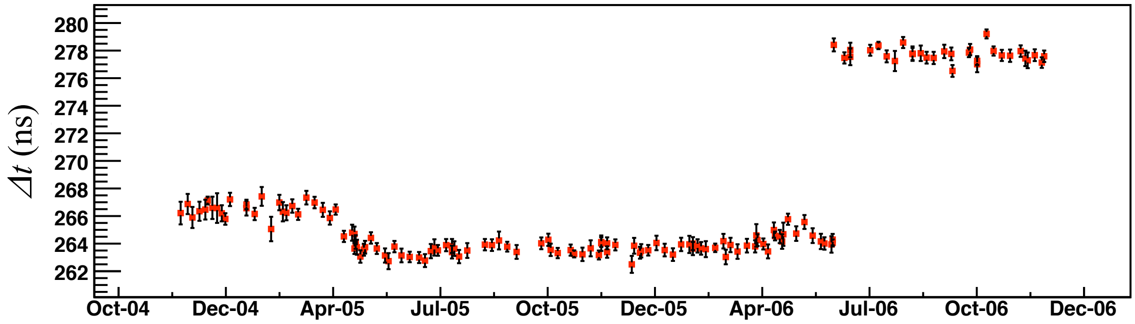

(a) Logamp parameter Δt.

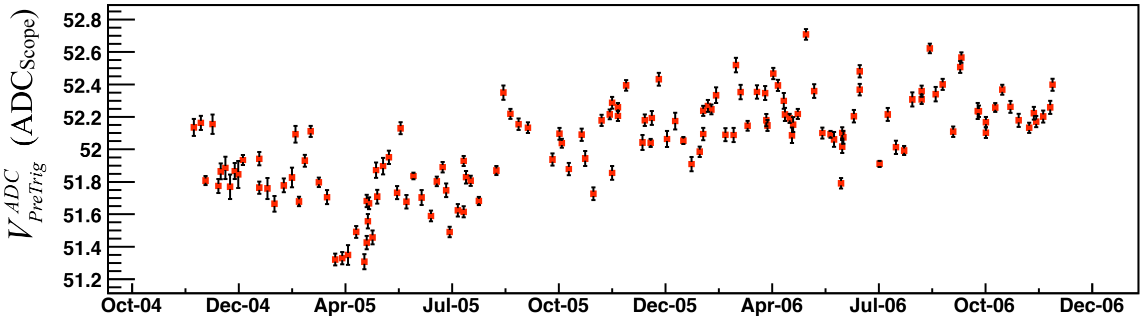

(b) Logamp parameter $V_{PreTrig}^{ADC}$.

Figure 5.11: The estimated logamp parameters Δt and $V_{PreTrig}^{ADC}$ for calibration events on NCD string 22 and oscilloscope 0.

Logamp calibration run 54278 (June 30, 2005) is used as an example. The measured parameters are shown in Fig. 5.12 and 5.13, and include results from all NCDs and both oscilloscopes. A subset of 10 NCDs have notably different logamp parameter b values (Table 5.3). The reason is due to a hardware difference between MUX box 0 and the other MUX boxes. The b parameter measures the total DC-offset added to the signal before it enters the logamp. A change to an internal MUX resistor, which affects this offset, was made to the other MUX boxes, but not changed on MUX 0.

In general, since there were two separate digitizing scopes with different sets of

Table 5.3: The following lists the MUX box number (0 - 3) for each NCD. MUX box 0 had a different hardware configuration, resulting in a greater negative DC-offset at the input of the logamp and subsequently smaller set of measured b parameters. In each column, the left number is the NCD string number and the right number is the MUX box number.

0	3	10	0	20	3	30	1
1	2	11	2	21	1	31	2
2	1	12	1	22	2	32	3
3	2	13	3	23	0	33	0
4	0	14	2	24	3	34	2
5	1	15	0	25	0	35	1
6	2	16	1	26	2	36	3
7	0	17	3	27	1	37	0
8	3	18	0	28	3	38	3
9	1	19	2	29	0	39	1

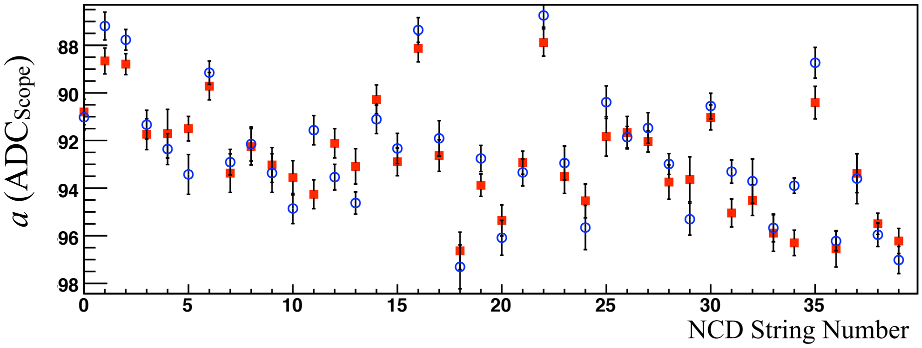

(a) Logamp parameter a.

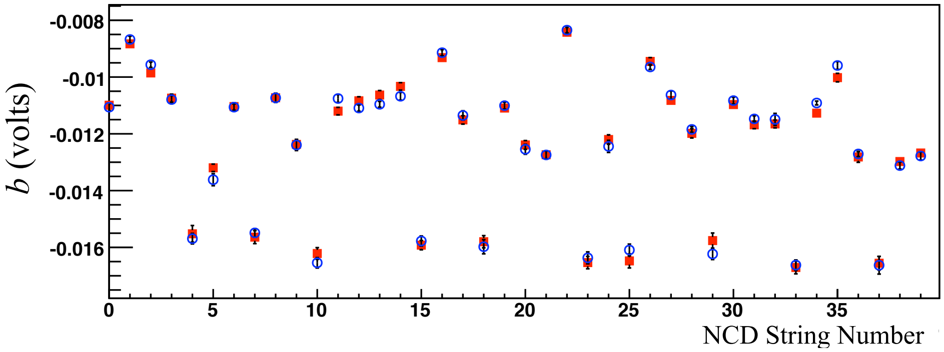

(b) Logamp parameter b.

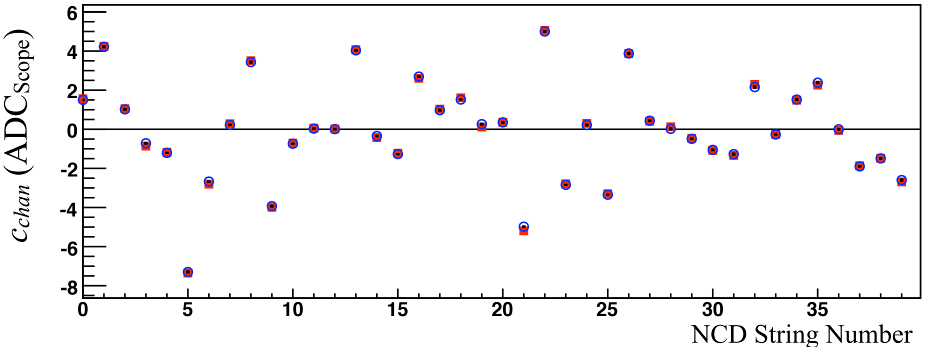

(c) Logamp parameter c_{chan}.

Figure 5.12: The estimated logamp parameters a, b and c_{chan} for all NCDs in run 54278. The solid red square markers are the measured values for events on scope 0 and the open blue circles are the measured values for events on scope 1.

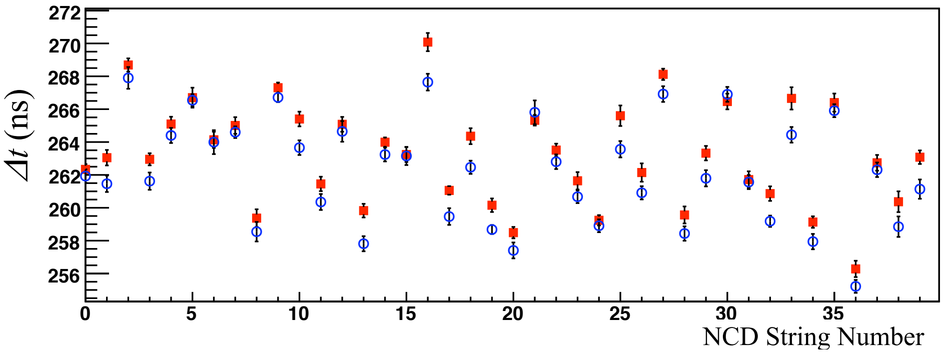

(a) Logamp parameter Δt.

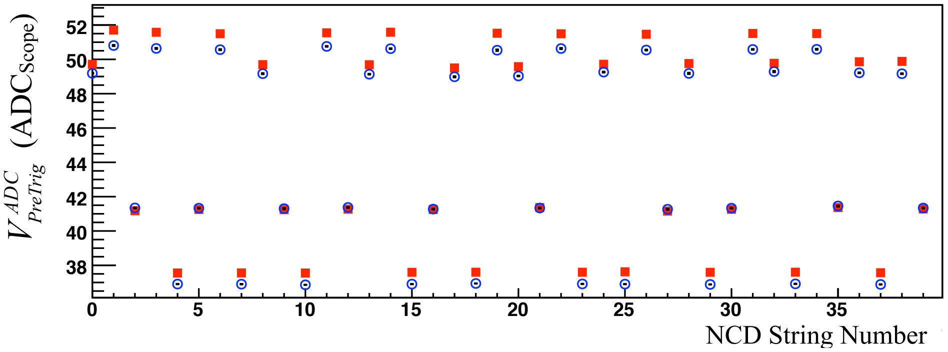

(b) Logamp parameter $V^{ADC}_{PreTrig}$.

Figure 5.13: The estimated logamp parameters Δt and $V^{ADC}_{PreTrig}$ for run 54278. The solid red square markers are the measured values for events on scope 0 and the open blue circles are the measured values for events on scope 1.

hardware, the logamp parameters will not be exactly the same. However, they should be *reasonably* similar for the same NCD string, which is consistently observed throughout the experiment as is shown in this example.

Logamp Parameter Distribution

Special, "high-statistics" logamp calibration runs were taken where ~800 calibration pulses were injected into four channels, one on each of the four MUX boxes. Another special logamp calibration run was taken where ~160 pulses were injected into each

NCD channel. From these high- and medium-statistics runs (§ 5.3.1), the gaussian distribution and correlations of the measured parameters were confirmed and measured. An example of the measured a parameter from the high-statistics data on NCD 2 is shown (Fig. 5.14). The variations of measured parameters from standard logamp calibrations were consistent with the distributions shown here.

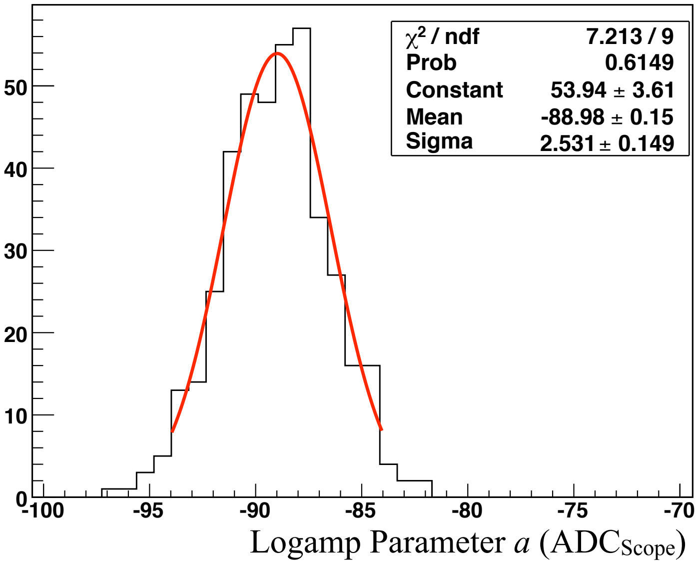

Figure 5.14: Histogram and gaussian fit of the measured logamp parameter a on NCD 2 and oscilloscope 1 during the special "high-statistics" run 52499.

Resistive Coupler Disconnect

In the data from logamp calibrations starting with runs 54531 and 55610, and then sporadically throughout the experiment, logamp parameters a and b for NCD string 31 deviated significantly from their typical values. Only logamp parameter a is shown here (Fig. 5.15(a)). On NCD 1, a similar observation was made starting with run 62288, taken on May 22, 2006. The logamp parameters on NCD 1 never returned to their previous values (Fig. 5.15(b)).

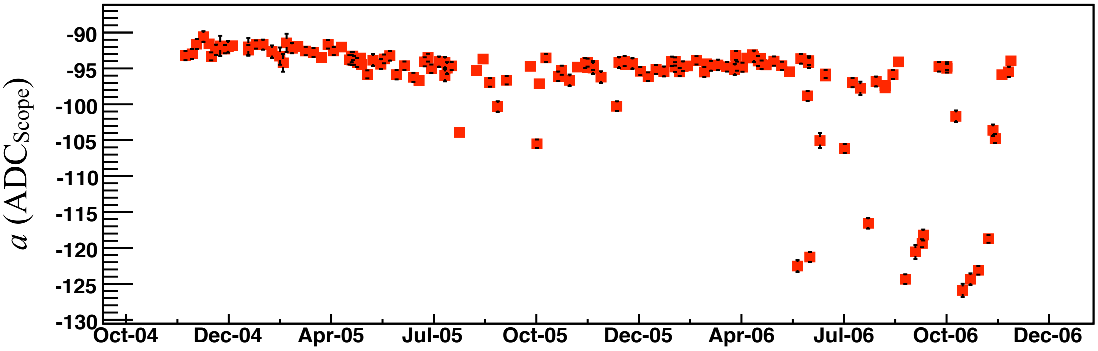

(a) NCD string 31 shows sporadic variations.

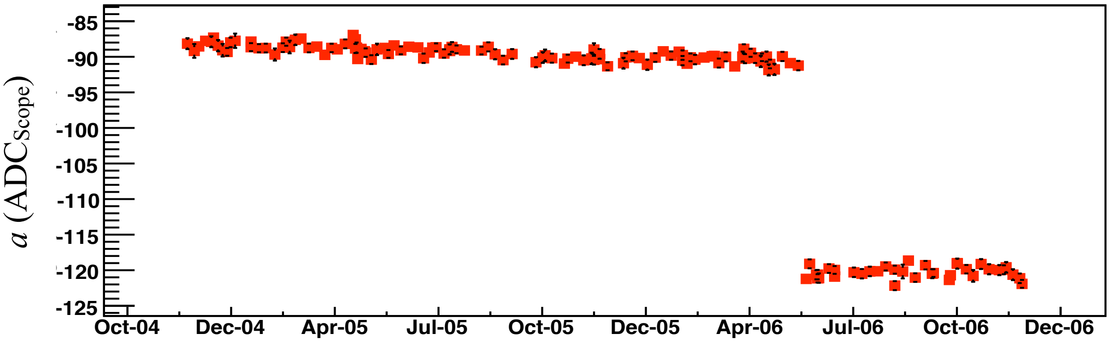

(b) NCD string 1 shows a sustained shift.

Figure 5.15: The measured logamp parameter a on scope 0 for NCD string 1 and 31. Significant deviations are observed in these strings that are not found on other NCDs.

The logamp calibration pulses measured on NCD string 31 were investigated further and a difference in the shape of the trigger-pulse became apparent. In Fig. 5.16(a), three peaks are seen, which correspond to the first, second, and third terms in Eq. 5.6. Compare this to Fig. 5.16(b), where it appears that the third peak is missing and the amplitude of the second peak has increased. The hypothesis for this behavior is that the resistive coupler connection between the NCD string and NCD cable was broken. This problem will be discussed in detail in Chapter 6.

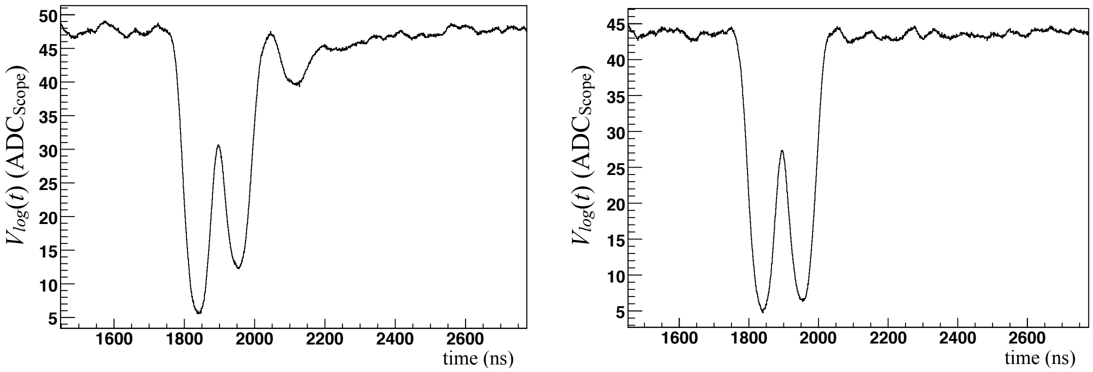

(a) Run 55665.

(b) Run 55610.

Figure 5.16: The logamp calibration pulses on NCD string 31 were averaged for two different calibration runs. The trigger-pulse region of the calibration signal is shown here. The third peak observed in run 55665 is missing in the average waveform from run 55610.

5.4.2 Threshold Task Results

The Threshold Task (§ 5.3.2) injected offset, single-cycle sine waves of known amplitude and width at a rate of 20 Hz for 5 seconds on each channel. The amplitude of the injected calibration pulse and the number of events observed on each shaper/ADC and MUX channel were recorded for each amplitude setting (the width of the threshold calibration pulse remained constant). The threshold levels of shaper/ADC and MUX channels were determined by finding the pulser amplitude at which half of the expected events were observed. The algorithm searches above and below the threshold, estimating the threshold value and its uncertainty [74]. Similarly, the threshold levels for the shaper/ADC channels were also measured by finding the shaper/ADC value at which half of the expected events were observed. Figure 5.17 shows an example for NCD 16 during run 54532, with the estimated threshold indicated in the figure.

The thresholds were stable over the course of the experiment except for when they were intentionally changed due to problems with a particular NCD string. These few changes were made to account for increased noise sources or a malfunctioning detector. From these measurements, the charge and current thresholds of the shaper/ADC and MUX channels, respectively, can be calculated.

5.4.3 Linearity Task Results

To measure the gain and offset and test for the linearity of a channel, the measured integrated charge of the linearity-task calibration pulses as a function of the calculated charge of the input signal were fit to a line. The following results were observed to be consistent over the course of the experiment.

Shaper/ADC Linearity

The shaper/ADC channels were found to be linear to within $\sim 0.5\%$. This level of agreement to linearity was found to be consistent across all channels. An example of the analysis of extended linearity calibration data on NCD string 15 is shown in Fig. 5.18.

MUX/Logamp/Scope Linearity

The integral of the digitized signals that have been de-logged (by inverting Eq. 5.5 and finding $V_{in}(t)$) should scale linearly with increasing total charge of the input signal. This was tested by using the linearity-task calibration pulses. The first step was to convert each linearity calibration pulse to its “linear equivalent” by inverting Eq. 5.5 to find the signal at the input of the MUX. The bandwidth filters in the MUX/Logamp/Scope did not affect this analysis since only the total charge of the pulse is considered and the pulse-shape was unimportant here. If the logamp parameter a was incorrectly estimated in the logamp calibrations, then the integrated “delogged” signals would not scale linearly. The logamp parameter a is a combination of parameters which are related to the logamp, MUX and oscilloscope. As well, a non-linearity could also indicate a problem elsewhere. Again, NCD string 15 is used as an example and the results of an analysis of an extended linearity calibration are shown in Fig. 5.19.

The intrinsic design of the logarithmic amplifier is responsible for the observed non-linearity [68]. The non-linear response measured by this calibration was confirmed in another study [69] (Fig. 5.20) and was found to be non-linear by up to $\sim 5\%$. If necessary for NCD data analysis, the model of the logamp may be modified to account for this behavior [69].

5.5 Conclusion

The NCD DAQ electronics, has been fully characterized throughout the operating period of the NCD experiment. The characterization was able to account for changes that occurred during the run as well as identify the unexpected behavior of some components. The electronics model was defined and the parameters which describe the electronic transfer functions of various components, gains and linear response were measured. These calibrations are required in order to extract the energy calibration, pulse-shape analysis, and neutron detection efficiency for the NCD data analysis. An important outcome of the weekly logamp parameter calibration was the discovery of the resistive coupler disconnect problem on two of the NCDs. This led to a new type of electronics calibration and a set of tests, discussed in the next few chapters.

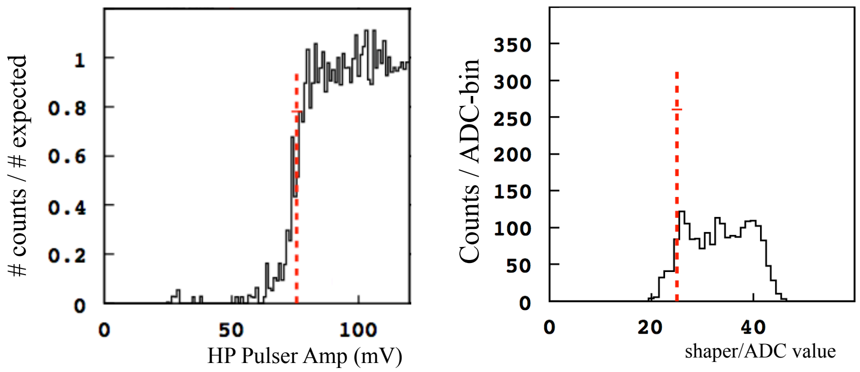

(a) shaper/ADC (b) shaper/ADC

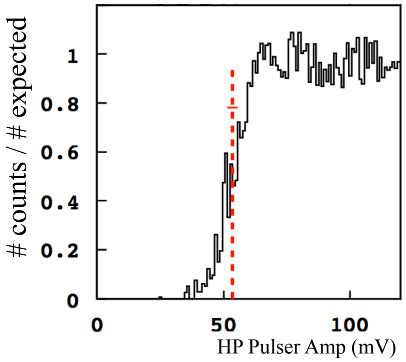

(c) MUX

Figure 5.17: Each histogram shows the rate of events on the shaper/ADC channel or MUX channel associated with NCD 16 during run 54532 (a threshold calibration run) as a function of the amplitude of the injected pulse. In (a) the number of counts detected by the shaper/ADC relative to the expected number of counts as a function of the amplitude of the HP Pulser is shown. In (b), the same data is plotted as the total number of counts as a function of the measured shaper/ADC values. In (c) the relative number of counts detected by the MUX as a function of the HP Pulser is shown. The measured thresholds are indicated by the vertical broken line in each histogram. Although the thresholds are shown here as amplitude of the HP Pulser and bin of the shaper/ADC, its possible converted the results into equivalent charge and current values [74].

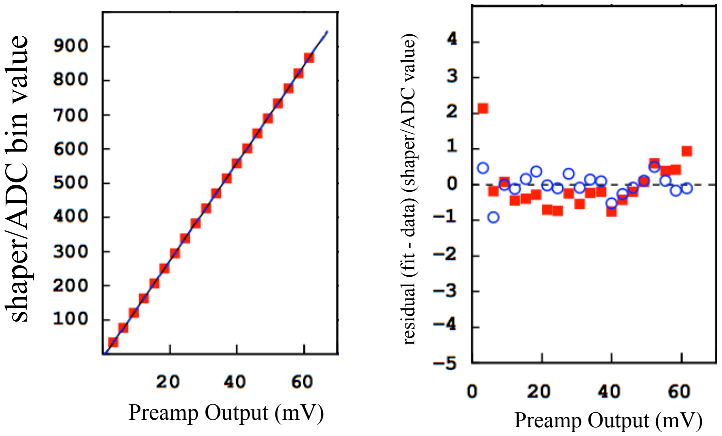

(a) Data and best-fit line. (b) Residuals.

Figure 5.18: The best-fit line and residuals for an extended linearity calibration of the shaper/ADC channel for NCD string 15.

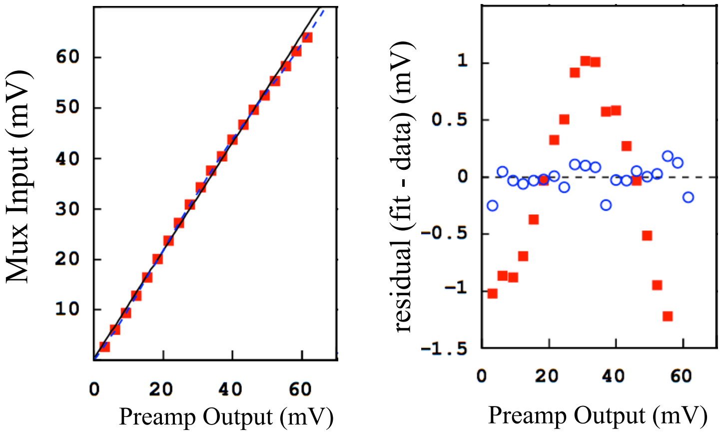

(a) Data and best-fit line. (b) Residuals.

Figure 5.19: This shows the MUX channel residuals (absolute) to the best-fit line from extended linearity data (red squares) and the residuals to the best-fit fourth order polynomial (blue circles) [74]. It should be noted that the output signal at the preamp should be equal to the input at the MUX.

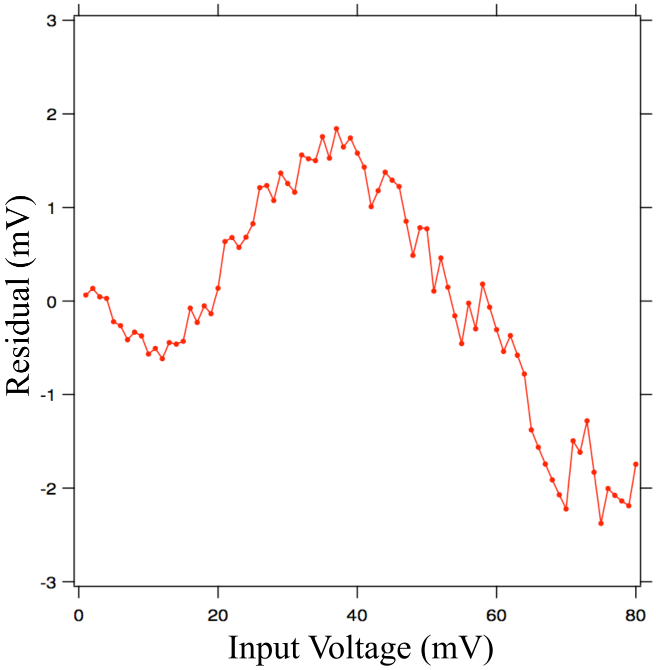

Figure 5.20: The logamp is found to be non-logarithmic by about 5% [69].

Chapter 6

RESISTIVE COUPLER DISCONNECT

6.1 Overview

In April, 2006, it was realized that a disconnected resistive coupler could explain some outlying data points observed in the NCD logamp calibration data for NCD 31 (§ 5.4.1). The hypothesis was that the points of contact between the resistive coupler (Fig. 6.1) and the copper endplugs of either the uppermost NCD or the NCD cable bell were unstable (Fig. 6.2). Shortly after this realization, event rates on NCD 31 and NCD 1 showed an unexplained drop in their rates of background noise. A logamp calibration revealed that both NCDs exhibited the same trigger-pulse reflection shown in § 5.4.1 (Fig. 5.16). This clearly became a major concern for the estimate of the live-time of the entire array during the NCD phase. The NCDs had such low activity and low background rates that it could go unnoticed if an NCD were disconnected from the DAQ for short durations and possibly as long as days. As a response to the problem, a new electronics calibration routine was implemented to test for the condition known as Resistive Coupler Disconnect (RCD). Each NCD was injected with a new calibration signal that tested for RCD. In the final six months of NCD data acquisition, based upon the results from this new calibration, only NCD 31 and 1 were found to conclusively exhibit RCD.

6.2 The Resistive Coupler and NCD Cable Bell

The resistive coupler and NCD cable bell apparatus were described earlier in § 4.2.1. To facilitate the following discussion, Figs. 4.2 and 4.3 are reproduced here (Figs 6.2 and 6.1).

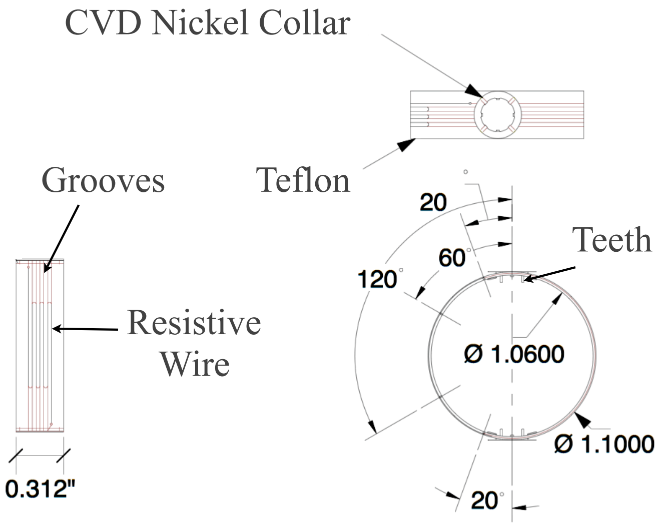

Figure 6.1: A schematic diagram of the resistive coupler. Modified from [50].

There were two independent physical mechanisms by which resistive coupler connected to the upper and lower copper endplugs. First, each copper endplug had a shelf which made contact with the CVD nickel collar on both sides of the resistive coupler. The purpose of the shelf was to prevent the nickel collars from sliding down the copper endplug, though it also provided some electrical contact. When the NCD and the cable bell were fitted together, the distance between the copper endplug shelves on the NCD and cable bell was less than the diameter of the teflon ring. The primary physical connection was provided by four "teeth" on the inner side of the nickel ring. These teeth could be bent with a pair of tweezers to increase or decrease the tightness of the fit. During the installation of the NCD cable bell to the upper NCD section, these teeth were bent inwards to make a friction contact with the endplugs.

The design of this coupling resulted from the necessity of having to insert a resister at this location in order to match the impedance of the NCD string to the NCD cable and to do so without generating any lateral force on the NCD fused silica feed-through.

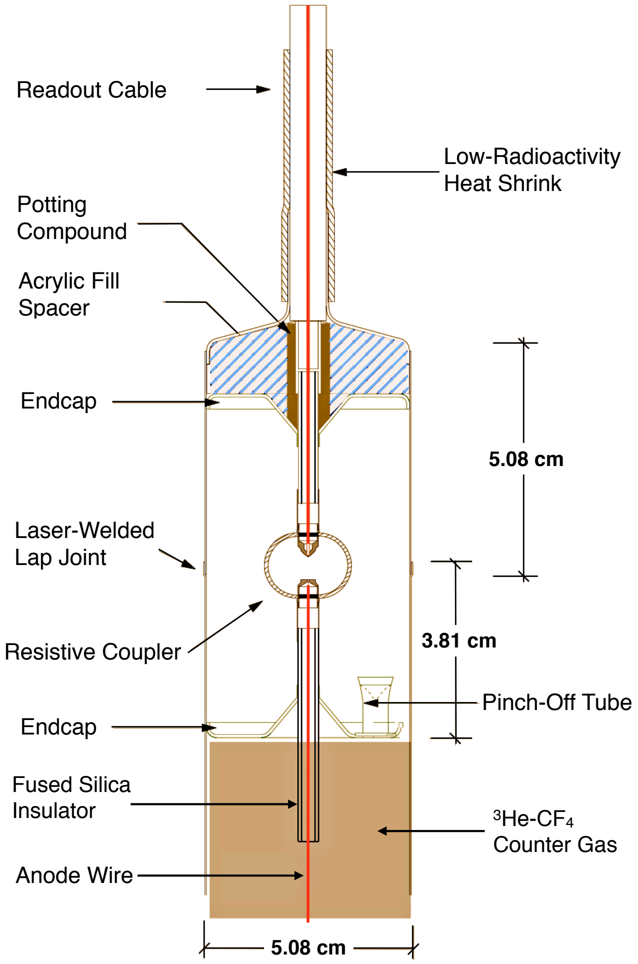

Figure 6.2: Each NCD string's upper-most segment connects to the NCD cable via the resistive coupler and the NCD cable bell [47].

The fused silica feed-though bridged the interface between the active volume of the NCD, containing the NCD gas, and the copper endplug. The NCD anode wire ran through this fused silica feed-through and connected to the copper endplug. Lateral force could break the fused silica feed-through allowing the NCD gas to escape[1]. Once the gas escaped in this way, the NCD became inoperable and irreparable.

---

[1] This happened more than once before and during the NCD installation.

The RCD hypothesis is that the mechanical connection failed. This produced an open electrical connection resulting in a change to the pulse reflection characteristics of electronic calibration, and subsequently to the measured logamp parameters. With the preamp and DAQ readout disconnected from the NCD, it is expected that the rate of physics events (neutrons and alphas) and instrumental noise events decreased during periods of RCD.

6.2.1 Trigger-Pulse Reflection Structure

In § 5.1.4, the shape of the trigger-pulse of the logamp calibration signal was briefly explained by the coupling of the calibration pulse injection input to the NCD cable and the impedance mismatch between the NCD cable and the electrical load of the resistive coupler and NCD string. This section describes in more detail how the pulse reflection structure can be used to test for RCD. Figure 6.3 shows a schematic of the pulse injection coupling to the NCD cable, and connection to the preamp and NCD string. Using Fig. 6.3 as a guide and reproducing Eq. 5.6, for a pulse arriving from the pulse injection input at point A, $I_A(t)$, the current-pulse at P is expressed as

$$\begin{aligned} I_p(t) = \frac{Z_C}{Z_P + Z_C} I_A(t) + \frac{Z_P}{Z_P + Z_C} \Bigg\{ & \frac{R + Z_N - Z_C}{Z_{sum}} \cdot I'_A(t - \delta t_{\text{cable}}) \\ & + \frac{4 Z_N Z_C}{Z_{sum}^2} \cdot I''_A(t - \delta t_{\text{cable}} - \delta t_{\text{ncd + delay line}}) \\ & + \frac{2 Z_N Z_C \cdot (R + Z_C - Z_N)}{Z_{sum}^3} \cdot I'''_A(t - \delta t_{\text{cable}} - 2\delta t_{\text{ncd + delay line}}) \Bigg\} \end{aligned} \tag{6.1}$$

where $Z_{sum} = Z_C + R + Z_N$. The characteristic impedances of the NCD cable, NCD, preamp and resistive coupler were $Z_C = 100\Omega$, $Z_N = 415\Omega$, $Z_P = 100\Omega$, and $R = 325\Omega$.

When the resistive coupler became disconnected at point B (Fig. 6.3(b)), the expression for the current-pulse at point P simplifies to

$$I_p(t) = \frac{Z_C}{Z_P + Z_C} I_A(t) + \frac{Z_P}{Z_P + Z_C} \cdot I'_A(t - \delta t_{\text{cable}}) \tag{6.2}$$

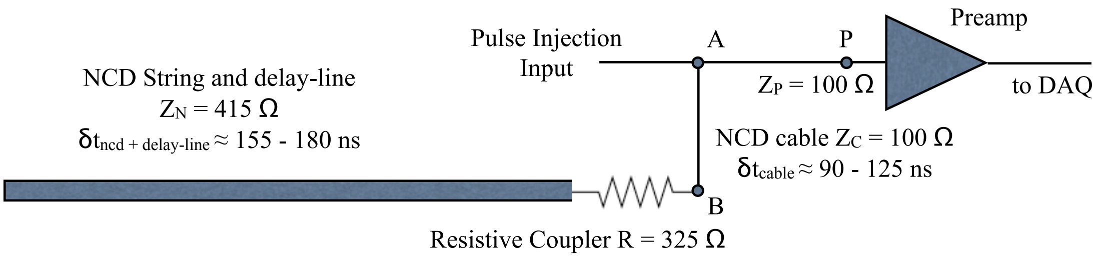

(a) Normal.

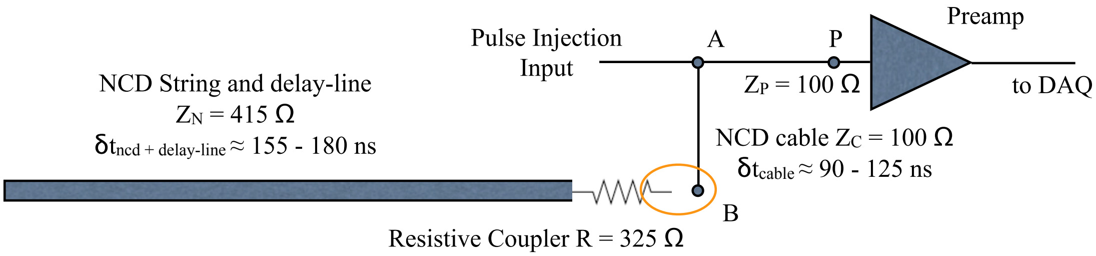

(b) RCD.

Figure 6.3: A schematic of the NCD DAQ front-end, showing the coupling of the NCD cable to the pulse injection input at point A. The NCD cable connected points A and B. This coupling was the cause of pulse reflections seen in the calibration signals and when the resistive coupler was disconnected (b), the reflections change, allowing for an indirect observation of RCD.

Thus, in normal operations, the rectangular-wave trigger-pulse injected at point A ultimately arrived at the DAQ as four, time-delayed, distorted rectangular pulses – only the first three had significant amplitude, however. When the resistive coupler disconnected, the third and fourth pulses no longer existed because no part of the signal propagated into the NCD. The result was two distorted rectangular pulses separated in time by $\delta t_{\mathrm{cable}}$[2]. Note that the amplitude of the two terms in Eq. 6.2 are

---

[2] The rectangular waveforms were distorted by the electronic transfer functions of various components. See Ch. 5.

nearly equal since $Z_P \approx Z_C$. Contrast this with the comparison of the first two terms in Eq. 6.1 – the second term contains an extra factor of $(R + Z_N - Z_C)/Z_{sum}$.

6.3 An Observation of Event Rate Change

The first observation of a drop in rate due to RCD was fortuitous. While monitoring event rates on May 21, 2006, it was observed that the event rates of NCDs 1 and 31 abruptly changed from about 30 and 10 events/hour, respectively, to nearly zero events/hour. SNO is monitored continuously by a detector operator and during each 8-hour shift, a shift report of all activity during the shift is generated. An examination of the shift reports indicated a possible correlation in event rates with local seismic events. On May 19, during run 62264, the shift report indicated spikes of shaper/ADC rates due to nearby mining activity (blasting). During the shift report on May 21, seismic activity was reported by the shift operator (who was at the remote control room on the surface - not underground) during run 62272. The seismic event generated a large number of background events and neutrino data acquisition was resumed on run 62276, which occurred 76 minutes later.

Figures 6.4 - 6.6 show these changes in event rate. In these figures, the number of all MUX triggers[3] per fifteen minute bins are plotted[4]. Only "good" neutrino runs, where the SNO+NCD systems were operating with nominal settings, were used in this analysis. For comparison, the rate of events on NCD 22, a well-behaved NCD, is shown in Fig. 6.4(a). By removing the bins in this figure when the NCD system was not acquiring data (the unshaded regions of Fig. 6.4(a)), the steady average rate over this period can be seen. This was similarly done for NCDs 1 and 31. Figures 6.5(a) - 6.5(b) and Figures 6.6(a) - 6.6(b) show the change in rates on NCDs 1 and 31, respectively. These abrupt changes in rate correlate to the time of seismic activity

---

[3] The sum of MuxScope events plus PartialMuxScope events, see § 4.3.2

[4] Since runs do not, in general, last an integer number of fifteen minute intervals, after dividing the run into fifteen minute intervals, the remaining time for each run was ignored in this analysis.

as indicated in the shift reports. Chapter 7 will discuss a full analysis of the rate of electronic noise events in the NCDs.

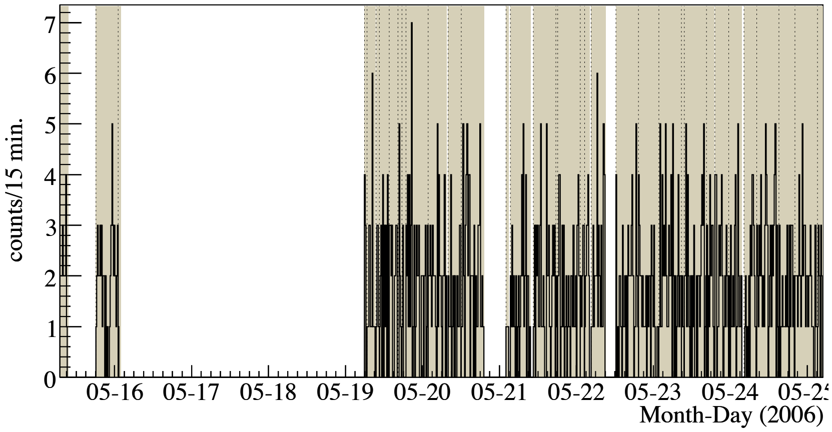

(a) Counts vs. date.

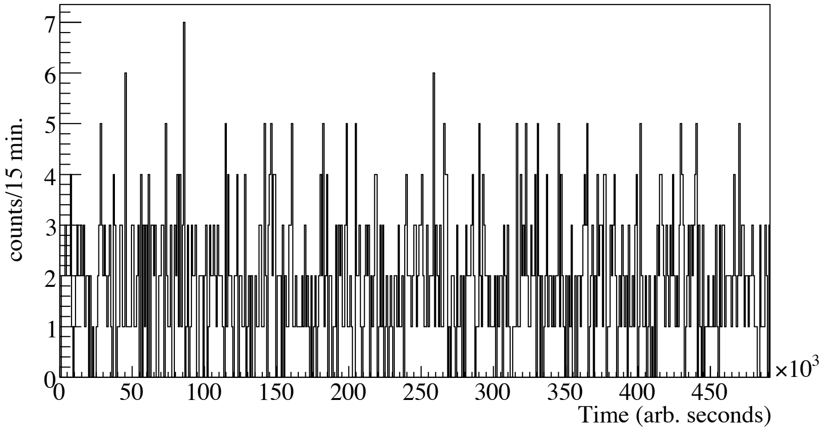

(b) Counts vs. live-time.

Figure 6.4: The number of MUX+Scope events on NCD 22 is steady during the period from May 15, 2006 to May 25, 2006. The shaded regions in (a) indicate when the system was acquiring data and the vertical dashed lines indicate the start of a new run. In (b), the unshaded regions of (a) have been removed and the shaded regions concatenated into a single histogram with fifteen minute bins.

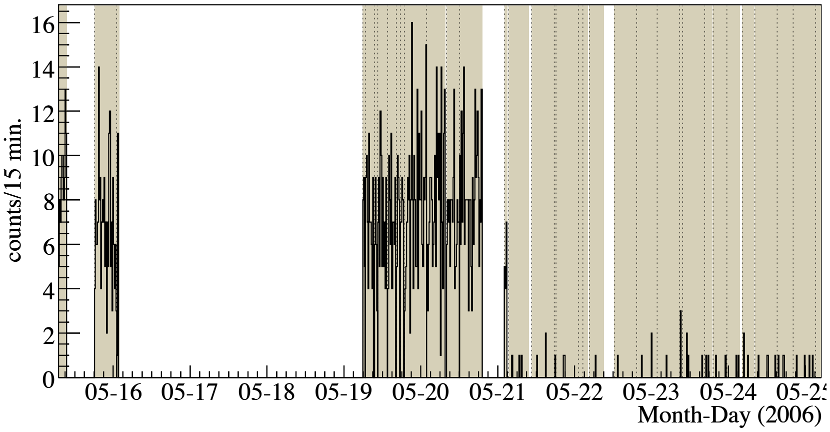

(a) Counts vs. date.

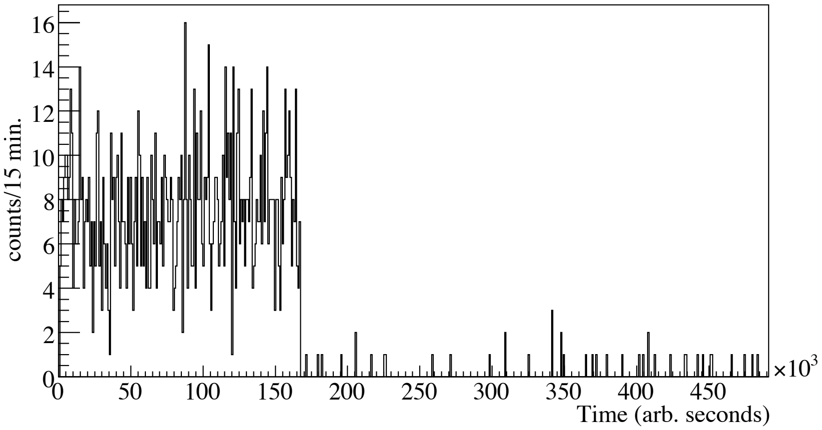

(b) Counts vs. live-time.

Figure 6.5: The number of MUX+Scope events on NCD 1 abruptly decreases on May 21, 2006. The shaded regions in (a) indicate when the system was acquiring data and the vertical dashed lines indicate the start of a new run. In (b), the unshaded regions of (a) have been removed and the shaded regions concatenated into a single histogram with fifteen minute bins.

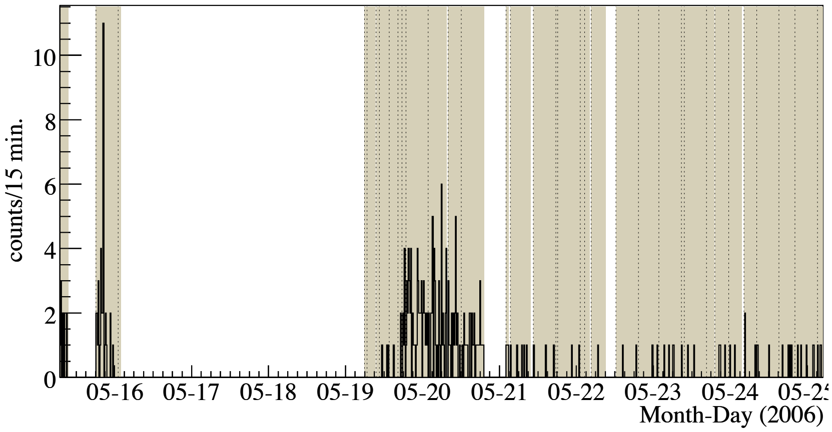

(a) Counts vs. date.

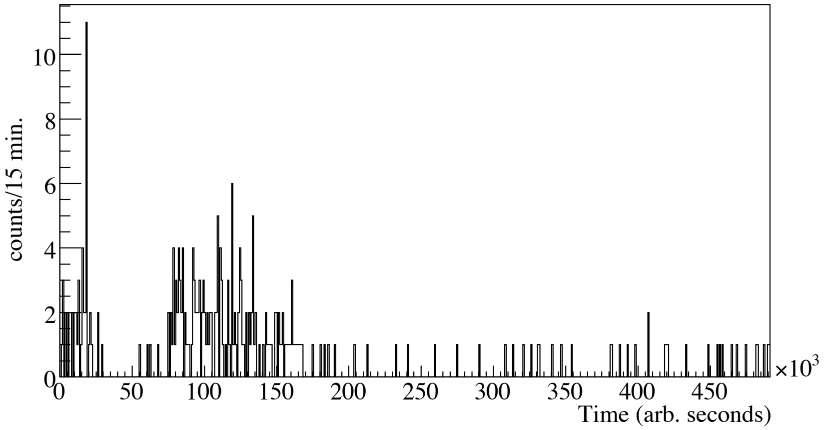

(b) Counts vs. live-time.

Figure 6.6: The number of MUX+Scope events on NCD 31 abruptly decreases on May 21, 2006 and appears to have been very low prior to May 19, 2006. The shaded regions in (a) indicate when the system was acquiring data and the vertical dashed lines indicate the start of a new run. In (b), the unshaded regions of (a) have been removed and the shaded regions concatenated into a single histogram with fifteen minute bins.

Immediately following this observation of the rate change, a logamp calibration run was initiated to test for RCD during run 62288. By measuring the difference in the amplitude of the initial and first reflected pulses in the logamp calibration trigger-pulse, one can determine if the reflection structure is more like Eq. 6.1 or like Eq. 6.2, and thus infer the condition of the resistive coupler's connectivity. The difference in the amplitudes of the initial and first reflected pulses of the digitized waveform (uncalibrated in units of the oscilloscope ADC) is parameterized by

$$P = \mathrm{V}_{\mathrm{log}}^{\mathrm{initial}} - \mathrm{V}_{\mathrm{log}}^{\mathrm{reflection\ 1}} \tag{6.3}$$

When the resistive coupler was connected, P was equal to about nine scope ADC units (out of 256), approximately equal to 9 mV at the input of the MUX channel. However, when the reflection structure changed due to RCD, the difference in the amplitude reduced to two or three scope ADC units ($\sim$2 mV at the MUX channel input). A histogram of the results of the measured value of P in logamp calibration run 62288 for each NCD string shows that NCDs 1 and 31 stand out (Fig. 6.7).

6.4 The NCD Resistive Coupler Disconnect Electronics Calibration

A new calibration was introduced to monitor the NCDs for RCD. The NCD RCD Electronic Calibration (NRE) task injected a high amplitude distinguishable square wave preceded by a trigger-pulse into the pulse injection input of each NCD preamp. The NRE trigger-pulse was similar to the logamp calibration trigger-pulse, but greater in amplitude (Fig. 6.8). The NRE pulse was injected into a different NCD preamp each minute for all (non-calibration) runs starting at run 63136 on June 13, 2006 and continued through the remainder of the NCD phase. The total live time of this data set was measured to be 58.05 ± 0.02 days (out of a total NCD phase live time of 385.17 ± 0.14 days) [75].

The difference in the amplitude of the initial and first reflected signals of the NRE trigger-pulse, P, were then measured. In 318 runs, over a total live-time of 58.05 ±

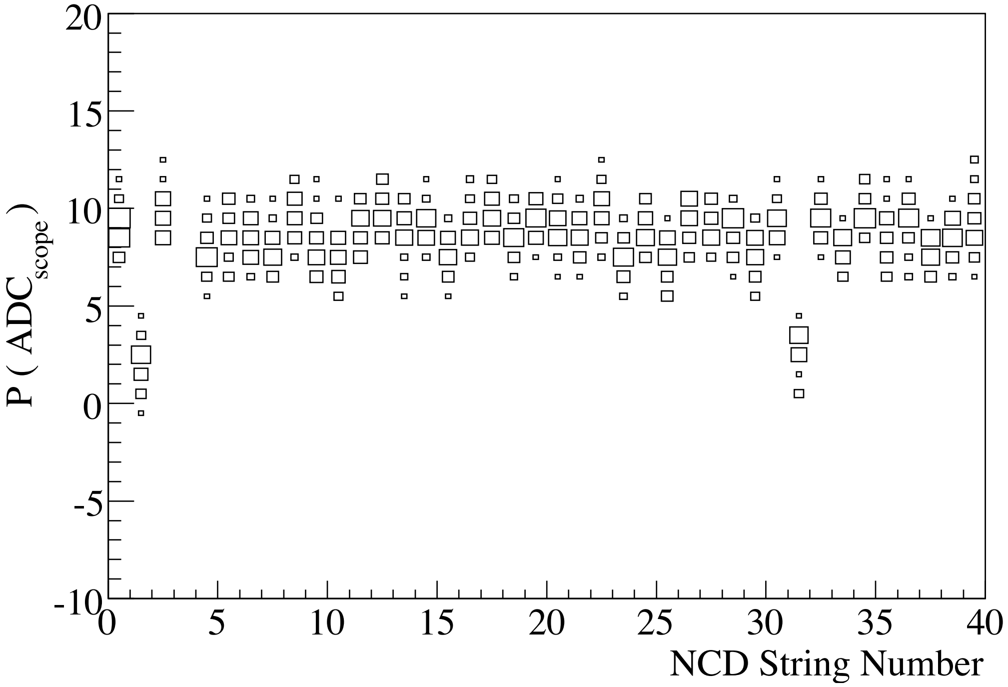

Figure 6.7: The measured values of P (Eq. 6.3) for logamp calibration run 62288. NCDs 1 and 31 stand out with small values of P, indicating RCD. NCD 3 was turned off during this run.

0.02 days, the histogram of measured values for P show that, with this method, RCD was only observed on NCDs 1 and 31 (Fig. 6.10).

6.5 Conclusions

Through the analysis of the logamp and NRE trigger-pulse peak differences and the observations of event rate change, it has been demonstrated that NCDs 1 and 31 exhibit evidence consistent with the hypothesis of Resistive Coupler Disconnect. Undetected and unaccounted for, the occurrence of an NCD disconnecting from the DAQ would have a significant impact on detector live-time and hence the measurement of the ^{8}B solar neutrino flux. Considering that for NCD 31, the disconnect is intermit-

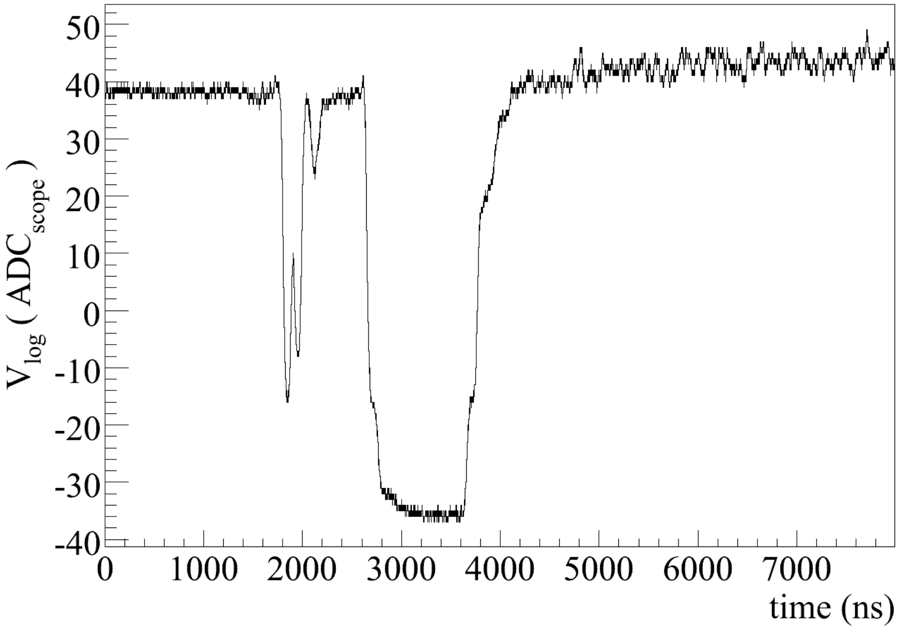

Figure 6.8: An NCD RCD Electronics Calibration Pulse that was injected into an NCD that was not afflicted with RCD.

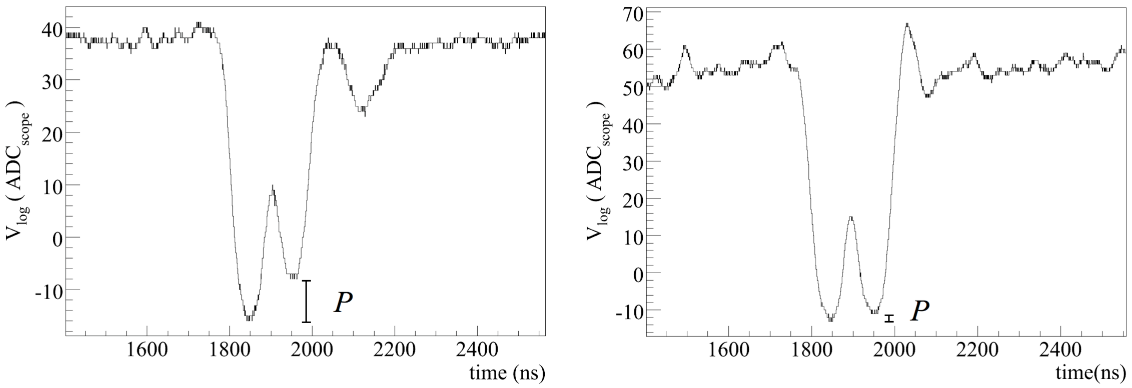

(a) No RCD.

(b) RCD.

Figure 6.9: The trigger-pulse region of the NRE pulse. The difference in amplitude between the initial pulse and the first reflection were measured. A small difference indicates the RCD condition.

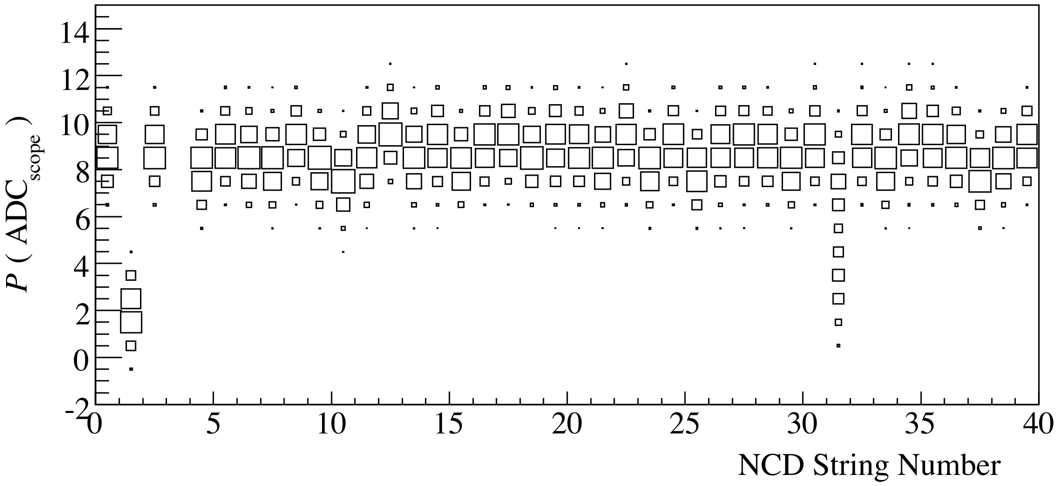

Figure 6.10: The measured values of P (Eq. 6.3) starting on June 13, 2006 through the end of the NCD phase (58.05 ± 0.02 live days). NCDs 1 and 31 stand out with small values of P, indicating RCD. NCD 3 was disabled during this time.

tent in nature, it is desirable to perform a more robust analysis on all strings of the rate of noise events and the rate of random processes such as the emission of alpha particles.

Chapter 7

BACKGROUND EVENT ANALYSIS

This chapter includes a summary of the instrumental noise events observed in the NCD data, a model for the distribution of the number of noise events found in a defined time interval, and a full description of the set of cuts used to select a particular subset of noise events. In § 6.3 it was shown that the rate of background events decreased abruptly during an episode of RCD. This chapter will present further analysis of the rate of background noise events as an effort to observe RCD. This is followed by a presentation of the measured distribution of noise events, the comparison of the distribution to the model, and conclusions about which NCDs exhibit RCD-type behaviors.

7.1 Electronic Noise Events

The vast majority of signals recorded in the NCD phase were instrumental backgrounds. These included microdischarges, electromagnetic interference (EMI), also called oscillatory noise, and baseline noise fluctuations that exceeded the MUX thresholds and were digitized. Most microdischarges occurred at the preamplifier, primarily during ramping of the high-voltage system (Fig. 7.1(a)), and were also observed to occur in the NCD delay-line near the junction between the delay-line and the bottom NCD segment. The preamplifiers were designed and tested [50] to have very low rates of microdischarge. The quality assurance program for the construction of the preamplifiers required that fewer than one microdischarge was observed in a 24-hour period while the preamplifiers were holding high-voltage. Preamp-microdischarge events were typically high-current, low-charge signals. The delay-line microdischarges were colloquially called a “fork” event due to its unique pulse-shape (Fig. 7.1(b)). These events occurred regularly on a few NCDs, usually in bursts that sometime required a NCD to be turned off (in order not to incur large amounts of dead-time). Fork events were found predominantly on a few particular NCDs, but their presence on other NCDs must also be assumed. The NCDs, NCD cables, and preamps were susceptible to EMI signals produced by nearby electronics even though care was taken to shield the detectors and electronics as much as possible (Fig. 7.1(c)). The most frequently occurring event observed during normal data acquisition, however, were baseline noise events (Fig. 7.1(d)). These events occurred at such relatively high rates because the digitization thresholds on the MUX were set as low as possible so as to maximize neutron detection efficiency, while not inducing significant dead-time [52]. There were also other types of instrumental noise events which occurred much less frequently. These include events that had multiple peaks in their pulse-shapes, had positive polarity, or were very large amplitude discharges that had a significant amount of charge. During neutrino data acquisition, the overall event rate was nominally around 0.15 Hz, for the entire array.

7.2 Baseline Noise Event Rates

It was observed from detector operations and analysis of the time between successive NCD events that the majority of the digitized waveforms in the NCD data set are much like those found in Fig. 7.1(d)) and that they appear to occur randomly at a constant average rate. Furthermore, the rate of digitized events were observed to change abruptly on NCDs 1 and 31 when they went into the RCD condition, as observed in § 6.3. These events are likely to be predominantly generated by a combination of the series and parallel Johnson noise at the input of the FET preamplifier [76]. This noise source is dependent upon the complex impedance of its input load, which is the combination of the NCD cable, resistive coupler and the NCD. The electronic noise for the NCDs has been thoroughly discussed already in [59, 77]. Based on

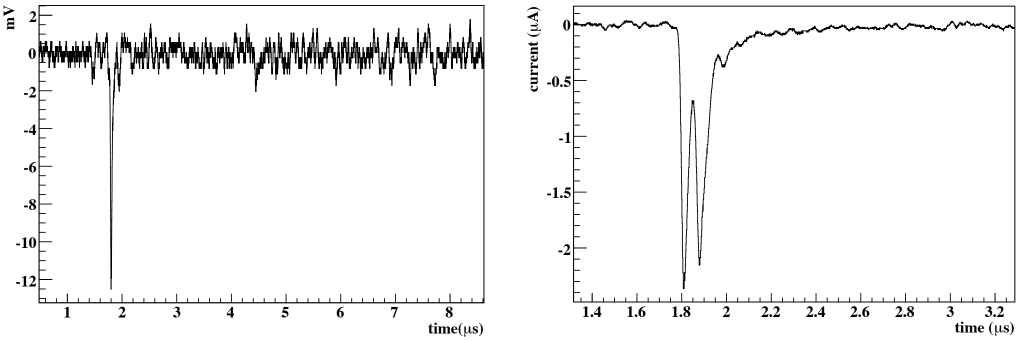

(a) Preamp microdischarge. (b) Delay-line microdischarge, or “Fork”.

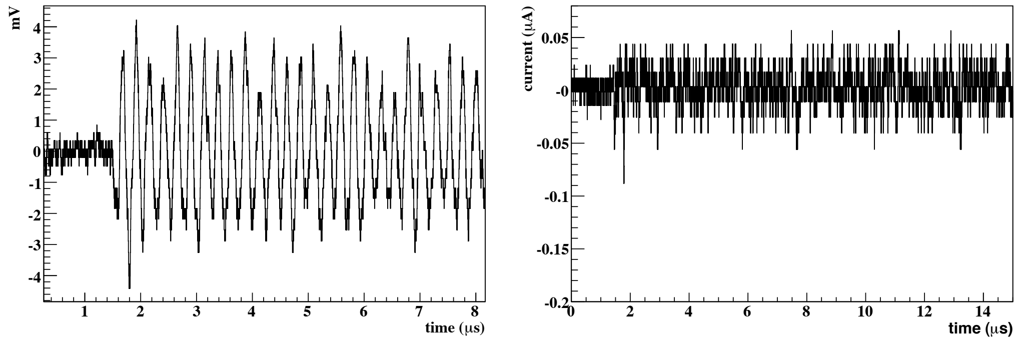

(c) EMI, or oscillatory noise. (d) Baseline noise.

Figure 7.1: Background events in the NCDs related to electronic effects. Note that the EMI and microdischarge events are shown in volts at the output of the preamplifier (50 Ω), rather than in current at the output of the NCD and that these plots do not all have the same time scale. [47].

these documents, an average MUX rate of 0.15 Hz corresponds to a trigger threshold of 50 nA, which is consistent with the event found in Fig. 7.1(d). The rms of the baseline of $\sim$ 20 nA is also consistent with the expected noise levels. The rate of these types of events will decrease by about 2 orders of magnitude for a change in the MUX threshold of about 6 nA. The two mechanisms by which the rate of these types of events will significantly decrease is an increase in the MUX threshold or decrease in the thermal noise amplitude at the input of the FET amplifier due to a decreased source resistance.

The distribution of the number of randomly occurring events found in a time interval is given by the Poisson distribution, neglecting any affects due to dead-time in the system. For an average rate r, the probability of finding n events in time T is given by the usual distribution

$$P(n, \rho, A) = A\frac{\rho^n}{n!}e^{-\rho} \tag{7.1}$$

where $\rho = rT$, is the mean number of events in T, and A is a normalization constant. A non-extended dead-time may also be considered, which, if large enough, could have an effect on the shape of the distribution [78, 79, 80, 81][1]. However, the dead-time for the digitizing oscilloscopes and MUX hardware is 0.750 seconds and ~600 μs, respectively. These are significantly smaller than the expected time between events and the observation time, T. Thus, a dead-time correction is unnecessary.

7.3 Data Set for Noise Analysis

The data set used in this analysis was the 7th version of the NCD phase data set, as determined by the run selection group within the SNO collaboration. There are two separate sets of runs that constitute the full NCD data set: the open data set, and the production data set. The open data set began on November 27, 2004 at run number 48220 and ended at run 48673. There were 128 valid runs in this set. The production data set began just after at the end of the open data set on January 3, 2005 at run number 50023 and ended at run 66498. There were 1885 valid runs in this set.

7.3.1 Removed Runs

For a variety of reason, within the set of data just described, a subset of runs were removed. There were 37 runs where the oscilloscopes were observed to behave unex-

---

[1] There are no extended dead-times in the NCD DAQ.

pectedly, which are summarized in Appendix D, that were removed from this analysis. In addition, runs 62449, 62452, 62464, 62465, 62466, 62470 and 62473 were removed because the ordering of events in these runs were not consistently chronological. It should be noted, however, that these runs were fixed after this analysis was completed and were included in the NCD phase neutrino flux measurement. Runs 60668 and 61746 were removed because of an incorrect calculation of dead-time. Run 51865 was removed because of a corrupt database file associated with this run. Run 61796 was removed because of a problem with the live-time clocks. Run 65884 was removed because there was a high rate of PMT and NCD event triggers which were not properly associated with an event (these are called orphaned events).

There was also an NCD-dependent set of runs that were removed in this analysis because the logamp calibration parameters for those runs were not properly associated with the events in those runs. The following list gives the run numbers that were excluded for the particular NCDs.

- NCD 0 Runs 59052, 60314 - 60326 and 61340.
- NCD 3 Runs 51705 - 51762.
- NCD 7 Runs 50500 - 50604.
- NCD 8 Runs 59052, 61753 - 61767.
- NCD 32 Runs 50500 - 50604, 53456 - 53496.

The logamp calibration parameters for these runs will be properly associated with the events in these runs and will be included in the NCD phase neutrino flux measurement.

It will be noted later in this chapter that the analysis of the production data set was broken into two subsets. One subset includes all data taken before the first NRE calibration was performed and the second subset includes the data taken after the first NRE calibration (see Chapter 6).

7.4 Selecting Baseline Noise Type Events

The baseline noise events generally have a set of unchanging characteristics that can be used for selecting them from other instrumental noise events. The baseline noise events have a constant standard deviation along the baseline, presumably a small current excursion that is slightly greater than the standard deviation, zero total charge, and a constant power spectrum throughout the entire waveform. In addition, they are not correlated with a shaper/ADC event and do not share power spectrum characteristics with fork events (Fig. 7.1(b)), oscillatory noise events (Fig. 7.1(c)) or physics events (neutrons or alphas). Throughout the rest of this chapter, only digitized waveforms that were not correlated with a shaper/ADC event were considered and are referred to as NSD waveforms (Non-Shaper/ADC Digitized waveform)[2].

A set of cuts based upon the above description was developed to select these events for the analysis. The cuts developed here were either an extension of a standard data cleaning cut [82] or a newly developed cut. In addition, some of the standard data cleaning cuts were utilized without modification. For each event, a set of measurements and calculations were made using the digitized waveform in the ADC-units of the oscilloscope – although, one of these cuts used the de-logged waveform. The tuning of the cuts developed here was done using a set of baseline noise events generated by simulation/Monte Carlo and through observations of the data from the open data set. It should be noted that due to the lack of a "calibration" source of baseline noise events, these cuts have unknown levels of efficiency.

First, I'll describe the set of simulation/Monte Carlo pulses and then each of the cuts that were developed.

---

[2] In the neutrino flux analysis, only digitized events that are correlated with a shaper/ADC event on the appropriate channel within 8 to 15 μs are considered a neutron or alpha candidate event. Digitized events without a shaper/ADC event typically have a total charge that is less than the shaper/ADC threshold.

7.4.1 Simulated Baseline Noise Events

The SNO Monte Carlo and Analysis Program (SNOMAN) was used to generate these simulated events. SNOMAN contains the latest NCD electronics model and was used to generate baseline noise. For each NCD, the average power spectrum was obtained from the baseline region between the trigger pulse and sine wave in the logamp calibration pulses that occurred after run 52366 (April 20, 2005). To generate noise for each event, SNOMAN generated a random power spectrum based upon each NCDs average power spectrum. Each simulated baseline noise event has two components. First, a rectangular pulse, 30-ns in width, was added at $t = 1800$ ns, approximately the scope trigger point plus the propagation time of the MUX delay-line. To reduce computational time, these rectangular pulses were added in order to induce event triggers in the Monte Carlo. These rectangular pulses are not physical, and their presence must be considered in the development of one of the baseline noise event selection cuts presented below (§ 7.4.4). Then, using SNOMAN, the signal was propagated through the NCD electronics model and then noise was added to the pulse. Eight different amplitudes for the rectangle-wave were used, ranging from 73.0 nA to 145.7 nA, in equal steps of 9.09 nA (equivalently, the amplitude of these pulses in mV at the output of the preamplifier would be 2 to 4 mV in steps of 0.025 mV). The Monte Carlo generated 100,000 events with amplitudes of 73, 82.1, and 91.2 nA, 75,000 events with amplitudes 100.3, 109.4, 118.5, 127.5, and 136.6 nA, and 50,000 events with an amplitude of 145.7 nA, equally distributed across all NCDs except for those filled with ^{4}He. Of these, 192,302 produced events which surpassed their respective channel thresholds. Only the average power spectrum for each NCD was used in the simulation, which accounts for some of the small discrepancies between the measured and calculated waveform parameters from the open data set and the simulated events. The simulations provide some assistance in the development of cuts, essentially verifying the assumptions made about the characteristics of the baseline noise events.

7.4.2 Definition of Pulse Regions

There were three regions of each waveform that were used for the various measurements and calculations required for the cuts. The regions were the *signal* region (1.6 - 7.6 μs), the *small signal* region (1.6 - 2.1 μs), and the *noise* region (9.0 - 15.0 μs) – Fig. 7.2. The size of the noise region was already set in the standard data cleaning cuts, and the same region was used here. In order to facilitate comparisons of the power spectra in the signal and noise regions, the signal region must be the same size as the noise region. The position in the waveform where the MUX gate closes is at $t \simeq 1.5$ μs. Because there is sometimes a small transient associated with the gate closing, the start of the signal region was set to $t = 1.6$ μs. The small signal region just focuses on the part of the waveform which caused the MUX to trigger.

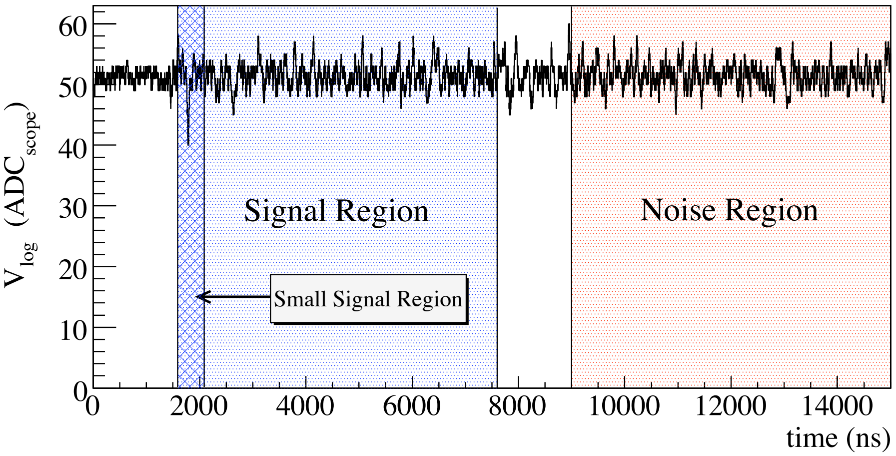

Figure 7.2: The three regions used for waveform-based cuts were the signal region (1.6 - 7.6 μs), the small signal region (1.6 - 2.1 μs) and the noise region (9.0 - 15.0 μs).

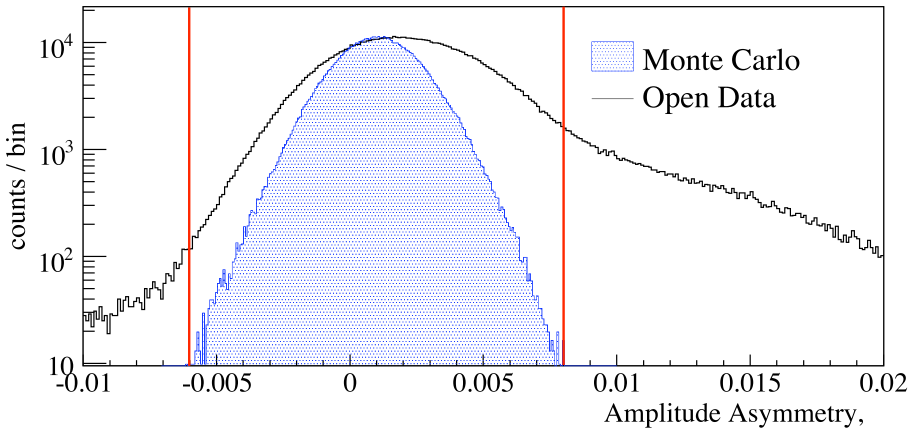

Figure 7.3: The distribution of the amplitude asymmetry, A, for the simulated baseline noise events and for the open data set. The vertical red lines indicate the allowed range of A. The number of events in the Monte Carlo histogram was scaled here to match the open data set histogram for comparison.

7.4.3 Amplitude Asymmetry Cut

The amplitude asymmetry measurement is a comparison between the integral of the digitized waveform in the noise region and the integral in the signal region. For the signal and noise regions, the integral of the digitized waveform is measured and the asymmetry parameter is defined as $A = 1 - \int \text{Signal}/\int \text{Noise}$. The measure, A, is the same as the amplitude asymmetry measure used in the standard neutrino data clean cuts. But in this instance, the allowed values of A are used to select noise events instead of alphas and neutrons. For baseline noise events, the asymmetry is expected to be distributed about zero. This cut was determined by finding the most restrictive range of A that still contained all of the Monte Carlo generated baseline noise events (Fig. 7.3). The allowed range of A was set to be between -0.006 and 0.008. Figure 7.4 shows the distribution of A for each NCD string.

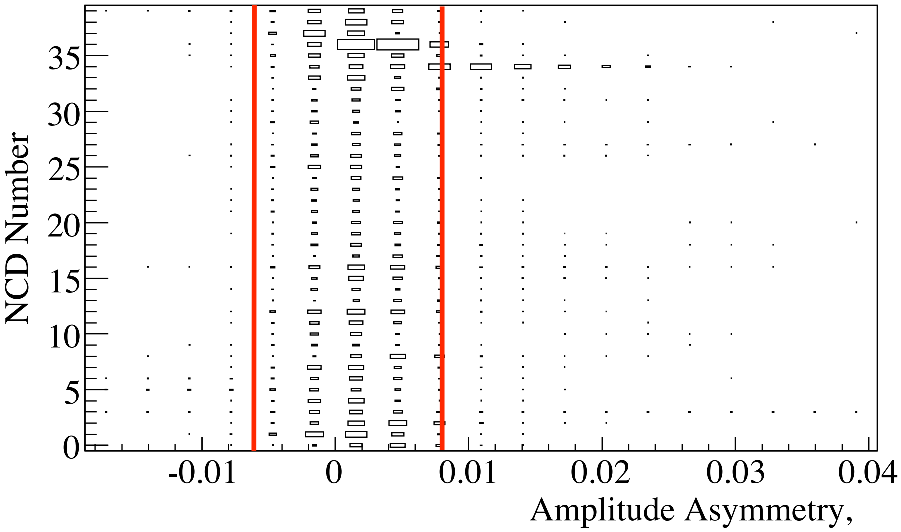

Figure 7.4: The distribution of the amplitude asymmetry, A, for the open data set for each NCD string. The vertical red lines indicate the allowed range of A.

7.4.4 Small Signal Region Integral Cut

For each NSD waveform, the signal was delogged and then integrated within the small signal region. This gave a measure of the total charge in the region and becomes more negative for large pulses. For baseline noise events, this measure should be distributed about zero or just slightly below. While this measurement would probably not distinguish baseline noise events from EMI events, it should remove microdischarge and fork events with a small total charge that were below the shaper/ADC thresholds.

Because the set of simulated events was generated with a set of distinct amplitude rectangular waves, the small signal region integral of the simulated events doesn't well represent the baseline noise events for this measurement. It was assumed that the majority of the open data set events that lacked a correlated shaper event were baseline noise events and so the cut was developed to include the majority of the events with zero integrated charge. The allowed range of values was set to between

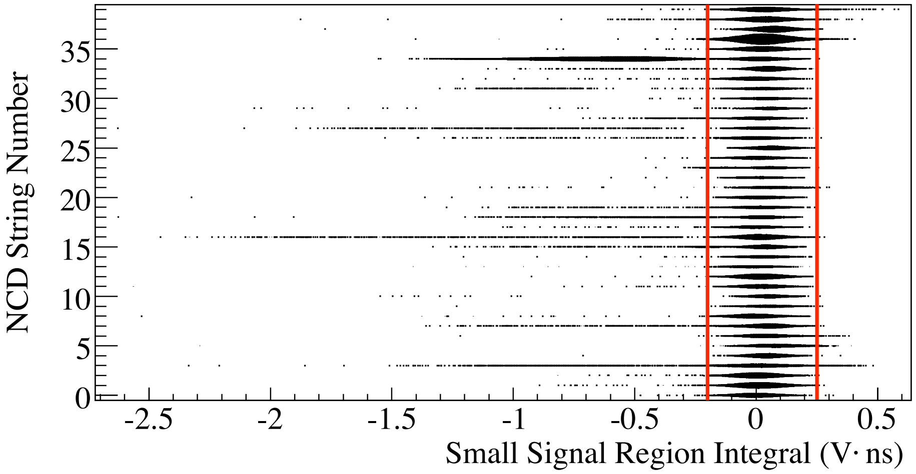

Figure 7.5: The distribution of the integral of the de-logged small signal region of waveforms in the open data set for each NCD string. The vertical red lines indicate the allowed range of this cut, between -0.02 and 0.025 volts·ns.

-0.02 and 0.025 volts·ns. It can be seen that some NCDs have subsets of events with a signal charge outside of this range (Fig. 7.5).

7.4.5 Maximum Amplitude Cut

The rate of thermal noise events as a function of the amplitude of noise deviation that triggers the MUX channel should decrease with increasing amplitude. That is, it is more likely to find a thermal noise event that is three standard deviations from zero than to find one that is five or six standard deviations from zero. Limiting the maximum amplitude allowed should cut out some larger amplitude EMI events, while still retaining the majority of the baseline noise events. This cut removed events that have a peak current that is greater than a defined threshold.

The MUX thresholds are set to be at nearly the same level for each NCD [52], but there exist slight variations in the observed distributions of the peak currents (using

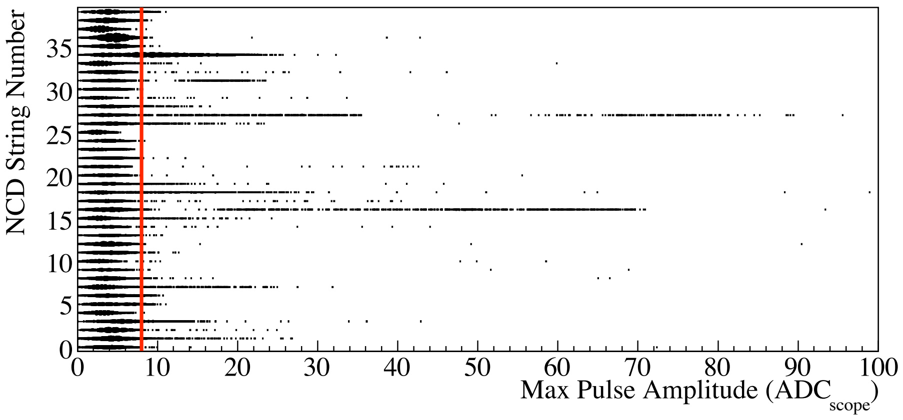

Figure 7.6: The distribution of the V_{max} measured in the open data set. The Maximum Amplitude Cut removes any NSD waveform with $V_{max} > 8.0$ ADC$_{\text{scope}}$

the open data set) which correspond to the different DC-level offsets applied at the inputs of the logamps (§ 5.1.3). For this reason, there are two steps to developing this cut. First, the maximum amplitude value in each NSD waveform from the open data set was measured, $V_{raw-max}$. From the set of measured $V_{raw-max}$ for each NCD, the minimum value was recorded – which is like determining a threshold for each channel in units of the oscilloscope ADC values, labeled here as V_{thresh}. From the distribution of $V_{max} = V_{raw-max} - V_{thresh}$, it was clear that V_{max} for most events were within a small range slightly greater than zero and that some strings had subsets of events with V_{max} significantly greater than 10.0 ADC$_{\text{Scope}}$ (Fig. 7.6). Since the only penalty for removing a small set of randomly occurring events was a small reduction in the rate of the randomly occurring NSD waveforms, this cut was set to include events with $V_{max} < 8.0$ ADC$_{\text{Scope}}$.

7.4.6 Noise Region Standard Deviation Cut

Within the noise region of the pulse, the standard deviation of the signal was calculated $\sigma_{noise} = \sqrt{\sum_{i=9.0}^{15.0}(V_i - \bar{V})^2/N}$, where i increments in steps of 1 ns. A waveform with a standard deviation that is significantly larger than the average baseline standard deviation could be an indicator of an EMI event of significant amplitude. The standard deviation is NCD-dependent and stable throughout the NCD phase except when there was a small, unexplained change in the DAQ. Specifically, σ_{noise} is dependent upon the DC offset at the input of the logamp, which is different for each NCD.

The mean and mode values of the distributions of σ_{noise} for the open data set and for the Monte Carlo are found to be slightly different, for reasons that are unknown at this time (Fig. 7.7). However, it is very likely that this difference is related to the change in the measured logamp parameters after the ex-situ electronics calibrations that took place in April 2005 since σ_{noise} is dependent upon the logamp input offset and the logamp parameter b is a measure of that offset. Except for NCD string 36 (and 3, 10, 20, and 30), the average difference in the mode was measured to be 5%. This is also observed with data from the production data set. In order not to make too strong of a cut, the NCD-dependent maximum standard deviation was set to be 10% greater than the maximum measured standard deviation from the Monte Carlo pulses for each NCD. The distribution of σ_{noise} for NCD string 36 is quite different from the Monte Carlo data. However, sampling a subset of the randomly occurring events on NCD 36 will still result in a set of randomly occurring events, which would follow the expected Poisson distribution.

Since the Monte Carlo did not include NCD strings 3, 10, 20, and 30, the standard deviation cut for those NCDs was determined in a less rigorous way. The distribution of σ_{noise} on a particular NCD should be similar to the distributions of σ_{noise} from other NCDs that are connected to the same MUX because σ_{noise} is correlated to the offset at the input of each logamp. The offset at the input of each logamp is nearly the same for all NCD channels on a particular MUX, although some variation exists. For NCD string 3, the other NCDs on MUX box 2 are 1, 6, 11, 14, 19, 22, 26, 31, and 34. From the logamp calibration data, it can be seen that NCDs 11, 14, 19, 31 and 34 have similar offsets at the logamp input. The distribution of the standard deviation is similar to the Monte Carlo distribution for NCD 11, so the maximum σ_{noise} value allowed for NCD string 3 was set to $\sigma_{noise} = 2.5$ ADC$_{\text{scope}}$, which was the same level for NCD 11. This same procedure was also done for NCDs 10, 20 and 30.

It should also be noted that a subset of the NCDs in Fig. 7.7 stand out by having relatively small average values of σ_{noise}. These are NCDs 4, 7, 10, 15, 18, 23, 25, 29, 33 and 37, which are all connected to MUX box 0. As was seen in the logamp calibrations, NCDs connected to MUX box 0 had larger DC-level offsets at the input of the logamp, and subsequently smaller baseline σ_{noise}.

7.4.7 Flatness Cut

The flatness parameter is a comparison of the power spectrum of the signal region to the average power spectrum of the noise region. It is useful in distinguishing pulses with significant power at low frequencies that may have been recorded without a shaper/ADC event. Neutron capture and alpha events have relatively significant amounts of power at low frequencies, as do other uncommon types of instrumental backgrounds. During data acquisition, dead-time in the system could have potentially prevented an event with significant charge to be measured by the shaper/ADC. This cut would remove such events.

Power Spectra and Flatness Parameter

The power spectra, obtained from the absolute square of the discrete Fourier transform of the signal region, were measured for each waveform. The amplitude of the power spectrum in the ith bin is $P_i = |\mathcal{F}_i|^2$, where $\mathcal{F}_i$ is the complex value of the

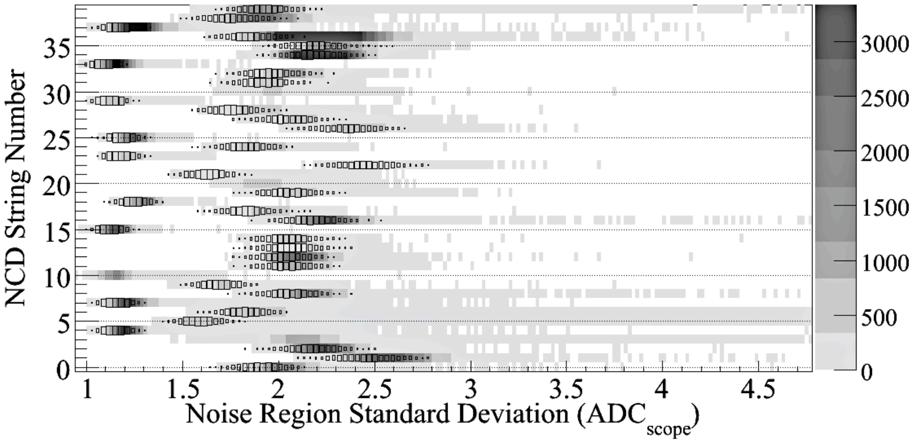

Figure 7.7: The distribution of the standard deviation of the noise region baseline, σ_{noise}, for the Monte Carlo baseline noise events (boxes) and for the open data set (grey-scale). The maximum σ_{noise} was determined for each NCD using the Monte Carlo data. The number of events in the Monte Carlo histogram was scaled here to match the open data set histogram. The NCDs with relatively small σ_{noise} were connected to MUX box 0.

ith bin of the discrete transform. The power spectra were obtained from the Fourier transform of the uncalibrated digitized waveform before baseline subtraction or delogging. The average power spectrum of the noise region was obtained from a set of neutron-source calibration runs that utilized an AmBe source placed in various locations throughout the AV[3]. It is desirable to use these data as a source of the average power of the noise region because neutrons (and alphas) are easily distinguished from EMI noise and other types of instrumental background events and are generally less than 6 μs wide. Thus, this provides a clean sample of baseline noise from events not caused by an instrumental background. The power spectrum of the baseline in the logamp calibration pulses could not be used because there was not a sufficient number of points between the trigger pulse and the start of the sine wave. The flatness parameter is defined as the logarithm of the ratio of first bin in the power spectrum of the signal region to the first bin in the power spectrum of the noise region, $F = \log_{10}(P_2^{signal}/P_2^{noise})$. Thus, this is really a comparison between the standard deviation of the signal region to the standard deviation of the noise region and will remove any events that have a significant broad pulse.

Maximum Allowed Flatness Parameter

This cut sets a maximum allowed value for the flatness parameter. This cut was originally developed to select neutrons and alphas from instrumental background events and accepted all events with a flatness parameter, F, greater than 2.1 for events that occurred on NCDs connected to MUX box 0, and greater than 2.0 for all other events[4]. Based upon the shape of baseline noise events, intuitively, one would expect to find F to be very near to zero. The distribution of F for the Monte Carlo events and for the open data set is shown in Fig. 7.8. From these distributions, the maximum flatness parameter was set to 0.7. The second peak in Fig. 7.8 is predominantly due

---

[3] Thanks to Nikolai Tolich for providing the average power spectra.

[4] As you may recall from Chapter 5, MUX box 0 had different characteristics than the other MUX.

to events on NCD string 34. It is known that bursts of fork events were found on NCD 27 and 34 during the open data set (there were also fork events on other NCDs as well). For NCD 34, the maximum flatness parameter was set to 0.05.

7.4.8 The Standard SNO Data Cleaning Cuts

In addition to the cuts described above, the following standard neutrino data cleaning cuts were used to remove unwanted background events such as EMI events and fork events, which have distinct power spectra [82].

Frequency-based EMI Cut While some of the cuts developed above may have removed some larger amplitude EMI events, they would not have removed small amplitude EMI events. A cut based upon a comparison of the power spectrum of the signal region to the average power spectrum of the noise region was already developed as part of the standard data cleaning cuts. This cut removes events that have significant power at frequencies between 3.7 MHz and 15 MHz. The full description of this cut is found in [82].

Frequency-based Fork Event Cut The fork event cut is similar to the Frequncy-based EMI Cut and removes events that have significant power above 12 MHz relative to the average power spectrum.

Multiple Peak Cut This cut removed any event that had multiple large peaks in the event [83].

Positive Signal Cut This cut removed all events which have a significant positive polarity signal. Any event with a positive signal that is 20 $\mathrm{ADC}_{\mathrm{scope}}$ above baseline is removed [83].

In summary, the baseline noise events were selected by 1) excluding all MUX events that were correlated in time with a shaper/ADC event, 2) then including the

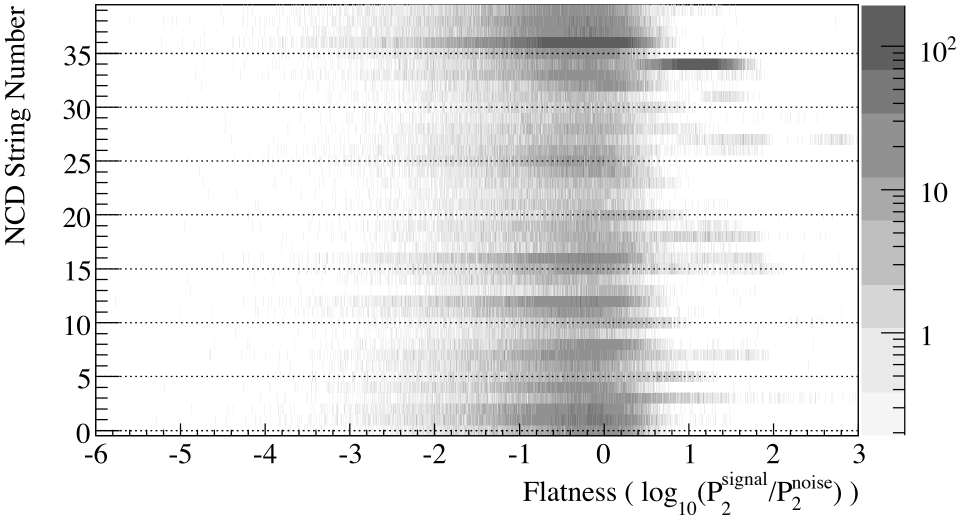

(a) Flatness for each NCD.

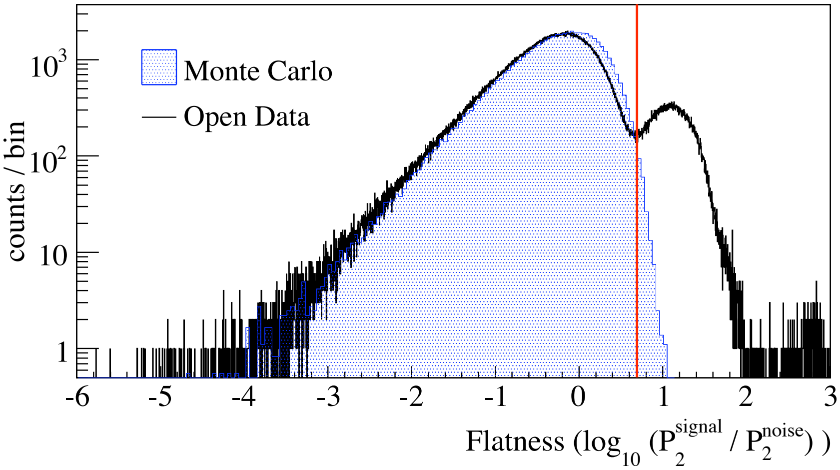

(b) Open data set and Monte Carlo.

Figure 7.8: The distribution of the Flatness measurement, F, for the Monte Carlo baseline noise events and for the open data set. The vertical red line in (b) indicates the maximum allowed F (0.7). The number of events in the Monte Carlo histogram was scaled here to match the open data set histogram.

subset of those events which passed the pulse-shape cuts described in this chapter and the previously developed data cleaning cuts.

7.5 Data Selection

Before applying the cuts described above, the appropriate sets of data were considered. First, only "neutrino" runs were used in this analysis since they constitute a set of runs where the detector was in a known and stable state that does not include influence from external sources, such as noise created by detector maintenance activities. This also excludes all types of calibration data. Second, the production data set was bifurcated in time at the date when the NRE calibration pulse was first initiated. The NRE calibration code was added to the DAQ on June 13, 2006 and tested in run 63136, which defines the boundary between the "pre-NRE" and "post-NRE" time periods. The injection of NRE pulses could potentially alter the rate of noise events due to an increase of dead-time and because the NRE calibrations induced a new type of noise event associated with changing channels on the Pulser Distribution System (§ 4.4). The NRE events occurred approximately once per minute.

Besides the cuts described above, data were excluded on a particular NCD if the MUX threshold or the high voltage for a particular NCD was different from the *nominal* settings. A changed threshold or high-voltage would presumably cause the rate of noise events to change. For each data set, a nominal detector state was defined. For the open data set, the nominal settings were defined to be the detector settings of run 48220. Run 52737 was defined as the nominal state for the pre-NRE production data set, and run 62418 for the post-NRE production data set. This is summarized in Table 7.1. The reason for the different nominal states was changes in threshold for a few NCDs, which persisted throughout each data period. Because of these threshold and high voltage changes, there exist periods in the data set where some NCDs were not tested for changes in their baseline noise rates.

Table 7.1: The starting dates, run numbers, and run number that defines the nominal NCD detector state for the open, pre-NRE and post-NRE data sets. The live-time for each data set was determined by [75].

Data Set	Start Date	Start Run	Nominal Detector State	Live-time (days)
Open	November 27, 2004	48220	48220	25.68 ± 0.01
Pre-NRE	January 3, 2005	50023	52737	301.44 ± 0.11
Post-NRE	June 13, 2006	63136	62418	58.05 ± 0.02
Total				385.17 ± 0.14

MUX Thresholds The MUX thresholds on a number of NCDs throughout the open and production data set were different from their respective nominal settings. This occurred on NCDs 0, 3, 6, 7, 8, 9, 21, 23, 32, 34, 35, 37 and 39. In the open data set, only NCDs 3 and 36 had thresholds different from nominal. The thresholds for all of the NCDs just listed were altered at some point in the pre-NRE data set. In the post-NRE data set, the MUX thresholds for NCDs 7, 8, 21, 23 and 37 were altered from their nominal settings.

High Voltage The high voltage settings on NCDs 0, 3, 7, 8, 32 and 34 were altered during the open and pre-NRE data sets. The high voltage for NCD 3 was off for the majority of the data, as it was found early-on that this NCD produced high rates of discharge events that produced unacceptable amounts of dead-time. NCDs 0, 7, 8, 32 and 34 had, at times, elevated high voltage – 2250 volts for significant durations of the production data.

7.6 Analysis Procedure

Each run was divided into an integer number of 15-minute bins. Then, the number of events, n, on each NCD that passed the baseline noise selection cuts were counted for each bin[5]. If the MUX threshold or the high-voltage setting for a particular NCD was different from the nominal settings, the data on that NCD from that run was ignored. The goal was to find instances where the rate of noise events on each NCD was anomalously small. In general, the method was to create a histogram of the number of events, n, found in each time bin and then fit that data to Eq. 7.1 using a binned maximum-likelihood algorithm. A comparison of the measured occupancy of the $n = 0$ bin, $O_{n=0}$ to the expected occupancy, $P(0, \hat{\rho}, \hat{A}) = y_0$, would then provide a method for finding anomalously low rates of baseline noise events. Because the rate of baseline noise events is small (approximately a total of 0.15 Hz rate on all NCDs), 15-minute bins were not large enough to discern low rates of baseline noise events since it was quite likely to find zero baseline noise events within 15 minutes for most NCDs. Thus, the 15-minute bins were concatenated together to create 120-minute bins (8 consecutive 15-minute bins) and 240-minute bins. The 15-min. bins that made up each 120-min. or 240-min. were not restricted to occur within the same run, but could come from different runs. The observations of the number of events, n, were placed into histograms. The occupancy of each bin in the histograms is labeled O_n. Then, the best-fit Eq. 7.1 to the distributions of n for the counting time, $T = 120$ min., was determined for each NCD.

For example, the best-fit Eq. 7.1 to number of baseline noise event counts in each 120-minute bin from the open data set on NCD 13 is found using ROOT's binned maximum-likelihood fitting routine. The best-fit curve for NCD 13 shown in Fig. 7.9(a) is the *continuous* Poisson distribution where the Gamma function,

---

[5] The remaining data beyond the last full 15-minute period of each run were discarded.

$\Gamma(n+1)$, is substituted for $n!$ in Eq. 7.1[6]. The best-fit expected number of events was $\hat{\rho} = 15.0 \pm 0.2$ events. The normalization constant was $\hat{A} = 307 \pm 18$ 120-min. observations. The expected occupancy of the $n = 0$ bin for Eq. 7.1 evaluated at these parameters $y_0 = 9.4 \pm 28 \times 10^{-5}$ occurrences – the measured occupancy $O_{n=0}$ was zero.

Unfortunately, not all NCDs had such predictable distributions. The distributions for many NCDs were not Poisson in shape and the resulting fits to the data did not pass a χ^2 goodness-of-fit tests. The reason for this is likely due to the inefficiency of the cuts above, which is a consequence of the inability to model all types of instrumental noise events in the NCDs and separate out just the baseline noise events. It is likely that a source of noise events that mimic baseline noise events, which occur infrequently and in bursts rather than randomly at an average rate, have passed the cuts described above and altered the distribution of n Thus, in order for this analysis to proceed, for many distributions, the average number of events $\hat{\rho}$ was estimated in a slightly subjective way. For example, the distribution of events for NCD string 34 in the open data set was clearly not Poisson (Fig. 7.9(b)). For this particular NCD, the range was restricted to between 0 and 34, the best-fit parameters are $\hat{A} = 133 \pm 13$, and $\hat{\rho} = 27.7 \pm 0.6$ events. From this result, the expected occupancy $y_0 = 1.2 \pm 21 \times 10^{-10}$ occurrences – the measured occupancy $O_{n=0}$ was zero.

Another example is NCD 38 (Fig. 7.9(c)). It appears that the rate of noise events changed throughout periods of the open data set, or an onset of bursty noise events that mimic the baseline noise events occurred. For these types of event distributions, I would restrict the range to a region about the smallest peak and then perform

---

[6] As the reader will be reminded at various times throughout this Chapter, the best-fit curves displayed here and in Appendix E are the continuous Poisson distributions

$$P(n, \rho, A) = A \frac{\rho^n}{\Gamma(n+1)} e^{-\rho}$$

which are equal to Eq. 7.1 when n is an integer. The continuous distributions simply look better and help distinguish the best-fit curve from the histograms. However, the data were fit to Eq. 7.1

the maximum-likelihood fit. If a peak was not observed in the data, the region was restricted to the leading edge of the distribution and then fit. Thus, the reported values for $\hat{\rho}$ are either the true rate of baseline noise events (if the fits are good), or the lowest likely rate of baseline noise events in the case of non-Poisson distributions. The general conclusion for many NCDs is that it's not possible using the method outlined in the previous sections of this Chapter to to select *just* the baseline noise events in a robust way. Nevertheless, the information obtained here was useful and conclusions about the presence of RCD were subsequently made.

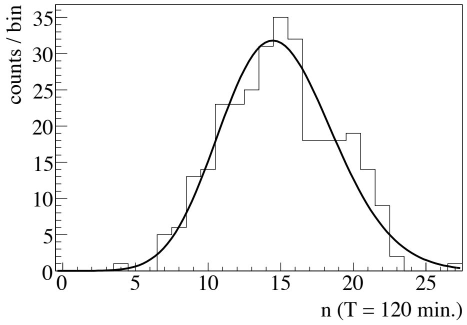

(a) NCD 13.

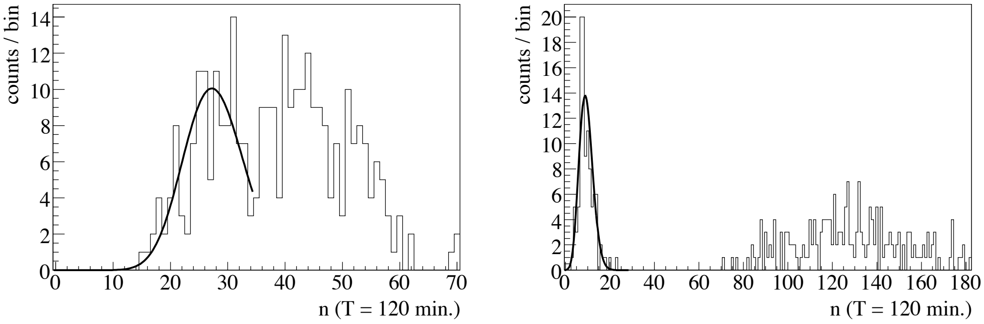

(b) NCD 34.

(c) NCD 38.

Figure 7.9: The distribution of the number of events found in 120-minute bins in the open data set for NCD strings 13 (a), 34, (b), and 38 (c). A maximum likelihood-fit of Eq. 7.1 to the data is shown in each figure, where the range was restricted in the fits for NCDs 34 and 38.

7.7 Noise Event Distributions

The results of the attempts to fit the distribution of n for $T = 120$ minutes to the data that passed the full set of cuts is presented in Tables 7.2, 7.3 and 7.4, for the open, pre-NRE, and post-NRE data periods, respectively. The χ^2 calculated here was the small-sample Poisson-likelihood chi-square, $\chi^2 = 2\sum[O_n \ln(O_n/y_n) + y_n - O_n]$ where y_n are the expected values from Eq. 7.1 evaluated at the best-fit parameters for bin n, and O_n are the measured occupancy of bin n. Bins where $O_n = 0$ were excluded, by prescription [84]. Also listed in the each table is the range set for each maximum-likelihood fit and the maximum value of n that had at least an occupancy of one, n_{max}. The value N_{120} lists the number of 120-min. bins where the detector settings were nominal for each NCD. In the open, pre-NRE, and post-NRE data sets, the maximum possible values of N_{120} were 307, 3612, and 716.

The distributions from a few NCDs, as indicated in the tables, fit acceptably well to Eq. 7.1, while many did not. It is noted that there are more good fits to the data in the open and post-NRE data sets than in the pre-NRE data set. This suggests that the greater amount of time in the pre-NRE data set allowed for the occurrence of more bursty noise, resulting in non-Poisson distributions of events.

A convenient way to observe this large selection of data is in a two-dimensional histogram with the distribution of $1 + n$ along a log-scale horizontal axis and the NCD string number along vertical axis[7]. Different levels of shading are used to represent the occupancy of each bin. In Fig. 7.10, the data from the open, pre-NRE and post-NRE data sets are shown (for $T = 120$ min.).

Open Data Set, $T = 120$ min.

In the open data set, there were 307, 120-min. bins of data. The MUX thresholds on NCDs 3 and 36 were altered for a few runs from their nominal values (N_{120} is less

---

[7] Plotting $1 + n$ is convenient for display purposes since on a log-scale, the $n = 0$ bin is displayed.

Table 7.2: The results of fitting to the baseline noise event distributions for the open data to Eq. 7.1 for $T = 120$ minutes. The column $O_{n=0}$ is the occupancy of the $n = 0$ bin, N_{120} is the number of 120-minute bins in the data set with nominal threshold and high-voltage settings, and n_{max} is the largest bin with an occupancy of at least one.

NCD	$O_{n=0}$	N_{120}	n_{max}	$\hat{\rho}$	$\hat{A}$	fit range, n (min - max)	χ^2/d.o.f
0	0	307	98	45.9 ± 0.7	152 ±14	0 - 54	23.4/21
1	0	307	220	69.6 ± 0.8	105 ±10	0 - 96	38.6/34
2	0	307	142	79.8 ± 1	121 ±12	0 - 90	41.8/26
3	0	293	905	28.3 ± 0.5	173 ±15	0 - 34	40.9/20
4	0	307	117	24.2 ± 0.5	106 ±10	0 - 38	22.7/21
5	0	307	44	22.3 ± 0.5	220 ±18	0 - 26	20.8/15
6	0	307	50	33.8 ± 0.3	307 ±18	0 - 50	41.7/31
7	0	306	870	43.3 ± 0.8	134 ±14	0 - 50	34.2/23
8	0	307	80	56.7 ± 0.4	307 ±18	0 - 80	32.2/39
9	0	307	25	12.3 ± 0.2	307 ±18	0 - 25	18.3/17
10	0	307	49	26.9 ± 0.3	307 ±18	0 - 49	54.1/31
11	0	307	64	44.1 ± 0.4	307 ±18	0 - 64	35.7/34
12	0	307	129	97.3 ± 0.6	307 ±18	0 - 129	59.2/54
13	0	307	27	15.0 ± 0.2	307 ±18	0 - 27	16.4/17
14	0	307	36	17.1 ± 0.2	306 ±18	0 - 32	27.2/20
15	0	307	66	42.6 ± 0.4	307 ±18	0 - 66	46.9/35
16	0	307	112	86.4 ± 0.5	307 ±18	0 - 112	64.0/49
17	0	307	42	20.9 ± 0.3	307 ±18	0 - 42	40.7/24
18	0	307	43	24.4 ± 0.3	307 ±18	0 - 43	30.0/27
19	0	307	39	18.1 ± 0.3	263 ±18	0 - 24	26.1/14
20	0	307	38	18.2 ± 0.5	205 ±18	0 - 22	12.2/14
21	0	307	23	10.4 ± 0.2	307 ±18	0 - 23	44.7/20
22	0	307	19	10.0 ± 0.2	307 ±18	0 - 19	11.4/16
23	0	307	28	14.6 ± 0.2	307 ±18	0 - 28	17.8/21
24	0	307	47	28.8 ± 0.3	307 ±18	0 - 47	49.3/30
25	0	307	74	35.5 ± 0.5	215 ±16	0 - 42	35.7/24
26	0	307	45	27.6 ± 0.3	307 ±18	0 - 45	41.0/28
27	0	307	37	14.2 ± 0.4	210 ±18	0 - 18	24.0/12
28	0	307	35	21.7 ± 0.3	307 ±18	0 - 35	36.8/25
29	0	307	26	14.3 ± 0.2	307 ±18	0 - 26	13.5/21
30	0	307	22	11.8 ± 0.2	307 ±18	0 - 22	24.7/16
31	0	307	30	14.6 ± 0.4	264 ±21	0 - 18	18.7/13
32	0	307	71	19.9 ± 0.5	101 ±10	0 - 32	14.0/18
33	0	307	100	54.1 ± 0.8	151 ±14	0 - 62	27.3/25
34	0	307	70	27.7 ± 0.6	133 ±13	0 - 34	21.5/19
35	0	307	154	48.6 ± 0.7	114 ±11	0 - 64	37.5/29
36	0	128	1562	40.3 ± 0.6	104 ±10	0 - 66	24.9/26
37	0	307	297	22.5 ± 0.5	105 ±10	0 - 42	29.9/23
38	0	307	182	9.32 ± 0.3	105 ±10	0 - 28	29.6/15
39	0	307	184	28.9 ± 0.5	105 ±10	0 - 42	15.3/21

Table 7.3: The results of fitting to the noise distribution after the cuts were applied for the pre-NRE data to Eq. 7.1 for $T = 120$ minutes. The column $O_{n=0}$ is the occupancy of the $n = 0$ bin, N_{120} is the number of 120-minute bins in the data set with nominal threshold and high-voltage settings, and n_{max} is the largest bin with an occupancy of at least one.

NCD	$O_{n=0}$	N_{120}	n_{max}	$\hat{\rho}$	$\hat{A}$	fit range, n (min - max)	χ^2/d.o.f
0	0	3485	117	52.2 ± 0.2	3094 ±65	0 - 59	79.5/30
1	111	3612	199	58.7 ± 0.3	965 ±36	8 - 66	64.4/31
2	0	3612	255	91.9 ± 0.4	1058 ±36	0 - 104	257.7/45
3	0	2196	452	20.1 ± 0.1	2100 ±46	0 - 39	64.3/32
4	0	3612	136	40.2 ± 0.2	1766 ±56	0 - 44	141.8/26
5	0	3612	56	28.6 ± 0.09	3612 ±60	0 - 56	714.3/47
6	0	3604	63	34.8 ± 0.1	3604 ±60	0 - 63	202.8/44
7	0	3206	138	50.6 ± 0.3	1117 ±36	0 - 60	111.5/32
8	0	2660	96	52.1 ± 0.3	2019 ±63	0 - 56	53.0/26
9	0	3605	27	12.7 ± 0.06	3605 ±60	0 - 27	16.4/23
10	0	3612	49	27.4 ± 0.09	3612 ±60	0 - 49	142.6/38
11	0	3612	68	43.1 ± 0.1	3612 ±60	0 - 68	67.3/42
12	0	3612	159	94.1 ± 0.2	2944 ±60	0 - 106	137.6/44
13	0	3612	32	16.4 ± 0.07	3612 ±60	0 - 32	33.7/26
14	0	3612	38	16.2 ± 0.07	3612 ±60	0 - 38	54.0/30
15	0	3612	88	36.9 ± 0.2	2955 ±62	0 - 43	68.8/24
16	0	3612	151	93.2 ± 0.2	2726 ±58	0 - 104	304.4/49
17	0	3612	47	22.9 ± 0.08	3612 ±60	0 - 47	78.6/36
18	0	3612	41	20.8 ± 0.08	3612 ±60	0 - 41	70.4/32
19	0	3612	38	17.8 ± 0.07	3612 ±60	0 - 38	174.0/32
20	0	3612	44	22.3 ± 0.08	3612 ±60	0 - 44	199.2/35
21	0	3575	27	10.1 ± 0.05	3575 ±60	0 - 27	181.4/24
22	0	3612	27	10.8 ± 0.05	3612 ±60	0 - 27	36.0/23
23	0	3575	73	12.3 ± 0.08	2648 ±54	0 - 17	83.9/14
24	0	3612	57	29.5 ± 0.09	3612 ±60	0 - 57	143.3/42
25	0	3612	80	36.7 ± 0.1	3612 ±60	0 - 80	371.1/55
26	0	3612	50	27.5 ± 0.09	3612 ±60	0 - 50	36.6/38
27	0	3612	34	14.1 ± 0.06	3612 ±60	0 - 34	72.1/28
28	0	3612	252	20.7 ± 0.08	3547 ±60	0 - 36	87.3/31
29	0	3612	40	13.5 ± 0.08	3162 ±61	0 - 18	68.9/15
30	0	3612	24	11.5 ± 0.06	3612 ±60	0 - 24	35.7/22
31	223	3612	27	9.59 ± 0.07	2816 ±55	5 - 15	104.6/10
32	0	3389	822	26.2 ± 0.09	3354 ±58	0 - 53	229.2/43
33	0	3612	101	56.3 ± 0.1	3612 ±60	0 - 101	353.7/59
34	0	3357	82	28.6 ± 0.09	3341 ±58	0 - 46	97.2/36
35	0	3421	244	49.4 ± 0.2	1827 ±50	0 - 56	92.9/27
36	1	3612	410	7.48 ± 0.07	3392 ±66	0 - 10	30.5/10
37	0	3269	413	37.2 ± 0.3	1114 ±41	0 - 42	131.8/24
38	0	3612	188	13.1 ± 0.06	3539 ±59	0 - 28	55.2/26
39	0	3330	261	34.4 ± 0.1	2473 ±51	0 - 45	181.9/29

Table 7.4: The results of fitting to the noise distribution after the cuts were applied for the post-NRE data to Eq. 7.1 for $T = 120$ minutes. The column $O_{n=0}$ is the occupancy of the $n = 0$ bin, N_{120} is the number of 120-minute bins in the data set with nominal threshold and high-voltage settings, and n_{max} is the largest bin with an occupancy of at least one. There was no data on NCD string 3 since its high-voltage was turned off during the post-NRE data set.

NCD	$O_{n=0}$	N_{120}	n_{max}	$\hat{\rho}$	$\hat{A}$	fit range, n (min - max)	χ^2/d.o.f
0	0	716	88	62.6 ± 0.3	716 ±27	0 - 88	71.3/46
1	616	716	2	0.15 ± 0.01	716 ±27	0 - 2	0.6/1
2	0	716	175	125.0 ± 0.7	470 ±24	0 - 138	102.1/45
3							
4	0	716	75	46.3 ± 0.3	716 ±27	0 - 75	89.5/43
5	0	716	55	36.9 ± 0.2	716 ±27	0 - 55	26.8/35
6	0	716	66	40.3 ± 0.2	716 ±27	0 - 66	68.9/42
7	56	699	8	2.6 ± 0.06	699 ±26	0 - 8	4.0/7
8	0	688	89	57.7 ± 0.3	688 ±26	0 - 89	61.5/44
9	0	716	31	15.2 ± 0.1	716 ±27	0 - 31	40.3/23
10	0	716	51	33.8 ± 0.2	716 ±27	0 - 51	24.5/31
11	0	716	74	48.4 ± 0.3	716 ±27	0 - 74	44.4/39
12	0	716	165	118.0 ± 0.4	716 ±27	0 - 165	87.6/66
13	0	716	37	19.2 ± 0.2	716 ±27	0 - 37	43.3/28
14	0	716	39	19.8 ± 0.2	716 ±27	0 - 39	38.5/27
15	0	716	96	63.9 ± 0.3	716 ±27	0 - 96	89.1/51
16	0	716	169	124.0 ± 0.4	716 ±27	0 - 169	102.3/66
17	0	716	52	31.3 ± 0.2	716 ±27	0 - 52	31.1/33
18	0	716	40	23.6 ± 0.2	716 ±27	0 - 40	28.3/27
19	0	716	50	27.2 ± 0.2	716 ±27	0 - 50	43.2/32
20	0	716	45	27.2 ± 0.2	716 ±27	0 - 45	37.3/29
21	647	699	2	0.08 ± 0.01	699 ±26	0 - 2	1.7/1
22	0	716	23	11.6 ± 0.1	716 ±27	0 - 23	12.6/18
23	329	485	3	0.41 ± 0.03	485 ±22	0 - 3	2.7/2
24	0	716	59	39.4 ± 0.2	716 ±27	0 - 59	33.8/36
25	0	716	70	44.1 ± 0.2	716 ±27	0 - 70	38.2/40
26	0	716	50	31.4 ± 0.2	716 ±27	0 - 50	34.7/31
27	0	716	33	19.1 ± 0.2	716 ±27	0 - 33	24.3/23
28	0	716	40	25.5 ± 0.2	716 ±27	0 - 40	23.7/28
29	0	716	43	22.9 ± 0.2	716 ±27	0 - 43	58.7/30
30	0	716	23	12.8 ± 0.1	716 ±27	0 - 23	23.2/19
31	318	716	17	8.4 ± 0.3	236 ±18	6 - 15	17.1/9
32	0	716	55	32.8 ± 0.2	716 ±27	0 - 55	46.8/33
33	0	716	100	65.7 ± 0.3	716 ±27	0 - 100	104.1/49
34	0	716	53	33.9 ± 0.2	716 ±27	0 - 53	39.0/34
35	0	716	92	53.4 ± 0.3	706 ±27	0 - 72	27.2/41
36	0	716	20	8.7 ± 0.1	716 ±27	0 - 20	29.3/18
37	392	699	6	0.58 ± 0.03	699 ±26	0 - 6	8.5/4
38	0	716	27	14.4 ± 0.1	716 ±27	0 - 27	17.3/22
39	0	716	63	43.6 ± 0.2	716 ±27	0 - 63	43.3/36

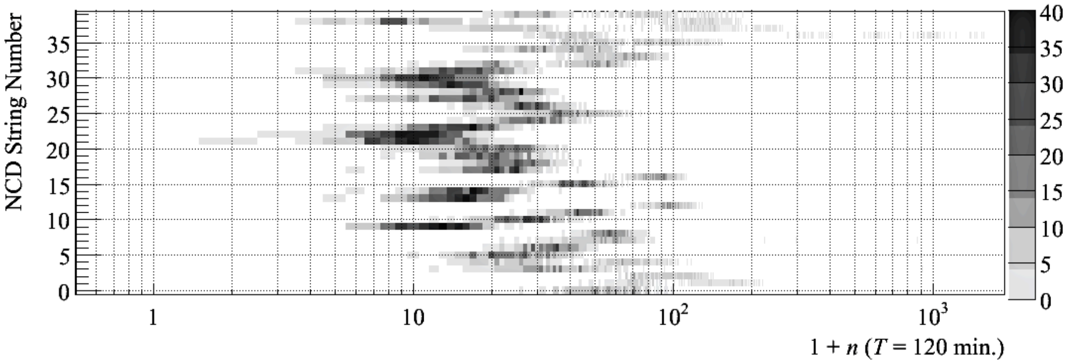

(a) Open Data Set.

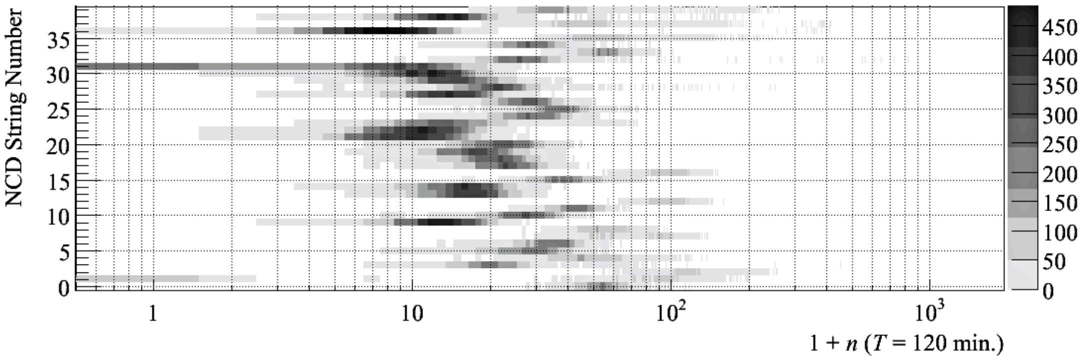

(b) Pre-NRE Data Set.

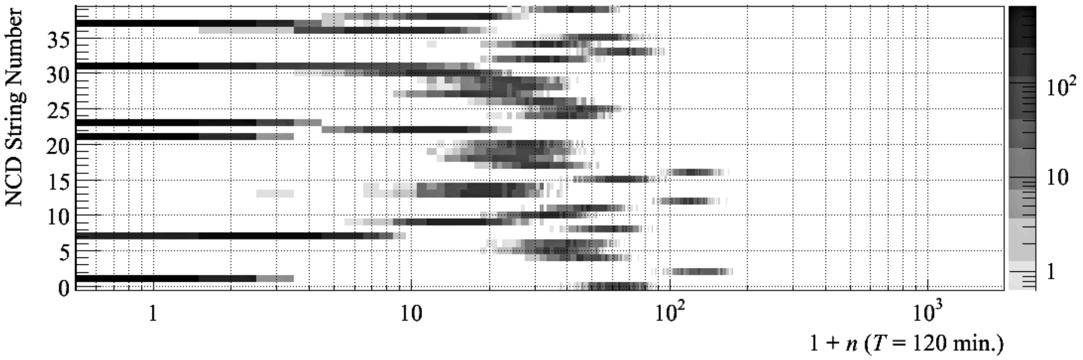

(c) Post-NRE Data Set.

Figure 7.10: The distribution of $1 + n_i$ for $T = 120$ min. in the open data set (a), pre-NRE data set (b), and the post-NRE data set (c).

than 307 in Table 7.2 for these NCDs). The measured occupancy $O_{n=0}$ for all NCDs was zero, indicating that all NCDs were acquiring data and that the level of noise at the input of the preamps had not significantly decreased (Fig. 7.10(a)). The minimum average number of events per 120 min., $\hat{\rho}$, that would result in an observed $O_{n=0} = 1$ can be calculated for comparison to the measured values. For Eq. 7.1, with $\hat{A} = 307$, the average number of events may be no more than $\rho_{min} = \ln \hat{A} = 5.73$ events in order to expect to find $O_{n=0} = 1$. No NCD in the open data set has an observed rate below this level, thus it is expected to find $O_{n=0} = 0$ for all NCDs. The NCD with the closest rate is NCD 38 where $\hat{\rho} = 9.32$ events.

Pre-NRE Data Set, T = 120 min.

In the pre-NRE data set, there were 3612, 120-min. bins of data. The MUX threshold or the high-voltage setting for NCDs 0, 3, 6, 7, 8, 9, 21, 23, 32, 34, 35, 37 and 39 were altered for some runs from the nominal settings of run 52737 (N_{120} is less than 3612 in Table 7.3 for these NCDs). The measured occupancy $O_{n=0}$ was non-zero for NCDs 1, 31 and 36 (Fig. 7.11). From the logamp calibrations (§ 5.4.1), it is known that during the pre-NRE data set NCD 1 went into the RCD condition and remained, while NCD 31 appeared to vacillate between the RCD condition and normal operation. For these NCDs it was expected to find $O_{n=0} \neq 0$. For NCD 36, the measured average rate was $\hat{\rho} = 7.48 \pm 0.07$ events per 120-min, which is low enough to expect $O_{n=0} \neq 0$, consistent with observation. The results from the maximum likelihood fits of Eq. 7.1 were used to compared the measured occupancy $O_{n=0}$ to the expected occupancy y_0 (Table 7.5). The histogram for NCD 31 would not fit to a sum of two Poisson distributions, even when the allowed range for the rates of the two Poisson distributions were severely restricted.

Table 7.5: The measured occupancy $O_{n=0}$ and the expected occupancy y_0, based on the best-fit parameters for Eq. 7.1 for data from the pre-NRE data set. The measured $O_{n=0} = 1$ is consistent with the expected occupancy y_0 for NCD 36.

NCD	$O_{n=0}$	$\hat{\rho}$	$\hat{A}$	Expected y_0
1	111	58.7 ± 0.3	965 ± 36	$3.1 \pm 54 \times 10^{-23}$
31	223	9.59 ± 0.07	2816 ± 55	0.19 ± 0.13
36	1	7.48 ± 0.07	3392 ± 66	1.9 ± 1.0

Post-NRE Data Set, T = 120 min.

In the post-NRE data set, there were 716, 120-min. bins of data. The MUX thresholds for NCDs 7, 8, 21, 23, and 37 were altered from the nominal settings of run 62418 for a relatively small number of runs (N_{120} is less than 716 in Table 7.4 for these NCDs). The high-voltage for NCD string 3 was set to zero, and the MUX threshold was maximized – effectively turning this NCD off. The occupancies $O_{n=0}$ were non-zero for NCDs 1, 7, 21, 23, 31, and 37 in this data set.

The non-zero $O_{n=0}$ for NCDs 7, 21, 23, and 37 can be explained due to an increase in the MUX thresholds for those channels prior to the post-NRE data set. The MUX thresholds on NCD strings 7, 21, and 23 were increased before run 62418, and also increased for NCD 37 before run 61787. This occurred *before* the start of the post-NRE data set and the thresholds were only changed from these settings during the post-NRE period for a few runs. The distribution of n for these NCDs in the post-NRE data suggest that the thresholds were significantly increased such as to reject the majority of baseline noise events, resulting in the high values for $O_{n=0}$ (Fig. 7.12). Thus, it cannot be concluded that these NCDs were afflicted with the RCD condition during this time. However, the rate of alphas measured on NCDs 7, 21, 23 and 37, measured in Chapter 8, were found to be consistent with a constant rate, and no

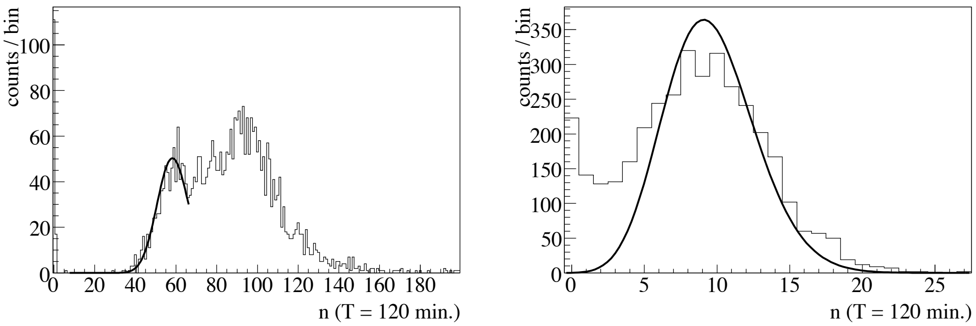

(a) NCD 1.

(b) NCD 31.

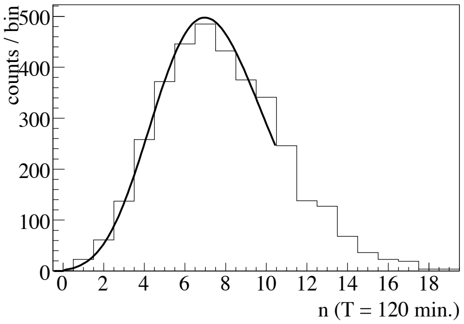

(c) NCD 36.

Figure 7.11: The distribution of the number of events found in 120-minute bins in the pre-NRE data set for NCD strings 1 (a), 31 (b) and 36 (c). A maximum likelihood-fit of Eq. 7.1 to the data is shown in each figure. The results of the fit are found in Table 7.3. The best-fit curve for NCD 31 is extended out beyond the range (n = 5 - 15) used for finding the best-fit parameters. The occupancy of the $n = 0$ ($O_{n=0}$) bin is 111, 223 and 1 for NCDs 1, 31 and 36, respectively.

evidence of RCD was observed through the NRE calibrations § 6.4.

On the other hand, NCDs 1 and 31, continued to have significant periods of no baseline events, as observed by $O_{n=0} \neq 0$. The nominal thresholds for NCDs 1 and 31 were the same in all three data sets.

Increased Time Bin (T = 240 min.)

The distribution of $1 + n$ was generated for a larger time window of $T = 240$ min, (Fig. 7.13) and were found to be consistent that the distributions for $T = 120$ min. Non-zero occupancy of $O_{n=0}$ was observed for NCDs 1 7, 21, 23, 31 and 37. Thus, this is a confirmation that these periods of low-rates occurred for at least 2 consecutive hours. The conclusions from the $T = 240$ min. is the same as before – the data is consistent with RCD on NCDs 1 and 31, and the low rates on NCDs 7, 21, 23 and 37 are caused by increased MUX thresholds. Note that now $O_{n=0} = 0$ for NCD 36 in the pre-NRE data set, as compared with the previous results for $T = 120$ min. The best-fit Eq. 7.1 to the distributions for NCD 36 were determined and the results are found in Fig. E.16 and Table E.1 in Appendix E. These results for NCD 36, rather than the results from data from when $T = 120$ min., are used to place a limit on the amount of time NCD 36 was afflicted with RCD, discussed in the next section of this chapter.

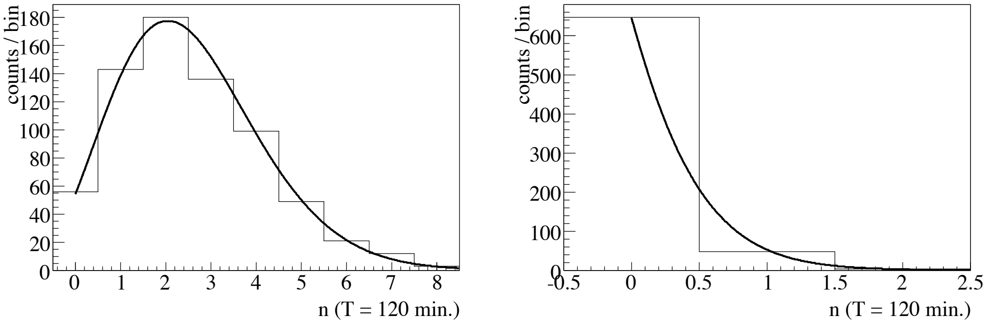

(a) NCD 7.

(b) NCD 21.

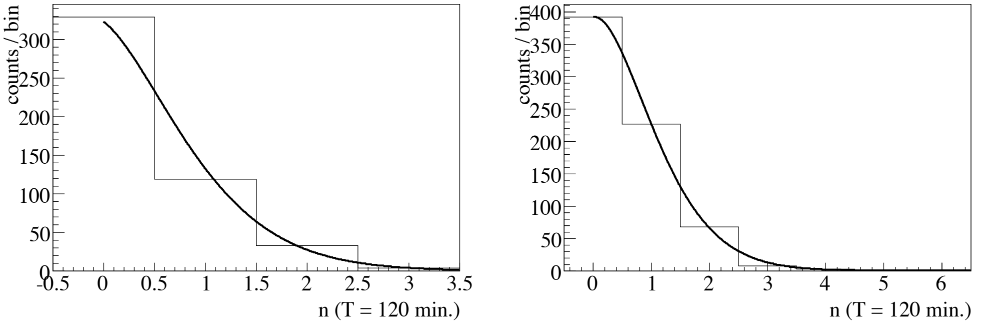

(c) NCD 23.

(d) NCD 37.

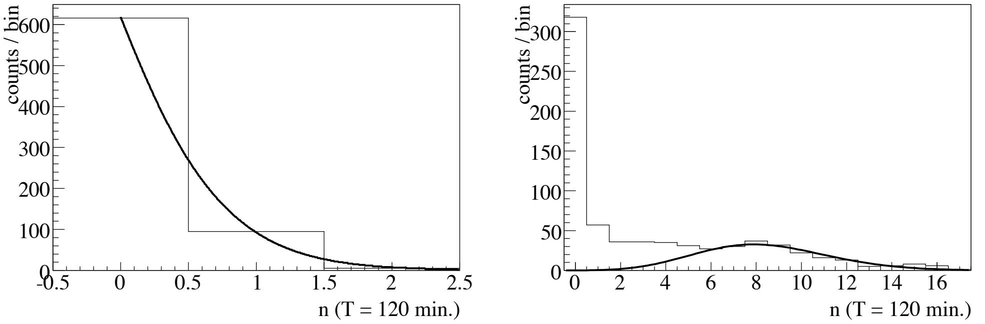

(e) NCD 1.

(f) NCD 31.

Figure 7.12: The distribution of the number of events found in 120-minute bins in the post-NRE data set for NCD strings 7 (a), 21 (b), 23 (c), 37 (d), 1(e) and 31 (f). A maximum likelihood-fit of Eq. 7.1 to the data is shown in each figure. The best-fit curve for NCD 31 is extended out beyond the range (n = 6 - 15) used for finding the best-fit parameters. The results of the fits are found in Table 7.4.

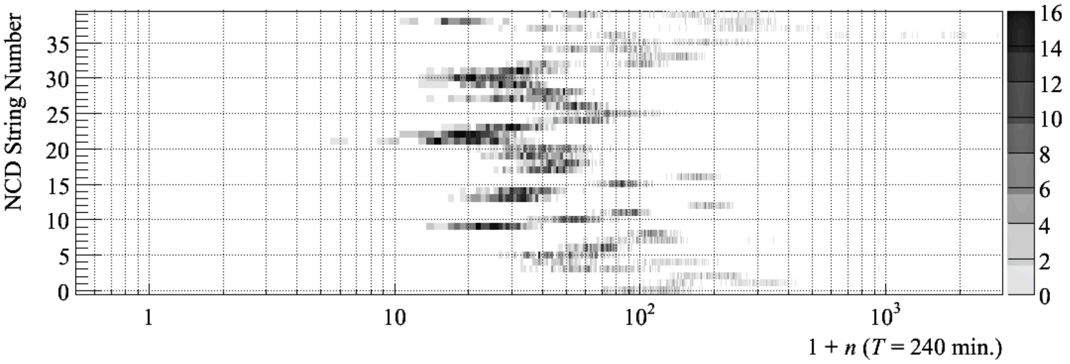

(a) Open Data Set.

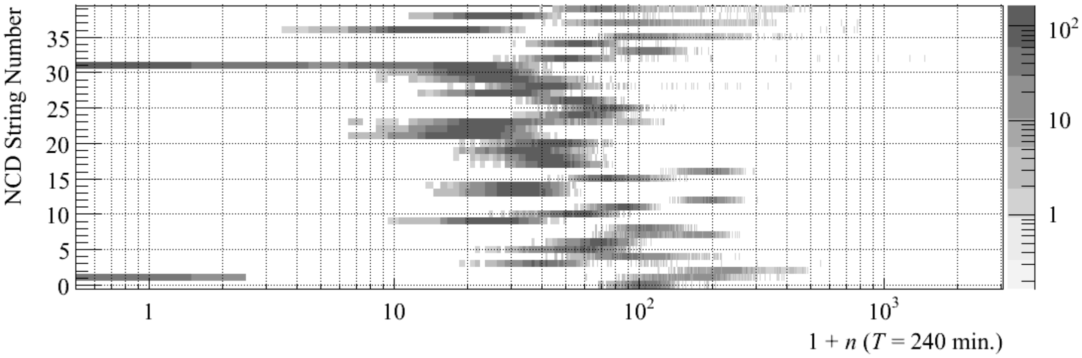

(b) Pre-NRE Data Set.

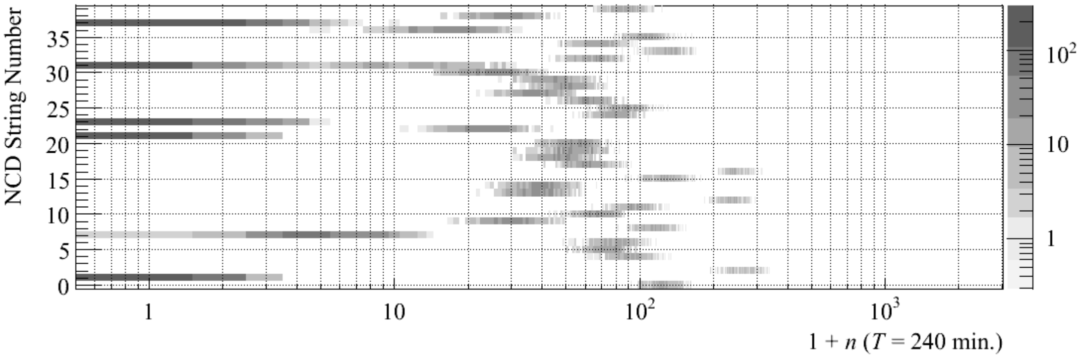

(c) Post-NRE Data Set.

Figure 7.13: The distribution of $1 + n$ for $T = 240$ min. in the open data set (a), pre-NRE data set (b), and the post-NRE data set (c). The distributions are consistent with the distributions for $T = 120$ min. and the conclusion that RCD occurs only on NCDs 1 and 31.

7.8 Estimates and Limits on RCD Dead-time

In this section, the amount of dead-time caused by RCD, T_{RCD}, on NCDs 1 and 31 is calculated. In addition, limits are estimated for the upper limit of T_{RCD} for the other NCDs.

Based upon the logamp calibrations, the NRE calibration and observations of event rates, the resistive coupler on NCD 1 was disconnected for all data taken from run 62276 on May 21, 2006 through the remainder of the NCD phase (from the detector shift logs, the resistive coupler likely disconnected due to a blast or local seismic activity during run 62272). The total live-time of runs from 62276 through the end of the NCD phase is 71.57 ± 0.03 days, which includes all final NCD phase neutrino runs. For NCD 31, the estimate of RCD time was based upon the results of fitting Eq. 7.1 to the distribution of noise events found in $T = 120$ min. bins from the previous section. For both the pre-NRE and post-NRE data sets, the estimate of RCD dead-time for NCD 31 is calculated by finding the excess number of counts in the distribution of n for $n \leq 6$, the value where the histogram and the best-fit Eq. 7.1 coincide. The formula is

$$T_{RCD}^{\text{NCD }31} = T_{live} \frac{1}{N_{120}} \left(\sum_{n=0}^{n=6} O_n - \sum_{n=0}^{6} \hat{A} \frac{\hat{\rho}^n}{n!} e^{-\hat{\rho}} \right) \tag{7.2}$$

where N_{120} is the number of 120-min. bins and T_{live} is the total live-time for the pre-NRE or post-NRE data sets, which includes *all* runs used in the NCD phase flux measurement [75][8]. The estimated amounts of RCD dead-time, T_{RCD}, are given in Table 7.6. It is noted that the estimate of $T_{RCD}^{\text{NCD }31}$ is based upon the assumption that Eq. 7.1 is a reliable model of the data for NCD 31.

The upper limit for T_{RCD} on each NCD is estimated in two ways. In both methods $T_{RCD} < 1/N_{obs}$, where N_{obs} is the number of observations made of the rate of noise events. Assuming that the best-fits of Eq. 7.1 are representative of the data, then

---

[8] These measurements of the live-time do not include DAQ (MUX, shaper/ADC or Oscilloscope) dead-time.

Table 7.6: The estimates of the amount of RCD dead-time for NCDs 1 and 31. For NCD 1, T_{RCD} is equal to the live-time from run 62276 through the end of the NCD phase. For NCD 31, T_{RCD} is estimated from Eq. 7.2. In parenthesis are the fractional RCD dead-times, which are equal to the product of $1/N_{120}$ and the term in parenthesis in Eq. 7.2.

NCD	Pre-NRE T_{RCD} (days)	Post-NRE T_{RCD} (days)	Total (days)
1	12.679 ± 0.005	58.05 ± 0.02	71.57 ± 0.02
31	71.7 ± 3.3 (23.8 ± 1.1 %)	38.8 ± 2.1 (66.8 ± 3.5 %)	110.5 ± 5.3

$N_{obs} = \sum \hat{A}$, where the sum is over the open, pre-NRE and post-NRE data sets. Alternatively, the number of observations is set to $N_{obs} = \sum N_{120}$. In this second method it is assumed that the distribution of noise events would normally follow Eq. 7.1, but includes periods of data with bursts of noise-like events added to the distributions. Or in other words, any noise is good noise and $n \neq 0$ is an observation of a functioning NCD (no RCD). Since there was an observation of $n = 0$ events for the $T = 120$ min. bins on NCD 36, which was consistent with the low average rate of events, the results from the distribution of events with $T = 240$ min. bins is used instead to set an upper limit. The MUX thresholds were increased on NCDs 7, 21, 23 and 37 in the post-NRE data set, resulting in low rates of noise events. For these NCDs only the open and pre-NRE data sets are used to place an upper limit. For NCD 3, only the open and pre-NRE data sets are used since NCD 3 was turned off in the post-NRE data set. The upper limits for T_{RCD}, in percent of the number observations, for $N_{obs} = \sum \hat{A}$ are found in Table 7.7 and for $N_{obs} = \sum N_{120}$ are found in Table 7.8.

Table 7.7: The upper limits (in percentage of the number of 120-min. observations) of RCD dead-time for each NCD estimated from the open, pre-NRE and post-NRE data sets. The number of 120-min observations is set to $N_{obs} = \sum \hat{A}$, where $\hat{A}$ is the best-fit number of observations (Eq. 7.1). *The RCD dead-time for NCDs 1 and 31 are estimated in Table 7.6. **The distribution of n for $T = 240$ min. is used to estimate the upper limit on NCD 36. †Only data from the open and pre-NRE data sets are used to set an upper limit on NCDs 7, 21, 23 and 37.

NCD	$O_{n=0}$	$N_{obs} = \sum \hat{A}$	$T^{\hat{A}}_{RCD}$ (%)	NCD	$O_{n=0}$	$N_{obs} = \sum \hat{A}$	$T^{\hat{A}}_{RCD}$ (%)
0	0	3962	< 0.025	20	0	4533	< 0.022
1	727	1783	$-^{\star}$	21	0	$3882^{\dagger}$	< 0.026
2	0	1679	< 0.060	22	0	4635	< 0.022
3	0	2273	< 0.044	23	0	$2955^{\dagger}$	< 0.034
4	0	2588	< 0.039	24	0	4635	< 0.022
5	0	4548	< 0.022	25	0	4543	< 0.022
6	0	4627	< 0.022	26	0	4635	< 0.022
7	0	$1251^{\dagger}$	< 0.080	27	0	4538	< 0.022
8	0	3014	< 0.033	28	0	4570	< 0.022
9	0	4628	< 0.022	29	0	4185	< 0.024
10	0	4635	< 0.022	30	0	4635	< 0.022
11	0	4635	< 0.022	31	541	3316	$-^{\star}$
12	0	3967	< 0.025	32	0	4171	< 0.024
13	0	4635	< 0.022	33	0	4479	< 0.022
14	0	4634	< 0.022	34	0	4190	< 0.024
15	0	3978	< 0.025	35	0	2647	< 0.038
16	0	3749	< 0.027	$36^{\star\star}$	0	2005	< 0.050
17	0	4635	< 0.022	37	0	$1219^{\dagger}$	< 0.082
18	0	4635	< 0.022	38	0	4630	< 0.023
19	0	4591	< 0.022	39	0	3294	< 0.030

Table 7.8: The upper limits (in percentage of the number of 120-min. observations) of RCD dead-time for each NCD estimated from the open, pre-NRE and post-NRE data sets. The number of 120-min observations is set to $N_{obs} = \sum N_{120}$. *The RCD dead-time for NCDs 1 and 31 are estimated in Table 7.6.**The distribution of n for T = 240 min. is used to estimate the upper limit on NCD 36. †Only data from the open and pre-NRE data sets are used to set an upper limit on NCDs 7, 21, 23 and 37.

NCD	$O_{n=0}$	$N_{obs} = \sum N_{120}$	T_{RCD} (%)	NCD	$O_{n=0}$	$N_{obs} = \sum N_{120}$	T_{RCD} (%)
0	0	4508	< 0.022	20	0	4635	< 0.022
1	727	4635	$-^{\star}$	21	0	$3882^{\dagger}$	< 0.026
2	0	4635	< 0.022	22	0	4635	< 0.022
3	0	2489	< 0.040	23	0	$3882^{\dagger}$	< 0.026
4	0	4635	< 0.022	24	0	4635	< 0.022
5	0	4635	< 0.022	25	0	4635	< 0.022
6	0	4627	< 0.022	26	0	4635	< 0.022
7	0	$3512^{\dagger}$	< 0.028	27	0	4635	< 0.022
8	0	3655	< 0.027	28	0	4635	< 0.022
9	0	4682	< 0.022	29	0	4635	< 0.022
10	0	4635	< 0.022	30	0	4635	< 0.022
11	0	4635	< 0.022	31	541	4635	$-^{\star}$
12	0	4635	< 0.022	32	0	4412	< 0.023
13	0	4635	< 0.022	33	0	4635	< 0.022
14	0	4635	< 0.022	34	0	4380	< 0.023
15	0	4635	< 0.022	35	0	4435	< 0.023
16	0	4635	< 0.022	$36^{\star\star}$	0	2239	< 0.045
17	0	4635	< 0.022	37	0	$3576^{\dagger}$	< 0.028
18	0	4635	< 0.022	38	0	4635	< 0.022
19	0	4635	< 0.022	39	0	4353	< 0.023

7.9 Noise Rate Analysis Conclusions

Baseline noise events are thermal excitations which caused small amplitude current fluctuations that randomly surpassed the MUX threshold on each channel, presumably at a constant average rate. This chapter describes the efforts made to employ these random signals as a tool for integrity tests of each NCD. A set of pulse-shape cuts aimed to select out baseline noise events from other types of instrumental noise events was developed from assumptions about the pulse-shape characteristics of baseline noise events and a set of simulated events. After applying these cuts to the NCD data set, only NCDs 1 and 31 were observed to have instances of anomalously low rates of baseline noise events that were inconsistent with their typical rate of these events. It was also observed that after baseline event selection, the resulting distribution of the number of events, n, in time, T (120 min. and 240 min.), were only sometimes consistent with a Poisson distribution. The source of these non-Poission distributions are speculated to be from an inefficient set of cuts, bursts of small-amplitude micro-discharge events that mimic baseline noise events, small changes in the MUX thresholds caused by drifts in the NCD electronics, or possibly all three.

Nevertheless, the best-fit Poisson distribution for each NCD in the open, pre-NRE, and post-NRE data sets were found, albeit in a subjective manner for those NCDs with clearly non-Poisson distributions. A more objective approach was to observe the occupancy of the $n = 0$ bin in the distributions of n events. From this analysis, NCDs 1, 7, 21, 23, 31, 36 and 37 were observed to have non-zero occupancy of the $n = 0$ bin with an observation time of 120 min. The occupancy of one in the $n = 0$ bin for the distribution of events on NCD 36, however, was consistent with the estimated Poisson distribution of noise events found on that NCD. In the post-NRE data set, the MUX thresholds were increased for NCDs 7, 21, 23 and 37, resulting in a very low rate of noise events that passed the baseline noise selection cuts. Although there was high occupancy of the $n = 0$ bin for these NCDs, the observations were consistent with a Poisson distribution of n for relatively low rates. RCD is not suspected on these NCDs since the NRE calibrations did not reveal RCD nor does the analysis of alpha rates presented in the next chapter indicate any reduction in rate of detected alphas. NCDs 1 and 31 are known to be afflicted with RCD and observation of $n = 0$ was expected.

Finally, estimates on the RCD dead-time for NCDs 1 and 31 (Table 7.6) and upper limits of RCD dead-time for the other NCDs were made. Assuming that the number of observations of Poisson-distributed thermal noise events were accurately measured by the fits to Eq. 7.1, the upper limits are given in Table 7.7. Alternatively, the upper limits on RCD dead-time were made assuming that all observations of a non-zero occupancy of the 120-min. bins were a lack of observation of RCD (Table 7.8). In both cases, the maximum amount of RCD dead-time is less that 0.1%, and typically below 0.03%. Given the expected total systematic uncertainty of the NCD phase to be around 4-6%, the systematic uncertainty due to RCD could be neglected. Alternatively, the upper limit percentages could be included into the NCD-dependent neutron detection efficiencies that are measured by neutron calibrations.

Chapter 8

EXAMINATION OF ALPHA RATES

When an observation is made of events that ought to occur at a constant average rate, a significant dead time on a particular NCD string (perhaps caused by RCD) could be apparent. Assuming that the rate of alpha production in the NCDs is on average constant, a measurement of the average rate of alpha-like events ($E > 1.0$ MeV) may provide sensitivity to any significant gaps in the data. Using the cleaned and blind NCD phase data set[1] the average number of events per day with energy greater than 1.0 MeV was observed over the course of the NCD phase. This chapter will present the fits of these data to a model of a constant event rate. This will show that there are no significant deviations in the rate of alphas in the NCD blind data set except on the few NCDs that were turned off at various times.

First, however, the data set is described and some definitions of SNO-specific terms are given.

NCD Data Set The NCD data set used in the analysis presented in this chapter is different than the data set used in the previous chapter. The data set used in the previous chapter included runs that were removed from the final run list due to various issues (for a partial list of the runs that were removed due to observations of the data during the analysis for this dissertation, see Appendix D). In total there were 41 fewer runs in the alpha rate analysis than used in the previous chapter[2].

As in the previous Chapter, the NCD data set was divided into two time periods –

---

[1] ncd_prod_data_jan05_nov06_v4.root

[2] The data set used here was the 8th version of the NCD phase runlist.

the open and production data sets. The open data set began on November 27, 2004, starting with run number 48220, and ended on January 3, 2005 at run number 48673. Within this time period, 121 runs were identified as valid data runs, after removing all calibration runs and runs taken during detector maintenance. The open data set provided two functions for the SNO collaboration's neutrino flux analysis, which must be mentioned here. First, the data cleaning cuts, which removed instrumental background noise events and selected neutron and alpha events, were developed using the open data set. Second, this data set was used for developing the methods for particle identification and for the initial measurements of ^{238}U and ^{232}Th contamination. The production data set, began on January 4, 2005 with run number 50023 and ended on September 31, 2006 at run number 66489. Within this data set, there were 1834 valid data runs that were used for neutrino analysis. The total live-time of the production data set (before DAQ dead-time corrections) was 359.47 ± 0.13 days [75]. This analysis of the constant rate of alphas used the production data set.

Data Cleaning The term "data cleaning" refers to the set of algorithms used to remove instrumental events from the NCD data set. The data cleaning algorithms examined the time-domain characteristics and power spectra of each digitized waveform and selected good "physics" events (neutrons and alphas) by removing events that did not conform to a certain set of measured and calculated parameters. The data cleaning algorithms were developed using the open data set and neutron calibrations and then applied to the full production NCD data set. When an event was identified by one of the data cleaning algorithms, a particular bit was set on one of two 32-bit words, the DAMN (Data Analysis Mask Number) bank or the DAMN1 bank. Events were not actually removed from the data set, but were instead flagged by setting the appropriate bits. Thus, in order to find all non-instrumental events, one would scan the data set and analyze the events where all of the DAMN and DAMN1 data cleaning bits are set to false. Some data cleaning cuts also included the flagging of all events within a defined time span from the onset of a particular type of event. For example, for each muon detected by the SNO PMT system, the subsequent 20 seconds and 60 seconds were flagged by setting two particular DAMN bits. Such data cleaning cuts flag all subsequent event triggers after a particular type of instrumental background event, even when the events are valid physics events. The amount of detector live-time removed by these types of data cleaning algorithms was measured and stored in the SNO database RLDT bank.

Wilkerson-Elliott Blindness Because of the small neutrino event rate, the significant impact of SNO's solar neutrino flux measurement on our understanding of neutrino physics, and the past controversies and doubts about the measurements of the solar neutrino flux, care was taken to remove bias from the the analysis of SNO data. To accomplish this, the Wilkerson-Elliott Blindness scheme (WE blindness), named after those who created it, was developed to randomly remove a fraction of events in the production data set. This fraction was unknown to the analysts working on SNO/NCD data. In addition, a fraction of events following the identification of a muon was added back into the data set. Muons produce spallation neutrons that are indistinguishable to neutrons produced by neutrino interactions. Adding a fraction of the "muon-follower" neutrons, unknown to the analysts of the NCD phase data, enhances the blindness scheme. Overall, blindess reduced the number of non-instrumental events available for analysis in the production data set by somewhere between 15% and 40%. The blindness fractions are only known to one person in the SNO collaboration, who did not participate directly in the neutrino data analysis. Implementation of the WE blindness was applied by setting an event-dependent bit (WE blindess bit) in the DAMN bank. Because of the simplicity, however, it is also relatively easy to undo by ignoring the WE blindess bit. Every member of the collaboration is ethically bound to adhere to blindness until the data is "unblinded", which occurs when the collaboration believes all of the analysis procedures are complete. The blindness scheme allows analysts to develop algorithms and techniques for measuring neutron rates and the neutrino flux without knowing the final flux results.

Blindness was only imposed on the production data set. The DAMN banks for the open data set were set by the data cleaning algorithms, but the WE blindness scheme was not applied and all muon-follower events were appropriately flagged and could be removed by the analyst. The open data set was utilized by Stonehill to make the first *in-situ* measurements of the ^{238}U and ^{232}Th contamination [52]. The low statistics of the open data set limits the precision of any neutrino flux measurement using this data. However, because the rate of alphas was much greater, the measurements of alpha rates made by Stonehill were not statistically limited. Thus, if one were to compare the measured alpha rates in the open data set with the measured rates of the "blind" data set, the overall blindness fraction could be determined. The following analysis conceals this blind fraction by not presenting any of the measured rates of events determined within the analysis algorithms. Only the blind-production data set is used in this analysis. The WE blindness scheme was not imposed upon the NCDs that were filled with ^{4}He (NCD 3, 10, 20, and 30) and the measured rate of events on these detectors are presented.

8.1 Expected Rate of Alphas Through NCD Phase

In order to use the rate of alpha events in the NCDs as a test of their integrity, it should be verified that the expected rate of alphas during the NCD phase is relatively constant. The rate of alpha events during the NCD phase expected in an "average" 10-m NCD string is developed here and is based upon the previous measurements [52]. This calculation serves as an argument for the plausibility of assuming a model of a constant rate of alphas, which will later be tested in this chapter.

There were two categories of alpha events in the NCDs – bulk alphas from nuclei within the ^{238}U and ^{232}Th decay chains, and surface alphas from ^{210}Po. It is possible that the decay chains were not in equilibrium, due to the CVD process of purifying the nickel bodies of the NCDs. This process is likely to preferentially remove Ra, breaking the ^{238}U chain at ^{226}Ra, and the ^{232}Th chain at ^{224}Ra and ^{228}Ra (Fig. 3.4) [47, 52]. Also, the half-life of ^{210}Po is 138 days, but it was likely to be supported by ^{210}Pb, which beta-decays to ^{210}Po with a half-life of 22.3 years. Polonium and lead were plated onto the NCD bodies when they were stored in an underground, radon-rich environment, though the majority of that contamination was removed [50, 48]. While the NCDs were exposed to radon, this gas would have been purged during the filling of the counters and any remaining amounts that were not in equilibrium with the decay-chains would have decayed away rapidly. Overall, alpha rates may have increased over the course of the NCD phase by the re-population of nuclei within the ^{238}U and ^{232}Th decay chains, or they may have decreased due to the decay of ^{210}Pb on the inner surface of the NCD.

The ^{238}U chain contains the nucleus ^{226}Ra, which has a half-life of 1600 years. In the disequilibrium scenario stated above, the rate of alphas from the ^{238}U chain will be nearly constant, given the measured level of ^{238}U. The relatively long-lived ^{210}Pb decays away with a 22.3-year half-life, while the number of ^{226}Ra nuclei will build up slowly.

If Ra is removed, there will be a change in the rate of alphas emitted from the ^{232}Th chain over the eight year period from the construction of the NCD bodies to the end of the NCD phase at SNO. The rate of alphas from the lower part of this chain will decay with the 1.9-year half-life of ^{228}Th, but then slowly recover as the amount of ^{228}Ra nuclei build back up. The recovery of ^{228}Ra is governed by its 5.75-year half-life.

Due to this preferential removal of Ra, a lower decay chain and an upper decay chain may be defined for each of the ^{232}U and ^{228}Th decay chains[3]. The upper decay chain alpha emitters of the ^{238}U chain are all nuclear isotopes with an atomic number

---

[3] These lower and upper chain defintions were used by Stonehill in the measurements of the U/Th contamination.

greater than 226. The upper decay chain of the ^{232}Th chain is only the ^{232}Th nucleus. Both lower decay chains contain five alpha emitters.

A calculation of the rate of alphas during the NCD phase can be made by using the generalized Bateman equation to estimate the number of nuclei within a decay chain with multiple nuclei [85]. The number of nuclei as a function of time, $N_i(t)$, is given by

$$N_i(t) = N_{i0}e^{-\lambda_i t} + \sum_{m=1}^{i-1} N_{m0} \prod_{q=m}^{i-1} \lambda_q \sum_{k=m}^{i} \frac{e^{-\lambda_k t}}{\prod_{j=m(j\neq k)}^{i}(\lambda_j - \lambda_k)} \tag{8.1}$$

where N_{i0} is the number of nuclei at time t=0 and λ_i is the decay rate for the ith nucleus. For this expression, $i = 1$ refers to the parent nucleus of the decay-chain – either ^{238}U or ^{232}Th. The average number of alpha events emitted from each decay chain is estimated by summing the products $N_i(t)\lambda_i$ for each alpha emitter in the chain.

In this calculation it was assumed that the U and Th chains were in equilibrium at the time of the CVD production ($t = 0$) of the nickel bodies, but that all Ra atoms were removed from the nickel. The vast majority of the nickel bodies were produced between March 1996 and June 1997 and the NCD open data set began in December 2004. Thus, the CVD production occurred approximately 8 years before the beginning of the open and commissioning data sets ($t = 8$ years). The amounts of U, Th, and Pb/Po at $t = 0$ years required to reproduce the measured rate of events in an average 10-m NCD during the open data set ($t = 8$ years) were calculated (Table 8.1).

Since the alpha detection efficiency for each nucleas in the decay chain was not reported by Stonehill, the detection efficiency for alphas from the lower decay chains of U and Th used in this calculation was approximated by dividing the detection efficiency for each lower decay chain, which was reported, by the number of alpha emitters in each lower chain (five). For the lower U chain, the number of alphas detected with an energy greater than 1.0 MeV for a single lower chain decay progression

Table 8.1: The measured amount of the lower decay chain event rate equivalent of ^{238}U and ^{232}Th, the rate of alphas from surface ^{210}Po, the upper U/Th decay chains (Table 7.5 in [52]) and the equivalent contamination levels and alpha rates for a 10-m (A = 1.596 m^2) NCD at $t = 0$ years. The amount of ^{238}U and ^{232}Th here is the amount within 22 μm from the surface of the inner NCD wall.

	Measured [52]	10-m NCD ($t = 0$ years)
Lower chain ^{238}U	$2.8^{+0.6}_{-0.8}$ ppt	875^{+187}_{-250} pg
Lower chain ^{232}Th	$5.7^{+1.0}_{-0.9}$ ppt	1782^{+312}_{-281} pg
Surface ^{210}Po rate	1.80 ± 0.03 α / m$^2\cdot$ day	3.68 ± 0.06 α / day
Upper U/Th rate	$1.00^{+0.06}_{-0.03}$ α / m$^2\cdot$ day	$1.60^{+0.10}_{-0.05}$ α / day

was 0.559. Similarly, for the lower Th chain, the number of alphas detected above 1.0 MeV was reported to be 0.624. In the calculations presented here, the average detection efficiencies for an alpha emitted in the lower decay chains were 0.112 and 0.125 for the U and Th chain, respectively.

The detected rates of alphas, rather than the actual rate of alphas emitted by ^{210}Po, were measured and reported by Stonehill. Thus, the amount of Po/Pb on the inner surface of the NCD in this calculation was determined from the secular equilibrium relation $r^{Po}_{10\,\mathrm{m}} = \lambda_{Po}N_{Po}(t = 8) = \lambda_{Pb}N_{Pb}(t = 8)$, where $r^{Po}_{10\,\mathrm{m}}$ is the expected rate of alphas from ^{210}Po for a 10-m NCD based upon the measured rate of 1.8 ± 0.03 α/m$^2\cdot$ day. For a 10-m NCD, this is $r^{Po}_{10\,\mathrm{m}} = 2.87 \pm 0.05$ α/day. Since the level of Pb/Po is calculated here from the *measured* rate of Po, there is no concern for estimating the detection efficiency for ^{210}Po-alphas. The amount of Pb/Po on the surface of the NCD in this calculation is the *effective* amount. The detected rate of alphas from the upper U/Th chains was also reported (1.0 α/m$^2\cdot$ day) and a similar procedure was done to determine the appropriate number of nuclei in the upper chains [52]. Similar to the Pb/Po calculations, the *effective* amounts of upper chain U/Th nuclei were determined.

Based upon the description above, the average rate of alphas detectable in a 10-m NCD from the CVD production time to beyond the NCD phase is calculated using ROOT's implementation of the Bateman equations and is shown in Fig. 8.1.

It should be noted that the measured average rate of alphas from ^{210}Po was dominated by a high level of contamination on NCD 10. Thus, for most NCDs the rate will be less than what is shown here. Also, it would be reasonable to believe that the change in rates for many NCDs will be less than the $\sim$ -0.2 α / day during the entire 2-year NCD phase epoch shown in Fig. 8.1, and smaller than the uncertainty of the rate. Disregarding NCD 10, which has a high level of Pb/Po contamination, the average rate of alphas from Pb/Po are reduced by about 10%. Furthermore, because not all NCDs were exposed to the Rn gas, the contamination level of Pb/Po is expected to vary between the NCDs more than the contamination level of U/Th, which is inherent to the construction process of all NCDs. It is shown by this calculation, that the rate of alphas during the NCD phase, under the assumption of the Ra-breaking disequilibrium scenario, should remain relatively constant except for the possibility of a very small change in rate due to the decay of ^{210}Pb and the re-population of the ^{232}Th chain. It will be shown in the analysis of the next sections that the observed rate of alphas above 1.0 MeV in the NCD phase is consistent with a model of a constant rate.

8.2 Binned Average Rates

Letting the rate of alphas serve as a constant source of events that behave in a relatively predictable way, the rate of alphas on each NCD can be tested for significant decreases. However, because the rate of alphas on a 10-m NCD string, based on the measurements in the open data set, is expected to be about 5.36 alphas/day, this test only has a sensitivity to dead-times that last on the order of days. For example, if

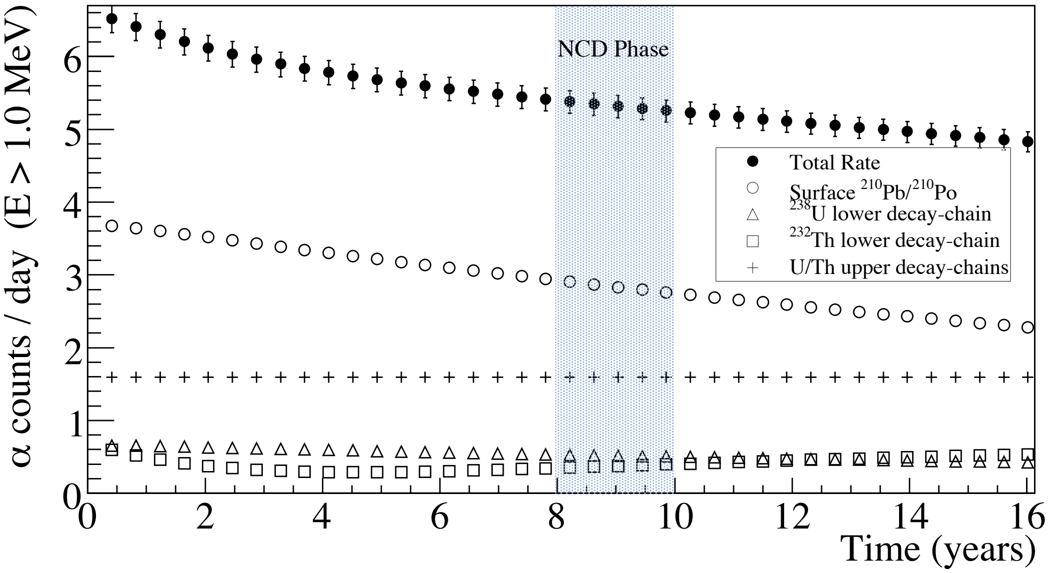

Figure 8.1: Estimated number of alpha events per day for a 10-m NCD string assuming average levels of ^{238}U, ^{232}Th and ^{210}Po measured in [52], and assuming that all Ra was removed from the NCDs in the CVD process. The time-span begins with the CVD-production of the NCD nickel bodies and the blue vertical band represents the epoch of the NCD phase. The levels of Pb/Po in the NCDs vary considerably and will be the dominant source of measurable change in the rate of alpha events. Although, it should be pointed out that the average levels of Pb/Po are influenced by the high rate observed on NCD 10 [52]. Disregarding NCD 10, the average rate of alphas from Pb/Po are reduced by about 10%.

the average rate of alphas is 5 per day and the number of alphas is observed over a 20-day period, the expected number of events would be 100 ± 10. To see a 4σ-effect, at most 60 alphas could be observed. This would suggest a dead-time of up to 8 days, and at minimum a dead-time of 2 days (assuming that a 3σ deviation from 100 events is due to statistical fluctuation). If the observed rate of alphas is larger than 60, it would be impossible to distinguish between a loss in live-time and a normal statistical fluctuation. It should also be noted that if RCD or any other string malfunction behaved like a random process (disconnecting and reconnecting randomly), and that the amount of "dead-time" produced by this process was not too great, it will not be possible to observe with this method. A randomly occurring dead-time would be observed simply as a reduced event rate. However, there is a limit to how great this dead-time could be. If the random dead-time were great enough, then the measured rate would be significantly smaller than the expected rate of alphas from U and Th contamination at the 1 ppt level and significantly smaller than the measured rates from the open plus commissioning data sets [52], and would thus be observable.

Also due to the low rate, the blind-production data set must be appropriately binned to obtain sufficient statistics. The easiest way to bin the data set is to create groups of runs, rather than bins of equal time lengths[4]. The number of expected alpha events on each NCD was used as a guide for determining an appropriate number of runs for each bin in the analysis. The size of the groups should be as small as possible in order to observe significant deviations in rate of alphas, but must be large enough to have sufficient statistics per group for all NCDs. The average number of alpha events for each NCD string was measured using the open and commissioning data sets and is summarized in Table 8.2. It should be noted that the rates given in Table 8.2 are estimates for the rate of alpha events across the entire energy spectrum.

---

[4] However, this results in nearly equal bin sizes.

Table 8.2: The estimated rate of alphas/m^2·day in the open plus commissioning data sets for the full energy range. The uncertainties in these measurements are not included in this table, but are found in the Table B.1 on page 212 in [52]. The rates in this table are the summed rates from the different alpha sources, as found in the referred Table B.1. From data in this table, the average rate is 4.02 alphas/m^2·day, which is heavily influenced by the rates on NCD 10.

NCD	α/m^2·day	NCD		NCD		NCD	
0	2.96	10	24.3	20	6.49	30	4.60
1	1.20	11	1.95	21	3.34	31	6.77
2	4.21	12	8.63	22	1.49	32	5.24
3	4.13	13	1.97	23	5.26	33	1.84
4	4.56	14	1.52	24	2.72	34	4.84
5	1.97	15	1.40	25	4.91	35	4.23
6	1.49	16	5.55	26	1.89	36	1.26
7	1.35	17	4.22	27	1.63	37	3.67
8	2.56	18	7.95	28	1.37	38	2.55
9	4.82	19	3.99	29	2.58	39	3.51

Approximately 90% of these alpha events will be above 1 MeV. According to this data, the string with the lowest rate of alpha events per day should be NCD string 36, which is a 9-m string with an average alpha rate of 1.63 events per day.

A histogram of the run-time (in hours) for each run in the production data is shown in Fig. 8.2. The average length of all the runs is 4.79 hours. The average number of events for NCD string 36 was used as an estimate to find the smallest number of runs per group with sufficient statistics (Table 8.3).

Because of the time-correlated production of alphas within the U and Th decay

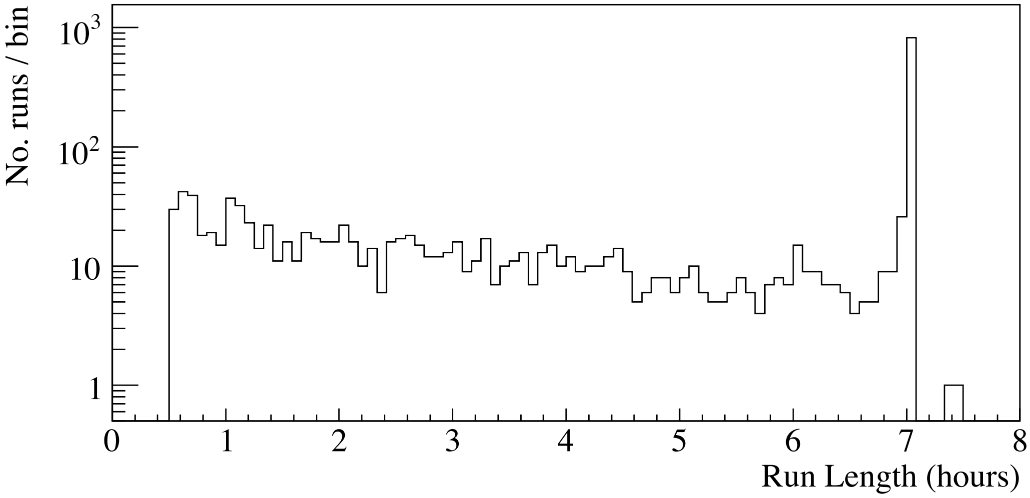

Figure 8.2: A histogram of the number of hours in length for each run in the NCD production data set.

Table 8.3: Estimated number of alpha events on NCD string 36 for different sizes of groups of runs. In the table are the number of live-days per group, T_{group}, the number detected alphas, N_{α}, number of detected alphas with energy greater than 1 MeV, $N_{E>1.0}$, an approximate number of events after blindess is imposed, N_{Blind}, and the standard deviation σ. In these estimates, the average run time was 4.79 hours, and it was assumed that 90% of alphas are measured to have $E\ > 1.0$ MeV, the blind fraction was approximated to be 30%, and $k = 1.036 \pm 0.012$ (§ 8.4)

No.runs/group	T_{group}	N_{α}	$N_{E>1.0}$	N_{Blind}	$\sigma = k \cdot \sqrt{N_{Blind}}$
50	10.0	16.3	14.6	10.2	3.3
100	20.0	32.5	29.3	20.5	4.7
150	29.9	48.8	43.9	30.7	5.7
200	39.9	65.0	58.5	41.0	6.6
250	49.9	81.3	73.8	51.2	7.8

chains, the variation in the number of alphas per day will be slightly greater than $\sqrt{N_{Blind}}$ [86, 87, 88, 89]. The factor k in Table 8.3 represents the ratio of the standard deviation of the number of events, σ, to the standard deviation of a purely Poisson process, $\sqrt{N}$:

$$\sigma = k \cdot \sqrt{N} \tag{8.2}$$

A Monte Carlo study, discussed later in § 8.4, was constructed to determine k accurately for the case of the NCDs. The factor k depends upon the relative rate of time-correlated alphas to the rate of the uncorrelated alpha events. For the average 10-m NCD, the ratio was determined to be $k = 1.036 \pm 0.012$. To ensure sufficient statistics for all NCD strings, the grouping size of 100 runs per group is used for the following alpha rate measurements, which gives a sensitivity to a change in the rate of at least 4.7 σ for each NCD.

8.3 Alpha Rate Model

A model for the number of alphas measured in a particular NCD string with energies above 1.0 MeV to be compared against the measured number of alphas in each group of runs, is constructed as follows. The measured rate of alphas[5] from the bulk contamination of U, Th and their progeny is considered to be constant, $R_o^{\mathrm{U,Th}}$, throughout the NCD data. The only long-term variation in the rate of alphas in this model may be due to the decay of ^{210}Pb. For each run, r, the number of alphas detected, N_r, is

$$N_r = R_o^{\mathrm{U,Th}}(t_{r,f} - t_{r,i}) f_r + \int_{t_{r,i}}^{t_{r,f}} R^{\mathrm{Po}}(t) f_r dt \tag{8.3}$$

where $R^{\mathrm{Po}}(t)$ is the measured rate of alphas emitted by ^{210}Po, f_r is the fractional live-time for run r, and $t_{r,i}$ ($t_{r,f}$) is the start (end) time of the run. For each group of runs, labeled by the index g, the number of measured alphas, N_g, is given by

$$N_g = \sum_r N_r = \sum_r R_o^{\mathrm{U,Th}} T_r f_r + R_o^{\mathrm{Po}} \frac{f_r}{\lambda_{\mathrm{Pb}}} \left(e^{-\lambda_{\mathrm{Pb}} t_{r,i}} - e^{-\lambda_{\mathrm{Pb}} t_{r,f}} \right) \tag{8.4}$$

---

[5] The measured rate is equal to the real rate of alphas times the detection efficiency.

where the substitution $T_r = (t_{r,f} - t_{r,i})$ was made, R_o^{Po} is the initial rate of alphas from the decay of ^{210}Po in the open data set, $\lambda_{\mathrm{Pb}} = \ln 2/(22.3 \text{ years})$ is the decay-rate of ^{210}Pb, and $R^{\mathrm{Po}}(t) = R_o^{\mathrm{Po}} e^{-\lambda_{\mathrm{Pb}} t}$ was used to evaluate the integral. Alternatively, the measured rate of alphas per day for each group of runs, R_g, is

$$R_g = \frac{N_g}{\sum_r T_r f_r} = R_o^{\mathrm{U,Th}} + R_o^{\mathrm{Po}} \frac{\sum_r f_r/\lambda_{\mathrm{Pb}} \left(e^{-\lambda_{\mathrm{Pb}} t_{r,i}} - e^{-\lambda_{\mathrm{Pb}} t_{r,f}}\right)}{\sum_r T_r f_r} \tag{8.5}$$

The fractional live-time, f_r, start time, $t_{r,i}$, and end time, $t_{r,f}$, for each run was obtained from the SNO detector status database[6]. The live-time of each run measured by the NCD Trigger Card's 10 MHz clock and the total dead time due to data-cleaning cuts (this does not include NCD hardware dead times, which have yet to be calculated), were compiled. For each NCD string, the number of events with energy greater than 1.0 MeV was counted for each group. The width of each bin in the histogram was unique, due to the unequal amount of live-time in each group. Also, a separate histogram was created that held the measured number of counts per live-time of each group.

Because of the relatively slow decay of ^{210}Pb and the relatively similar rate of alphas from the U,Th decay chains and from ^{210}Po, a sufficient model for many of the NCD strings is simply a constant rate of alphas. This makes it impossible for fitting routines to differentiate between bulk alphas from the U, and Th decay-chains and surface alphas from ^{210}Po decays, when looking strictly at the rate of events, as was done here. Due to this, the average rate of events in each group was approximated to be just a constant

$$N_g = \sum_r R_o T_r f_r \tag{8.6}$$

$$R_g = \frac{N_g}{\sum_r T_r f_r} = R_o \tag{8.7}$$

For each NCD string, the data were fit to Eq. 8.6/8.7 (Fig.8.3)

---

[6] The RLDT bank, a component of the SNO detector status database, was used.

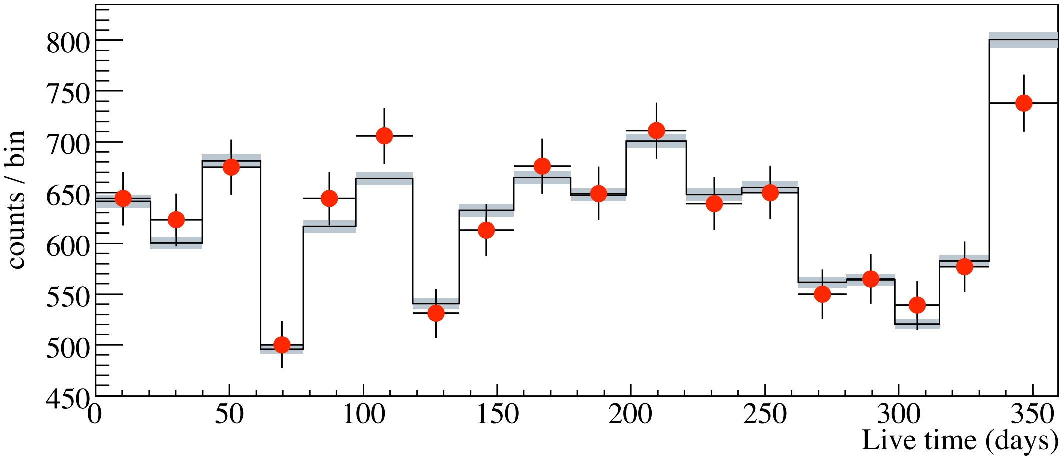

(a) Total counts per group of runs.

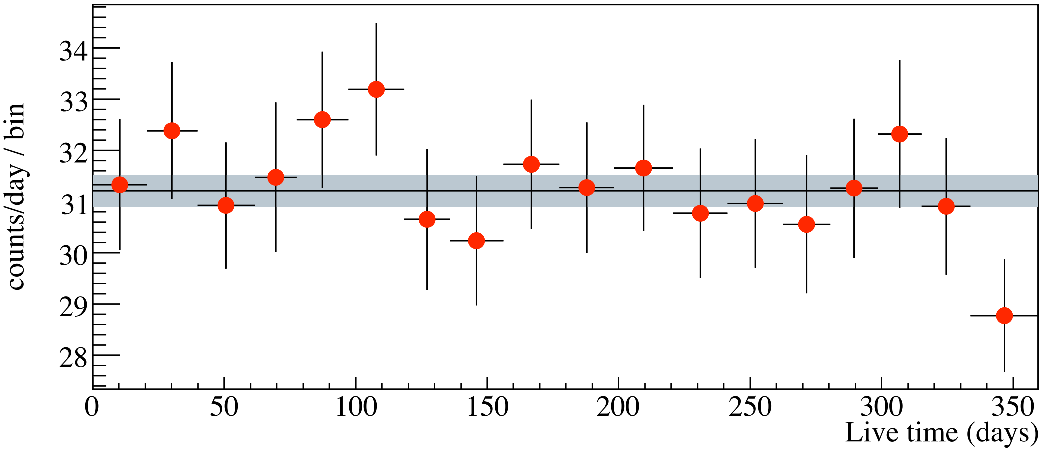

(b) Average rate per group of runs.

Figure 8.3: Events with E > 1.0 MeV on NCD string 10 are shown for each group (a), and shown as events per day for each group (b) with statistical error bars. Also shown are the results from fitting to Eq. 8.6/8.7, where the grey box indicates the uncertainty of the best-fit value. In this fit, $\chi^2/\mathrm{dof} = 11.34/17$, and $R_o = 31.2 \pm 0.3\ \alpha/\mathrm{day}$. There were 1834 runs in the production data set grouped into 17 groups of 100 runs and a final group of 134 runs. Blindess was not imposed upon NCD string 10 because it was filled with ^{4}He.

8.4 *Alpha Rate Monte Carlo*

The purpose of the Monte Carlo study was to determine the properties of the statistical fluctuation of the number of alphas emitted in the NCDs. Specifically, the goal was to measure the increase in the standard deviation of the number of events in a 20-day bin caused by the time-correlated alpha decays in the U and Th decay chains. The distribution of the number of events in the Monte Carlo was also useful for interpreting the measured distribution of the number of alphas in the NCD phase.

This Monte Carlo simulation has three components – the NCD detector geometry, the specific energy loss of alphas in nickel and the NCD gas, and the decay rates of the nuclei in the U and Th chains. The NCD detector geometry was a reproduction of the geometric configuration previously developed [52]. The specific energy loss for energetic particles traversing a medium is qualitatively described by the Bethe-Bloche formula (Eq. 3.3), but has been more precisely calculated using the SRIM code [55] (Fig. 3.6). The tables of data from SRIM are the same tables used in SNO's Monte Carlo and Analysis program (SNOMAN). The rate of decays were set to reproduce the previously measured rates during the NCD open data set.

There are four steps to the Monte Carlo. First, the rate of alphas from the decay-chains were randomly generated according to the amount of material in a 10-m NCD and the respective decay rates[7]. Second, the initial depth of the parent nucleus within 22 μm and the direction of the alphas were randomly generated. The depth of 22 μm is the maximum distance an alpha particle generated in the Th chain may propagate in nickel and was the depth of contamination assumed in Stonehill's measurements. Then, using SRIM tables for alpha propagation in nickel and the direction of propagation of each alpha, it was determined whether each alpha reached the NCD gas volume. (In this simple Monte Carlo, the NCDs did not have end-

---

[7] Only a 10-m NCD is considered, which is shown to be okay because k only depends upon the relative amount of Po, U and Th and not on the absolute level (Table 8.4) for contamination levels on the order found in the NCDs.

caps for the alphas to run into. The effect of this omission should, however, be small.) Next, using SRIM tables for alpha propagation in the NCD gas, the amount of energy deposited in the detector was determined. The amount of energy detected could be less than the energy of the alpha when it entered the NCD gas volume if the alpha particle subsequently reached the NCD wall before depositing all of its kinetic energy. Finally, the detected energy of the event was smeared by a gaussian-distributed detector resolution of 2%. The effects of space-charge distortions on the energy spectrum were not considered in this Monte Carlo because only the number of alphas with energy above 1.0 MeV were of concern and not the shape of the energy spectrum. Space-charge effects only slightly decrease the overall rate of events above 1.0 MeV.

The time range of each Monte Carlo production of alphas in a 10-m NCD started at the CVD production time ($t = 0$ years) and progressed beyond the NCD phase to $t = 11$ years[8]. The number of total alphas detected with energies above 1.0 MeV were stored in 20-day bins. Within the NCD epoch ($t = 8 - 10$ years) there were 36 20-day bins, labeled by the index j. There were 5000 ensembles of the 11-year simulation, labeled by the index i. The number of alphas produced in the jth bin of the ith ensemble is labeled N_{ij}. An example of a single Monte Carlo ensemble and the average rate from 5000 Monte Carlo ensembles is shown in Fig. 8.4

As mentioned, due to the time-correlated production of alphas in the lower U and Th decay chains, the uncertainty of the number of alphas detected in a 20-day bin is greater than the usual estimate, $\sqrt{N_{ij}}$. The deviation of the uncertainty from $\sqrt{N_{ij}}$ can be determined by an analysis of the 5000 ensembles. The distribution of the total number of detected alphas, N_{ij}, in the 5000 Monte Carlo ensembles is shown in Fig. 8.5(a) (note that this figure shows the total number of events per 20-day bin instead of the average rate). For the distribution of events in each of the 20-day bins

---

[8] Many thanks to Brent VanDevender for a significant amount help in developing this Monte Carlo code.

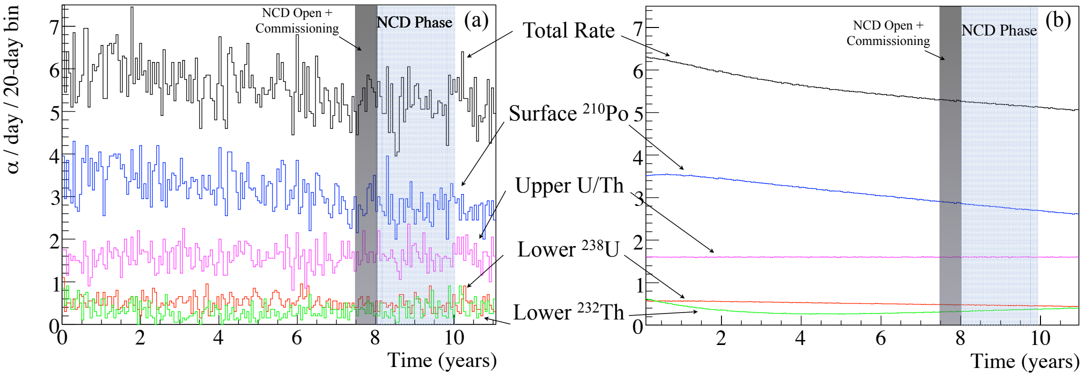

Figure 8.4: For the average rate of alphas on a 10-m NCD, shown here are (a) a single Monte Carlo ensemble and (b) the average of 5000 ensembles. Each alpha source is labeled as well as the NCD open + commissioning data and NCD production data epochs.

(Fig. 8.5(b)), the variance is estimated in the usual way

$$\sigma_j^2 = \frac{1}{n-1}\sum_{i=1}^{n}(N_{ij} - \bar{N}_j)^2 \tag{8.8}$$

where $\bar{N}_j$ is the mean of the 5000 ensembles in the jth 20-day bin. The value of k_j is the ratio of $\sigma_j/\sqrt{\bar{N}_j}$ for each 20-day distribution. There are 36 20-day bins where k_j is measured (Fig. 8.6). For the average 10-m NCD, the average measured value is $k = \bar{k}_j = 1.036 \pm 0.012$. If all of the alphas were uncorrelated, the expected value for k would be 1.0.

The values of k were measured for different scenarios of total alpha rate and relatively different rates of time-correlated and uncorrelated alphas. To vary the rate of the uncorrelated alphas, the amount of ^{238}U and ^{232}Th used to generate the upper decay chains were varied. For each scenario, 5000 Monte Carlo ensembles were generated and the same procedure outlined above was used to measure k. The different measured values for k for each of the scenarios tested are listed in Table 8.4, along with the relative rate of alphas from each source compared to the average rate.

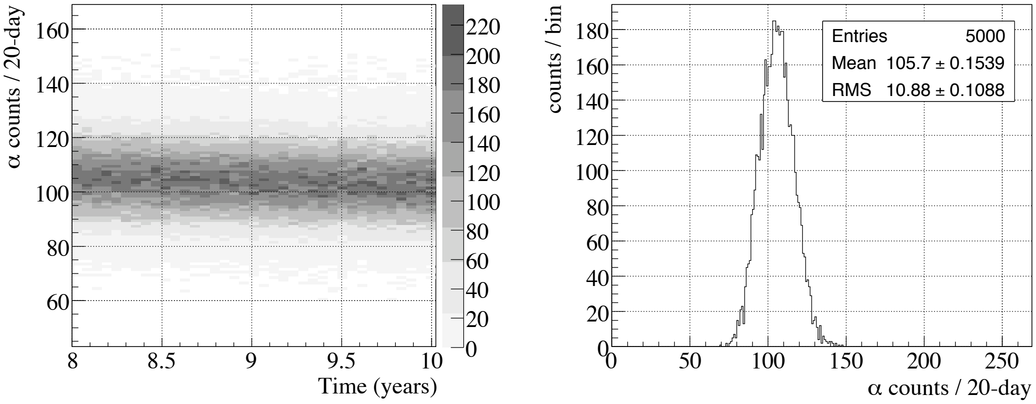

(a) N_{ij} (b) $N_{ij=1}$

Figure 8.5: The (a) distribution of N_{ij} and (b) $N_{ij=1}$ for the NCD epoch from the 5000 Monte Carlo ensembles. For the distribution in (b), the measured value for k_1 is 1.058.

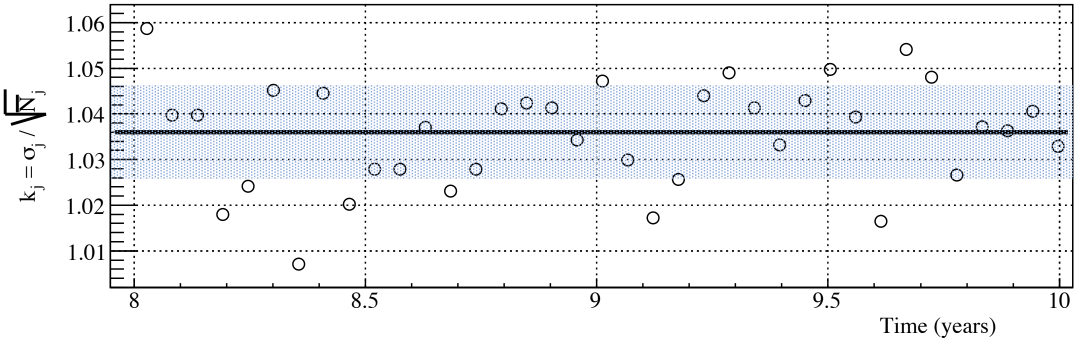

Figure 8.6: The 36 measured values of k_j for the scenario with average level of alphas. The horizontal black line indicates the average value of 1.036 and the blue band is the standard deviation of the measured values, 0.012.

Table 8.4: The calculated values of k for Monte Carlos with different rates of alphas from the various sources. Shown here are the rate of alphas from the various sources relative to the measured average rates. † Due to computational time-constraints only 2000 Monte Carlo ensembles were generated for these scenarios.

k	^{210}Po	^{238}U lower chain	^{232}Th lower chain	upper U/Th
1.036 ± 0.012	1.0	1.0	1.0	1.0
0.997 ± 0.011	1.0	0.0	0.0	1.0
1.074 ± 0.010	0.0	1.0	1.0	1.0
1.037 ± 0.011	0.9	1.0	1.0	1.0
1.037 ± 0.016 †	2.0	2.0	2.0	2.0
1.034 ± 0.015 †	5.0	5.0	5.0	5.0
1.035 ± 0.015 †	10.0	10.0	10.0	10.0

It is noted that for the scenario with the amount of lower chain ^{238}U and ^{232}Th set to zero, the value of k was measured to be 0.997 ± 0.011, consistent with the expected value of 1.0.

Finally, for each of the 5000 ensembles, the average number of events in each of the 20-day bins was found, $\bar{N}_i$. For each of the 20-day bins in each ensemble, the pull, $p_{ij} = (N_{ij} - \bar{N}_i)/k\sqrt{N_{ij}}$, was measured. The 5000 × 36 measurements of p_{ij} are shown in a histogram in Fig. 8.7. It is noted that this distribution of p_{ij} does not follow a normal gaussian distribution with a mean of zero and standard deviation of one. The skewness of the distribution is also non-zero and found to be -0.176 ± 0.077. Furthermore, there is an increase in the tendency to find a particular N_{ij} more than three standard deviations below the mean than would normally be found. These observations will be useful when examining these same distributions for the NCD data.

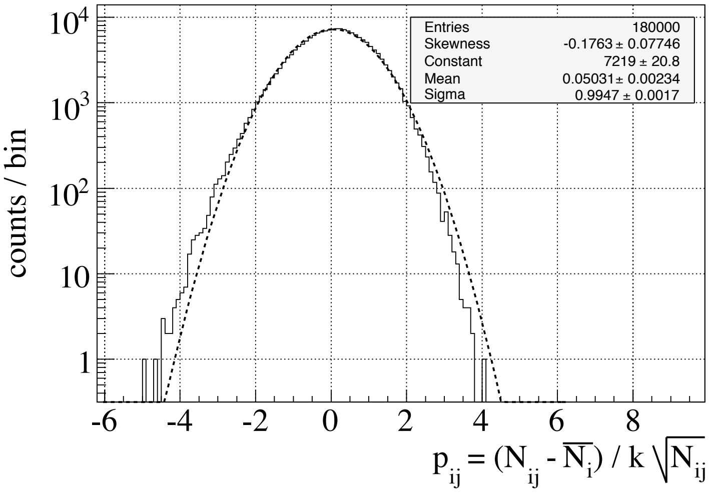

Figure 8.7: The distribution of the measured pulls, p_{ij}, from the 5000 Monte Carlo ensembles. This distribution is not a normal gaussian, as shown by the dashed line. The vertical axis is on a log-scale to better show the deviation from a normal gaussian distribution.

8.5 Constant Rate Fits to NCD Data

For each NCD, the number of non-instrumental events with energy above 1.0 MeV, which should consist entirely of alphas, was measured for each group of 100 runs and placed in a histogram. Each group of 100 runs spanned approximately 20 live-days and approximately 360 live-days in total over the entire data set.

The results from the fit to a constant rate (a χ^2-minimization routine) and a summary of strings that exhibit anomalous rates of alphas are presented in this section. Due to restrictions from blindness, however, the measured rates of events on each NCD will not be given unless that NCD was filled with ^{4}He. It should be noted that some NCD strings were problematic and will be removed from the NCD data set for the neutrino flux measurement (Appendix A) [90]. Of these, the NCDs 0, 3, and 8 were turned off at various times during the data set (by either disconnecting the high voltage, setting the MUX and shaper/ADC thresholds to maximum, or both). As such, the rate of alphas on these NCDs were zero during these periods.

Table 8.5 shows the results from the fits to the total number of events in each group of 100 runs (Eq. 8.6) for events with E > 1.0 MeV. The NCDs 0, 3 and 8, which are to be excluded in the NCD phase analysis, were turned off at various times during the data acquisition, resulting in poor fits, as expected (Fig. 8.8). The NCD 1 was not physically turned off, but was afflicted with RCD starting with run 62276 on May 21, 2006. Due to RCD, no events were observed on this NCD after that date.

The data were searched for instances where the measured number of events in a group was more than three standard deviations, $\sigma_g = k\sqrt{N_g}$ from the expected count. Each group was tested for

$$N_g - \bar{N}_g > 3k\sqrt{N_g} \tag{8.9a}$$

$$\bar{N}_g - N_g > 3k\sqrt{N_g} \tag{8.9b}$$

where $\bar{N}_g = \sum_r \bar{R}_o T_r f_r$, and $\bar{R}_o$ is the best-fit constant rate for each NCD string. Four groups were found to be outside of the $3\sigma_g$ on NCDs 7, 12, 19, and 34 (Table 8.6 and Fig 8.9). One group was above the average rate by more than $3\sigma_g$ and three groups were below the average rate by more than $3\sigma_g$. Of the 18 groups in 36 NCDs, a total of 648 bins, a gaussian distribution of rates would expect to find 1 or 2 groups more than $3\sigma_g$ from the mean ($648 \cdot$ (1 - 0.9973) = 1.75). From the distribution of events found in the Monte Carlo however, the probability of finding a bin more than 3σ below the average is 0.003 and more than 3σ above the average is 0.0007. For 648 bins, the expected number of bins below and above 3σ from the mean is 1.9 bins and 0.5 bins, respectively. Thus, the observations listed in Table 8.6 are consistent with the results of the Monte Carlo.

Small P-values (P-value < 0.05) were found on NCD strings 7, 19, 24, 28, 34, and 38 (Fig. 8.9(a), 8.9(c) and8.10), where only 2 of the 36 fits to a constant rate were expected to have a P-value less than 0.05. The distribution of P-values for all NCDs,

Table 8.5: Summary of the results of a χ^2-minimization fit to Eq.8.6 for events on each NCD string with energy greater than 1.0 MeV. Due to the restrictions from the WE blindness, only the measured rates of events for NCDs filled with ^{4}He are reported here. Bins where no events were observed were not included in the fits.

NCD	R_o α/day	χ^2/d.o.f	P-value	NCD	R_o α/day	χ^2/d.o.f	P-value
0	–	76.63/17	0.0000	20	8.01 ± 0.15	19.66/17	0.2920
1	–	12.94/14	0.5309	21	–	16.17/17	0.5119
2	–	13.78/17	0.6824	22	–	17.93/17	0.3935
3	4.91 ± 0.15	244.22/10	0.0000	23	–	19.44/17	0.3040
4	–	14.21/17	0.6521	24	–	32.05/17	0.0148
5	–	22.78/17	0.1566	25	–	14.98/17	0.5970
6	–	19.16/17	0.3192	26	–	13.82/17	0.6797
7	–	30.27/17	0.0244	27	–	21.92/17	0.1878
8	–	277.45/12	0.0000	28	–	41.57/17	0.0008
9	–	17.56/17	0.4171	29	–	17.62/17	0.4135
10	31.20 ± 0.31	11.34/17	0.8383	30	5.57 ± 0.13	11.00/17	0.8567
11	–	20.05/17	0.2718	31	–	24.90/17	0.0971
12	–	23.47/17	0.1347	32	–	20.10/17	0.2689
13	–	13.94/17	0.6715	33	–	14.22/17	0.6517
14	–	14.85/17	0.6059	34	–	30.81/17	0.0211
15	–	15.61/17	0.5514	35	–	18.51/17	0.3574
16	–	9.41/17	0.9265	36	–	12.00/17	0.8001
17	–	16.47/17	0.4907	37	–	22.31/17	0.1730
18	–	6.63/17	0.9878	38	–	28.68/17	0.0376
19	–	27.62/17	0.0496	39	–	21.99/17	0.1849

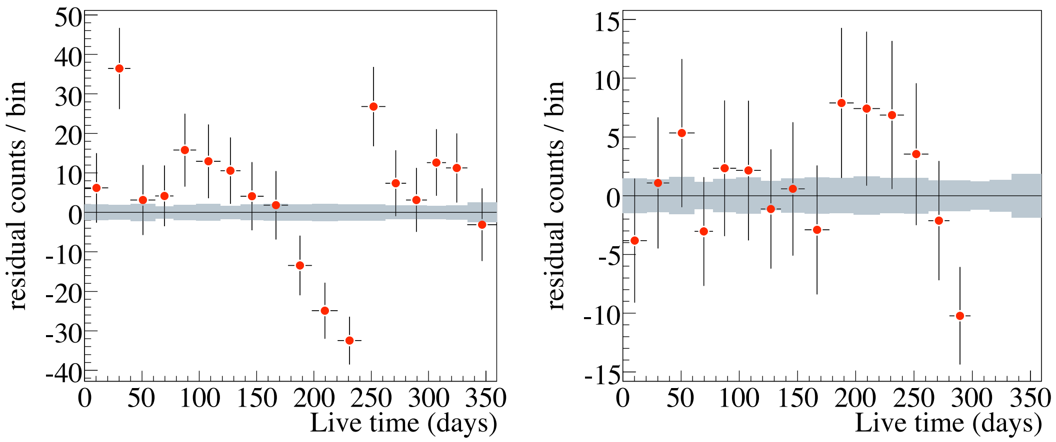

(a) NCD 0.

(b) NCD 1.

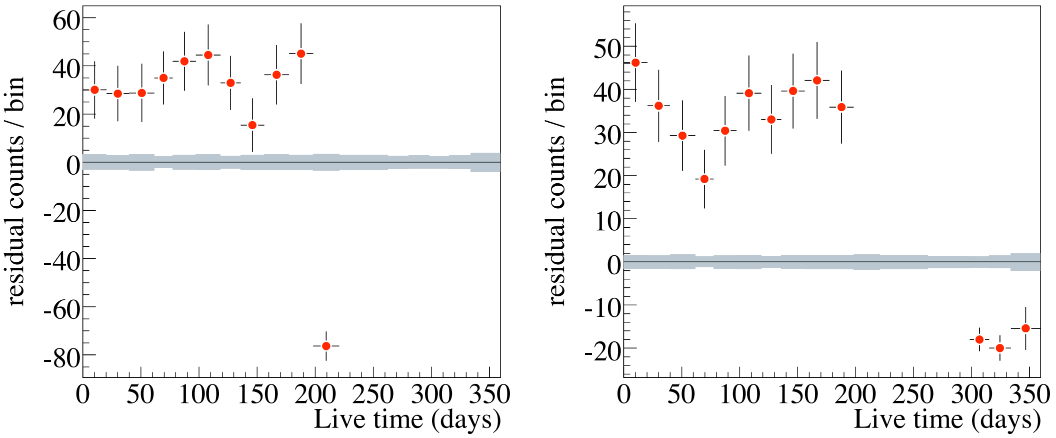

(c) NCD 3.

(d) NCD 8.

Figure 8.8: Residuals to the average number of events for E > 1.0 MeV for NCDs 0, 1, 3 and 8. The fits to a constant rate for these strings resulted in a poor P-value (Table 8.5). NCDs 0, 3, and 8 were disconnected from the DAQ, and RCD was observed on NCD 1. Bins where zero events were recorded are not shown in these figures, which includes the final three bins on NCD 1. The residuals to the average rates are presented here, rather than the measured rates, in order to conceal the overall blindness fraction.

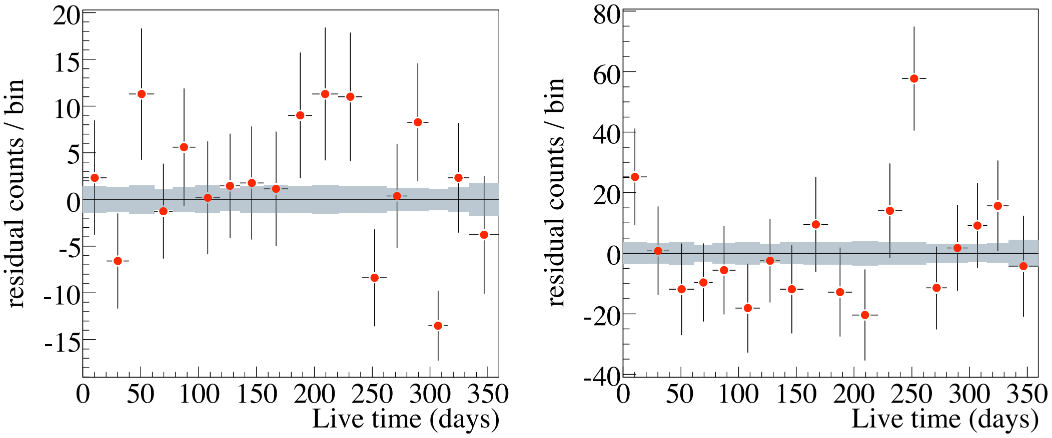

(a) NCD 7.

(b) NCD 12.

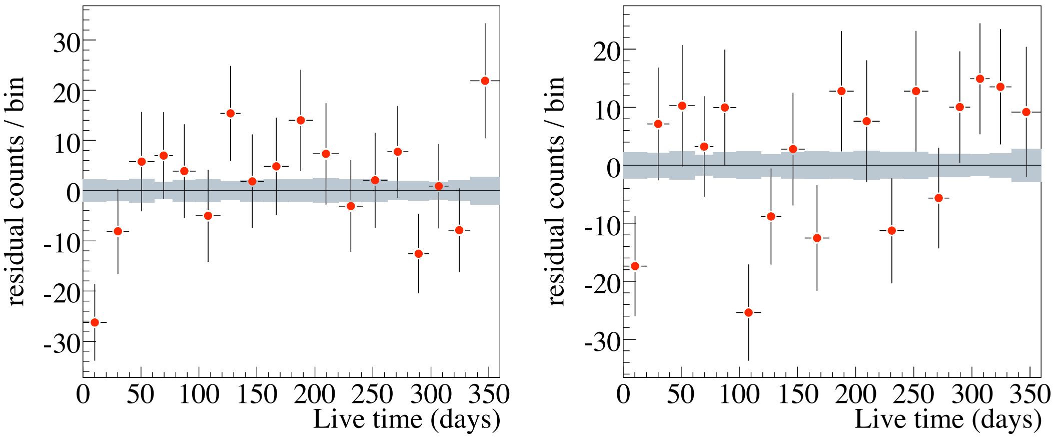

(c) NCD 19.

(d) NCD 34.

Figure 8.9: Residuals to the average number of events for E > 1.0 MeV for NCDs 7, 12, 19, and 34. Table 8.6 lists the bins that were more than $3\sigma_g$ from the measured average rate for each NCD.

Table 8.6: There were instances found where the measured number of events with E > 1.0 MeV were more than three standard deviations from the expected number of events based upon the measured average rate, R_o, on NCDs 7, 12, 19, and 34.

NCD	Group (bin)	σ from R_o
7	16	-3.62
12	13	+3.36
19	1	-3.45
34	6	-3.06

excluding 0, 1, 3, and 8, is shown in Fig. 8.11, However, a Kolmogorov-Smirnov test of this distribution to a uniform distribution returned a probability of 0.42, indicating that this distribution is consistent with an uniform distribution [91].

A test of the distribution of pulls, $p = (N_g - \bar{N}_g)/\sigma_g$, was performed. The measured values of p for each NCD is seen in Fig. 8.12 and a histogram of p is found in Fig. 8.13(a). Removing NCDs 7, 12, 19, 24, 28, 34 and 34 improves the distribution (Fig. 8.13(b)). Both distributions shown here are consistent with the distribution of pulls found in the Monte Carlo (Fig. 8.7), having a slightly positive mean and negative skewness. The Monte Carlo p_{ij} distribution was normalized and then fit to the data using a maximum-likelihood fit. The χ^2 calculated here was the small-sample Poisson-likelihood chi-square,

$$\chi^2 = 2\sum[p_m \ln(p_m/y_m) + y_m - p_m] \tag{8.10}$$

where y_m are the expected values from best-fit normalized p_{ij} Monte Carlo distribution for bin m, and p_m is the measured occupancy of bin m. Bins where $p_m = 0$ were excluded, by prescription [84]. The mean, RMS, and skewness of data distribution are listed in Fig. 8.13 and are consistent with Monte Carlo.

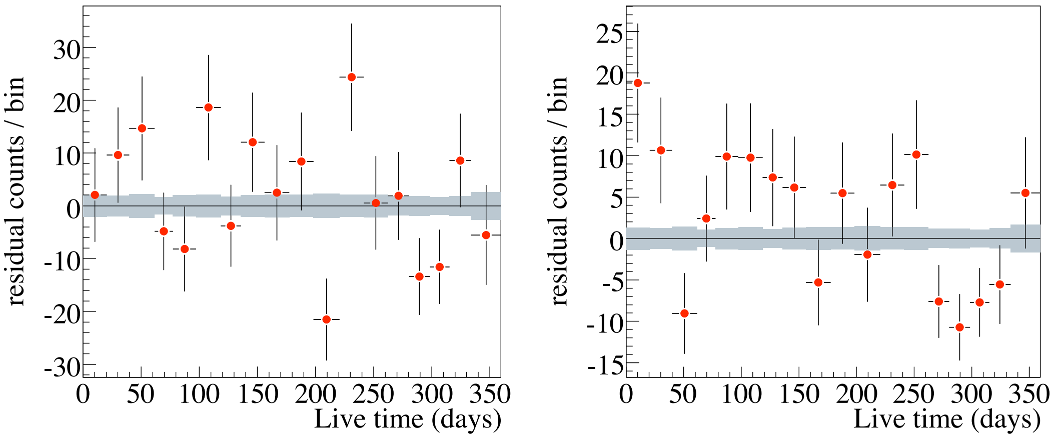

(a) NCD 24.

(b) NCD 28.

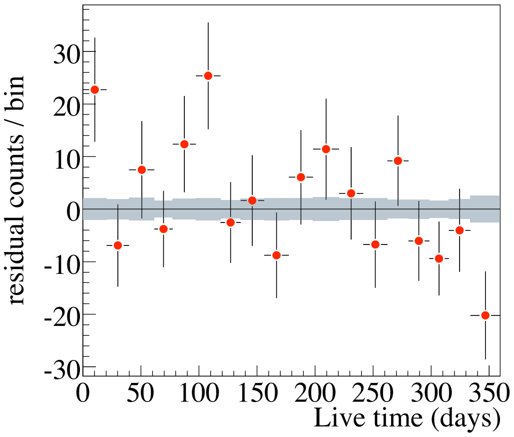

(c) NCD 38.

Figure 8.10: Residuals to the average number of events for E > 1.0 MeV for NCDs 24, 28 and 38. The fits to a constant rate for these strings resulted in a poor P-value (Table 8.5).

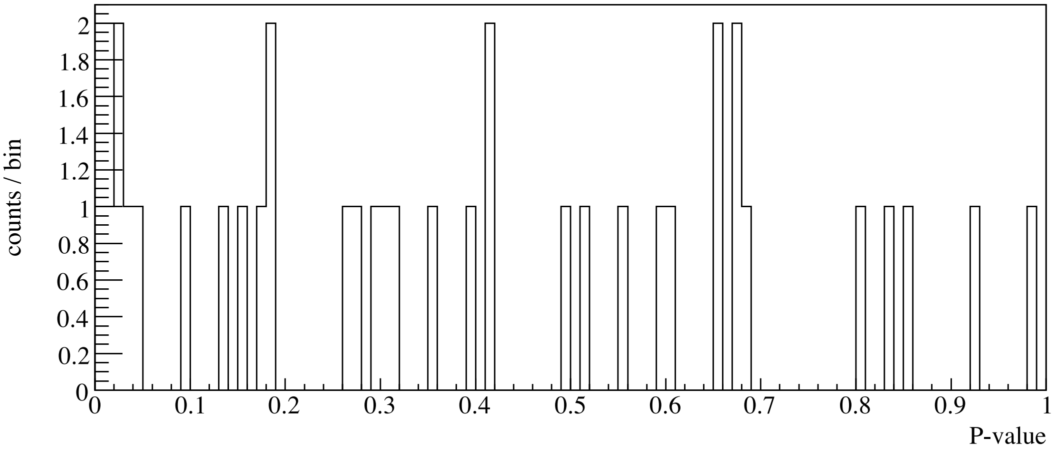

Figure 8.11: The distribution of P-values from the goodness-of-fit tests to Eq. 8.6 for all NCDs, excluding NCDs 0, 1, 3, and 8 (Table 8.5).

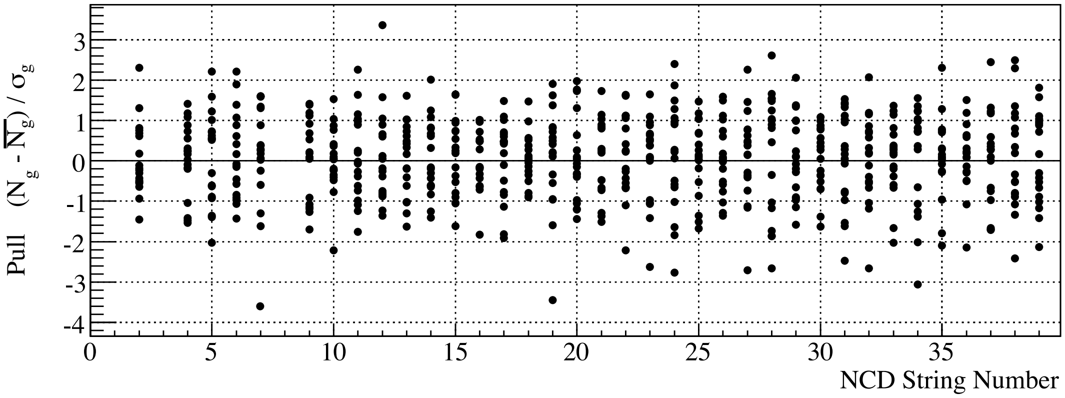

Figure 8.12: The measured pulls for each NCD string, excluding NCDs 0, 1, 3 and 8.

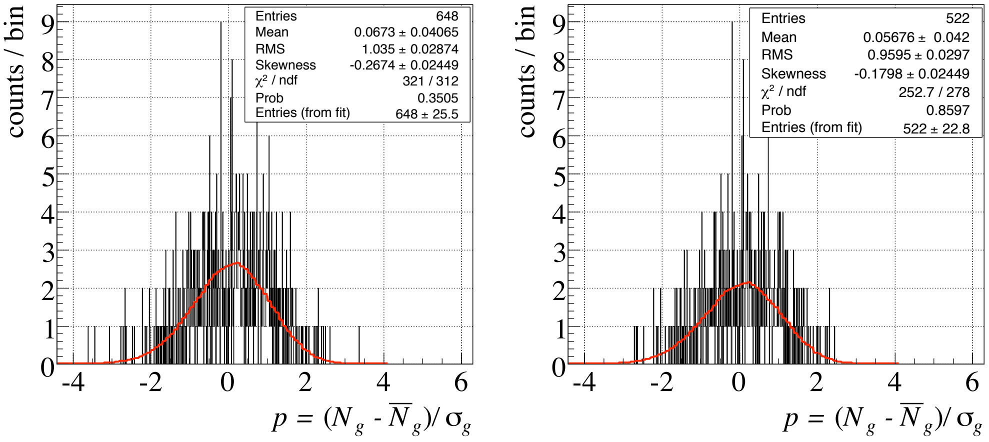

(a) All NCDs except 0, 1, 3, and 8.

(b) All NCDs except 0, 1, 3, 8, 7, 12, 19, 24, 28, 34 and 38.

Figure 8.13: The measured distributions of p were fit to the normalized distribution obtained from the Monte Carlo. Both distributions are consistent with the Monte Carlo.

8.6 Conclusions of the Constant Rate Measurements

In this chapter, the rate of events with energy greater than 1.0 MeV, which consist entirely of alpha events, was found to be statistically consistent with a constant rate model. No anomalously low rates of events were observed. The distribution of the P-values were found to be consistent with a K-S test of a uniform distribution. In addition, the distribution of the pulls from the data, p, were found to be consistent with the same distribution produced by Monte Carlo.

From the Monte Carlo study, the increase in the variance of the number of alphas detected per 20-day bin due to the presence of time-correlated events caused by the short-lived nuclei within the lower U and Th decay chains was verified. The ratio, k, between the standard deviation of the distribution and the expected standard deviation, $\sqrt{N}$, was found to be $k = 1.036 \pm 0.012$ for an average 10-m NCD. It should be noted that the Monte Carlo did not include the run boundaries in the NCD data set. The maximum length of each run was set to 7 hours, but some runs occurred back-to-back, producing longer periods of continuous live-time. As clearly shown by Adams [86] (and more generally by Ruark and Devol [88, 92]), the increase in the variance is dependent upon the time-scale of the counting device relative to the half-life of nuclei within the Th decay chain. Since each group in the NCD data set is not a continuous observation of alpha events, the ratio k is expected to be slightly larger than the value used here. Furthermore, if some NCDs were not exposed to the Rn gas and do not have Po or Pb plated on their inner surface, the ratio k would increase further (see row 3 of Table 8.4).

To conclude, the measurement of the rate of alphas does not implicate RCD on any NCDs, except on NCD 1. The NCDs 0, 3 and 8 were physically turned off by disconnecting them from the high voltage supplies or raising their respective MUX and shaper/ADC thresholds. However, NCD 1 was never physically turned off or had its thresholds raised – once RCD occurred on this NCD the rate of alphas went to zero. It should be noted that a statistically significant drop in rates on NCD 31 was not observed, even though this NCD is known to be afflicted with RCD. Thus, this analysis shows that if RCD were occurring briefly on some NCDs, it would have little to no impact on the measured rates of alphas and subsequently on the measured rate of neutrons, assuming that RCD is not a randomly occurring process. If RCD is a randomly occurring process, this method would have no way of determining the impact since the rate of alphas would be suppressed over the NCD phase in a random manner. However, RCD is not a random process since it is known to be correlated with local mining activity.

One explanation for the lack of a reduced observation of rates on NCD 31 is the idea of partial RCD and signal-induced reconnect. If the NCD disconnects from the NCD cable, which is connected to the high-voltage power supply, the voltage maintained on the NCD slowly decreases due to leakage currents. Then, a potential difference occurs between the NCD anode and the NCD cable anode. A current of electrons would then further this potential difference, providing enough force to reconnect the resistive coupler to the NCD cable and allow for the signal to propagate to the DAQ. Under this scenario, RCD would not produce as much loss of data as compared to full RCD (NCD 1), depending upon the rate of leakage current, the physical distance of the disconnection and the total charge of the signal. Since alpha pulses tend to have significantly greater currents (§ 3.3.2) and if this resistive coupler reconnect scenario was occurring, the loss in neutron capture events could be greater than the loss in alpha events.

Chapter 9

CONCLUSIONS: IMPACT ON THE NEUTRAL CURRENT FLUX MEASUREMENT

This work has impacted the total ^{8}B solar neutrino flux in two primary ways. First, the systematic uncertainty in the number of neutrons identified via the pulse-shape analysis techniques due to variations in the measured logamp parameters was estimated. In general, the systematic uncertainty on the neutron identification methods (and subsequently the neutrino flux measurement) is quite small.

Second, the NCD strings with RCD have been identified and the amount of RCD dead-time has been estimated. Also, in the related alpha rate analysis, it has been shown that the measured rate of alpha events were constant over the NCD phase even on NCDs that were suspected of having RCD. Thus, one could argue that if the rate of alphas, which are approximately a factor of 100 times greater than the rate of neutrons, were statistically consistent with a constant rate, then instances of RCD should not affect the measured rate of neutrons, and subsequently the neutrino flux. This would be true unless a potential mechanism could overcome *partial* RCD, as conjectured in the conclusions of Chapter 8.

9.1 Improvements to the Methods

In hindsight, for both the noise rate analysis (Chapter 7) and the alpha rate analysis (Chapter 8), the methods could be slightly improved in a few ways. I will list some of these possible improvements.

In the noise analysis, the obvious problem is the lack of a pure source of thermal baseline noise events that could be used to train a set of pulse-shape parameters to improve recognition of these types of events. Its conceivable that a low-noise laboratory environment could be constructed using NCD detector components (test NCD, resistive coupler, NCD cable and DAQ) to record a set of thermal noise events. In addition, the rate of these noise events as a function of MUX threshold could be determined. Also, given a great amount of computational time, the simulated thermal noise event could be simulated in a more physical way without the need for adding the small-amplitude rectangular wave.

The pre-NRE data set could have been broken up into subsets that were about the same size of the open and post-NRE data set. This would still allow sufficient statistics for the $T = 120$ min. counting time, while improvement comes by having more data sets that are not influenced by bursts of noise. Furthermore, this would reduce the impact on the distribution of events if the average rate of thermal noise events were fluctuating. The result would be distributions of the number of observed thermal noise events that better fit to a Poisson distribution (Eq. 7.1).

The analysis of the rate of alphas could be more sensitive to changes in rates if the group sizes were tailored for each NCD according to the average rate of events. For example, NCD 10 has a significantly larger rate than NCD 36 and the group size could have been reduced and still have a sufficient amount of statistics. The Monte Carlo for the alpha analysis could utilize the start and stop times of each NCD run, which would likely affect the estimate of the parameter $k = \sigma/\sqrt{N}$. In addition, space-charge effects could be added and instead of counting the number of alphas above 1.0 MeV, the energy spectrum could be fit for each group of runs to determine the relative rates of alphas from the ^{238}U and ^{232}Th chains and from ^{210}Po as a function of time over the NCD production data set.

9.2 Logamp Calibration Parameter Impact on Systematic Uncertainties in the Neutrino Flux

Independent groups within the SNO collaboration have developed methods for identifying neutron capture events in the NCD data. This section will briefly describe these techniques and the results of a study of the systematic change caused by variations of the logamp model parameters. At this stage in the NCD data analysis, the final pulse-shape analysis neutron identification method has not been chosen by the SNO Collaboration. The following sections will briefly describe the four neutron identification methods and state the systematic uncertainties due to variations in the logamp calibration parameters.

9.2.1 The FTD Method

The FTD[1] method is a pulse-shape fitting method that incorporates a SPICE model of the NCD electronics. The FTD method estimates an electronics transfer function for signals which propagate along the NCD. The transfer function was calculated using waveforms measured at the output of an NCD after injecting an impulse current signal. A study on the variability of the estimated number of neutrons observed in the blind-production data set as a function of a one standard deviation variation in the logamp parameters found that the systematic uncertainty contribution from the logamp parameters was 1.65% [93].

9.2.2 The DWK Method

The DWK method (Deconvolved Width Kurtosis) is a neutron identification technique that attempts to first deconvolve the pulse-transformation effects from the NCD electronics and from the ion mobility (the ion mobility induces the ion-tail on neutron

---

[1] FTD is not a real acronym, but loosely means “Fitter Deng”, named after the person who developed this method.

and alpha events). A set of parameters were developed that are related to the width, rise-time, and asymmetry of each pulse-shape. Another parameter used in this analysis is developed from a principal-component analysis using a set of alpha and neutron events. Based upon the distribution of these sets of parameters, neutrons, alphas and non-neutron non-alpha (NNNA) events are distinguishable[2]. A study of the systematic uncertainties revealed that variations in the logamp parameters contribute a 0.05% uncertainty in the measured number of neutrons [94].

9.2.3 The Queen's Grid Fitter Method

The Queen's Grid Fitter (QGF) method detects neutron events by comparing each waveform in the NCD data set to a library of neutron pulses (obtained from ^{24}Na calibration data) and alphas pulses (obtained from events observed in ^{4}He NCDs). For each pulse within the neutron energy window (0.2 MeV $< E <$ 0.9 MeV), a goodness-of-fit χ^2_n was calculated for each event in the neutron library, and for each event in the alpha library, χ^2_α. Neutrons were separated from alphas by making a cut in the χ^2_n-χ^2_α space. Following the cut, the energy spectrum of events within the neutron energy window were fit to a neutron energy distribution obtained from calibrations plus a background distribution. Various background distributions were considered as a way to constrain the problems caused by contamination of NNNA events. The systematic uncertainty in the neutron identification efficiency due to the logamp calibration parameters was found to be 0.67% [95, 96][3].

---

[2] NNNA events are a subset of instrumental background events which are rare, occur primarily on NCDs 26 and 0, look considerably like neutrons, and have been difficult to remove from the neutron identification analysis or estimate their rate.

[3] The author of this document reports 0% because the uncertainty was obviously much smaller than other uncertainties, but the number quoted here was extracted from plots within the QGF documentation.

9.2.4 The Fisher Discriminant Method

The Fisher Discriminant method combines the rise-time (the time between the 10% to 50% maximum amplitude points), the 2nd moment and 4th moment measurements of each pulse-shape into a single likelihood variable, called the Fisher variable. A set of cuts removes alphas and NNNA events from with the neutron energy window of 0.4 MeV $< E <$ 0.9 MeV. Then a fit to the two-dimensional distribution of the Fisher variable vs. energy allows for the extraction of the number of neutrons. In this method, no dependence on the logamp parameters were found and the systematic uncertainty is quoted to be 0% [97].

Recent Measurements of Hardware Impedances

Recently, measurements of the frequency dependent impedance for the NCD, NCD cables and the input of the preamplifiers were made, with unexpected results. The characteristic impedance has been measured to be 357 ± 1 Ω, 92 ± 7 Ω, and 100.3 ± 0.4Ω for the NCD string, NCD cable and preamp input, respectively in the range of 5 to 15 MHz [98, 60]. This is a preliminary result and the impact of these measured impedances should be studied to assess their impact on the measured logamp parameters and the neutrino flux measurement. It is also noted that these impedances are measured in the 5 - 15 MHz range, while the logamp calibration pulse sine wave has significant power in the 1 to 5 MHz range. A comparison of the logamp parameters for the normal set of electronics model characteristic impedances and for these new impedances were made for the logamp calibration run 60352. The average changes observed for this calibration run for logamp parameters a and b were 0.63% and 0.5%, respectively. Since c_{chan} is usually somewhere around ±5 mV, the average absolute difference was measured in this example and is 0.01 mV. No change was observed in the measured values of $V_{PreTrig}^{ADC}$ and Δt, as expected. The typical one standard deviation uncertainties for logamp parameters a and b are around 1% and for c_{chan}

is around 0.05 mV. Given the small impact of the logamp parameters on the neutron identification methods mentioned above, implementation of the newly measured characteristic impedances in the logamp calibration parameter estimate routines is not expected to significantly impact the neutrino flux measurements. However, once the characteristic impedance measurements are finalized, a check on the variation of the logamp parameters should be made to ensure the insignificance of this change.

9.3 Comparison of RCD Observational Methods

There were four methods used to observe RCD described in this dissertation. In the end, problems were found with just NCDs 1 and 31 and not with any other NCD. The four methods were

- Logamp Calibration
- NCD Resistive Coupler Disconnect Electronics Calibration
- Rate of Noise Analysis
- Rate of Alpha ($E > 1.0$ MeV) Analysis

The RCD condition was first observed in the logamp calibration results (§ 5.4.1). The measured logamp parameters for NCD 31 were observed, early on, to deviate significantly from their typical values (Fig. 5.16). Upon further inspection of the trigger pulse of the logamp calibration pulse, it was found that the structure of the signal was different during the calibrations where the measured parameters significantly deviated. The structure of the trigger pulse is caused by impedance mismatches in the NCD front-end electronics and the distinct change in that structure implicated the disconnection of the NCD to the NCD cable. Then, on May 22, 2006, this same observation was made with calibrations taken on NCDs 1 and 31. This occurrence is clearly correlated with local seismic mine activity.

Following the development of the RCD hypothesis, the NRE calibration was initiated and performed for the remained of the NCD data set, which covered the last

58 live days of the NCD phase (Chapter 6). The NRE calibration injected a signal on each NCD once per hour, providing a reasonably frequent check of each NCDs connection to the DAQ. From these data, the RCD condition was continuously observed on NCD 1 and frequently observed on NCD 31, though the RCD state was not persistent on NCD 31.

In Chapter 7, an analysis of the rate of thermal noise events was presented. The goal was to observe the Poisson statistics of the rate thermal noise events, which would significantly decrease during RCD. This method was partially successful. It failed in selecting out just thermal noise events and observing a well-behaved Poisson distribution of events for all NCDs. But it did succeed in showing that only NCDs 1 and 31 have unexplained instances of very low rates of events that were inconsistent with their typical rate of noise events.

Finally in Chapter 8, the rate of alphas emitted by ^{210}Po and nuclei within the U and Th decay chains within the NCD nickel walls was measured for each NCD. The rate of alpha events in the NCDs was expected to be constant throughout the NCD phase. Again, the rate of events on NCD 1 was observed to drop to zero around the time of the May 22, 2006 incident. However, no observation of a decrease in rates on NCD 31 was made with this data. It is speculated that high energy events occurring on NCD 31 could have caused the resistive coupler to reconnect as the event pulse arrived at the NCD cable. At this time, however, there have not been any quantitative or qualitative calculations made to determine the feasibility of this phenomenon.

In conclusion, from these four types of observations made of the integrity of the NCD array, the RCD condition affected NCDs 1 and 31 and was not found on other NCDs.

9.4 RCD Impact

The impact of the discovery of RCD can be quantified in two ways. First, if RCD was not found on NCDs 1 and 31 and they were left in the data set, the neutrino flux measurement would be too small. The change in the accuracy of the total ^{8}B solar neutrino flux measurement can be found by estimating the number of neutrons that NCDs 1 and 31 would have missed due to RCD. The estimate of the amount of RCD dead-time for these NCDs 1 and 31 is estimated to be 71.57 ± 0.02 days and 110.5 ± 5.4 days, respectively (Table 7.6). The total NCD phase live-time × NCD length for the 32 good ^{3}He NCDs, including the RCD detectors 1 and 31, is 123,825.73 ± 45.01 days·m.[4] Now, the RCD dead-time for NCDs 1 and 31 may be accounted for by effectively reducing the length of each NCD. The total live-time of the NCD phase remains the same. This reduces the *effective* length of NCDs 1 and 31 from 10.5 m to 8.549 ± 0.001 m and from 10.0 m to 7.13 ± 0.14 m, respectively. Then, the NCD phase live-time × NCD length becomes 121,968.95 ± 69.25 days·m. Assuming that each NCD absorbs neutrons at the same rate (this is roughly true), and that RCD dead-time would not be detected by NCD neutron detection efficiency measurements, if NCDs 1 and 31 are included in the neutrino flux measurement, the measured flux would be 1.50 ± 0.07 % smaller. It should be noted that this estimate is based upon the assumption that Eq. 7.1 sufficiently models the distribution of noise rates observed on NCD 31. Performing the same calculation for just NCD 1 shows that NCD 1 would contribute to an inaccuracy of the neutrino flux of 0.61 ± 0.05 % if it were to be included into the NCD analysis without any type of correction for RCD. Since it is quite clear when NCD 1 became afflicted with RCD, it may be plausible to consider that data from NCD 1 be included in the neutrino flux measurement so long as the final neutral-current flux measurement was increased by ∼0.61 % to correct for RCD losses. However, this value of 0.61% would have to be recalculated using the correct values for the NCD-dependent neutron detection efficiencies.

The impact of RCD may also be quantified as an uncertainty in the live-time of the NCD phase. The average of the upper limit on RCD dead-time according to the

---

[4] The lengths of each NCD string are reported on page 86 of [52].

estimates of Table 7.8, $\bar{T}_{RCD}$, is $< 0.024\%$, which obviously excludes NCDs 1 and 31. This will undoubtedly be significantly below the level of uncertainty of any other live-time estimate or systematic uncertainty in the NCD phase.

Furthermore, analysis of the rate of alphas implies that there are not any instances of significant dead-time that anomalously reduced the measured rate of background alpha events. One could then argue that since the rate of alphas is about a factor of 100 times larger than than the rate of neutron capture events, any instances of RCD (except for on NCDs 1 and 31) would reduce the neutrino flux measurement much less than the statistical precision. As previously mentioned, partial RCD that reconnects due to a current signal could reconnect the resistive coupler, resulting in a greater loss of neutron detection than for high energy ($E > 1.0$ MeV) alphas.

It is concluded from these studies that NCDs 1 and 31 should be removed from the NCD data set due to RCD, as observed in the NRE calibrations, the baseline noise event analysis and alpha rate analysis. The impact of these studies goes beyond the quantitative statements. Without this analysis, the NCD phase flux measurement would be highly questionable without ensuring that all of the NCDs in the analysis were functioning properly.

9.5 Runs Removed From The Final Data Set

In the process of these analysis a number of runs were found to have oscilloscope-related problems. This manifested in two ways. There were a set of runs where the rate of oscilloscope triggers abruptly dropped to zero for the entire array. It is unlikely that every NCD in the array went into the RCD condition at the same time. This is especially unlikely since the oscilloscope triggers appeared to resume after the start of a new run. The second observation was abnormally long time intervals between oscilloscope triggers for a handful of runs. The set of runs that were excluded based upon observations of these problems are listed in Table D.1 and described in Appendix D. Inclusion of these runs would have resulted in an inaccurate measurement of the detector live-time by approximately 24 hours.

9.6 Final Remarks

I have worked on a variety of aspects of experimental work at SNO. I developed software drivers for the DAQ communication with the MUX Controller Card, contributed to the commissioning and testing the final NCD DAQ systems, participated in the selection process to find the most radioactively clean NCDs to be installed (this was already documented in [52]), and installed and commissioned the NCD array, developed the NCD electronics model and electronics calibrations, and uncovered the RCD condition and other hardware-related problems that would have resulted in an inaccurate flux measurement.

The NCD electronics model is a necessary component for most pulse-shape analysis techniques for neutron identification. The parameters that describe the logarithmic transformation of the signal were found to be sufficiently precise so as to contribute less than 1% systematic uncertainty in the neutrino flux measurement (except for the FTD method, for which the uncertainty is 1.65%).

Regardless of the exact quantitative estimate on the neutrino flux measurement due to RCD, this work has demonstrated that RCD likely only occurred on NCDs 1 and 31. It is completely clear that these NCDs should be removed from the neutrino flux measurement. Most of the NCD array works as expected and all “problematic” NCDs and data acquisition runs will be excluded from the ^{8}B solar neutrino flux measurement. Due to the work found in this dissertation and from other members of the SNO collaboration who worked to ensure the integrity of this experiment, the physics community should be confident in the results from the NCD phase at SNO. The combined measurements of the neutrino flux from the three phases of SNO will be excellent tests of predictions from the standard solar models and will further constrain the neutrino mixing parameters (Fig. 2.4).

BIBLIOGRAPHY

[1] J. N. Bahcall, A. Bahcall, and G. Shaviv, Phys. Rev. Lett. **20**, 1209 (1968).

[2] J. Davis, R., D. S. Harmer, and K. C. Hoffman, Phys. Rev. Lett. **20**, 1205 (1968).

[3] H. A. Bethe, Phys. Rev. **55**, 434 (1939).

[4] K. K. S. Miknaitis, *A Search for Matter Enhanced Neutrino Oscillations through Measurements of Day and Night Solar Neutrino Fluxes at the Sudbury Neutrino Observatory*, PhD thesis, University of Washington, 2005.

[5] J. N. Bahcall, *Neutrino Astrophysics* (Cambridge, UK: Univ. Pr., 1989).

[6] M. Asplund, N. Grevesse, and A. Suaval, ASP Conf. Ser. **336**, 25 (2005).

[7] N. Grevesse and A. J. Sauval, Space Sci. Rev. **85**, 161 (1998).

[8] J. N. Bahcall, A. M. Serenelli, and S. Basu, Astrophys. J., Suppl. Ser. **165**, 400 (2006).

[9] S. N. Ahmed *et al.*, Phys. Rev. Lett. **92**, 181301 (2004).

[10] A. M. Serenelli, Nucl. Phys. B, Proc. Suppl. **168**, 115 (2007).

[11] L. C. Stonehill, J. A. Formaggio, and R. G. H. Robertson, Phys. Rev. C **69**, 015801 (2004).

[12] J. N. Bahcall, A. M. Serenelli, and S. Basu, Astrophys. J., Lett. **621**, 85 (2005).

[13] J. N. Bahcall, Physica Scripta **T121**, 46 (2005).

[14] J. N. Bahcall, Phys. Rev. Lett. **12**, 300 (1964).

[15] J. N. Bahcall and A. Ulmer, Physical Review D (Particles, Fields, Gravitation, and Cosmology) **53**, 4202 (1996).

[16] J. N. Abdurashitov *et al.*, J. Exp. Theor. Phys. **95**, 181 (2002).

[17] M. Altmann *et al.*, Physics Letters B **616**, 174 (2005).

[18] Y. Fukuda *et al.*, Phys. Rev. Lett. **77** (1996).

[19] Super-Kamiokande Collaboration, J. Hosaka *et al.*, Phys. Rev. D **73**, 112001 (2006).

[20] H. H. Chen, Phys. Rev. Lett. **55**, 1534 (1985).

[21] V. Gribov and B. Pontecorvo, Physics Letters B **28**, 493 (1969).

[22] M. Grünewald *et al.*, Phys. Rep. **427**, 257 (2006).

[23] Z. Maki, M. Nakagawa, and S. Sakata, Prog. Theor. Phys. **28**, 870 (1962).

[24] B. Pontecorvo, Zh. Eksp. Teo. Fiz. **53**, 1717 (1967).

[25] B. Pontecorvo, Sov. Phys. JETP **7**, 172 (1958).

[26] M. Apollonio *et al.*, Eur. Phys. J. C **27**, 331 (2003).

[27] L. Wolfenstein, Phys. Rev. D **17**, 2369 (1978).

[28] H. A. Bethe, Phys. Rev. Lett. **56**, 1305 (1986).

[29] S. P. Mikheyev and A. Y. Smirnov, Nuovo Cimento C **9C**, 17 (1986).

[30] Q. R. Ahmad *et al.*, Phys. Rev. Lett. **87**, 071301 (2001).

[31] J. Boger *et al.*, Nucl. Instrum. Meth. A **449**, 172 (2000).

[32] S. D. Ellis and J. N. Bahcall, Nucl. Phys. A **114**, 636 (1968).

[33] P. Vogel and J. F. Beacom, Phys. Rev. D **60** (1999).

[34] L. B. Auerbach *et al.*, Phys. Rev. D **63**, 112001 (2001).

[35] R. C. Allen *et al.*, Phys. Rev. D **47** (1993).

[36] B. Aharmim *et al.*, Phys. Rev. C **75**, 45502 (2007).

[37] R. Ahmad, *Muon Correlated Background at The Sudbury Neutrino Observatory*, PhD thesis, Brown University, 2002.

[38] J. A. Dunmore and R. G. H. Robertson, SNO Technical Report, SNO-STR-95-025, Background Neutron Sources to the Neutral-Current Signal in SNO, 1998.

[39] Q. R. Ahmad *et al.*, Phys. Rev. Lett. **89**, 11301 (2002).

[40] B. Aharmim *et al.*, Phys. Rev. C **72**, 055502 (2005).

[41] J. Dunmore, *Separation of CC and NC events in the Sudbury Neutrino Observatory*, PhD thesis, University of Oxford, 2004.

[42] KamLAND Collaboration, T. Araki *et al.*, Phys. Rev. Lett. **94**, 081801 (2005).

[43] G. F. Knoll, *Radiation Detection and Measurement*, 2 ed. (Wiley, 1989).

[44] T. J. Bowles *et al.*, Neutral-Current Detection in the Sudbury Neutrino Observatory, Los Alamos National Laboratory, FIN-94-ER-E324, 1992.

[45] A. Bandyopadhyay, S. Choubey, S. Goswami, S. Petcov, and D. Roy, Phys. Lett. B **608**, 115 (2005).

[46] J. F. Amsbaugh, Private Communication, 2007.

[47] J. F. Amsbaugh *et al.*, Nucl. Instrum. Meth. A **579**, 1054 (2007).

[48] M. Browne, *Preparation for Deployment of the Neutral Current Detector (NCDs) for the Sudbury Neutrino Observatory (SNO)*, PhD thesis, North Carolina State University, 1999.

[49] C. A. Duba, *Electronics for the Neutral Current Detection Array at the Sudbury Neutrino Observatory*, PhD thesis, University of Washington, 2006.

[50] K. M. Heeger, *Model-Independent Measurement of the Neutral-Current Interaction Rate of Solar* ^8B *Neutrinos with Deuterium in the Sudbury Neutrino Observatory*, PhD thesis, University of Washington, 2002.

[51] M. W. E. Smith, *An Investigation of Matter Enhanced Neutrino Oscillation with the Sudbury Neutrino Observatory*, PhD thesis, University of Washington, 2002.

[52] L. C. Stonehill, *Deployment and Background Characterization of the Sudbury Neutrino Observatory Neutral Current Detectors*, PhD thesis, University of Washington, 2005.

[53] P. M. Thornewell, *Neutral-Current Detectors for the Sudbury Neutrino Observatory*, PhD thesis, University of Oxford, 1997.

[54] J. Farine, PhD thesis, University of Neuchatel, 1996.

[55] J. F. Ziegler, J. P. Biersack, and U. Littmark, *The Stopping and Range of Ions in Solids* (Pergamon Press, New York, 1985).

[56] B. Monreal, Private Communication, 2007.

[57] W.-M. Yao *et al.*, J. Phys. G: Nucl. Part. Phys. **33** (2006).

[58] P. Doe *et al.*, Construction of an Array of Neutral-Current Detectors for the Sudbury Neutrino Observatory, SNO-STR-95-023, 1995.

[59] R. G. H. Robertson, Neutral-Current Detector Front-End Electronics, SNO Internal Document, 2002.

[60] N. Oblath, PhD thesis, University of Washington, 2008.

[61] H. W. C. Tseung, PhD thesis, University of Oxford, 2008.

[62] A. . Uritani, C. . Mori, T. . Watanabe, and A. Miyahara, Journal of Nuclear Science and Technology **27**, 712 (1990).

[63] A. Uritani, C. Mori, T. Watanabe, and A. Miyahara, Proc. 7th Symp. on Rad. Meas. and Appl., University of Michigan, Ann Arbor, MI, May 21-24, 1990 .

[64] M. M. Fowler, S. B. Larson, and J. B. Wilhelmy, SNO-STR-90-95 (1990).

[65] S. McGee, Determination of ncd electronic parameters with direct pulse injection, Private Communication, 2005.

[66] J. Heise, *A Search for Supernova Neutrinos with the Sudbury Neutrino Observatory*, PhD thesis, University of British Columbia, 2001.

[67] R. G. H. Robertson and T. Van Wechel, Log Amplifier Application in SNO NC Detectors, SNO Internal Report, 2004.

[68] Analog Devices, One Technology Way, P.O. Box 9106, Norwood, MA 02062, U.S.A., *Low Cost DC-500MHz, 92 dB Logarithmic Amplifier AD8307*, 1999.

[69] R. G. H. Robertson and T. D. Van Wechel, Characteristics of AD8307 Logarithmic Amplifier, SNO-STR-05-003, 2005.

[70] Tektronix, *Tektronix 754A Oscilloscope Manual*, 2006.

[71] M. A. Howe *et al.*, IEEE Trans. Nucl. Sci. **51**, 878 (2004).

[72] G. A. Cox *et al.*, IEEE Trans. Nucl. Sci. **51**, 2227 (2004).

[73] A. Technologies, *Agilent 33120A 15 MHz Function / Arbitrary Waveform Generator*, 5301 Stevens Creek Blvd, Santa Clara , CA 95051, United States. http://www.home.agilent.com/.

[74] T. Burritt *et al.*, NCD ECA Unidoc, SNO Internal Document, 2005.

[75] E. Guilllian and K. Rielage, Private Communication, 2008.

[76] L. R. Fortney, *Principles of Electronics: Analog and Digital* (Harcourt Brace Jovanovich, 1987).

[77] M. A. Howe *et al.*, NCD System Livetime and Efficiency Measurements, SNO Internal Document, 2004.

[78] J. W. Muller, Counting Statistics of a Poisson Process with Dead Time, Bureau International des Poids et Mesures, Rapport BIPM-111, 1970.

[79] J. W. Muller, Nucl. Instrum. Methods **117**, 401 (1974).

[80] J. W. Muller, A General Test for Detecting Dead-Time Distortions in a Poisson Process, Bureau International des Poids et Mesures, Rapport BIPM-1972/10, 1972.

[81] J. W. Muller, Nucl. Instrum. Methods **112**, 47 (1973).

[82] N. Tolich, NCD Data Cleaning: FREquency Analysis Kit, SNO Internal Document, 2005.

[83] H. Deng, S. Seibert, and L. Stonehill, Data Cleaning in NCD Phase, SNO Internal Document, 2005.

[84] G. Cowan, *Statistical Data Analysis* (Oxford Univrsity Press, 1998).

[85] D. S. Pressyanov, Am. J. Phys. **70**, 444 (2002).

[86] N. I. Adams, Phys. Rev. **44** (1933).

[87] L. Devol and A. Ruark, Phys. Rev. **51** (1937).

[88] A. Ruark and L. Devol, Phys. Rev. **49** (1936).

[89] A. Ruark, Phys. Rev. **56** (1939).

[90] K. Rielage, Proposal to Remove NCD Strings From Final NC Analysis, SNO Internal Document, 2007.

[91] A. G. Frodesen, O. Skjeggestad, and H. Tøfte, *Probability and Statistics in Particle Physics* (Universitetsforlaget, Oslo, 1979).

[92] A. E. Ruark and L. Devol, Phys. Rev. **48** (1935).

[93] H. Deng, FTD Pulse Shape Analysis, SNO Internal Document, 2007.

[94] N. Tolich, DWK Description and Performance, SNO Internal Document, 2007.

[95] R. Martin, The Queen's Grid Fitter, SNO Internal Document, 2006.

[96] R. Martin, The Queen's Grid Fitter Companion, SNO Internal Document, 2007.

[97] M. Miller, A Fisher vs. Energy Sig-Ex, SNO Internal Document, 2007.

[98] N. Oblath, Private Communication, 2007.

[99] H. Deng, Private Communication, 2007.

Appendix A

REMOVED NCDS

The following list of NCDs are to be removed from the NCD phase analysis due to the reasons summarized [90]. This list includes the two NCDs found to be afflicted with RCD, NCDs 1 and 31.

- NCD 0 – A significant number of low-energy events that arrived in bursts were found to contaminate the data set even after data cleaning cuts. Due to the high-rate bursts of these events, this string was purposefully removed from the DAQ system at various times throughout the NCD data set.

- NCD 1 – From logamp calibration data and the NRE calibration data, it was concluded that this string's resistive coupler became disconnected. Further analysis of the rate of thermal noise events and alpha rates confirmed RCD on this detector.

- NCD 3 – Occasionally, high rates of low-energy noise events were observed on this string. When this occurred, this detector was turned off by maximizing its threshold or removing it from the high-voltage supply.

- NCD 8 – The energy spectrum of events in this NCD during various neutron-source calibration data was observed to be unstable. One hypothesis is that a partially disconnected resistive coupler, i. e. have a high, but not infinite resistance, could mimic such behavior.

- NCD 18 – One of the counters in this NCD string leaked ^{3}He through its end-cap. This NCD also produced a large number of photodisintegration neutrons due to a localized region of high levels of radioactive contamination on the external surface.

- NCD 26 – A very low rate of events with unexplainable pulse shapes that were similar in shape to neutron capture events were observed on this NCD. While this NCD was removed from the neutrino flux analysis, alpha rates above 1.0 MeV should not have been affected.

- NCD 31 – From logamp calibration data and the NRE calibration data, it was concluded that this string's resistive coupler became disconnected. Further analysis of the rate of thermal noise events confirmed RCD on this detector.

Appendix B

PULSE REFLECTIONS

This appendix describes the pulse reflections seen in NCD electronics calibration pulses. It is necessary to calculate these effects in order to properly calibrate the electronics.

B.1 Pulse Reflections Between Two Mediums with Different Impedance

For a pulse of current I (and voltage V) traveling along a transmission line of impedance Z, the Thevenin equivalent circuit at an open end (imagine Fig. B.1 with nothing attached on the right side of point A) is twice the voltage, $2V$ in series with the transmission line's impedance Z. If a load $R + Z_2$ is attached to a transmission line of impedance Z_1, then the voltage of the signal propagating to the right between point A and ground (Fig. B.1) is

$$V_A = \frac{R + Z_2}{Z_1 + R + Z_2} \cdot 2V \tag{B.1}$$

Subsequently, the voltage at point B is given by

$$V_B = \frac{Z_2}{R + Z_2} \cdot V_A = \frac{Z_2}{Z_1 + R + Z_2} \cdot 2V \tag{B.2}$$

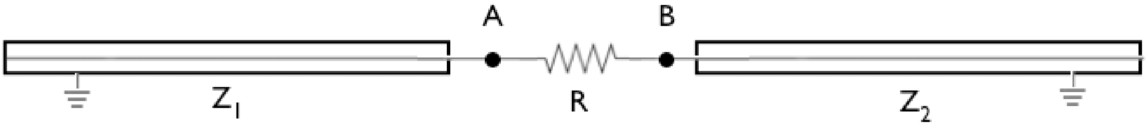

Figure B.1: Two transmission lines of impedances Z_1 and Z_2, connected by a resistor of strength R.

The current that flows into the second transmission line is $I_B = V_B/Z_2$.

The amplitude of the signal that is reflected at the resistor is given by

$$V_{Reflected} = V_A - V = \frac{R + Z_2 - Z_1}{Z_1 + R + Z_2} \cdot V \tag{B.3}$$

The current reflected back into the first transmission line is $I_{Reflected} = V_{reflected}/Z_1$.

From these simple equations, the relative amplitudes of the reflected pulses in the NCD hardware due to impedance mismatches can be calculated. The NCD is treated as a transmission line.

B.2 NCD Reflections

The hardware involved in the pulse reflections are the NCD cable, NCD counter + delay line, the resistive coupler and the preamp. Their impedances are denoted as Z_C, Z_N, R, and Z_P, respectively. The initial pulse that is injected into the preamp is of amplitude V_{in}. At the input of the preamp, there exists a 100 kΩ resistor with a 50 Ω load.

The current from the initial pulse, $I_{in} = V_{in}/100.05\ \text{k}\Omega$ is split into two at the junction between the NCD cable and the preamp. The section of the pulse that travels immediately to the NCD DAQ is defined as the 'first pulse," or "primary pulse." Alternatively it could be called the zeroth reflection. The amplitude of the first pulse is given by,

$$I_1 = \frac{Z_C}{Z_P + Z_C} \cdot \frac{V_{in}}{100.05\ \text{k}\Omega} \tag{B.4}$$

The remaining fraction of the input amplitude travels down the NCD cable and has an amplitude I_C equal to

$$I_C = \frac{Z_P}{Z_P + Z_C} \cdot \frac{V_{in}}{100.05\ \text{k}\Omega} \tag{B.5}$$

Comparing Fig. B.2 to Fig. B.1, one can see that the amplitude of the signal that arrives at the resistive coupler, V_E (that is propagating toward the NCD) is

$$V_E = \frac{R + Z_N}{Z_{sum}} \cdot 2V_C, \tag{B.6}$$

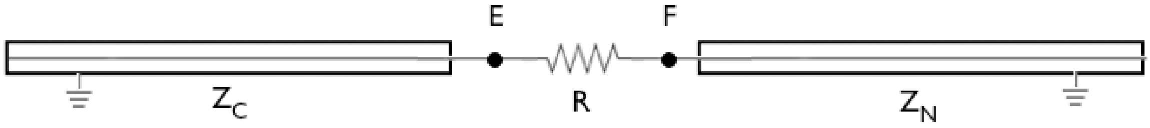

Figure B.2: The NCD cable with impedance Z_C connected to the resistive coupler of strength R, connected to the NCD counter with impedance Z_N. In the electronics model $Z_C = 100\ \Omega$, $R = 325\ \Omega$, and $Z_N = 415\ \Omega$.

where $V_C = Z_C I_C$ and $Z_{sum} = Z_C + R + Z_N$ has been defined for convenience. It follows that the amplitude of the reflected signal, defined as the "second pulse", or the first reflection, which arrives at the preamp a time δt_1 later (known as the NCD-cable propagation-time), is

$$V_2 = \frac{R + Z_N - Z_C}{Z_{sum}} \cdot V_C(t - \delta t_1) = \cdot \frac{R + Z_N - Z_C}{Z_{sum}} \cdot Z_C I_C(t - \delta t_1) \tag{B.7}$$

The current that propagates back to the preamp is $I_2 = V_2/Z_C$,

$$I_2 = \frac{R + Z_N - Z_C}{Z_{sum}} \cdot I_C(t - \delta t_1) \tag{B.8}$$

The amplitude of the signal that propagates down the NCD at point F in Fig. B.2 is given by

$$V_N = \frac{Z_N}{Z_{sum}} \cdot 2 Z_C I_C \tag{B.9}$$

with a current

$$I_N = V_N/Z_N = \frac{2 Z_C I_C}{Z_{sum}} \tag{B.10}$$

Now the current I_N that is propagating along the NCD bounces off of the end of the delay line and arrives at the resistive coupler at a time δt_2 after arriving at the input of the NCD counter. This is called the "third pulse", or the second reflection. The amplitude of the signal that propagates through the resistive coupler and along the NCD cable onto the preamp is calculated in the same way (Eq. B.2).

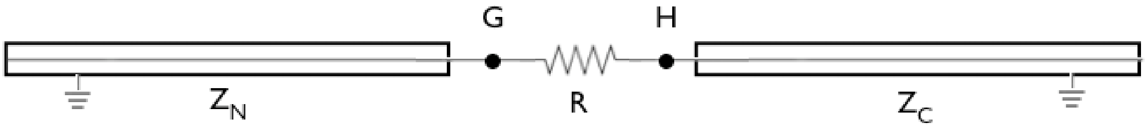

Figure B.3: The NCD counter with impedance Z_N connected to the resistive coupler of strength R, connected to the NCD cable with impedance Z_C. In the electronics model $Z_C = 100\ \Omega$, $R = 325\ \Omega$, and $Z_N = 415\ \Omega$.

The signal propagating toward the NCD cable at point H (Fig. B.3) V_3 is

$$V_3 = \frac{Z_C}{Z_{sum}} \cdot 2V_N = \frac{4Z_N Z_C}{Z_{sum}^2} Z_C I_C(t - \delta t_1/2 - \delta t_2) \tag{B.11}$$

Since this is the pulse at point H, the pulse still propagates another $\delta t_1/2$ before it arrives at the preamp. Hence the time argument for I_C in the above equation. The current is

$$I_3 = \frac{4Z_N Z_C}{Z_{sum}^2} I_C(t - \delta t_1/2 - \delta t_2) \tag{B.12}$$

Due to the mismatch between the sum of the NCD cable impedance and resistive coupler and the impedance of the NCD counter, a small amount of this signal is reflected back down along the NCD. This is known as the “fifth pulse”, or fourth reflection. (The “fourth pulse”, or third reflection will be discussed later.)

The amplitude of the fifth pulse at point G is given by

$$V_G = \frac{R + Z_C - Z_N}{Z_{sum}} \cdot V_N \tag{B.13}$$

The current of this signal is $I_G = V_G/Z_N$ and the same prescription is applied again. When this signal arrives back at the resistive coupler, the amplitude of the signal that gets transmitted to the NCD cable is

$$V_5 = \frac{Z_C}{Z_{sum}} \cdot 2V_G = \frac{2Z_N Z_C(R + Z_C - Z_N)}{Z_{sum}^3} \cdot Z_C I_C(t - \delta t_1/2 - 2\delta t_2) \tag{B.14}$$

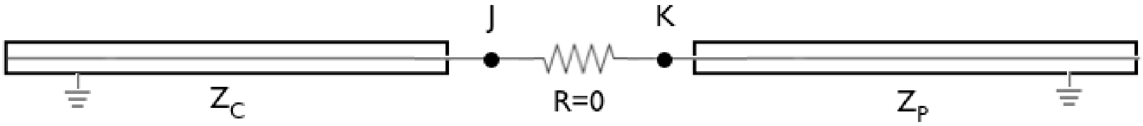

Figure B.4: The NCD cable with impedance Z_C connected to the NCD preamp with impedance Z_P. In the electronics model $Z_C = 100\ \Omega$ and $Z_P = 100\ \Omega$.

with a current $I_5 = V_5/Z_C$. There will subsequently be more reflections as this pulse bounces back and forth along the NCD. However, the amplitude of these reflections decreases significantly and becomes much smaller than the RMS of the baseline noise. The current logamp pulse injects a sine wave of amplitude 750 mV (peak-to-peak) through a 30 dB attenuator and the PDS with gain of ~ 7.3. The amplitude of the pulse of the fourth reflection that arrives at the input of the MUX (after the 27.5 mV/μA preamp gain) is equal to 0.033 mV, 0.13% of the original signal.

B.3 The Third Reflection

If there exists an impedance mismatch between the NCD cable and preamp, then reflections will occur at that junction. The most significant effect will be when the first reflection (or, the second pulse), which reflected back off of the resistive coupler, arrives at the preamp's input. The calculation of the amplitude of this is straight forward and aided by Fig. B.4.

A signal of amplitude V_C propagating along the NCD cable toward the preamp has an amplitude of V_K which is equal to

$$V_K = \frac{Z_P}{Z_C + Z_P} \cdot 2V_C \tag{B.15}$$

A reflection due to an impedance mismatch would create a signal traveling V_J in the opposite direction with amplitude

$$V_J = \frac{Z_P - Z_C}{Z_P + Z_C} \cdot V_C \tag{B.16}$$

The impedances of the NCD, NCD cable, and preamp are all frequency dependent. However, we are currently using the model where the cable and preamp impedances are matched. If there was a difference, modifications to the full expression for the injected pulse with all the reflections would need to be modified.

B.4 The Final Reflection Equation

Putting all of the reflections together, the final expression of the signal $I_p(t)$ that arrives at the preamp is

$$I_p(t) = I_1(t) + I_2(t) + I_3(t) + I_5(t) \tag{B.17}$$

$$\begin{aligned} I_p(t) = \frac{Z_C}{Z_P + Z_C}\frac{V_{in}(t)}{100.05\ \text{k}\Omega} + \frac{Z_P}{Z_P + Z_C}\Bigg\{ & \frac{R + Z_N - Z_C}{Z_{sum}} \cdot \frac{V_{in}(t - \delta t_1)}{100.05\ \text{k}\Omega} + \\ & \frac{4Z_N Z_C}{Z_{sum}^2} \cdot \frac{V_{in}(t - \delta t_1 - \delta t_2)}{100.05\ \text{k}\Omega} + \frac{2Z_N Z_C \cdot (R + Z_C - Z_N)}{Z_{sum}^3} \cdot \frac{V_{in}(t - \delta t_1 - 2\delta t_2)}{100.05\ \text{k}\Omega} \Bigg\} \end{aligned} \tag{B.18}$$

The voltage of the signal at the output of the preamp is $V_p(t) = I_p(t) \cdot g_{preamp}$, where g_{preamp} is the gain of the preamp and has been measured to be 27.5 mV/μA.

Appendix C

NCD STRING NUMBER TO STRING NAME CONVERSION

Table C.1: Initially, the NCD strings were labeled using an alphanumeric system. However, in the data acquisition system, a numbering system was used since this was an easier way to organize data and string information. It is common to find both naming systems throughout documentation on the NCDs. This dissertation strictly uses the numbering system. For cross-referencing purposes, this table gives the conversion between these two NCD naming conventions.

0	N4	10	I6	20	I3	30	I2
1	M8	11	K6	21	K4	31	K2
2	K8	12	M6	22	M4	32	J2
3	I7	13	J6	23	J4	33	M2
4	J8	14	N3	24	L4	34	L1
5	L2	15	L3	25	N2	35	J1
6	J7	16	J5	26	J3	36	I1
7	M7	17	M5	27	M3	37	K1
8	K7	18	K5	28	K3	38	M1
9	I8	19	I5	29	I4	39	N1

Appendix D

DETECTOR PERFORMANCE

This appendix describes two system checks that were performed on the 7th version of the NCD data-set. Each of these checks searched the data for instances where either the oscilloscopes were not acquiring data, or the shaper/ADCs stopped acquiring data. The runs identified in these tests were eventually removed from the data-set, along with the removal of runs from different tests performed by others, resulting in the 8th version of the NCD data-set run list.

D.1 Oscilloscope Trigger Checks

In the process of analysis described in this dissertation, it was observed that the rate of oscilloscope triggers for one or both oscilloscopes dropped to zero. Using the runs from the 7th NCD data set, the number of events per hour for each hour of data was measured. Each instance where either oscilloscope trigger rate was zero or the difference in the trigger rates was greater than 10% is reported here.

In addition, the average rate of PULSE_GT triggers was measured. The PULSE_GT triggers were "global trigger" events in SNO that triggered the detector at a rate of 5 Hz. The PULSE_GT events were used for measuring the PMT system live-time and monitoring backgrounds (normally, a minimum number of PMT fires are required to produce an event, but the PULSE_GT creates an event regardless). These events are employed here as a tool to ensure the detector was taking data since the code in this analysis measured the rate of events over a period of time without regard for the start and stop times of each run. A threshold of a PULSE_GT rate of 4.4 Hz was set to ensure that the SNO/NCD DAQ was running[1]. When an oscilloscope trigger rate was found to be zero or when the rate of the two oscilloscope triggers differed significantly, and the PULSE_GT rate was greater than 4.4 Hz, I went back through the data set to determine the run number.

D.1.1 Results

Table D.1 lists the neutrino runs that were found to have an average rate of oscilloscope triggers of zero for at least one oscilloscope. During runs 48302 and 51390 there were a few hours of these runs where neither oscilloscope digitized an event. During run 63759, no events were digitized by scope 0. Finally, during run 65900, no events were digitized by scope 1. Figures D.1(a)-D.1(d) display histograms of the average rate of triggers on both oscilloscopes and the average rate of the PULSE_GT triggers. It is not known why the oscilloscope trigger rates were zero during these runs.

D.1.2 Time Between Successive Oscilloscope Triggers

If A events occur randomly with an average rate, r, then the distribution of the time between successive triggers, Δt is

$$P(A, r, \Delta t) = Ae^{-r\Delta t} \tag{D.1}$$

The distribution of Δt for oscilloscope triggers in the entire NCD data set, removing only the events which occur in bursts[2], along with Eq. D.1 evaluated at $A = 2.7 \times 10^6$ and $r = 0.27$ Hz, is shown in Fig. D.1.2. The data shows, approximately, that oscilloscope triggers occur randomly. For some runs, however, there are anomalously large values of Δt, which could be indicative of problems with the data acquisition system. For each run, the time between successive oscilloscope triggers was recorded

---

[1] The measured PULSE_GT rate in the data files is less than 5 Hz because of the NHIT monitor, which produced dead-time in measure of the PULSE_GT rate.

[2] These were removed using the MUX and shaper/ADC burst cut.

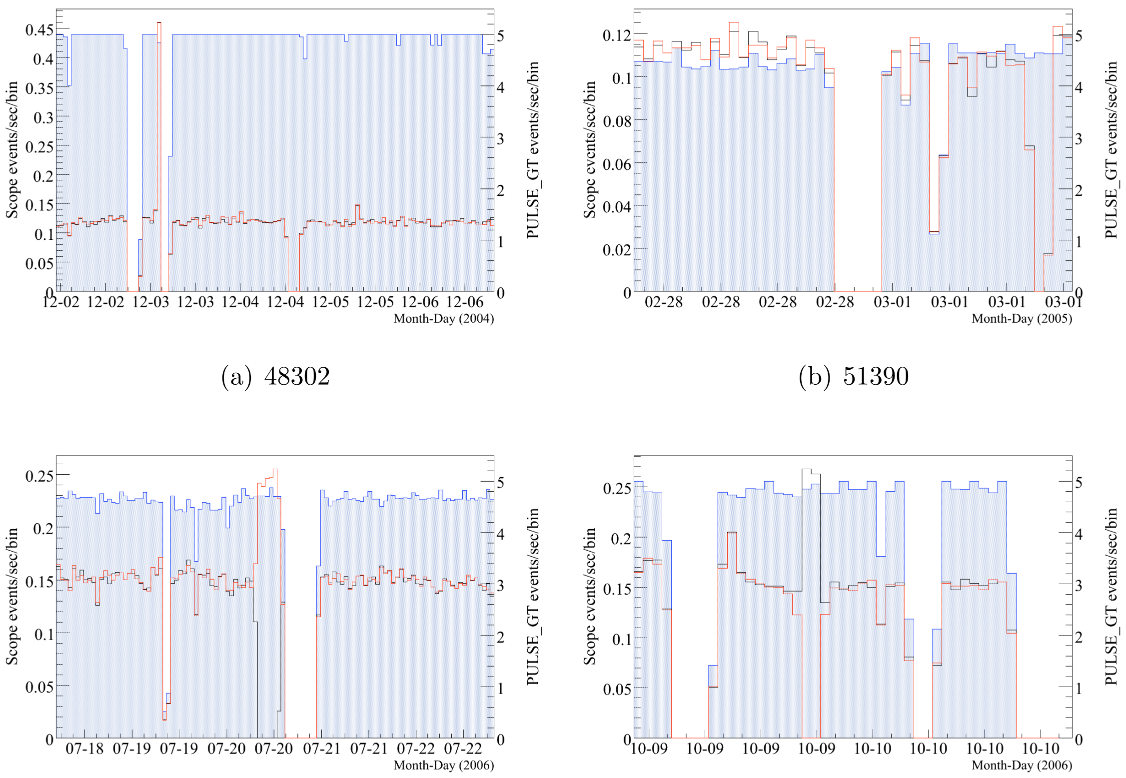

(a) 48302

(b) 51390

(c) 63759

(d) 65900

Figure D.1: The period near the Instances where an oscilloscope trigger rate was zero are shown. The run number for the particular run where the trigger rate was zero is shown. The PULSE_GT trigger rate is shaded blue, rate of events on oscilloscope 0 is the black histogram and the rate of events on oscilloscope 1 is the red histogram.

Table D.1: The following runs were found to have a locked-out oscilloscope and they were subsequently removed from the final run list. The estimated dead-time caused by locked-out oscilloscopes is listed (T_{dead}) – the uncertainty in the last digit is the value in parenthesis. † For runs 63759 and 65900, only one oscilloscope was locked-out. During these runs one oscilloscope digitized all of the events, but since there was only one working oscilloscope the detection efficiency during these runs is unknown. Thus these runs were removed from the neutrino flux analysis.

Run Number	Date (M-D-Y)	Comment	T_{dead} (hours)	Fig.
48302	12-4-2004	Scope 0 and 1 rate is zero	3.398(5)	D.1(a)
51390	3-1-2005	Scope 0 and 1 rate is zero	2.226(5)	D.1(b)
63759	7-20-2006	Scope 0 rate is zero	6.018(2)†	D.1(c)
65900	10-9-2006	Scope 1 rate is zero	2.316(1)†	D.1(d)

for events on each oscilloscope. Then, for each run, the maximum observed Δt was determined, labeled Δt_{max}. Runs where $\Delta t_{max} > 70$ sec. were removed from the NCD data set. Fig. D.3 shows the distribution of Δt_{max} for each run in the 7th neutrino runlist and Table D.2 lists the runs that were subsequently removed.

In addition, a similar analysis, performed by another member of the SNO Collaboration, measured the time between successive triggers on each oscilloscope and removed runs where $\Delta t_{max}^{\text{scope } 0/1} > 100$ sec. [99]. The list of runs removed by this cut is found in Table D.3. An examination of each run's Δt distribution would be needed for further investigation.

D.2 Shaper/ADC Acquisition Checks

Like the tests for the instances of zero MUX+Scope rates, a search was done for zero shaper/ADC counts per hour. These tests were performed in the same manner as

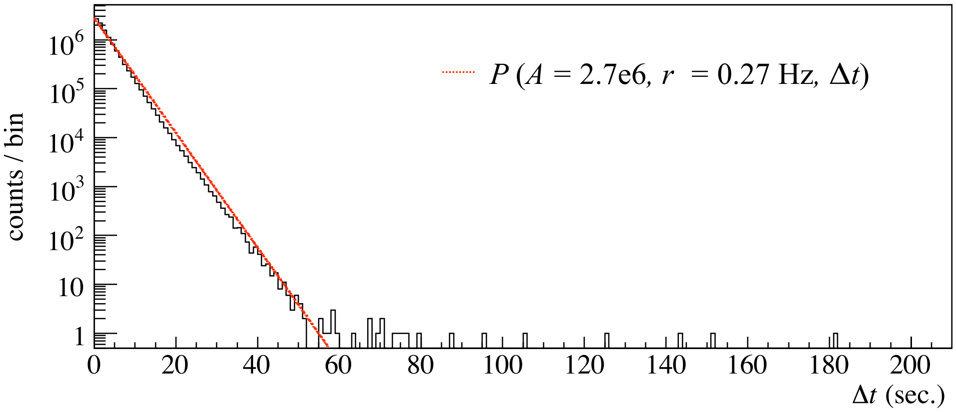

Figure D.2: The distribution of the time between successive oscilloscope triggers, Δt, approximately follows a distribution expected for randomly occurring events.

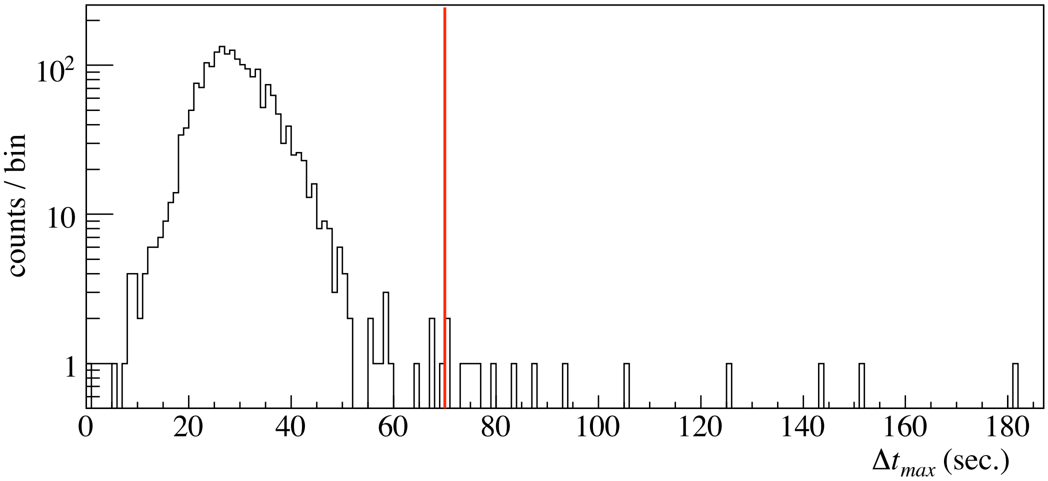

Figure D.3: A cut at $\Delta t_{max} > 70$ seconds was made to remove runs where the oscilloscopes may have been locked out for large amounts of time.

Table D.2: The list of run numbers that were removed by the $\Delta t_{max} > 70$ seconds cut.

Run Number	Δt_{max}	Run Number	Δt_{max}
48224	70.8	58394	83.5
48493	75.4	59258	74.8
55035	73.4	60218	143.3
55447	79.3	60220	125.6
55588	76.7	60241	181.2
57362	151.1	61891	93.6
57379	105.9	62299	70.4
57478	87.7		

Table D.3: The list of run numbers that were removed by the $\Delta t_{max}^{\text{scope } 0/1} > 100$ seconds cut.

48408
48412
48595
48614
50026
50756
50758
50760
51899
54842
57399
59315
61884
63228
63502
63628

for the oscilloscope trigger rate checks. No instances of zero shaper/ADC counts per hour were found in the data set and there is no reason to suspect the shaper/ADC system stopped acquiring data.

Appendix E

NOISE ANALYSIS FITS

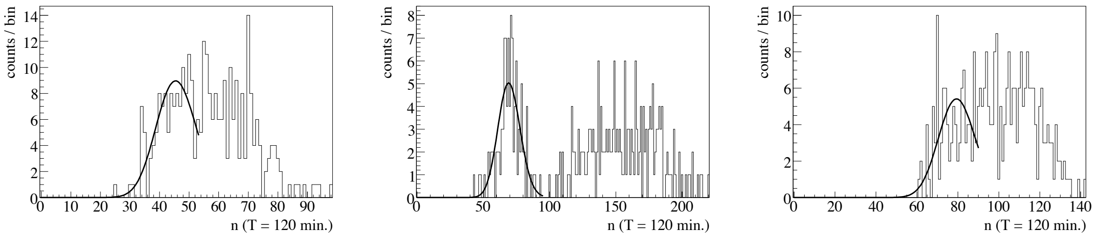

(a) NCD 0. (b) NCD 1. (c) NCD 2.

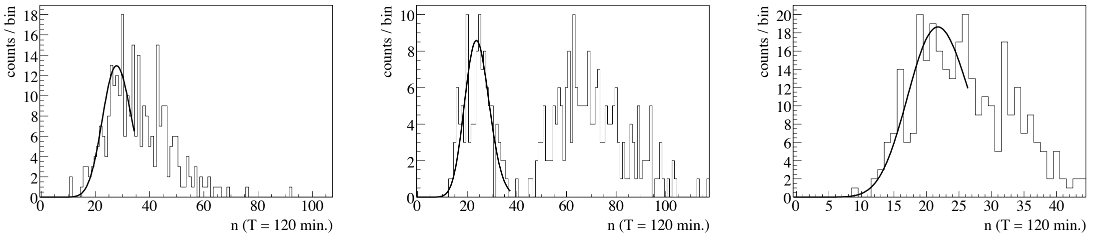

(d) NCD 3. (e) NCD 4. (f) NCD 5.

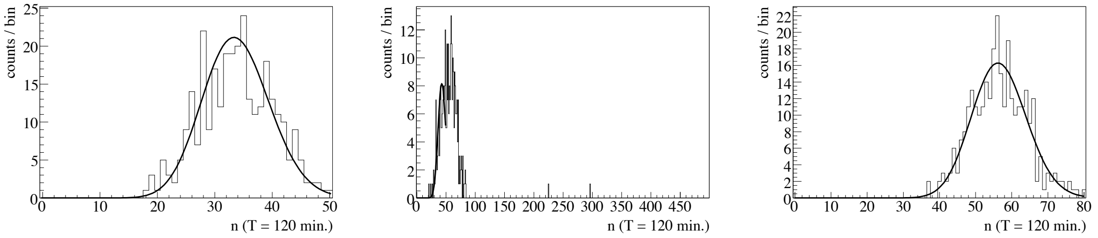

(g) NCD 6. (h) NCD 7. (i) NCD 8.

Figure E.1: The distribution of the number of baseline noise events in the open data set from the analysis in Chapter 7 for NCDs 0 to 8. Also shown are the best-fit Eq. 7.1 curve for each NCD. The best-fit Eq. 7.1 curve is the continuous Poisson distribution, as noted in the footnote 6 in § 7.6.

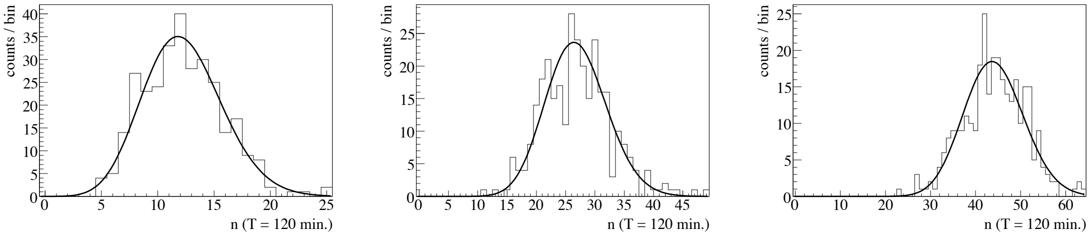

(a) NCD 9. (b) NCD 10. (c) NCD 11.

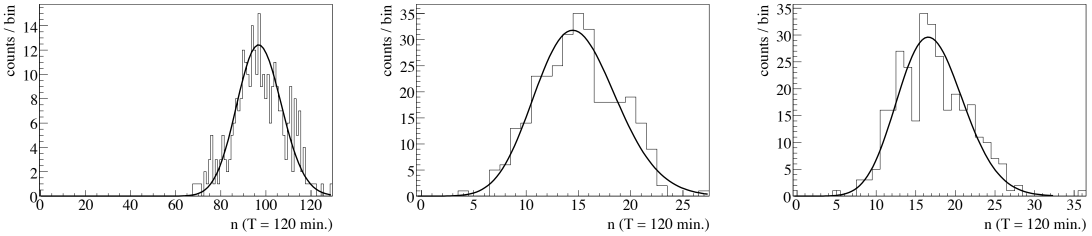

(d) NCD 12. (e) NCD 13. (f) NCD 14.

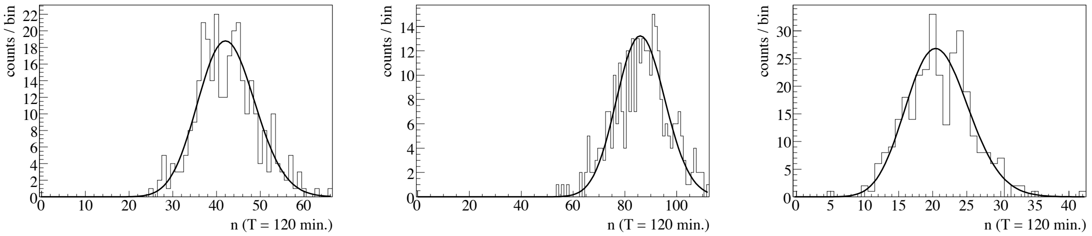

(g) NCD 15. (h) NCD 16. (i) NCD 17.

Figure E.2: The distribution of the number of baseline noise events in the open data set from the analysis in Chapter 7 for NCDs 9 to 7. Also shown are the best-fit Eq. 7.1 curve for each NCD. The best-fit Eq. 7.1 curve is the continuous Poisson distribution, as noted in the footnote 6 in § 7.6.

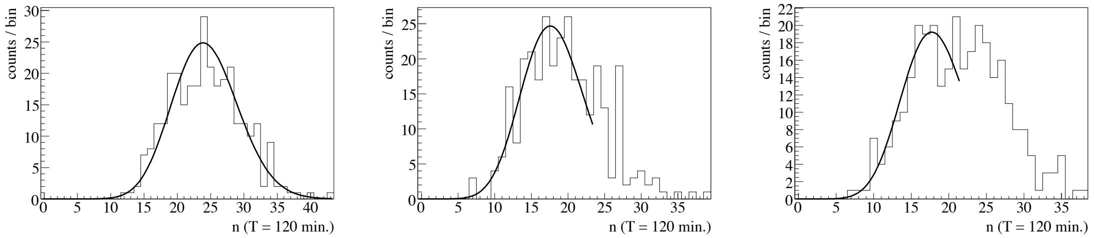

(a) NCD 18. (b) NCD 19. (c) NCD 20.

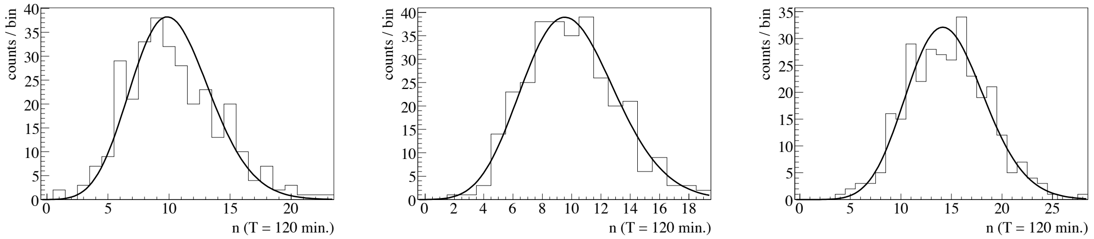

(d) NCD 21. (e) NCD 22. (f) NCD 23.

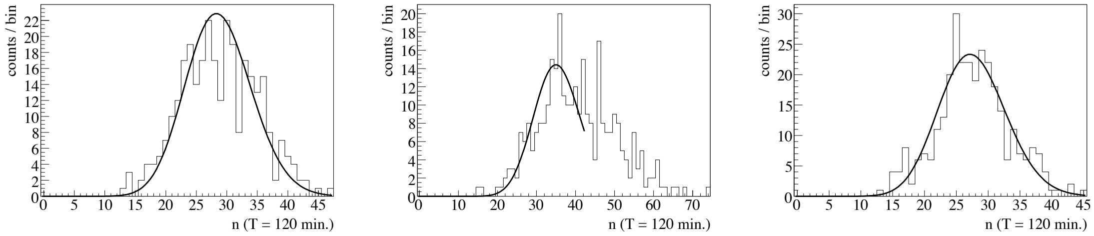

(g) NCD 24. (h) NCD 25. (i) NCD 26.

Figure E.3: The distribution of the number of baseline noise events in the open data set from the analysis in Chapter 7 for NCDs 18 to 26. Also shown are the best-fit Eq. 7.1 curve for each NCD. The best-fit Eq. 7.1 curve is the continuous Poisson distribution, as noted in the footnote 6 in § 7.6.

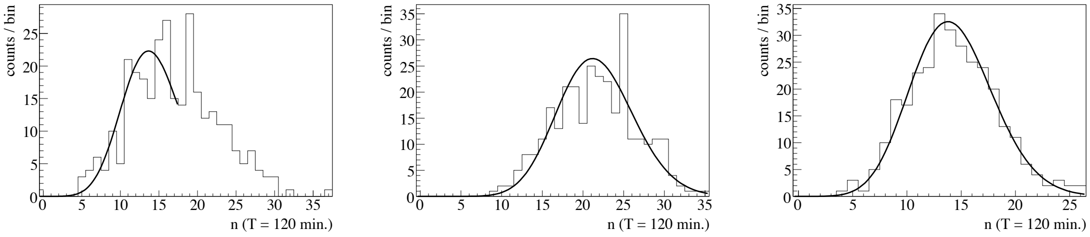

(a) NCD 27. (b) NCD 28. (c) NCD 29.

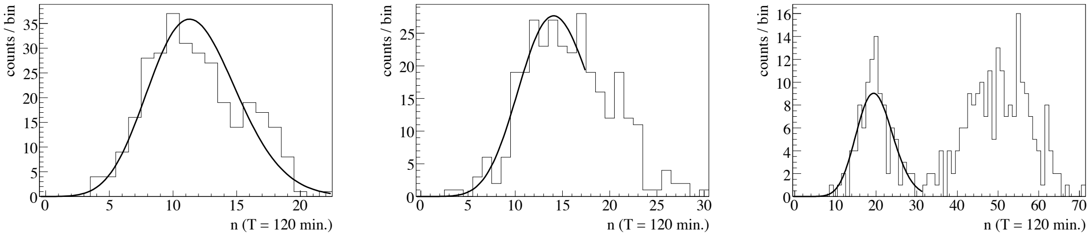

(d) NCD 30. (e) NCD 31. (f) NCD 32.

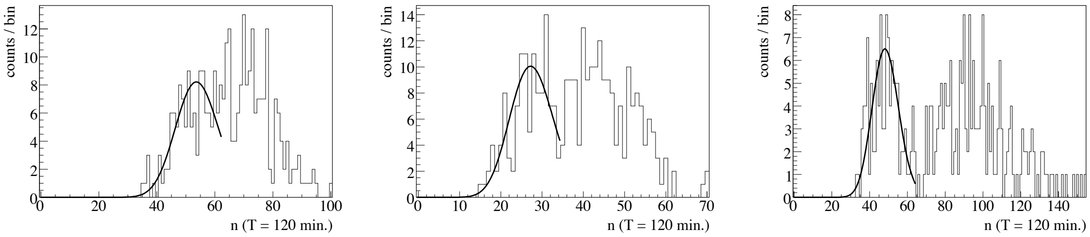

(g) NCD 33. (h) NCD 34. (i) NCD 35.

Figure E.4: The distribution of the number of baseline noise events in the open data set from the analysis in Chapter 7 for NCDs 27 to 35. Also shown are the best-fit Eq. 7.1 curve for each NCD. The best-fit Eq. 7.1 curve is the continuous Poisson distribution, as noted in the footnote 6 in § 7.6.

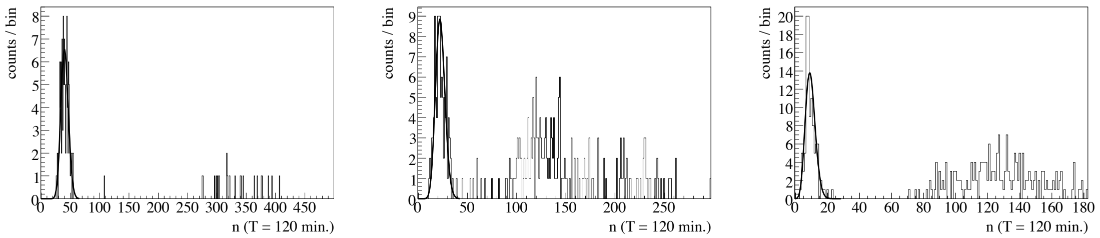

(a) NCD 36.

(b) NCD 37.

(c) NCD 38.

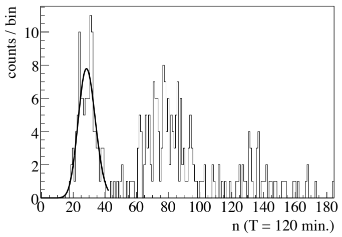

(d) NCD 39.

Figure E.5: The distribution of the number of baseline noise events in the open data set from the analysis in Chapter 7 for NCDs 36 to 39. Also shown are the best-fit Eq. 7.1 curve for each NCD. The best-fit Eq. 7.1 curve is the continuous Poisson distribution, as noted in the footnote 6 in § 7.6.

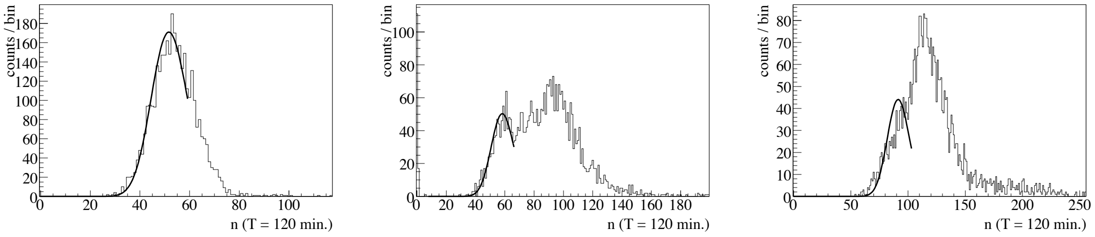

(a) NCD 0. (b) NCD 1. (c) NCD 2.

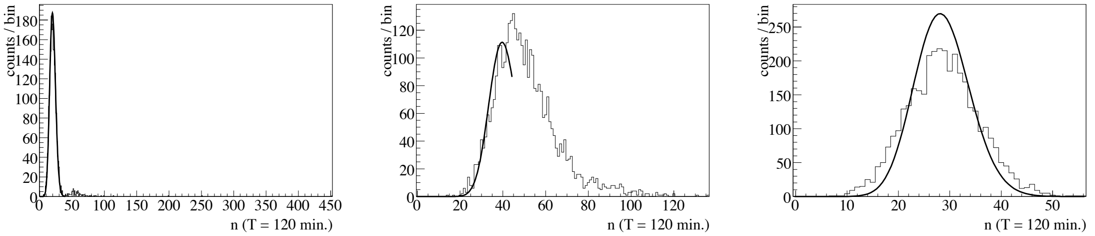

(d) NCD 3. (e) NCD 4. (f) NCD 5.

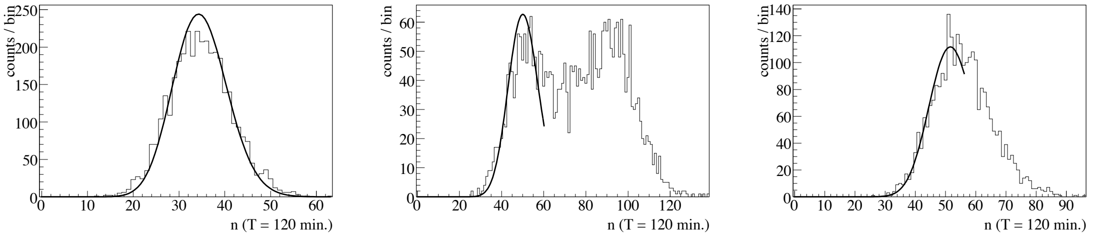

(g) NCD 6. (h) NCD 7. (i) NCD 8.

Figure E.6: The distribution of the number of baseline noise events in the pre-NRE data set from the analysis in Chapter 7 for NCDs 0 to 8. Also shown are the best-fit Eq. 7.1 curve for each NCD. The best-fit Eq. 7.1 curve is the continuous Poisson distribution, as noted in the footnote 6 in § 7.6.

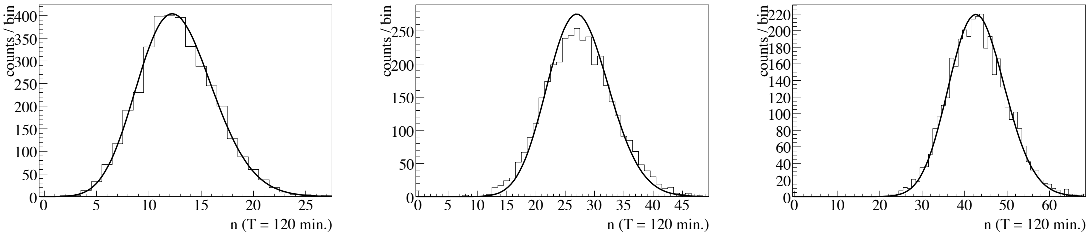

(a) NCD 9.

(b) NCD 10.

(c) NCD 11.

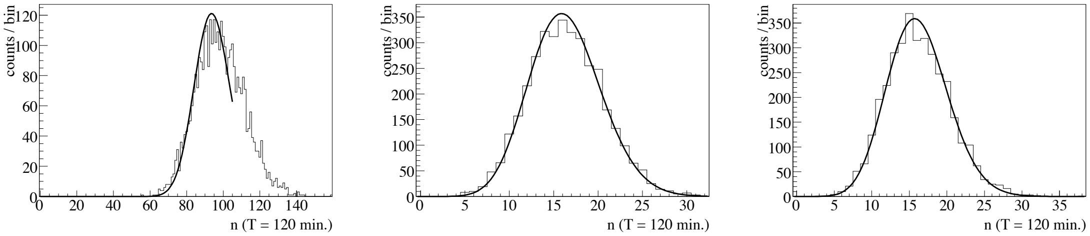

(d) NCD 12.

(e) NCD 13.

(f) NCD 14.

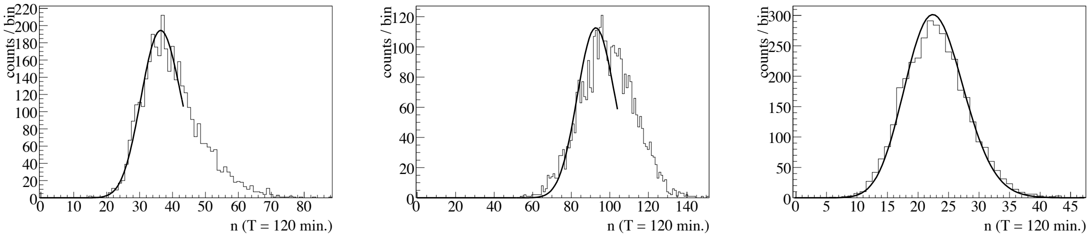

(g) NCD 15.

(h) NCD 16.

(i) NCD 17.

Figure E.7: The distribution of the number of baseline noise events in the pre-NRE data set from the analysis in Chapter 7 for NCDs 9 to 17. Also shown are the best-fit Eq. 7.1 curve for each NCD. The best-fit Eq. 7.1 curve is the continuous Poisson distribution, as noted in the footnote 6 in § 7.6.

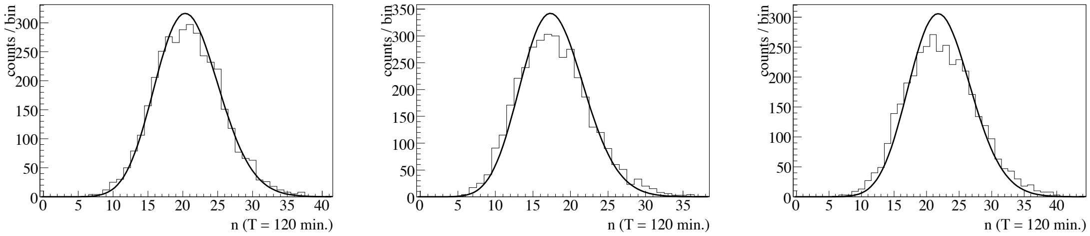

(a) NCD 18.

(b) NCD 19.

(c) NCD 20.

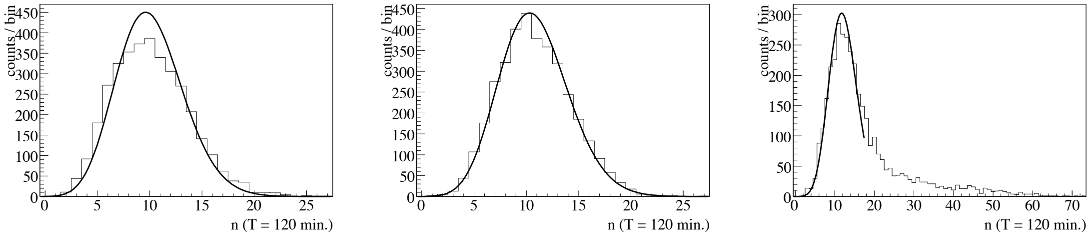

(d) NCD 21.

(e) NCD 22.

(f) NCD 23.

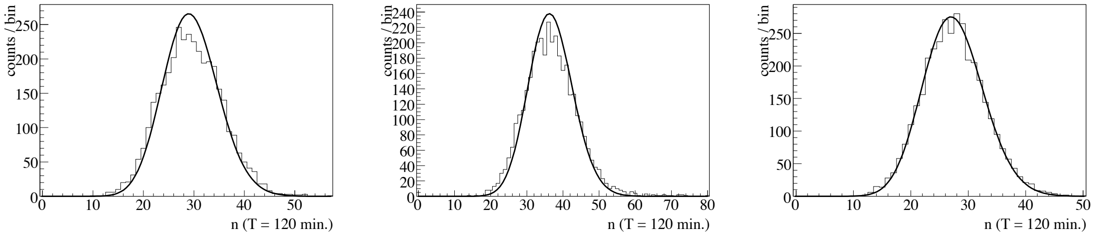

(g) NCD 24.

(h) NCD 25.

(i) NCD 26.

Figure E.8: The distribution of the number of baseline noise events in the pre-NRE data set from the analysis in Chapter 7 for NCDs 18 to 26. Also shown are the best-fit Eq. 7.1 curve for each NCD. The best-fit Eq. 7.1 curve is the continuous Poisson distribution, as noted in the footnote 6 in § 7.6.

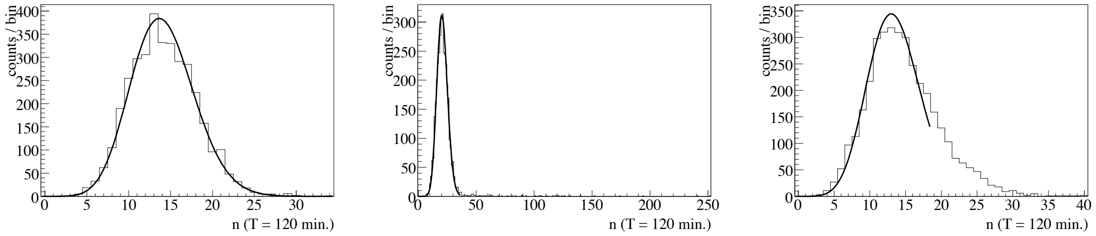

(a) NCD 27.

(b) NCD 28.

(c) NCD 29.

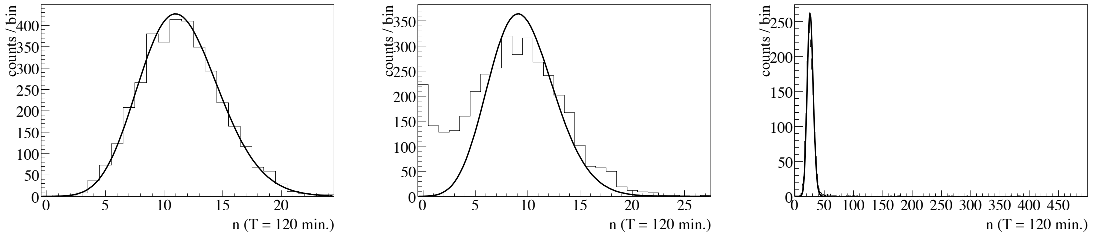

(d) NCD 30.

(e) NCD 31.

(f) NCD 32.

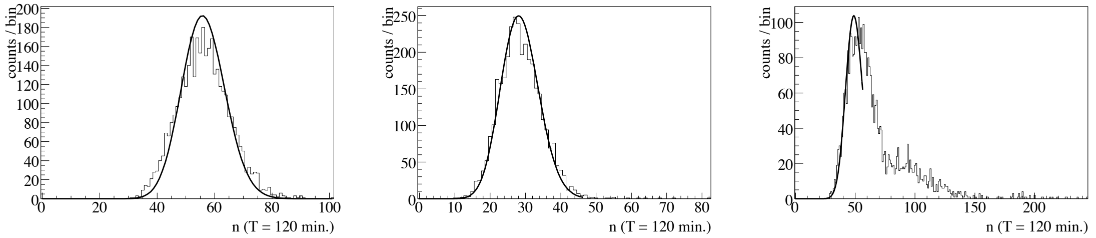

(g) NCD 33.

(h) NCD 34.

(i) NCD 35.

Figure E.9: The distribution of the number of baseline noise events in the pre-NRE data set from the analysis in Chapter 7 for NCDs 27 to 35. Also shown are the best-fit Eq. 7.1 curve for each NCD. The best-fit Eq. 7.1 curve is the continuous Poisson distribution, as noted in the footnote 6 in § 7.6.

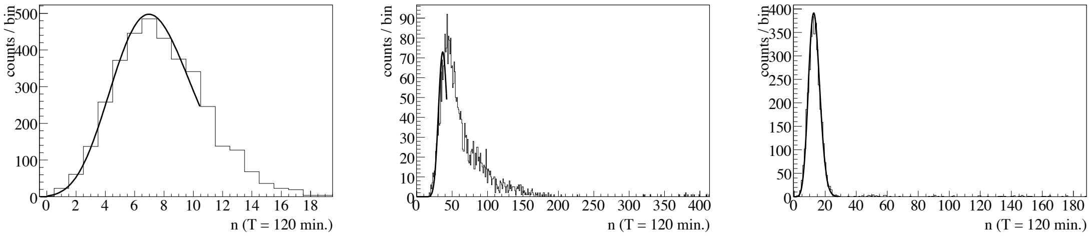

(a) NCD 36.

(b) NCD 37.

(c) NCD 38.

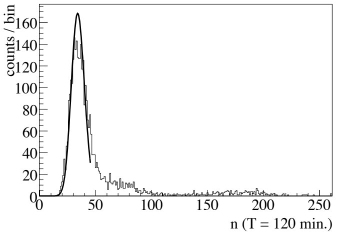

(d) NCD 39.

Figure E.10: The distribution of the number of baseline noise events in the pre-NRE data set from the analysis in Chapter 7 for NCDs 36 to 39. Also shown are the best-fit Eq. 7.1 curve for each NCD. The best-fit Eq. 7.1 curve is the continuous Poisson distribution, as noted in the footnote 6 in § 7.6.

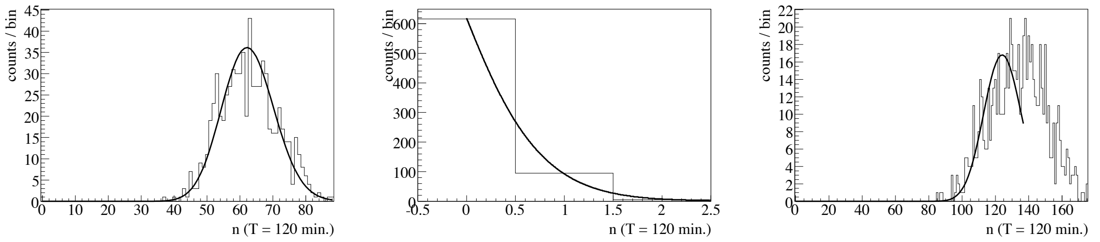

(a) NCD 0. (b) NCD 1. (c) NCD 2.

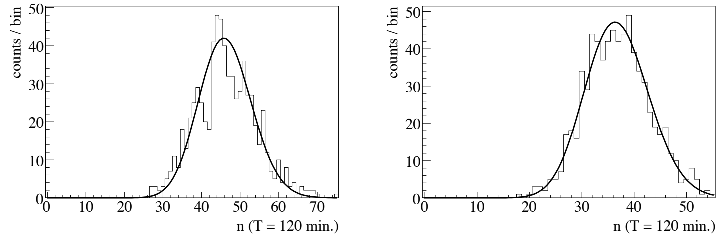

(d) NCD 4. (e) NCD 5.

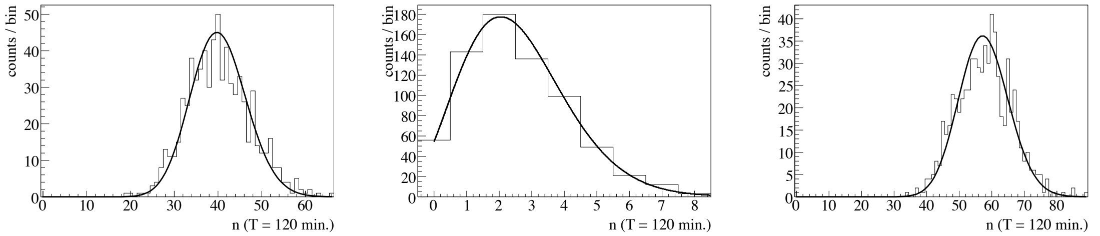

(f) NCD 6. (g) NCD 7. (h) NCD 8.

Figure E.11: The distribution of the number of baseline noise events in the post-NRE data set from the analysis in Chapter 7 for NCDs 0 to 8. Also shown are the best-fit Eq. 7.1 curve for each NCD. The best-fit Eq. 7.1 curve is the continuous Poisson distribution, as noted in the footnote 6 in § 7.6.

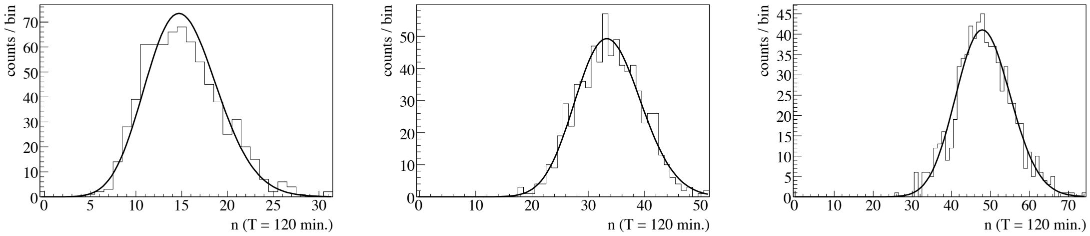

(a) NCD 9.

(b) NCD 10.

(c) NCD 11.

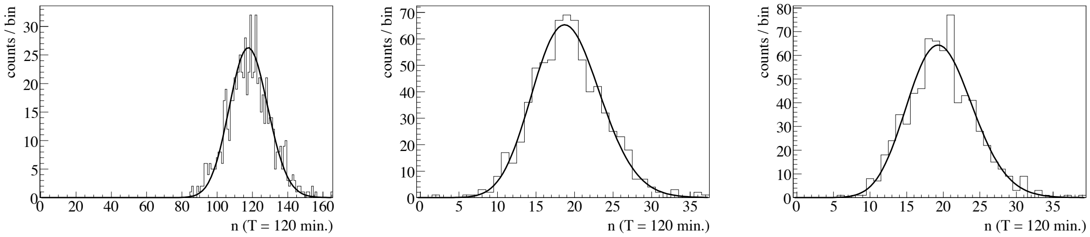

(d) NCD 12.

(e) NCD 13.

(f) NCD 14.

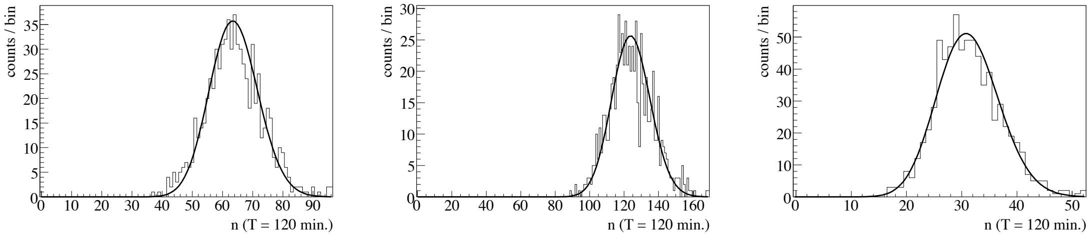

(g) NCD 15.

(h) NCD 16.

(i) NCD 17.

Figure E.12: The distribution of the number of baseline noise events in the post-NRE data set from the analysis in Chapter 7 for NCDs 9 to 17. Also shown are the best-fit Eq. 7.1 curve for each NCD. The best-fit Eq. 7.1 curve is the continuous Poisson distribution, as noted in the footnote 6 in § 7.6.

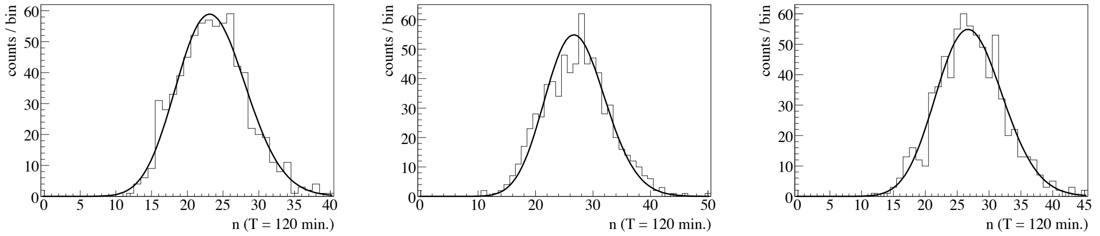

(a) NCD 18. (b) NCD 19. (c) NCD 20.

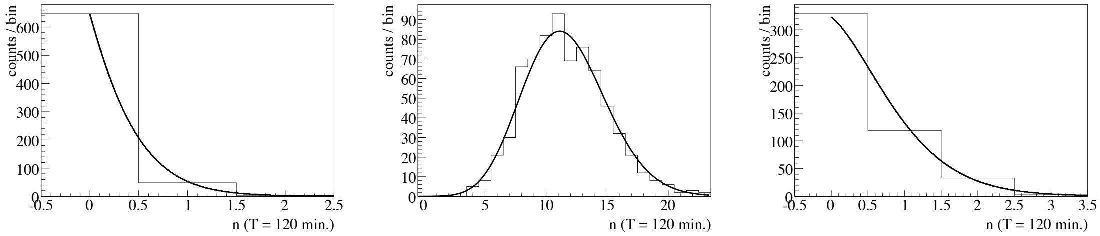

(d) NCD 21. (e) NCD 22. (f) NCD 23.

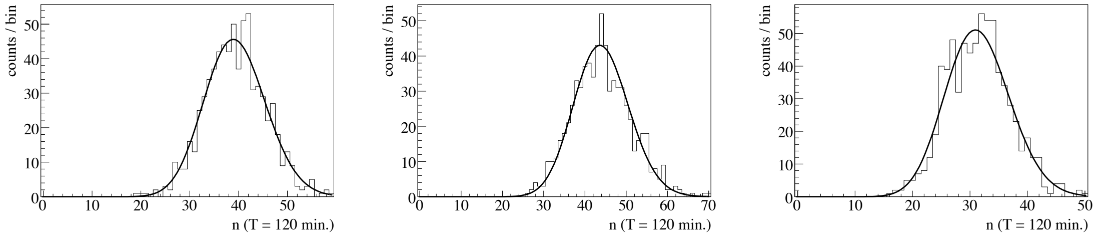

(g) NCD 24. (h) NCD 25. (i) NCD 26.

Figure E.13: The distribution of the number of baseline noise events in the post-NRE data set from the analysis in Chapter 7 for NCDs 18 to 26. Also shown are the best-fit Eq. 7.1 curve for each NCD. The best-fit Eq. 7.1 curve is the continuous Poisson distribution, as noted in the footnote 6 in § 7.6.

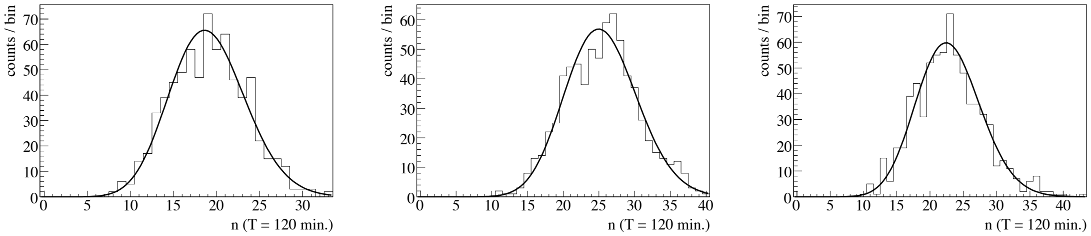

(a) NCD 27. (b) NCD 28. (c) NCD 29.

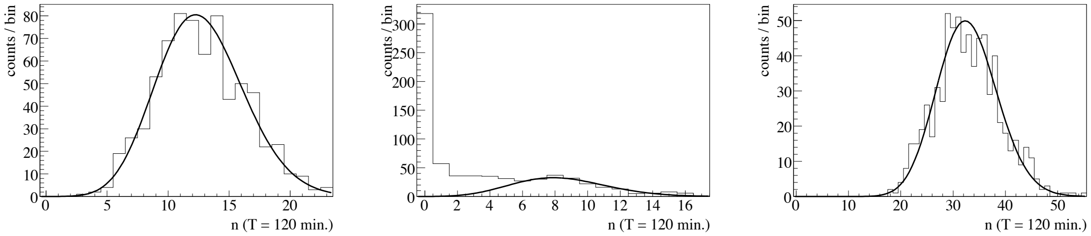

(d) NCD 30. (e) NCD 31. (f) NCD 32.

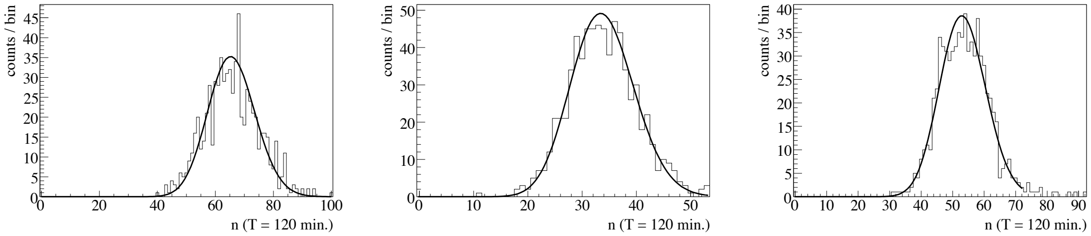

(g) NCD 33. (h) NCD 34. (i) NCD 35.

Figure E.14: The distribution of the number of baseline noise events in the post-NRE data set from the analysis in Chapter 7 for NCDs 27 to 35. Also shown are the best-fit Eq. 7.1 curve for each NCD. The best-fit Eq. 7.1 curve is the continuous Poisson distribution, as noted in the footnote 6 in § 7.6.

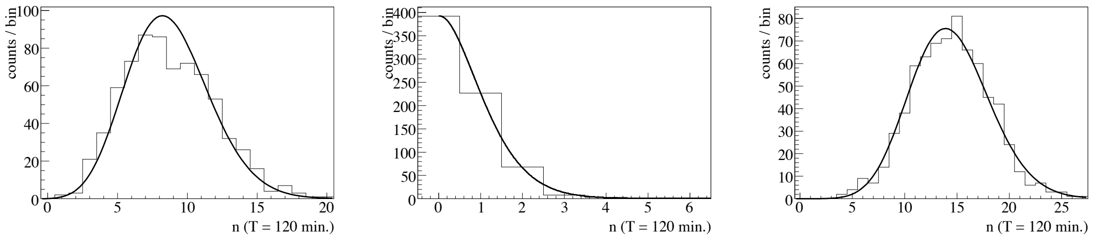

(a) NCD 36.

(b) NCD 37.

(c) NCD 38.

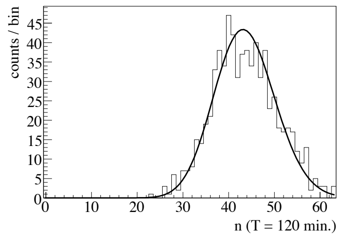

(d) NCD 39.

Figure E.15: The distribution of the number of baseline noise events in the post-NRE data set from the analysis in Chapter 7 for NCDs 36 to 39. Also shown are the best-fit Eq. 7.1 curve for each NCD. The best-fit Eq. 7.1 curve is the continuous Poisson distribution, as noted in the footnote 6 in § 7.6.

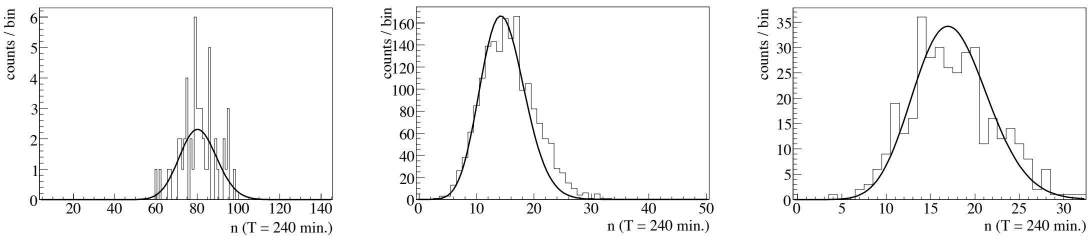

(a) Open.

(b) Pre-NRE.

(c) Post-NRE.

Figure E.16: The distribution of the number of baseline noise events on NCD 36 in (a) the open data set, (b) the pre-NRE data set and (c) the post-NRE data set for T = 240 min. Also shown are the best-fit Eq. 7.1 curve for each data set. The best-fit Eq. 7.1 curve is the continuous Poisson distribution, as noted in the footnote 6 in § 7.6. See Table E.1 for the fit results.

Table E.1: The results of fitting to the noise distribution to Eq. 7.1 for $T = 240$ minutes for NCD 36 in the open, pre-NRE and post-NRE data sets. The column $O_{n=0}$ is the occupancy of the $n = 0$ bin, N_{tot} is the number of 240-minute bins in the data set with nominal threshold and high-voltage settings, and n_{max} is the largest bin with an occupancy of at least one.

Data Set	$O_{n=0}$	N_{tot}	n_{max}	ρ	A	fit range, n (min - max)	χ^2/d.o.f
Open	0	93	3105	80.6 ± 1	52 ±7.2	0 - 500	23.3/23
Pre-NRE	0	1789	774	14.7 ± 0.2	1596±52	0 - 17	24.8/14
Post-NRE	0	357	32	17.5 ± 0.2	357 ±19	0 - 32	45.3/25

VITA

Dr. G. Adam Cox-Mobrand, born in Crawfordsville, Indiana, attended Arizona State University and earned a Bachelor of Science degree (*magna cum laude*) in Physics in 2000. He earned his Master of Science degree in 2003 and Doctor of Philosophy in 2008 at the University of Washington. His is a member of the American Physical Society and has been involved in the Forum for Graduate Student Affairs within the APS. He and his wife, Amanda, reside in Karlsruhe, Germany where he has accepted a Postdoctoral research position working on the KATRIN experiment.